Measurement of the $e^+e^- \to \pi^+\pi^-$ cross section using initial state radiation at BESIII

Dissertation
zur Erlangung des Grades
"Doktor der Naturwissenschaften"
am Fachbereich Physik, Mathematik und Informatik
der Johannes Gutenberg-Universität
in Mainz

Benedikt Kloss

geboren in Wiesbaden

Mainz, den 10. Dezember 2015

Benedikt Kloss: *Measurement of the* $e^+e^- \to \pi^+\pi^-$ *cross section using initial state radiation at BESIII*

1. Berichterstatter:
2. Berichterstatter:
Tag der mündlichen Prüfung: 09.12.2015

Zusammenfassung

Das zukünftige Ziel der modernen Physik ist die Entdeckung von Physik jenseits des Standardmodells. Einer der deutlichsten Hinweise für Neue Physik findet sich im anomalen magnetischen Moment des Myons a_μ. Dieses steht im Zusammenhang mit der Kopplung des Myons, eines Elementarteilchens, an ein externes elektromagnetisches Feld und ist definiert als $a_\mu = (g_\mu - 2)/2$, wobei g_μ der gyromagnetische Faktor des Myons ist. Die Myonanomalie ist mit einer relativen Genauigkeit von $0{,}5 \cdot 10^{-6}$ vermessen worden. Allerdings tritt zwischen direkter Messung und Standardmodell-Vorhersage eine Differenz von 3,6 Standardabweichungen auf. Dies könnte ein Hinweis für Neue Physik sein. Für eine Entdeckung ist diese Abweichung leider noch zu gering, weshalb noch präzisere Messungen und Rechnungen durchgeführt werden müssen.
Die Myonanomalie hat drei Beiträge, wobei diejenigen der Quantenelektrodynamik und der schwachen Wechselwirkung mittels Störungstheorie berechnet werden können. Im Falle des hadronischen Beitrages kann dies bei niedrigen Energien nicht getan werden. Jedoch kann der führende Beitrag, die hadronische Vakuumpolarisation, durch ein Dispersionsintegral berechnet werden, das in Verbindung mit hadronischen Wirkungsquerschnitten in Elektron-Positron-Annihilationen steht. Für eine präzise Vorhersage von a_μ ist es deshalb essentiell, diese hadronischen Wirkungsquerschnitte, $\sigma(e^+e^- \to \text{Hadronen})$, mit hoher Präzision zu vermessen. Mit einem Beitrag von über 70 % ist der Endzustand mit zwei geladenen Pionen in diesem Zusammenhang der wichtigste. Dieser wurde bereits hochpräzise beim KLOE Experiment in Frascati, Italien, und dem BaBar Experiment in Stanford, USA, vermessen. Die Unsicherheit beider Experimente im Energiebereich unterhalb von 1 GeV, der von der $\rho(770)$ Resonanz dominiert wird, ist kleiner als 1 %. Jedoch unterscheiden sich die beiden Ergebnisse um bis zu 5 %. Deshalb wurde im Rahmen dieser Doktorarbeit eine unabhängige Messung mit vergleichbarer Präzision am BESIII Experiment durchgeführt.
Das BESIII Experiment befindet sich am symmetrischen e^+e^- Beschleuniger BEPCII in Peking, China. Es werden 2,9 fb^{-1} Daten analysiert, die bei einer Schwerpunktsenergie von 3,773 GeV genommen wurden. Dabei wird die Methode der Photonabstrahlung im Anfangszustand verwendet. Eines der einfallenden Strahlteilchen emittiert ein hochenergetisches Photon, wodurch die verfügbare Energie um einen hadronischen Endzustand zu erzeugen, reduziert wird und die wichtige $\rho(770)$ Resonanz Region studiert werden kann. Auf Grund von Unvollkommenheiten der Detektorsimulation treten Unterschiede zwischen den gemessenen Daten und der verwendeten Monte-Carlo Simulationen auf. Mittels präziser Studien dieser Unterschiede ist es möglich die angestrebte Präzision zu erreichen. Um den Hauptuntergrund mit zwei Myonen im Endzustand zu unterdrücken wurde ein künstliches neuronales Netz verwendet, um Myonen und Pionen effizient voneinander zu unterscheiden. Ein präziser QED Test wird durchgeführt, indem $e^+e^- \to \mu^+\mu^-\gamma$ Ereignisse aus Daten mit der MC Vorhersage verglichen werden. Mittels der in dieser Arbeit entwickelten Methoden haben wir weiterhin eine Suche nach einem Dunklen Photon durchgeführt und die elektrische Breite der J/ψ Resonanz mit bisher unerreichter Präzision bestimmt.
In dieser Arbeit wird eine neue Messung des Wirkungsquerschnittes $\sigma(e^+e^- \to \pi^+\pi^-)$ und des Pion Formfaktors $|F_\pi|^2$ am BESIII Experiment durchgeführt. Dabei wird in der wichtigen $\rho(770)$ Resonanzumgebung zwischen 600 und 900 MeV eine Präzision von 0,9% erreicht. Mit dem Ergebnis dieser Arbeit wird der zwei-Pion Beitrag zur führenden Ordnung der hadronischen Vakuumpolarisation von $(g-2)_\mu$ zu $a_\mu^{\pi\pi,\text{LO}}(600 - 900\ \text{MeV}) = (368{,}2 \pm 2{,}5_{\text{stat}} \pm 3{,}3_{\text{sys}}) \cdot 10^{-10}$ berechnet. Dieses Ergebnis ist in guter †bereinstimmung mit dem KLOE Experiment wobei eine Abweichung von etwa 1,7 Standardabweichungen zum BaBar Resultat besteht. Mit dieser Arbeit leisten wir einen wichtigen Beitrag zur Lösung des $(g-2)_\mu$ Rätsels.

Summary

The future goal of modern physics is the discovery of physics beyond the Standard Model. One of the most significant hints for New Physics can be seen in the anomalous magnetic moment of the muon a_μ - one of the most precise measured variables in modern physics and the main motivation of this work. This variable is associated with the coupling of the muon, an elementary particle, to an external electromagnetic field and is defined as $a_\mu = (g_\mu - 2)/2$, whereas g_μ is the gyromagnetic factor of the muon. The muon anomaly has been measured with a relative accuracy of $0.5 \cdot 10^{-6}$. However, a difference between the direct measurement and the Standard Model prediction of 3.6 standard deviations can be observed, called the $(g-2)_\mu$ puzzle. This could be a hint for the existence of New Physics. Unfortunately, it is, yet, not significant enough to claim an observation and, thus, more precise measurements have to be performed. The muon anomaly has three contributions, whereas the ones from quantum electrodynamics and weak interaction can be determined from perturbative calculations. This can not be done in case of the hadronic contributions at low energies. The leading order contribution - the hadronic vacuum polarization - can be computed via a dispersion integral, which needs hadronic cross sections from electron-positron annihilations as input. Hence, it is essential for a precise prediction of a_μ to measure these hadronic cross sections, $\sigma(e^+e^- \to \text{hadrons})$, with high accuracy.
With a contribution of more than 70%, the final state containing two charged pions is the most important one in this context. The two most accurate measurements of the hadronic cross section $\sigma(e^+e^- \to \pi^+\pi^-)$ have been obtained by the KLOE collaboration in Frascati, Italy, and the *BABAR* collaboration in Stanford, USA. Both experiments claim an accuracy of better than 1% in the energy range below 1 GeV, in which the $\rho(770)$ resonance is dominating the cross section. However, discrepancies of up to 5% between both experiments are observed. This shows the necessity of a reference measurement with a precision also in the order of 1%, in order to solve this discrepancy.
This measurement, which is the topic of this thesis, is performed at the BESIII experiment, located at the symmetric e^+e^- collider BEPCII in Beijing, China. Using a data set of 2.9 fb^{-1} taken at a center-of-mass energy of 3.773 GeV, the method of initial state radiation is exploited for this measurement. One of the incoming beam particles radiates a high energetic photon and, thus, the available energy to produce a hadronic final state is reduced and the important $\rho(770)$ resonance region can be studied. Detailed studies of possible discrepancies between data and Monte Carlo samples due to imperfections of the detector simulation are performed to achieve the targeted accuracy. To suppress the dominating background stemming from muons in the final state, a muon-pion separation based on an artificial neural network method is utilized. As cross check, a precise QED test is performed by confronting $e^+e^- \to \mu^+\mu^-\gamma$ events from the data and the Monte Carlo prediction. With the tools developed in this work, we performed in addition a search for a dark photon signal and measured the electronic width of the J/ψ resonance with unrivaled precision.
In this thesis, a new measurement of the $\sigma(e^+e^- \to \pi^+\pi^-)$ cross section and the pion form factor $|F_\pi|^2$ is performed with an accuracy of 0.9% in the dominant $\rho(770)$ resonance region between 600 and 900 MeV at the BESIII experiment. The two-pion contribution to the leading-order (LO) hadronic vacuum polarization contribution to $(g-2)_\mu$ from the BESIII result, obtained in this work, is computed to be $a_\mu^{\pi\pi,\text{LO}}(600-900\text{ MeV}) = (368.2 \pm 2.5_{\text{stat}} \pm 3.3_{\text{sys}}) \cdot 10^{-10}$. It is found to be in good agreement with the corresponding value of the KLOE measurement, while there is a discrepancy of about 1.7 standard deviations to the *BABAR* value. With the result presented in this thesis, we make an important contribution on the way to solve the $(g-2)_\mu$ puzzle.

Contents

Chapter 1

Introduction

In the first chapter, the anomalous magnetic moment of the muon a_μ is introduced, which is the main motivation of this work. Afterwards, the impact of hadronic cross section measurements at e^+e^- accelerators on the theoretical calculation of this quantity is explained. Finally, the importance of the $e^+e^- \to \pi^+\pi^-$ cross section for a_μ is described, as well as its current experimental situation.

1.1 The standard model of particle physics

Physics is the natural science of matter and its interactions, and one of the oldest philosophical disciplines. Our todays understanding of the world has its roots in ancient greece, when the philosophers started to study the night sky. In the 16th century, Newton developed the equations of motion, which are certainly one of the milestones of classical science, as well as Maxwell's equations. The development of quantum mechanics and Einstein's theories of special and general relativity herald a new era of modern physics. They paved the way for the discovery of the elementary particles, the description of the fundamental forces in quantum field theories, and the standard model (SM) of modern particle physics.

The SM was recently tested in its completeness with the discovery of the Higgs Boson in 2012 at CERN [1, 2]. It describes the elementary point-like particles and their interaction with the three fundamental forces: electromagnetic, weak, and strong interaction. It does not include Gravitation as described by general relativity. The components of the SM are displayed in Fig. 1.1. The elementary particles can be divided into two subgroups, the carriers of the fundamental forces, called gauge bosons, and the elementary particles building the SM matter in the universe, called quarks and leptons. The charged leptons e, μ, τ and their corresponding neutral partners, the neutrinos, are only affected by the weak interaction and, only in the charged case, also by the electromagnetic force. The fundamental quarks u, d, c, s, b and t, instead, are charged under all three forces. The massless photon γ is the carrier of the electromagnetic force. The neutral Z^0 and the charged $W^{\pm}$ bosons are the exchange particles of the weak interaction, and the massless gluon g carries the interaction with the strong force. The Higgs mechanism describes the origin of the mass of the elementary particles via the Higgs boson H.

The SM is extremely successful and has not been falsified until today. However, there are some open questions. The masses of the fundamental particles and several parameters that describe their interactions, enter as input in the SM and need to be measured. Why are there exactly three generations? Why is there a matter-antimatter asymmetry within the universe? How does the existence of dark matter and energy fit in?

A main goal of modern particle physics is to find New Physics beyond the SM. There are two directions of impact: On the one hand, measurements at ever increasing energies, as it is done at the Large Hadron Collider (LHC) at CERN. On the other hand, high precision measurements at, mostly, lower energies, to test the predictions of the standard model with high accuracy.

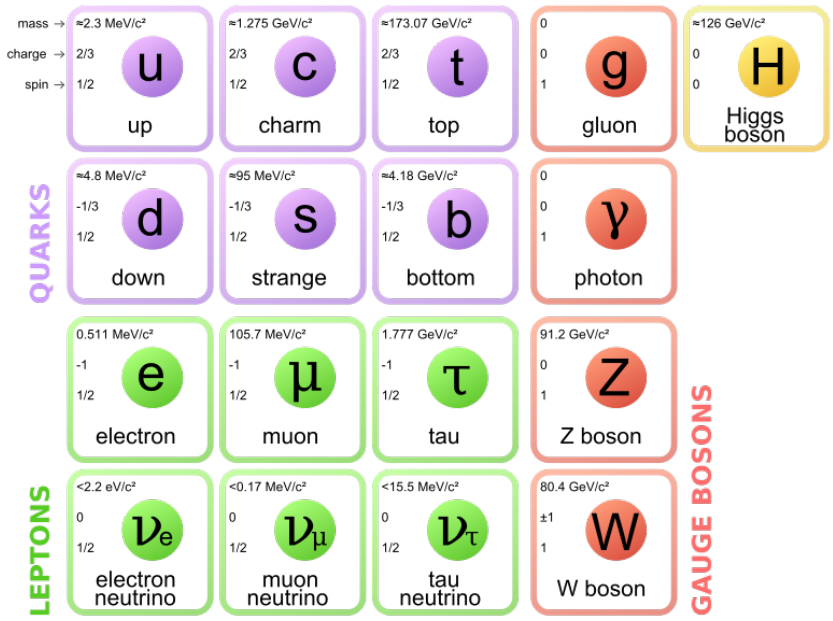

Figure 1.1: The particle content of the standard model of particle physics. The purple and green particles are the six fundamental quarks and leptons. In red, the gauge bosons of the three fundamental forces are displayed, together with the Higgs boson in yellow. The gluon belongs to the strong, the photon to the electromagnetic, and the W and Z bosons to the weak force. (taken from *http://www.pbs.org/wgbh/nova* and *http://en.wikipedia.org/wiki/File:Standard_Model_of_Elementary_Particles.svg*)

Some hints for deviations between SM and experiments have been found in high precision measurements. However, all these clues are not significant enough till today and, hence, the existence of New Physics has not been proven, yet. The largest deviation between theory and experiment is seen in the anomalous magnetic moment of the muon a_μ. The discrepancy between experiment and SM prediction amounts to 3.6 standard deviations [3]. Or in other words, the probability that this difference is caused by a statistical fluctuation is smaller than 0.1%. However, only a discrepancy greater than 5.0 standard deviations would count as observation.

This work investigates this anomaly and tries to improve the theoretical prediction. Its hadronic part can not be calculated by means of perturbative calculations and, thus, measurements of hadronic cross sections are needed as input for the calculation. The $(g-2)_\mu$ puzzle is explained in detail in the upcoming section, to motivate the need of this analysis[1].

[1]Note: Natural units are used in this work, i.e. $\hbar = c = 1$. Thus, masses, momenta and energies are given in the unit electron volts (eV).

1.2 The anomalous magnetic moment of the muon

A muon is a charged lepton with a mass of $m_\mu = (105.6583715 \pm 0.0000035)$ MeV [4], about 200 times heavier than an electron. It is a fermion and, thus, carries a spin $|\vec{S}| = \frac{1}{2}$. Its magnetic moment $\vec{\mu}$ can be described as

$$\vec{\mu} = g_\mu \frac{e}{2m_\mu} \vec{S} \,, \tag{1.1}$$

where g_μ is the gyromagnetic factor, and e the elementary charge. $\vec{\mu}$ describes the coupling of the muon to a magnetic field $\vec{B}$. Dirac's theory predicts $g_\mu = 2$ [5]. However, quantum fluctuations, described by Quantum Electrodynamics (QED), Quantum Chromodynamics (QCD), and weak interaction, yield to a difference $a_\mu = (g_\mu - 2)/2$ from this exact value, called muon anomaly. Figure 1.2 shows on the left side the case of Dirac's theory, i.e. the interaction of a muon with a $\vec{B}$ field without any quantum correction, represented by a Feynman graph. On the right side, the first order quantum correction is displayed, called Schwinger term, which is the first order QED correction and accounts for more than 99% of a_μ. As Schwinger has calculated analytically, it has the exact solution $\frac{\alpha}{2\pi}$ [6], where α is the electromagnetic coupling constant.

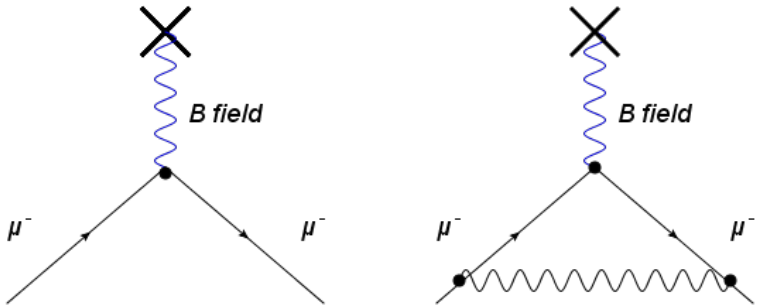

Figure 1.2: Left: Feynman diagram illustrating the prediction of Dirac's theory: There are no quantum corrections and it is $g_\mu = 2$.
Right: First order QED correction, called Schwinger term. This correction contains over 99% of a_μ and has the exact solution $\frac{\alpha}{2\pi}$.

Experimental measurement and SM prediction yield the following values for a_μ [3, 7]:

$$a_\mu^{\text{exp}} = (116\,592\,091 \pm 63) \cdot 10^{-11} \quad [3], \tag{1.2}$$

$$a_\mu^{\text{SM}} = (116\,591\,803 \pm 49) \cdot 10^{-11} \quad [7], \tag{1.3}$$

which have an accuracy better than the parts per million (ppm) level. However, theory and experiment differ by 3.6 standard deviations [3]. Is this a hint for New Physics beyond the standard model?

1.3 Measurement of a_μ

Nine Experiments have been performed from 1961 to 2001 at CERN and BNL with ever increasing accuracy. Their results are listed in Tab. 1.1 in chronological order.

experiment	year	$a_\mu \cdot 10^{10}$	$\Delta a_\mu \cdot 10^{10}$	$\frac{\Delta a_\mu}{a_\mu}$ [ppm]
CERN I	1961	11 450 000	220 000	4300
CERN II	1962 - 1968	11 661 600	3 100	270
CERN III	1974 - 1976	11 659 100	110	10
CERN III	1975 - 1976	11 659 360	120	10
BNL	1997	11 659 251	150	13
BNL	1998	11 659 191	59	5
BNL	1999	11 659 202	15	1.3
BNL	2000	11 659 204	9	0.73
BNL	2001	11 659 214	9	0.72

Table 1.1: Summary of the CERN and BNL experiments [7, 8, 9, 10, 11, 12, 13, 14, 15]. Table taken from [7].

Figure 1.3: The storage ring of the BNL experiment [16].

The measurement of a_μ, yielding to the highest precision, was performed at the Brookhaven National Laboratory (BNL) in New York, USA [7]. It is a high precision measurement, that exploits the character of weak interaction. If one considers, that parity is maximally violated in weak interaction, it becomes clear, that massless particles are always left-handed, i.e. their helicity is negative, while massless antiparticles are always right-handed, corresponding to a positive helicity. In order to generate muons at BNL, the weak decay of charged pions $\pi^\pm$ to

muons was exploited. The muons decay further to electrons:

$$\pi^+ \longrightarrow \mu^+ + \nu_\mu \longrightarrow e^+ + \nu_e + \overline{\nu}_\mu + \nu_\mu \,, \tag{1.4}$$

$$\pi^- \longrightarrow \mu^- + \overline{\nu}_\mu \longrightarrow e^- + \overline{\nu}_e + \nu_\mu + \overline{\nu}_\mu \,. \tag{1.5}$$

Due to leptonic family number conservation, the corresponding neutrinos and anti-neutrinos are generated, too. The neutrinos are nearly massless and, hence, their helicity is explicitly known. This fact implies, that, on the one hand, the muons are polarized, and, on the other hand, the generated electrons are emitted in the direction of the spin of the polarized muons. This is sketched in Fig. 1.4.

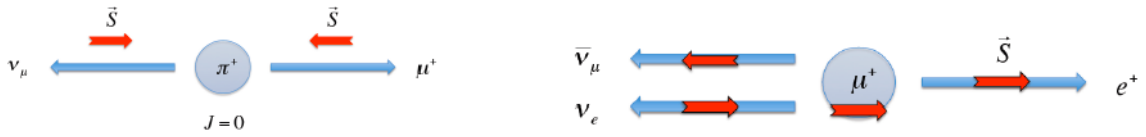

Figure 1.4: Deacys of π^+ and μ^+.
Left: The helicity of the neutrino is negative. Hence, spin $\vec{S}$ and momentum (or flight direction) have to be back-to-back in the pion rest frame. The pion has an angular momentum $J = 0$ and, thus, the spins of the generated μ^+ and ν_μ have to add to zero. Therefore, also the helicity of the μ^+ has to be negative. It is polarized.
Right: The polarized muon has $\vec{S} = \frac{1}{2}$. After its decay, the helicity of the e^+ is well-known, since the ones of the neutrinos are fix. This yields to the fact, that the positron is emitted in the direction of the spin of the μ^+.

In the experimental setup at BNL, protons with a momentum of 24 GeV were accelerated on a target to generate charged pions, which decay further to polarized muons. These muons are injected in a storage ring with a diameter of 14 meters, which is displayed in Fig. 1.5. A constant magnetic field $\vec{B}$ of 1.45 Tesla holds the muons on an orbit. Because of their charge, the muons rotate with the cyclotron frequency $\vec{\omega}_C = \frac{e}{m_\mu}\vec{B}$. Furthermore, their spin precesses with the Larmor frequency $\vec{\omega}_L = \frac{g_\mu e}{2m_\mu}\vec{B}$. Since $g_\mu \neq 2$ there is a remaining anomalous frequency when subtracting them, which is proportional to a_μ:

$$\vec{\omega}_a = \vec{\omega}_L - \vec{\omega}_C = \frac{e}{m_\mu}\left(a_\mu \vec{B} - \left[a_\mu - \frac{1}{\gamma^2 - 1}\right]\vec{\beta} \times \vec{E}\right) \simeq a_\mu \frac{e}{m_\mu}\vec{B} \,, \tag{1.6}$$

with the velocity of the muon $\beta = v/c$ in units of the speed of light, the relativistic factor $\gamma = 1/\sqrt{1-\beta^2}$, and the electric field $\vec{E}$ of the quadrupoles, which are needed to focus the beam. A value of $\gamma_{mag} = 29.378$ yields to $a_\mu - \frac{1}{\gamma_{mag}^2 - 1} \approx 0$ and, thus the second part of the formula vanishes. At BNL, the energy of the muons is set to the "magic" energy $E_{mag} = \gamma_{mag} m_\mu = 3098$ MeV, to make the anomalous frequency independent of $\vec{E}$.

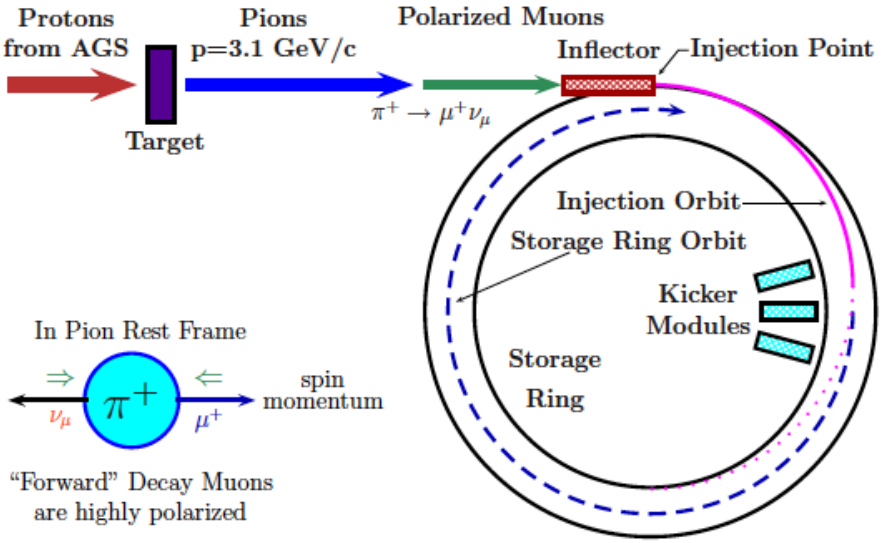

Figure 1.5: Experimental setting at BNL. A proton beam from the Alternating Gradient Synchrotron (AGS) is shot on a target to produce positive charged pions, which decay to polarized muons as explained in the text. The muons are injected into a magnetic field via an inflector, where they describe a circle. [16].

The lifetime of the muons is increased by the factor γ_{mag} at this energy. The muons are circulating in the storage ring and decay as given in formulas (1.4) and (1.5), and as sketched in Fig. 1.4. The positrons or electrons are emitted in direction of the muon spin, which precedes with the anomalous frequency $\vec{\omega}_a$. If it points to the inner region of the storage ring, the generated leptons can be detected by the electromagnetic calorimeters in the inner region, as displayed in Fig. 1.6, which allows the measurement of $|\vec{\omega}_a|$.

Considering the exponential decay law, the number of detected positrons with an energy higher than a certain threshold E_{min}, can be measured as [16]

$$N(t) = N_0(E_{min}) \cdot e^{-\frac{t}{\gamma\tau_\mu}} \cdot [1 + A(E_{min}) \cdot sin(\omega_a t + \varphi(E_{min}))] \,, \tag{1.7}$$

where τ_μ is the life time in the muon rest frame, $N_0(E_{min})$ is a normalization factor, $A(E_{min})$ is the asymmetry and $\varphi(E_{min})$ a phase. The outcome of the BNL measurement with $E_{min} = 2$ GeV is shown in Fig. 1.7. The exponential decay, modulated at the $|\vec{\omega}_a|$ frequency, which can be extracted from this, can be seen.

To achieve the experimental precision required, $\vec{B}$ has to be determined very precisely. The magnetic field is measured with 375 fixed sensors and with a wagon, measuring the field at 6000 different points. With the magnetic resonance technique a precision of 0.05ppm is reached [17, 18]. The muon mass is determined very precisely with the microwave spectrum

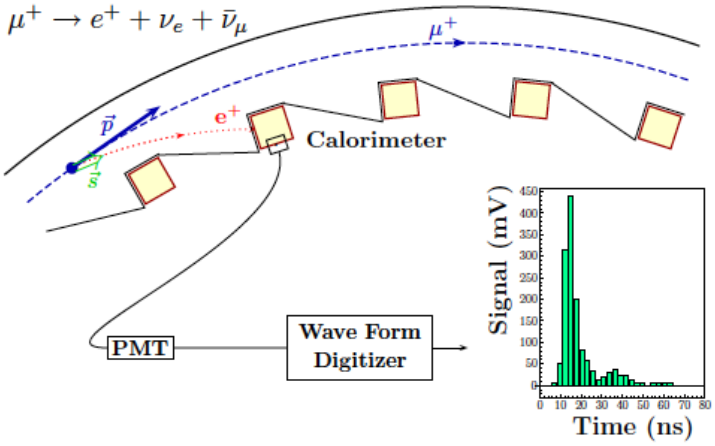

Figure 1.6: The positron from the μ^+ decay flies in the direction of the muon spin, which processes with $\vec{\omega}_a$. If they fly into the inner part of the storage ring, they are measured by calorimeters [16].

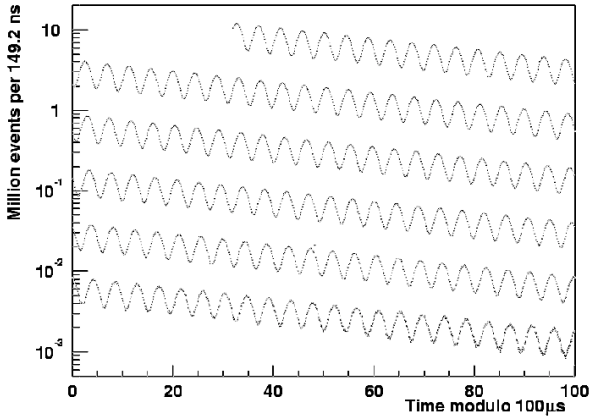

Figure 1.7: Counting of the number of positrons versus time modulo 100 μs, achieved with the calorimeters in the inner part of the BNL storage ring. [7]

of ground state muonium [19], and with the theoretical prediction of the muonic hyperfine splitting [20, 21, 22].

The BNL experiment was able to achieve an accuracy of 0.54ppm [7], when averaging the results using μ^+ and μ^- decays [7]:

$$a_\mu^{\text{exp}} = (116\,592\,091 \pm 63) \cdot 10^{-11} \; .$$

Two new experiments are planned, to improve a_μ^{exp}. The first one will take place at Fermilab in Chicago, USA [23]. The plan is to start operating in 2017. It uses the BNL storage ring and setup but, with the accelerators at Fermilab, higher statistics can be achieved. The goal is to improve the error on a_μ^{exp} by a factor of four. The second one will take place at the Japan

Proton Accelerator Research Complex (J-PARC) in Tokai, Japan [24]. It will use an ultra-cold muon beam, where no focussing by an electric field is necessary. Thus, it is an independent approach to the experiment at Fermilab and will reach an independent result, which aims for a precision of the order of 0.1ppm.

1.4 Standard model prediction of a_μ

The standard model prediction of a_μ has three contributions, from QED, weak, and strong (hadronic) interaction [16]:

$$a_\mu^{\mathrm{SM}} = a_\mu^{\mathrm{QED}} + a_\mu^{\mathrm{weak}} + a_\mu^{\mathrm{had}} \ . \tag{1.8}$$

Figure 1.8 displays their first order Feynman diagrams. The QED part includes all photon

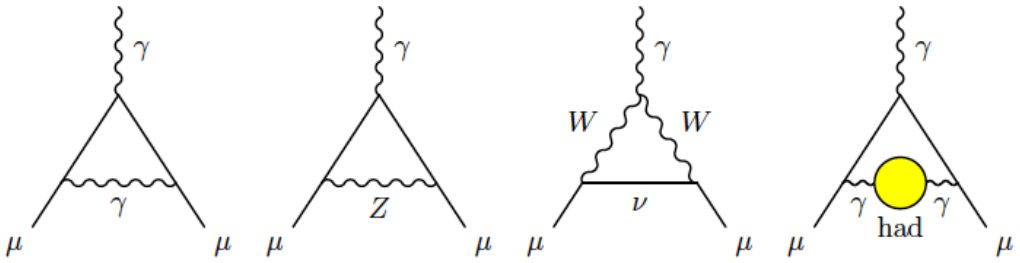

Figure 1.8: Leading order contributions to a_μ^{SM} from QED, weak, and strong interactions. From left to right: first order QED (Schwinger term), lowest order weak, and lowest order hadronic (vacuum polarization) [4].

corrections and leptonic (e, μ, τ) loops. It can be calculated up to the four-loop diagrams analytically [25]. The leading order contribution, the Schwinger term, has the solution $\frac{\alpha}{2\pi}$ [6]. The a_μ^{QED} contribution has been computed up to 5th order [26, 27, 28, 29, 30, 31, 32, 33], where the five-loop calculation is numerical, yielding:

$$\begin{aligned} a_\mu^{\mathrm{QED}} =& \frac{\alpha}{2\pi} + 0.765\,857\,425(17)\left(\frac{\alpha}{\pi}\right)^2 + 24.050\,509\,96(32)\left(\frac{\alpha}{\pi}\right)^3 \\ &+ 130.879\,6(6\,3)\left(\frac{\alpha}{\pi}\right)^4 + 753.3(1.0)\left(\frac{\alpha}{\pi}\right)^5 + \ldots \end{aligned} \tag{1.9}$$

The final result for the QED contribution to a_μ is found to be [4]

$$a_\mu^{\mathrm{QED}} = (116\,584\,718.95 \pm 0.08) \cdot 10^{-11} \ , \tag{1.10}$$

and it dominates the value of a_μ^{SM} by far. Its negligible error, compared to the experimental precision, is mainly due to the uncertainty in the fine structure constant α.

The weak contribution a_μ^{weak} contains heavy $W^\pm$, Z^0, and Higgs boson contributions. Fig. 1.9 shows the leading order diagrams. They are suppressed by a factor of $\frac{\alpha}{\pi} \cdot \frac{m_\mu^2}{M} < 10^{-9}$, whereas M is the mass of the W, Z^0 or Higgs boson. They are computed up to the second order, higher orders are found to be negligible [34, 35]. The number of computed diagrams is comparable to the 5th order QED computation. The calculation is limited by input parameters like the Weinberg angle $\sin^2\theta_W$ and the Higgs boson mass. This leads to a total contribution of [34, 35, 36, 37, 38, 39, 40, 41, 42, 43, 44, 45, 46]:

$$a_\mu^{\mathrm{weak}} = (153.6 \pm 1.0) \cdot 10^{-11} \tag{1.11}$$

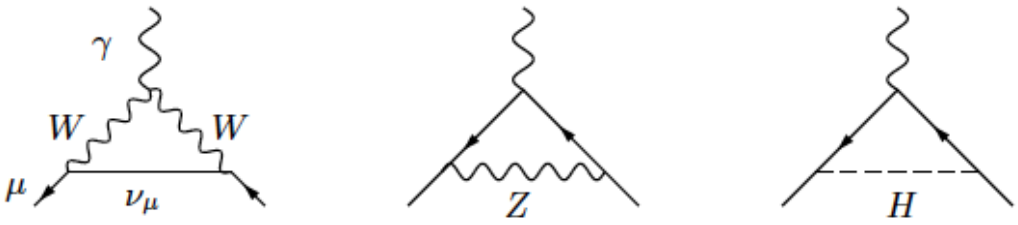

Figure 1.9: Leading order weak contributions to a_μ^{SM} [16].

The hadronic contribution a_μ^{had} contains quark-loops and, hence, hadronic interactions come into play. At low energies the strong coupling constant $\alpha_s \sim \mathcal{O}(1)$, and therefore, perturbation theory can not be used for the calculation of a_μ^{had}. Instead, one needs experimental measured quantities as input. For this reason, this contribution dominates the uncertainty of a_μ^{SM}. The two different hadronic contributions are, on the one hand, the hadronic vacuum polarization (VP) in leading (LO) and higher orders (HO) and, on the other hand, the hadronic light-by-light scattering (LBL) [16]:

$$a_\mu^{\mathrm{had}} = a_\mu^{\mathrm{had,VP}}[\mathrm{LO}] + a_\mu^{\mathrm{had,VP}}[\mathrm{HO}] + a_\mu^{\mathrm{had,LBL}} \ . \tag{1.12}$$

Their feynman graphs can be found in Fig. 1.10 and 1.11. The $a_\mu^{\mathrm{had,VP}}$ contribution can be calculated via a dispersion relation, using hadronic cross sections of the form $\sigma(e^+e^- \to \mathrm{hadrons})$ as input [16]

$$a_\mu^{\mathrm{had,VP}}[\mathrm{LO}] = \frac{1}{4\pi^3} \int_{4m_\pi^2}^{\infty} K(s)\sigma(e^+e^- \to \mathrm{hadrons})ds \ , \tag{1.13}$$

with the center of mass energy (cms) squared s of the hadronic reaction and the QED Kernel

function $K(s)$ [47]. Both, $K(s)$, as well as $\sigma(e^+e^- \to \text{hadrons})$, have a $1/s$ dependence. Due to this, $a_\mu^{\text{had,VP}}[\text{LO}]$ is dominated by lower s values, mainly $s < 1$ GeV^2. Therefore, the ρ, $\omega(782)$, and $\phi(1020)$ resonances are of utmost importance. Graph 1.12 represents the distribution of contributions of hadronic cross sections from different energy regions to $a_\mu^{\text{had,VP}}[\text{LO}]$. Displayed is the contribution to the mean value (left side) and the error (right side). The ρ and ω resonances contribute with more than 75% to the mean value. As the $\rho(770)$ resonance decays to almost 100% to the final state $\pi^+\pi^-$, the cross section $\sigma(e^+e^- \to \pi^+\pi^-)$ is the most important input for the calculation of $a_\mu^{\text{had,VP}}[\text{LO}]$. For its error, hadronic channels with higher multiplicities, like $e^+e^- \to \pi^+\pi^-\pi^0$, $\pi^+\pi^-\pi^0\pi^0$, or $\pi^+\pi^-\pi^+\pi^-$, become also very important.

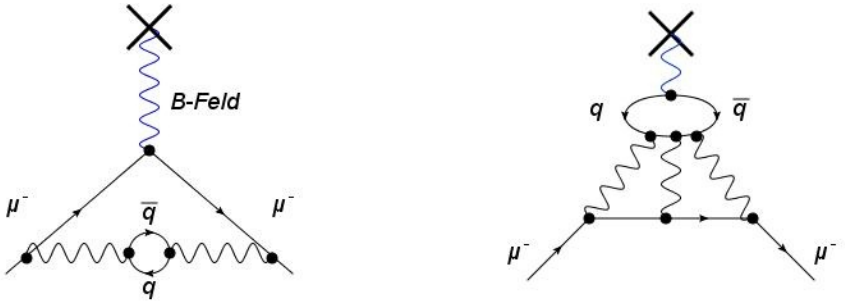

Figure 1.10: Hadronic vacuum polarization (left) and light-by-light scattering (right).

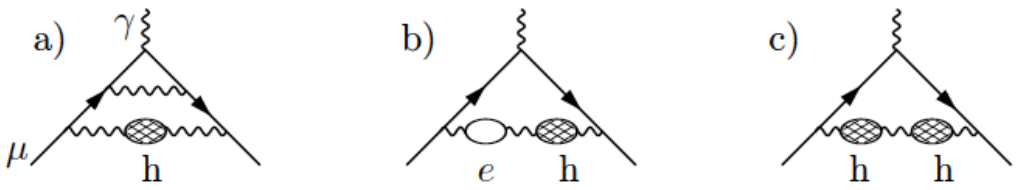

Figure 1.11: Second order contributions to $a_\mu^{\text{had,VP}}[\text{HO}]$ [16].

The leading order hadronic contribution, using the world averages of these hadronic cross sections, is found to be [3]

$$a_\mu^{\text{had,VP}}[\text{LO}] = (6\,923 \pm 42) \cdot 10^{-11} \ . \tag{1.14}$$

Higher order contributions $a_\mu^{\text{had,VP}}[\text{HO}]$ can also be computed via dispersion relations and using $\sigma(e^+e^- \to \text{hadrons})$ measurements as input [49, 50, 51]. However, they are found to be negligible compared to the LO case [16].

The light-by-light scattering contribution as shown in Fig. 1.10 is also small compared to the hadronic vacuum polarization part. However, it can only be estimated with model-dependent methods and, thus, its relative error is in the order of 25%. Therefore, it adds a main part to the uncertainty of a_μ^{SM}. One can use methods from large-N_C QCD [52] or a dispersive relation for

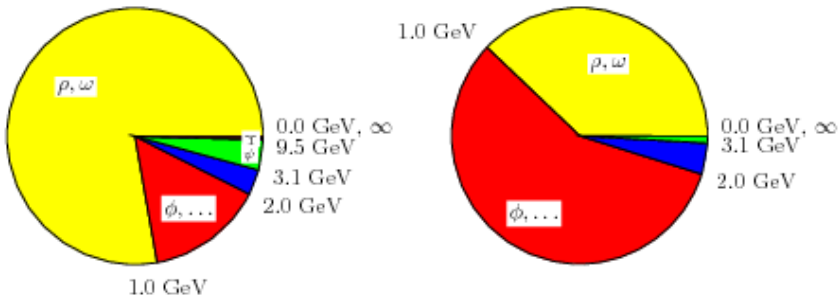

Figure 1.12: Distribution of contributions (left) and errors (right) in percent to a_μ^{had}[LO] from different energy regions [48].

the calculation, which needs measurements of scalar transition form factors as input [53]. These transition form factors are also under investigation at BESIII (see section 11.4). Combining results from different model assumptions one finds [54]

$$a_\mu^{\text{had,LBL}} = (10.5 \pm 2.6) \cdot 10^{-11} \,. \tag{1.15}$$

Finally, one can calculate the total SM value [3]

$$a_\mu^{\text{SM}} = (116\,591\,803 \pm 49) \cdot 10^{-11} \,, \tag{1.16}$$

yielding to a difference between direct measurement and SM prediction of [3]

$$\Delta a_\mu = a_\mu^{\text{exp}} - a_\mu^{\text{SM}} = (288 \pm 80) \cdot 10^{-11} \,, \tag{1.17}$$

which corresponds to the before-mentioned discrepancy of 3.6 standard deviations.

1.5 The $\sigma(e^+e^- \to \pi^+\pi^-)$ cross section

As explained in the previous section the $\sigma_{\pi\pi} \equiv \sigma(e^+e^- \to \pi^+\pi^-)$ cross section is the most important input for the calculation of the mean value of a_μ^{had}. In particular, the energy range around the broad $\rho(770)$ interference, at a mass of $m_\rho = 775$ MeV [4], is of utmost importance.

The quantity $\sigma_{\pi\pi}$ has been measured over decades with ever increasing accuracy at accelerators in Novosibirsk [55, 56, 57], Orsay [58] and Frascati. More recently, the two most accurate measurements have been obtained by the KLOE [59, 60, 61, 62], and the *BABAR* collaboration [63, 64]. Both experiments exploited the method of initial state radiation (ISR), which is explained in chapter 3. The *BABAR* experiment took data at $\sqrt{s} = 10.6$ GeV, corresponding

to the mass of the $\Upsilon(4S)$ resonance, and measured $\sigma_{\pi\pi}$ up to 3 GeV. The KLOE experiment, located in Frascati, Italy, was running at a center of mass energy $\sqrt{s} = 1.02$ GeV, corresponding to the ϕ resonance. Three different measurements were performed in 2008, 2010, and 2012, a tagged one, an untagged one, and one using the *BABAR* approach. The 2010 analysis is based on a data run slightly below the ϕ resonance. The terminology tagged and untagged is described in section 3.2. Comparisons of the results are shown in Fig. 1.13 (full spectrum) and 1.14 (zoom at different energy regions), also presenting measurements from TOF [65], OLYA [66], CMD [67], CMD2 [55, 56], SND [57], DM1 [68], and DM2 [69].

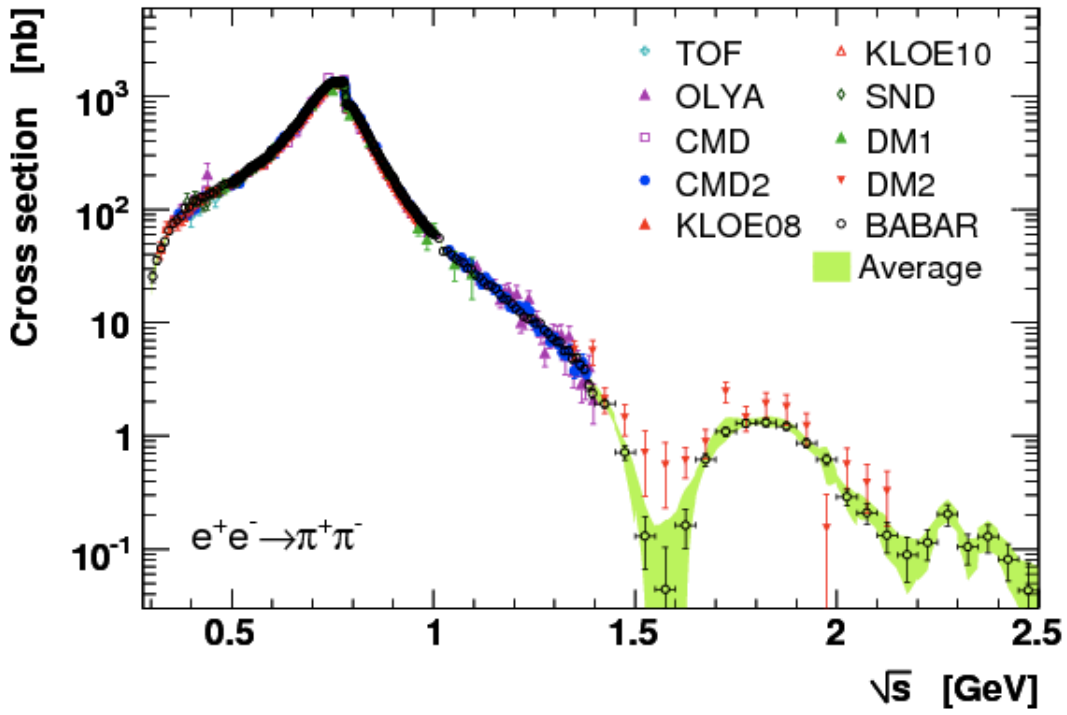

Figure 1.13: Measured $e^+e^- \to \pi^+\pi^-$ cross section versus the center of mass energy. Shown are the data of the KLOE [60, 61], *BABAR* [64], TOF [65], OLYA [66, 67], CMD [67], CMD2 [55, 56], SND [57], DM1 [68] and DM2 [69] experiments [3].

Both experiments, KLOE and *BABAR*, claim an accuracy of better than 1% in the energy range below 1 GeV, in which the $\rho(770)$ resonance is dominating the hadronic cross section. It is important to mention, that the KLOE 05 [59] result was superseded by the KLOE 08 result [60]. However, a discrepancy between the *BABAR* and all three KLOE data sets of approximately 3% on the peak of the $\rho(770)$ resonance is observed. The discrepancy is even increasing towards higher energies. Fig. 1.15 shows a comparison of the *BABAR* result, which is represented by a fit performed to data, using the Gounaris-Sakurai Parametrization [64], and the three different KLOE measurements. Shown is the pion form factor squared $|F(\pi)|^2$, which

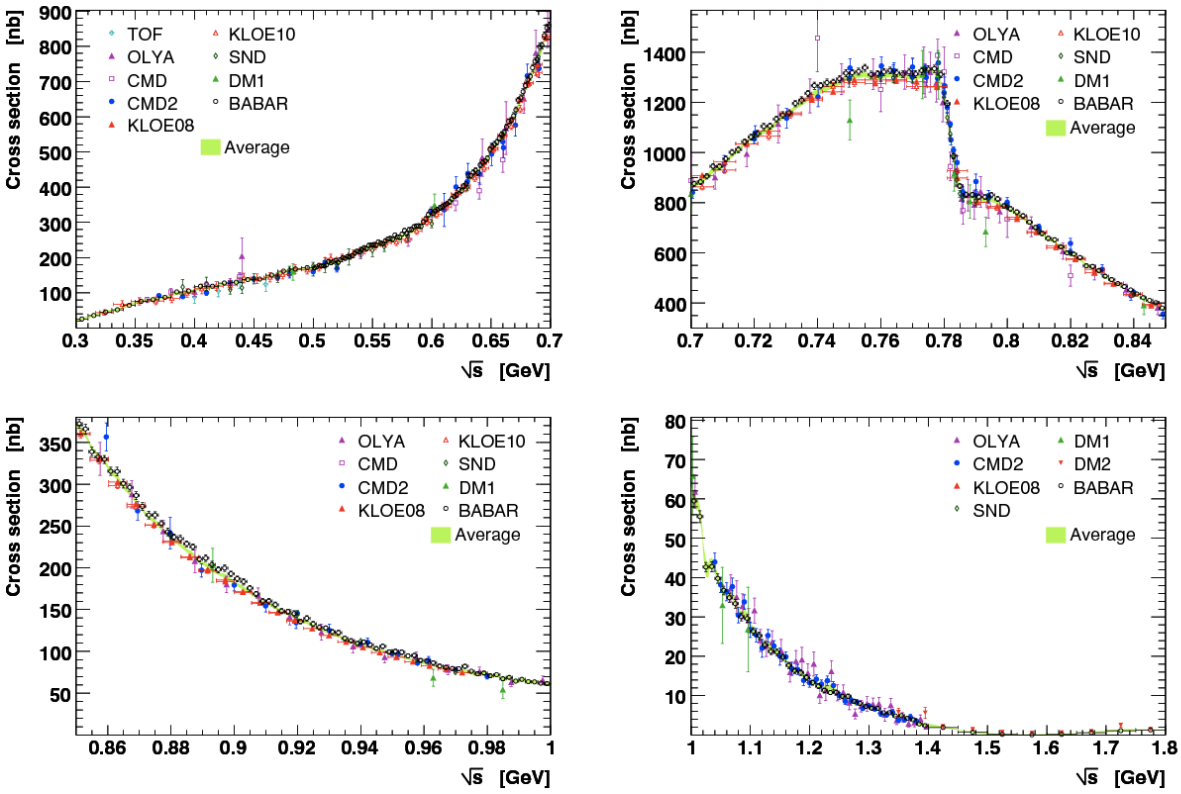

Figure 1.14: Results of the same experiments mentioned in Fig. 1.13 for different energy ranges [3].

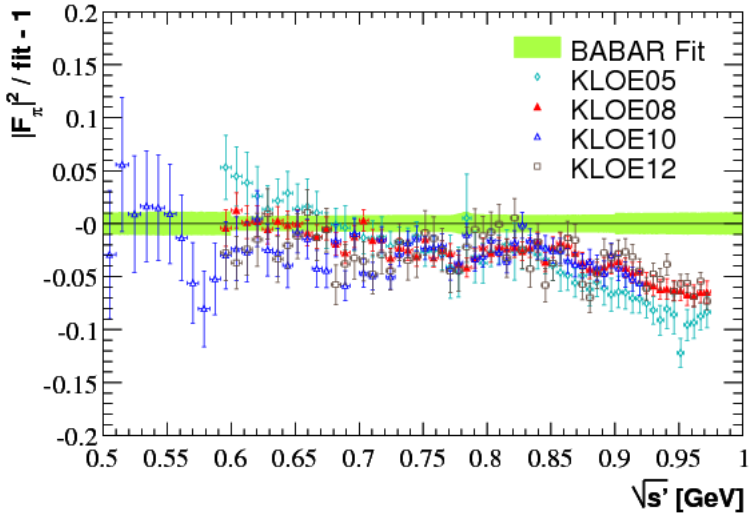

Figure 1.15: Comparison of pion form factor $|F_\pi|^2$ measurements from KLOE [60, 61, 62] and *BABAR* [64]. The *BABAR* result has been parametrized using the Gounaris-Sakurai parametrization as fit function, displayed by the green band, including statistical and systematic errors. The KLOE data is normalized to this function. The error bars are statistical and systematic added in quadrature. Important note: KLOE 05 was superseded by KLOE 08 [3].

is proportional to $\sigma_{\pi\pi}$ and can be calculated as [70]

$$|F_\pi(s)|^2 = \frac{3s}{\pi\alpha\beta_\pi^3(s)}\sigma_{\pi\pi}(s) \ , \tag{1.18}$$

with the pion velocity $\beta_\pi(s') = \sqrt{1-4m_\pi^2/s'}$, and the charged pion mass m_π.

1.6 Motivation and goal of this work

Currently, a discrepancy of 3.6 standard deviations (σ) [3] is found between the direct measurement of a_μ and its SM prediction. However, the discrepancy reduces to 2.4σ [71], when only *BABAR* $\sigma_{\pi\pi}$ data is used as input to the dispersion relation. Using only the KLOE data, it rises above 4σ. This shows the necessity of an independent reference experiment, to solve this puzzle.

This analysis is performed with data acquired by the BESIII experiment in Beijing, China, at $\sqrt{s} = 3.773$ GeV, corresponding to the $\psi(3770)$ resonance, and exploiting the method of initial state radiation. To be competitive to prior measurements we need to achieve a precision of the same order of magnitude, that is 1%. The data is analyzed in an energy range between 600 and 900 MeV, which corresponds to about 70% of the whole $\pi^+\pi^-$ contribution $a_\mu^{\pi\pi,\mathrm{VP}}$ and about 50% of a_μ^{had}.

Chapter 2

The BESIII experiment

This work uses 2.9 fb^{-1} data, collected at the BESIII experiment, located at the symmetric e^+e^- collider BEPCII at the Institute for High Energy Physics in Beijing, China. This chapter deals with a description of the accelerator facility, as well as an overview of the main components and software framework of the multipurpose BESIII detector.

2.1 The BEPCII Collider

The Beijing Electron Positron Collider (BEPC) was in operation from 1989 to 2004 at the Institute of High Energy Physics (IHEP) in Beijing, China [72]. It was a single symmetric electron-positron storage ring. In 2004, it was upgraded to the double-ring multi-bunch collider BEPCII [73]. Data taking started in 2009. BEPCII has a design luminosity of $\sim 10^{33}$ $\mathrm{cm}^{-2}\mathrm{s}^{-1}$, optimized at an energy of $2 \cdot 1.89$ GeV, which corresponds to the mass of the charmonium resonance $\psi(3770)$. The center of mass (cms) energy $\sqrt{s}$ can be varied from 2 - 4.6 GeV. The multi-bunch mode operates with 93 bunches per beam, stored in each ring, and spaced by 8 ns, which corresponds to 2.4 m. The crossing angle of the two beams is ± 11 mrad at the collision point. The total running time per year is around 10^7s. These values are summarized in Tab. 2.1, Fig. 2.1 shows an aerial view of the accelerator facility at IHEP.

Figure 2.1: Aerial view of the accelerator facility, housing the BEPCII collider and the BESIII detector, located at IHEP, Beijing. The figure is taken from *http* : *//www. ihep. ac. cn.*

Center of mass energy	2 - 4.6 GeV
Designed Peak luminosity at $2 \cdot 1.89$ GeV	$\sim 10^{33}$ $\mathrm{cm}^{-2}\mathrm{s}^{-1}$
Number of bunches	$2 \cdot 93$
Beam current	$2 \cdot 0.91$ A
Bunch spacing	2.4 m / 8 ns
Relative energy spread	$5 \cdot 10^{-4}$
Crossing angle	$\pm$ 11 mrad

Table 2.1: Design parameters of BEPCII [74].

The physics goal of the BESIII experiment is to make contributions to charmonium physics, light hadron spectroscopy, search for new hadronic states, D-physics, τ-physics, XYZ physics, as well as Quantum Chromodynamics (QCD) studies [73]. The discovery of the charged charmonium-like particle [75], called Z_c, came as a major surprise certainly is a highlight of

the physics results.

The world largest data sets at $\sqrt{s} = 3.096$ GeV, $\sqrt{s} = 3.684$ GeV, and $\sqrt{s} = 3.773$ GeV, corresponding to the J/ψ, ψ', and $\psi(3770)$ resonances, have been taken at the BESIII experiment, which is sketched in Fig, 2.2.

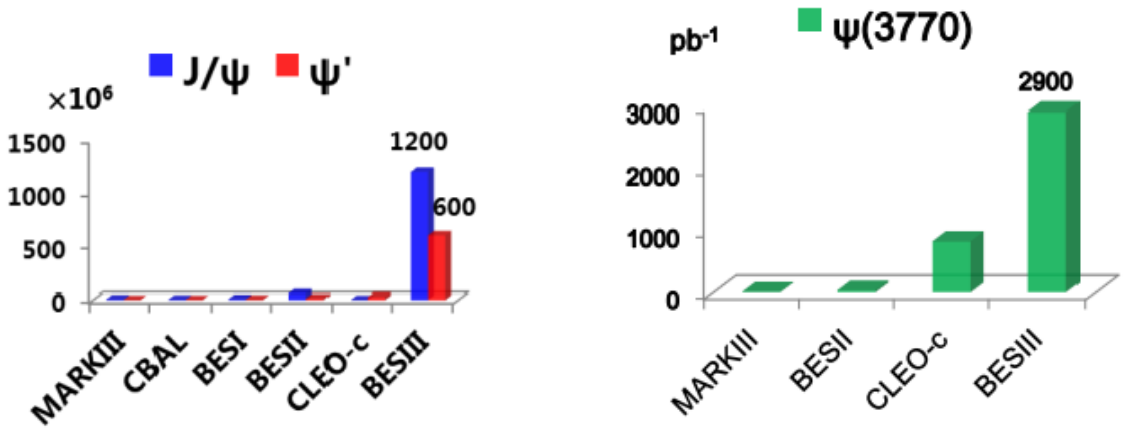

Figure 2.2: World data sets, taken at cms energies corresponding to the masses of the J/ψ, ψ', and $\psi(3770)$ resonances. In the left histogram the number of events is shown, in the right one the luminosity in pb^{-1}. BESIII has taken the world largest data sets at this energies, compared to the MARKIII, CBAL, and CLEO-c experiments. The figure is taken from *http : //www. ihep. ac. cn.*

2.2 The BESIII Detector

2.2.1 Overview of the components

The Beijing Spectrometer III (BESIII) is a multipurpose detector, located at BEPCII. BESIII is cylindrical, symmetric around the beam axis, and covers nearly 93% of the whole solid angle of 4π. In cylindrical coordinates, the dimension along beam axis is called z, the angle around the beam axis ϕ, and the polar angle θ. The upper half of the detector profile is shown in Fig. 2.3. BESIII consists of the following detector systems, which are described in more detail in the upcoming sections:

Multilayer Drift Camber (MDC): The MDC is filled with a $\mathrm{He}/\mathrm{C_3H_8}$ gas mixture. Incoming charged particles ionize the Helium and leave a trace. The momentum is calculated via the curvature of the helix, which they describe in a magnetic field.

Time-of-Flight System (TOF): The TOF consists of scintillators to measure charged particles. The passing time of these particles is detected to determine the mass of the

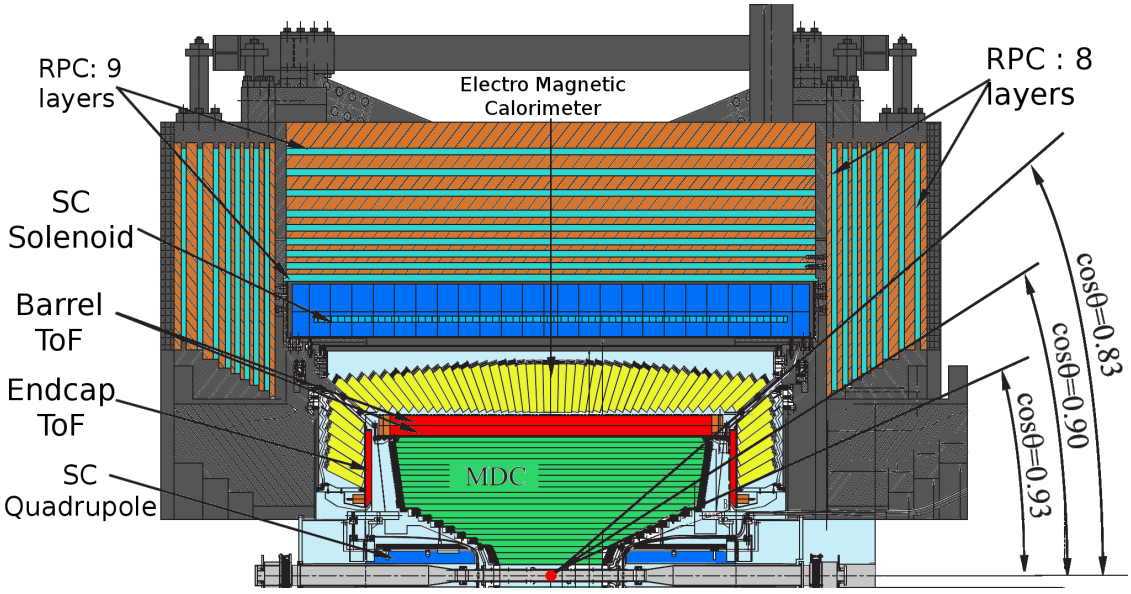

Figure 2.3: Profile of the upper half of the BESIII Detector (with courtesy of Matthias Ulrich).

particle, by using the measured momentum in the MDC. Also cosmic background rays can be identified and filtered.

Electromagnetic Calorimeter (EMC): The EMC measures the deposited energy of charged and neutral particles with CsI crystals.

Muon Chamber (MUC): The MUC discriminates muons from hadrons. Iron absorbers stop hadrons, so that only muons reaches the MUC and can be detected within resistive plate chambers (RPC).

Superconducting Solenoid Magnet (SSM): The SSM produces a magnetic field of 1 T, which curves the trajectory of charged particles.

Trigger System: The trigger system reads out the electronics and filters the events. The trigger rate is about 4000 Hz. The total data volume is 50 MBytes/s for this trigger rate.

2.2.2 Multilayer Drift Chamber

The Multilayer Drift Chamber (MDC) has a cylindrical form with two joined sub chambers, an inner and an outer one. The inner chamber radius is 63 mm, with a distance of 2 mm to the beam pipe, the one of the outer chamber is 810 mm. The length of the whole chamber in z direction is 2400 mm. The inner chamber covers the polar angular range with respect to the beam pipe $|cos(\theta)| < 0.93$, the outer one a range of $|cos\theta| < 0.83$. A detailed drawing of the mechanical structure of the MDC can be seen in Fig. 2.4. The main functions are the reconstruction of charged tracks, their momentum determination, and measuring the energy

loss dE over a flight distance dx, dE/dx, used for particle identification.

The MDC cylinders are made of carbon. 7000 gold-plated tungsten wires are placed in 43 layers, with 22000 gold-plated Al wires for field shaping. It is filled with a gas mixture of 40% propane and 60% helium. The single wire spatial resolution is 130 μm. The dE/dx resolution is 6%, which allows a 3σ K/π separation up to momenta of 770 MeV. The transverse momentum p_t resolution is better than 0.5% for 1 GeV momentum tracks at $\theta = 90°$. This information is summarized in Tab. 2.2.

The reconstruction is done by a tracking algorithm, which links the wire hits to circular traces, and uses the least-square method to perform a circular fit. These traces are treated as track candidates and are iteratively fitted with a helix. After that, additional hits possibly belonging to the tracks are added and the tracks are refitted with a Kalman-filter method. This algorithm has a tracking efficiency of more than 98% [73], if the transverse momentum is greater than 150 MeV. A further algorithm, based on the GEANT4 framework [82, 83], extrapolates the MDC tracks to outer sub-detectors. Therefore, the magnetic field and ionization losses in the several detector components are considered.

radius inner chamber	86 mm
radius outer chamber	810 mm
total length	2 400 mm
angular acceptance inner chamber	$\|cos\theta\| < 0.93$
angular acceptance outer chamber	$\|cos\theta\| < 0.83$
number of layers	43
sense wire	gold-plated W, diameter 25μm
field wire	gold-plated Al, diameter 110 μm
transverse momentum resolution	$< 0.5\%$ for 1GeV tracks at 90°
dE/dx resolution	6%
single wire resolution	< 130 μm
position uncertainty	< 0.4 mm

Table 2.2: Properties of the MDC [74].

2.2.3 Time-of-Flight System

The Time-of-Flight system (TOF) measures the flight time of charged particles. This measurement, together with momentum and dE/dx determination in the MDC, are the basis for particle identification at BESIII.

The TOF consists of two layers with 176 plastic scintillator bars in total, arranged in a barrel

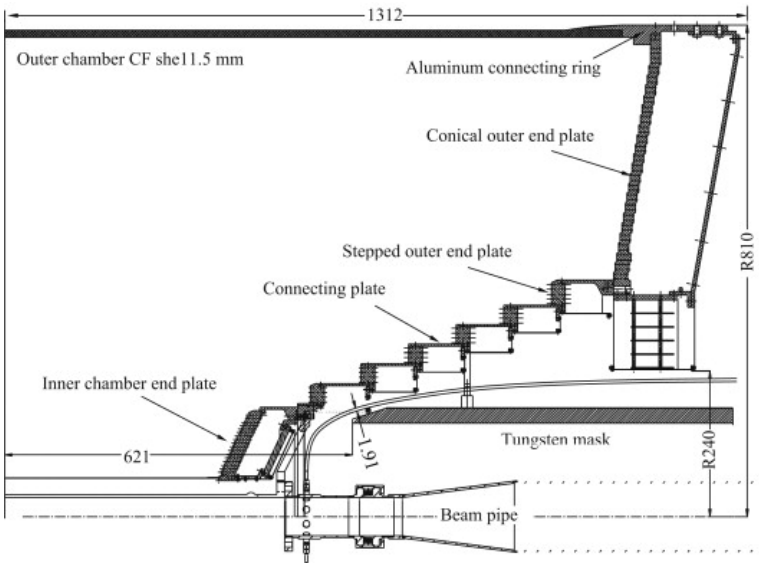

Figure 2.4: Detailed drawing of the mechanical structure of the MDC [74].

with an end cap part at each end. It is located between the MDC and the Electromagnetic Calorimeter. The mean radius of the barrel is 870 mm. Each scintillator is a cuboid, with a quadratic base of 50×50 mm^2 and a hight of 2380 mm. 48 fan-shaped scintillators form the end caps. The barrel covers an angular range of $|cos(\theta)| < 0.83$, the end caps $0.85 < |cos(\theta)| < 0.95$.

The total time resolution of the TOF can be calculated as

$$\sigma = \sqrt{\sigma_i^2 + \sigma_b^2 + \sigma_l^2 + \sigma_z^2 + \sigma_e^2 + \sigma_t^2 + \sigma_w^2}\,, \tag{2.1}$$

where i stands for the intrinsic time resolution, l for the inaccuracy of the bunch length, b for the uncertainty of the clock system, z for the z-position uncertainty, e for the accuracy of the electronics, t for the inaccuracy in the flight time, and w for the time walk uncertainty. The detailed values can be found in [74]. Barrel and end caps have a total time resolution of $\sim$100 ps. This time resolution allows the separation of charged pions from charged kaons for momenta up to 0.9 GeV on a 2σ level.

inner radius barrel	810 mm
outer radius barrel	870 mm
scintillator dimensions	2380mm x 50mm x 50mm
angular acceptance barrel	$\|cos\theta\| < 0.83$
angular acceptance endcaps	$0.85 < \|cos\theta\| < 0.95$
total time resolution	$\sim$ 100 ps

Table 2.3: Properties of the TOF [74].

The TOF reconstruction searches for extrapolated tracks from the MDC, that matches to entries in the TOF. Then, the flight time of charged particles from the interaction point to the TOF is calculated with various corrections, like for example the effective light velocity in the scintillators. The dE/dx energy deposition in the TOF is determined, too, and added to the one in the Electromagnetic Calorimeter to gain a better shower resolution.

2.2.4 Electromagnetic Calorimeter

The Electromagnetic Calorimeter (EMC) measures the energy deposition of charged and neutral tracks. It consists of 6240 CsI(Tl) crystals in a barrel and two end cap parts. Each crystal is 28 cm long, with a front area of nearly 27 cm^2 and a back area of nearly 41 cm^2. The crystals are arranged such, that they point to the interaction point, as shown in the mechanical arrangement in Fig. 2.5.

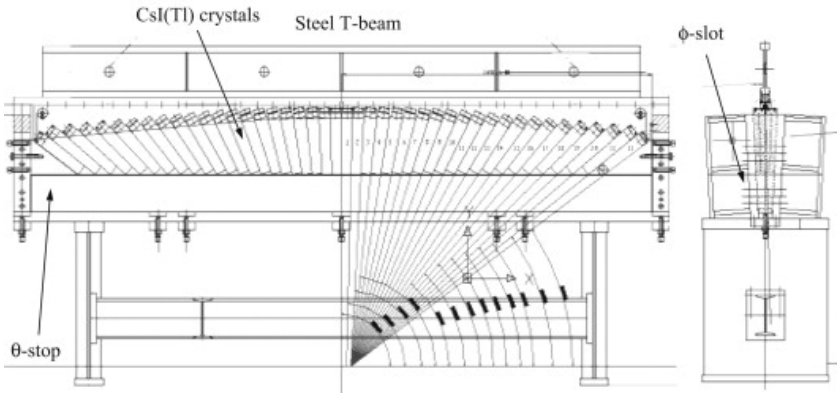

Figure 2.5: Mechanical arrangement of the CsI(Tl) crystals in the EMC [74].

The barrel has an inner radius of 940 mm, a length of 2750 mm, and covers an angular range of $|cos(\theta|) < 0.83$. The end caps have an inner radius of 500 mm and cover an angular range of $0.85 < |cos(\theta|) < 0.95$. The total acceptance of the EMC is 93% of 4π.

The energy resolution of the EMC is better than 2.5% at 1 GeV photon energies [74], whereas $E(\mathrm{GeV})$ is the deposited energy in GeV. The measurable energy range for photons and electrons is from 20 MeV to 2.3 GeV. The position resolution in the xy-plane for an electromagnetic shower is $\sigma_{xy} \leq \frac{6\mathrm{mm}}{\sqrt{E(\mathrm{GeV})}}$ [74]. The measured energy resolution for photons is shown in Fig. 2.6.

The reconstruction of EMC showers has three parts. First, the corresponding calibration constants are used to convert the information of each crystal into an energy value using an analog-to-digital converter (ADC). Then, the crystals with the maximum energy depositions are chosen and clusters are formed around them. The energies of these clusters are added to

the total energy of a shower. At least, the determined energy depositions in the TOF, which can be matched to the showers, are added.

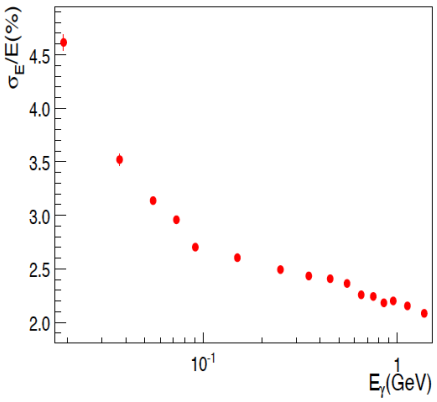

Figure 2.6: Measured energy resolution σ_E/E of photons, depositing an energy E_γ in the EMC [73].

inner radius barrel	940 mm
barrel length	2750 mm
inner radius endcaps	500 mm
Number of CsI(Tl) crystals	6240 (5280 in barrel and 960 in endcaps)
crystal length	280 mm
crystal front and rear sizes	5.2×5.2 cm^2 and 6.4×6.4 cm^2
angular acceptance barrel	$\lvert cos\theta\rvert < 0.83$
angular acceptance endcaps	$0.85 < \lvert cos\theta\rvert < 0.95$
total acceptance of 4π	93%
energy resolution	$\leq 2.5\%$ at 1 GeV photon energy
position resolution in xy-plane	$\sigma_{xy} \leq \frac{6\text{mm}}{\sqrt{E(\text{GeV})}}$

Table 2.4: Properties of the EMC [74].

2.2.5 Muon Chamber

The Muon Chamber (MUC) distinguishes muons from hadrons. The MUC consists of 9 layers of Resistive Plate Chambers (RPC) in the barrel and 8 RPC layers in the end caps. The layers in the barrel are arranged in octants (see Fig. 2.7). The iron absorbers have a total thickness of 56 cm. The angular acceptance of the barrel is $|cos\theta| < 0.75$ and $0.75 < |cos(\theta)| < 0.89$ in the end caps.

The reconstruction algorithm looks for hits in the MUC and matches them to extrapolated tracks from the MDC. After that, several parameters considered for muon/hadron separation, like e.g. the the depth of the track in the MUC, are calculated for each muon candidate. These information is used for muon identification. Figure 2.7 shows the performance of the MUC as

function of the transverse momentum p_t for muon and pion tracks.

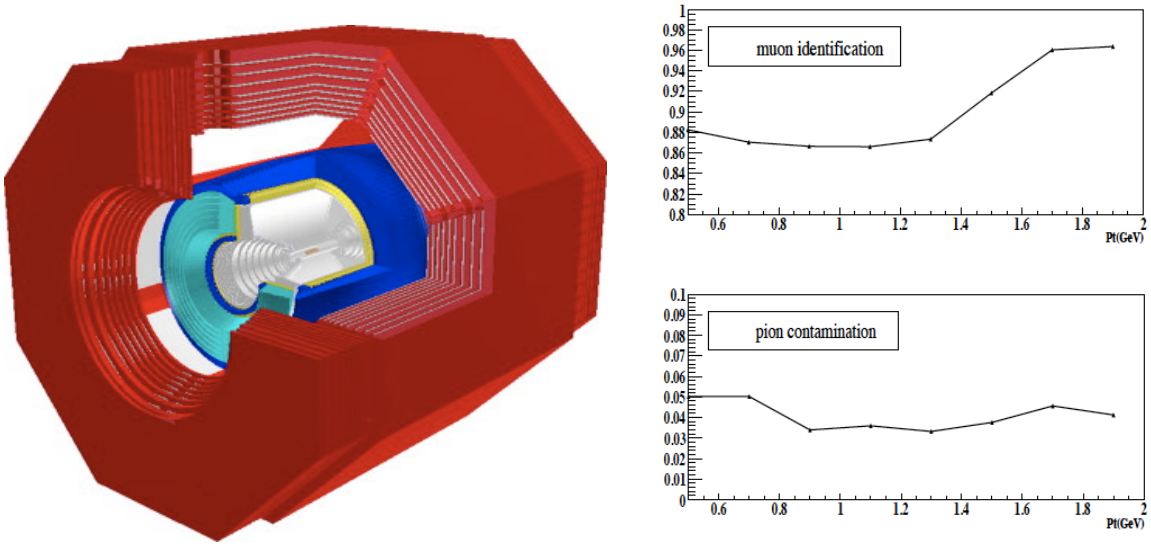

Figure 2.7: Left: Simulation of the Muon Chamber, displayed in red [77].
Right: The muon identification and pion contamination of the MUC as a function of the transverse momentum [73].

inner/outer radius barrel	1700 mm / 2620 mm
total steel plate thickness barrel	56 cm
inner/outer distance to IP end caps	2050 mm / 2800 mm
total steel plate thickness end caps	43 cm
number of layers barrel/end caps	9 / 8
angular acceptance barrel	$\|cos(\theta)\| < 0.75$
angular acceptance endcaps	$0.75 < \|cos(\theta)\| < 0.89$
total acceptance of 4π	89%
average efficiency barrel/end caps	96% / 95%

Table 2.5: Properties of the MUC [74].

2.2.6 Superconducting Solenoid Magnet

The Superconducting Solenoid Magnet (SSM) creates a magnetic field of 1.0 T at a current of 3400 A. This magnetic field forces the charged particles on a helix, and the momentum of charged particles can be measured by the MDC. The magnet has a length of 3.52 m and a radius of 1.48 m. It is positioned between EMC and MUC. It uses an Al stabilized NbTi/Cu conductor. The magnetic field inside the detector was measured with a precision better than 1 mT. Therefore, an automated field mapping device was used, which can move precisely in z and ϕ direction. The distribution of the magnetic field in z direction, B_z, is shown in Fig. 2.8.

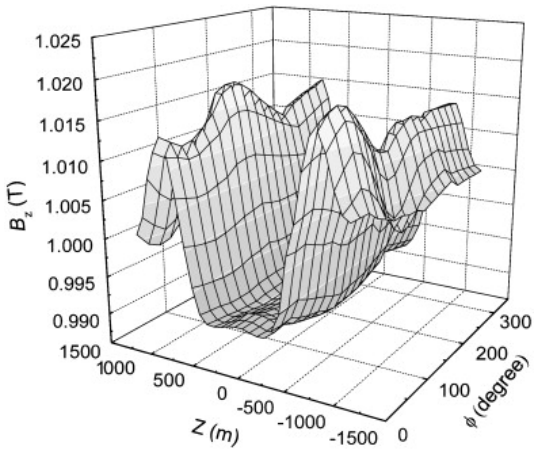

Figure 2.8: Distribution of the magnetic field in z direction, B_z, in a mapping volume in z and ϕ direction [74].

radius	1.48 m
length	3.52 m
SC core wire material	Nb-Ti/cu/Al (1/0.9/28.2) with 99.998% Al
Number of turns	848
current	3369 A
central field	1.0 T
stored energy	9.8 MJ
collant	liquid He at 4.5 K

Table 2.6: Properties of the SSM [74].

2.3 Trigger System

The Trigger System has to identify interesting events from a physics point of view, and to suppress contamination from cosmic rays or machine background. The number of saved events has to be be as low as the data acquisition system (DAQ) can handle. The total trigger rate is 4000 Hz. Background and Bhabha scattering events are reduced to nearly 2000 Hz. The rate for cosmic background is nearly 90 Hz. The rejection for beam backgrounds, which have a rate of about 40 MHz, is $5{\cdot}10^{-5}$.

The Trigger consists of two parts, a level-1 hardware trigger and a level-2 software event filter. The signals from the sub detectors are split into information for the hardware trigger and for the digitization storage. The trigger logic is saved in FPGA chips, with a trigger latency of 6.4 μs. The total data volume is 50 Mbytes/s. A chart of the trigger logic is shown in Fig. 2.9, more detailed information can be found in Ref. [78].

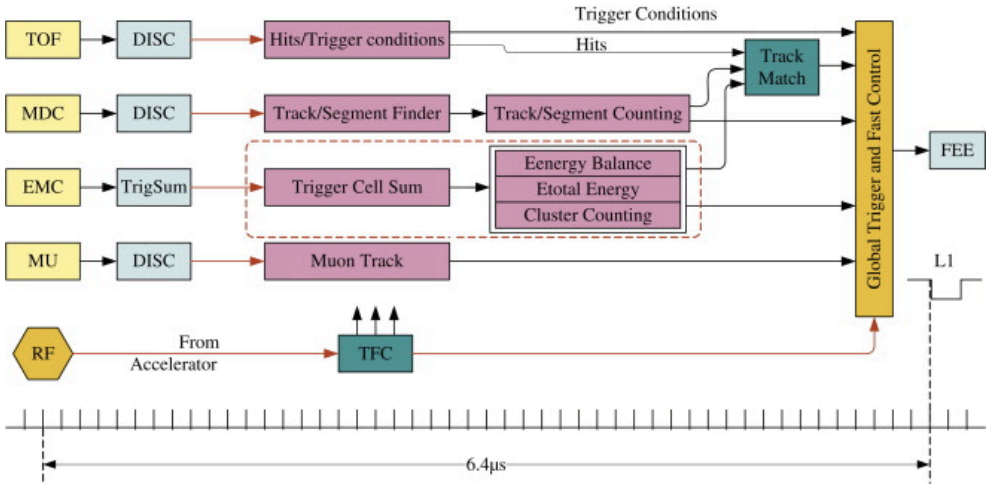

Figure 2.9: Trigger logic at BESIII [78].

2.4 The BESIII Offline Software System

The BESIII computing center is arranged at IHEP. The PC farm has about 2000 nodes for data and Monte Carlo (MC) production. Also other collaborating universities are involved. The BESIII Offline Software System (BOSS) is a C++ based, object oriented programming environment, running primarily on the Scientific Linux CERN (SLC4) [80] operating system. The software system consists of five parts: framework, simulation, reconstruction, calibration and analysis. The BOSS architecture can be seen in Fig. 2.10, more detailed information can be found in Ref. [74].

The framework is based on the Gaudi package [81]. This package allocates utilities for event simulation, development and analysis. The framework also provides other services, like tools for calculating the magnetic field at each point in the detector, tracing back reconstructed tracks to their Monte Carlo origin, or a random trigger to simulate background contributions.

The detector simulation is based on the GEANT4 package [82, 83]. It simulates the particle tracks and their interaction with the detector material. The information for material and geometry of the detector is stored in the Geometry Design Markup Language (GDML) [84]. The detector response is modeled by the digitization code, which simulates readout electronics, noise, dead channels, and the trigger system. The detector simulation has four parts: event generators, detector description, particle tracking and detector response. The event generators produce the raw data, based on the MC information.

The reconstruction and calibration package transforms the raw data to Data-Summary-Tape

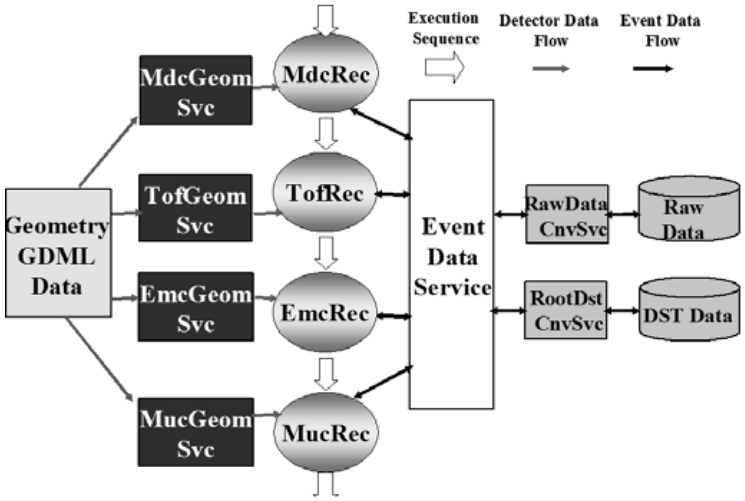

Figure 2.10: The BOSS architecture [74].

(DST) data. The MDC reconstruction uses a track finding algorithm and a Kalman-filter trace fitting algorithm.

The particle identification algorithm is based amongst others on the dE/dx and Time-of-Flight measurements, as described in section 2.5. In the TOF reconstruction, the MDC tracks are extrapolated to the TOF system and are matched with the hits in this system. After that, corrections are applied, like attenuation modifications. The shower- and cluster-finding algorithm measures the energy and position in the EMC. EMC reconstruction has three parts. First, the ADC value of each crystal is converted to an energy value. Second, the clusters are simulated by a clustering algorithm. Third, the showers, with their energy and position, are ascertained. Last, a muon track finder determines tracks in the MUC. The MUC reconstruction searches for hits in the muon chamber and calculates the track candidates. Then, these candidates are matched with tracks from the MDC.

The analysis part is a C++ program to select the physics of interest. Such a program has to be developed by the BOSS user. This program transforms the DST data to root ntuples, which can be analyzed by the CERN analysis data framework root [85]. The BOSS version used in the analysis presented in this thesis is release 6.6.2.

2.5 The BESIII particle identification system

The BESIII particle identification (PID) system can use the information of all sub detectors, calculating a likelihood for a specific particle hypothesis. It is implemented in the BOSS

framework. The user can decide the detector parts and particle hypotheses used, that shall be considered in the calculation of the likelihood. The different methods of the detector systems, MDC, TOF, EMC and MUC are described in the following:

MDC: The MDC measures the energy loss dE/dx of charged particles. The normalized pulse height is calculated, which is a function of the momentum and mass of the particle. Figure 2.11 shows the normalized pulse height as a function of the momentum p. Kaons with $p < 0.5$ GeV and protons with $p < 0.9$ GeV can be separated from electrons, muons, and pions with this detector system on a 3σ level.

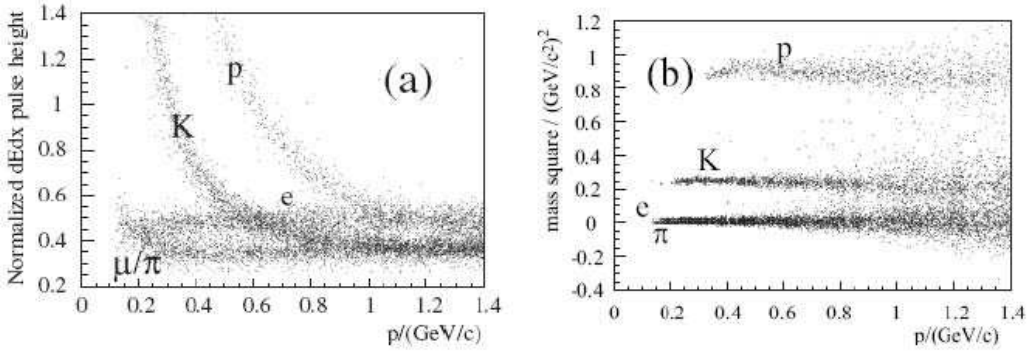

Figure 2.11: (a) normalized pulse height of $\frac{dE}{dx}$ vs. momentum for kaons K, protons p, electrons e, muons μ, and pions π [73].
(b) Mass squared distribution from the TOF system [73].

TOF: With the measured flight time t_{meas} and flight length L, the mass squared of a particle with momentum p can be calculated as

$$m^2 = p^2 \cdot \frac{1-\beta^2}{\beta^2} \,, \tag{2.2}$$

$$\beta = \frac{L}{c \cdot t_{meas}} \,, \tag{2.3}$$

whereas c is the speed of light. The m^2 distributions as a function of p can be seen Fig. 2.11 for different particles. Like this, it is possible to separate protons and kaons from electrons and pions.

EMC: The EMC uses the deposited energy and the shape of the electromagnetic showers as input for the PID. The energy deposition for electrons, muons, and pions is shown in Fig. 2.12 (a). Electrons and positrons deposit nearly their whole energy in the EMC. Hence, the ratio energy over momentum E/p is close to one. Muons and pions can not be separated by this quantity.

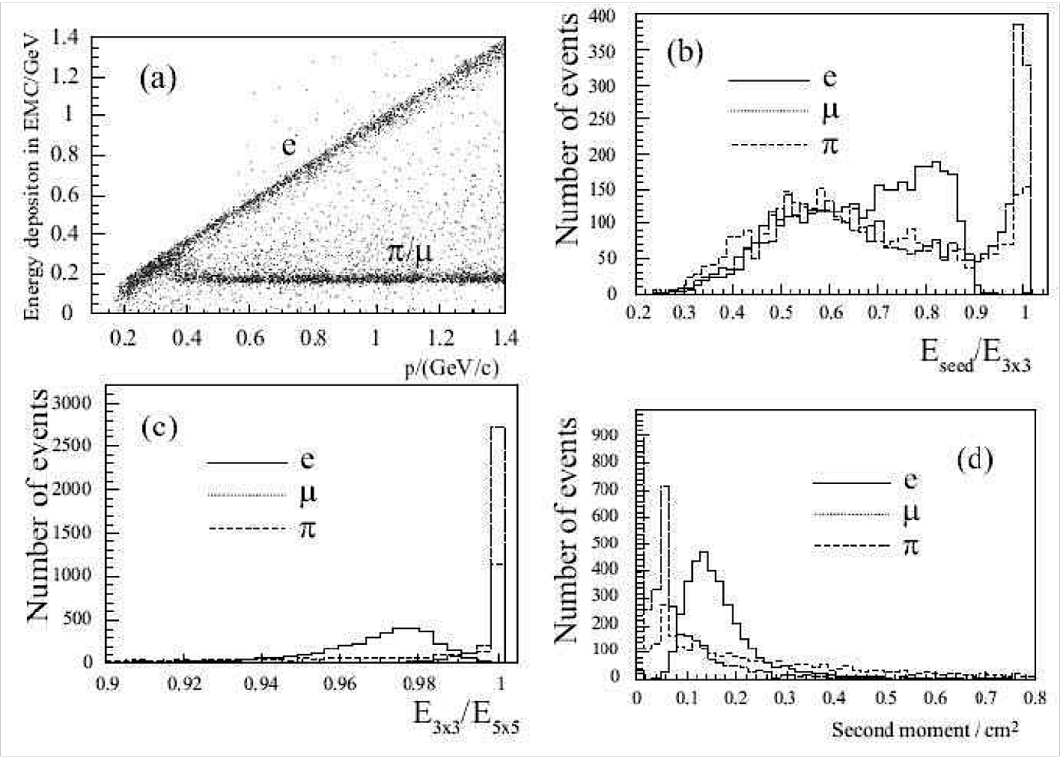

Figure 2.12: (a) Energy deposition vs. momentum of charged particles [73].
(b) and (c): $E_{seed}/E_{3\times3}$ and $E_{3\times3}/E_{5\times5}$ for a momentum of 1 GeV [73].
(d) Second moment for a momentum of 1 GeV [73].

Three variables are chosen to characterize the shape of an electromagnetic shower. E_{seed} is the deposited energy in the central crystal, $E_{3\times3}$ and $E_{5\times5}$ are the energy depositions in the central 3×3 and 5×5 crystal arrays. The fractions $E_{seed}/E_{3\times3}$ and $E_{3\times3}/E_{5\times5}$ are used to characterize the shower shapes. They are presented in Fig. 2.12 (b) and (c) for particles with a momentum of 1 GeV. The third quantity is the second moment P, defined as

$$P = \frac{\sum_i E_i \cdot d_i^2}{\sum_i E_i} \ , \tag{2.4}$$

where E_i is the energy deposition in the i-th crystal and d_i the distantce of this crystal to the center of the reconstructed shower. It is shown in Fig. 2.12 for momenta of 1 GeV. A π/μ separation is hardly visible in the shower shape variables.

MUC: If a hadron reaches the MUC, it usually produces many hits in one of the first layers and is stopped, while a muon penetrates many layers, due to its larger interaction length. Figure 2.13 shows the depth and total number of hits in the MUC layers for muon and charged pion tracks. With The MUC information, it is possible to distinguish between pions and muons quite efficiently.

Anticipating the further analysis, the BOSS PID system is not able to separate pions and muons efficiently enough, to reach the accuracy needed for this analysis. Therefore, a new PID is developed, an artificial neural network, as presented in chapter 5.

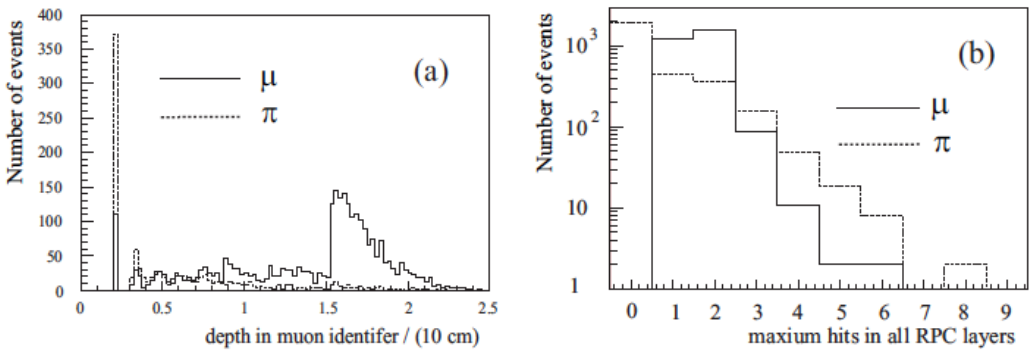

Figure 2.13: Depth (a) and total hits in MUC layers (b) for muons and pions [73].

2.6 Data set and Monte Carlo production

This work uses the BESIII data set taken at $\sqrt{s} = 3.773$ GeV. Two run periods in 2010 and 2011 were accomplished, with a total integrated luminosity of 2916.94 pb^{-1} [86]. The exact numbers are listed in Tab. 2.7.

round	**run number**	**integrated luminosity $\mathcal{L}$**
round 1	11414 - 13988 and 14395 - 14604	927.67 ± 0.10 ± 9.28 pb^{-1}
round 2	20448 - 23454	1989.27 ± 0.15 ± 19.89 pb^{-1}
sum		2916.94 ± 0.18 ± 29.17 pb^{-1}

Table 2.7: Collected data at $\sqrt{s} = 3.773$ GeV. The first error is statistical and the second error systematic [86]. Round 1 was taken in 2010, round 2 in 2011.

The Monte Carlo (MC) generators used to produce the signal channel $\pi^+\pi^-\gamma$ and various background channels are PHOKHARA [87, 88, 89, 90], KKMC [91], and BABAYAGA [92, 93, 94]. They are described in the following, more detailed information can be found in the references listed below.

PHOKHARA

PHOKHARA [87, 88, 89, 90] is a MC event generator for simulating initial state radiation (ISR) for several exclusive leptonic and hadronic final states. It is designed to simulate ISR up to next-to-leading order (NLO). The theoretical precision is better than 0.5%. The following final states can be generated with PHOKHARA: $\pi^+\pi^-$, $\mu^+\mu^-$, K^+K^-, $\bar{K}^0K^0$, $\bar{p}p$, $\bar{n}n$, $\pi^+\pi^-\pi^0$,

$2\pi^+2\pi^-$, $2\pi^0\pi^+\pi^-$ and $\bar{\Lambda}(\to \pi^+\bar{p})\Lambda(\to \pi^-p)$.
The leading order (LO) final state radiation (FSR) corrections are implemented for $\pi^+\pi^-$, $\mu^+\mu^-$, K^+K^- and $\bar{p}p$. For muon and pion pair production, also the NLO FSR corrections are included. Experimental results from *BABAR* , CMD2, CLEO-c and ALEPH were used to improve the model description of the pion channels.
A large number of input parameters can be changed. The cms energy, the maximum hadronic or leptonic invariant mass, the minimum photon energy, as well as the angular range of the hadronic system, can for instance be set. In addition, the minimum and maximum photon angle of the LO ISR photon can be adjusted. Furthermore, the NLO ISR correction can be switched off, also the FSR corrections, if they are implemented for the final state. Finally, also the vacuum polarization can be turned on and off via a flag in the input card. These possible settings and the high precision are adequate to study ISR events at BESIII. Hence, PHOKHARA is the most used MC generator of choice for the ISR analyses described in this thesis. The PHOKHARA settings can be found in Tab. 2.8.

minimum photon energy LO	0.05 GeV
minimum photon energy NLO	0.1 MeV
minimum photon angle	0.0°
maximum photon angle	180.0°
minimum hadrons/muons angle	0.0°
maximum hadrons/muons angle	180.0°
CMS energy	3.773 GeV
vacuum polarization	yes
pion form factor	Gounaris-Sakurai parametrization
NLO	yes
FSR LO	yes if possible
FSR NLO	yes if possible

Table 2.8: Settings of PHOKHARA in this work.

KKMC

KKMC [91] is a Monte Carlo event generator for the process $e^+e^- \to f\bar{f} + n\gamma$, $f = \mu$, τ, u, d, s, c, b, and n = 0,1,2,.... It is based on precise predictions of the Standard Model. ISR and FSR effects are calculated in QED up to second order. Electroweak corrections are implemented in first order. To produce n-body decays, generic phase space calculations to n-body final states can be used. The non-radiative final state continuum ($q\overline{q}$), D^+D^-, $D^0\overline{D^0}$, and $\tau^+\tau^-$ are already generated by the collaboration and are available in the BOSS framework.

BABAYAGA

BABAYAGA [92, 93, 94] is an exclusive event generator for $e^+e^- \to e^+e^-(n\gamma)$, $e^+e^- \to$

$\mu^+\mu^-(n\gamma)$, and $e^+e^- \to \gamma\gamma$ events, reliable for cms energies below 12 GeV. It is of high interest for precise luminosity measurements at e^+e^- colliders. The calculations are based on the matching of exact NLO order corrections, together with a parton shower algorithm, including also two-loop corrections, hadronic vacuum polarization, and light pair contributions. The claimed precision of KKMC 3.5 is 0.5% [93], reduced to 0.1% by its successor BABAYAGA@NLO [94].

Several final states are produced to study background contributions to the signal channel $e^+e^- \to \pi^+\pi^-\gamma$. Therefore, the run numbers of the data taking (see Tab. 2.7) are taken into account for the simulation. This is necessary for comparing simulated events with data. Like this, one can take the status of the several detector components into account, as it has been at the moment of data taking.

final state	**cross section [pb]**	**MC generator**	**events**
$\pi^+\pi^-\gamma$	1194	PHOKHARA	$2 \cdot 10^7$
$\pi^+\pi^-\pi^0\gamma$	187	PHOKHARA	$2 \cdot 10^6$
$\pi^+\pi^-\pi^0\pi^0\gamma$	356	PHOKHARA	$4 \cdot 10^6$
$\pi^+\pi^-\pi^+\pi^-\gamma$	245	PHOKHARA	$2 \cdot 10^6$
$\mu^+\mu^-\gamma$	2864	PHOKHARA	$2 \cdot 10^7$
$K^+K^-\gamma$	253	PHOKHARA	$3 \cdot 10^6$
$K^0\overline{K^0}\gamma$	499	PHOKHARA	$4 \cdot 10^6$
$p\bar{p}\gamma$	8	PHOKHARA	$1 \cdot 10^5$
continuum	12 200	KKMC	$183 \cdot 10^6$
$\tau^+\tau^-$	3 000	KKMC	$45 \cdot 10^6$
$e^+e^-(n\gamma)$	520 500	BABAYAGA 3.5	$400 \cdot 10^6$
$\psi(3770) \to D^+D^-$	2 880	KKMC	$83 \cdot 10^6$
$\psi(3770) \to D^0\overline{D^0}$	3 660	KKMC	$111 \cdot 10^6$
$\psi(3770) \to$ non $D\overline{D}$	500	KKMC	$10 \cdot 10^6$
$e^+e^- \to \gamma\ J/\psi$	1 100	KKMC	$11 \cdot 10^6$

Table 2.9: Produced MC samples for the signal and background studies. The last seven samples are already provided by the collaboration. The cross sections are calculated at $\sqrt{s} = 3.773$ GeV.

Chapter 3

Initial state radiation at BESIII

To measure the $e^+e^- \to \pi^+\pi^-$ cross section at BESIII, the method of initial state radiation is used. Events, where a photon is emitted in the initial state, are exploited. This allows for measurements of $\pi^+\pi^-$ invariant masses between 06 and 0.9 GeV, although the data is taken at $\sqrt{s}$ = 3.773 GeV.

The ISR method is introduced in the following, together with the BESIII specific constraints and possibilities.

3.1 Initial state radiation

As input for $a_\mu^{\mathrm{had,VP}}$, hadronic cross sections as a function of the nominal energy $\sqrt{s'}$ needs to be measured. Two different approaches can be applied.

On the one hand, one can perform a scan experiment. Setting the cms energy of the collider to $\sqrt{s'}$, one can measure events of the type $e^+e^- \to \pi^+\pi^-$, in case of the signal process investigated. The advantage of this method is a high gain in statistics. The disadvantage is, that it is a costly procedure, since the collider has to be calibrated for each $\sqrt{s'}$ energy point. Most recently, the cross section $\sigma_{\pi\pi}$ has been measured at CMD2 [55, 56] and SND [57] in this way, for example.

On the other hand, one can use data, taken at a fixed $\sqrt{s}$, and exploit events of the type $e^+e^- \to \pi^+\pi^-\gamma$. If a photon γ is emitted from the initial e^+e^- system, the effective energy to produce the $\pi^+\pi^-$ pair is lowered to $\sqrt{s'}$ ($\sqrt{s'} < \sqrt{s}$). Measurements of $\sigma_{\pi\pi}$ from threshold to $\sqrt{s}$ are possible. This method is called initial state radiation (ISR). The advantage of ISR versus the scan mode is, that one can use one large data set. The difference is, that ISR events are suppressed by a factor of the electromagnetic fine structure constant α, which lowers the statistics by $\approx 1/137$. This was the approach followed by the *BABAR* [64] and KLOE [59, 60, 61, 62] experiments.

This work exploits the ISR method and, thus, follows the *BABAR* and KLOE approaches.

3.2 Leading Order ISR

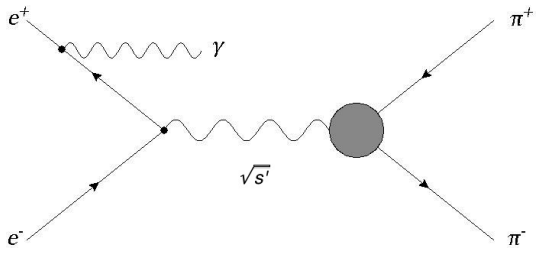

Figure 3.1: Leading order initial state radiation. Exactly one photon is emitted in the initial state, which means by one of the incoming beam leptons.

In case of leading order (LO) ISR, where exactly one ISR photon is emitted, the invariant mass of the hadronic system m can be calculated as [95]:

$$m^2 = s - 2 \cdot \sqrt{s} \cdot E_\gamma \,, \tag{3.1}$$

where E_γ is the energy of the ISR photon.

The probability, that an ISR photon is emitted with the energy $x \cdot \sqrt{s}$ $(0 < x < 1)$ under a polar angle θ_γ, can be expressed by the following formula in LO [95]:

$$h_0(s,x,\theta) = \frac{\alpha}{\pi x}\left[\frac{(1-x+\frac{x^2}{2})sin^2\theta - \frac{x^2}{2}sin^2\theta}{(sin^2\theta + \frac{4m_e^2}{s}cos^2\theta)^2} - \frac{4m_e^2}{s}\frac{(1-2x)sin^2\theta - x^2cos^4\theta}{(sin^2\theta + \frac{4m_e^2}{s}cos^2\theta)^2}\right), \quad (3.2)$$

where m_e is the electron mass and $x = \frac{2E_\gamma}{\sqrt{s}}$. The relative probability, that the photon is emitted in the angular range $\theta_0 < \theta_\gamma < 180°$ - θ_0, can be seen in Fig. 3.2 for three different values of x.

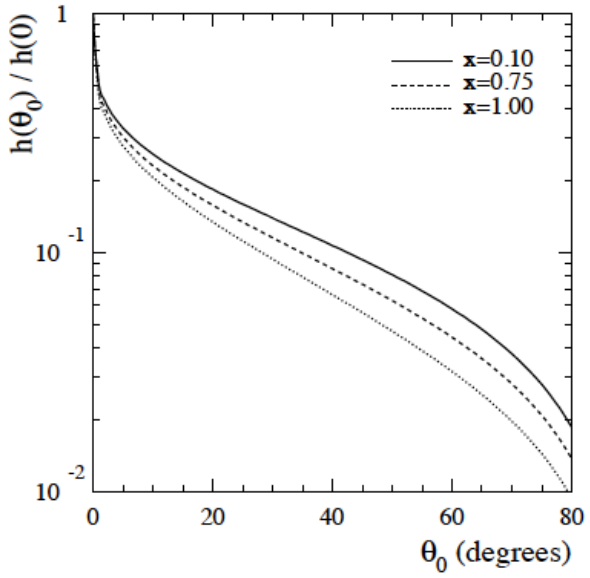

Figure 3.2: Relative probability for the ISR photon to be emitted in the angular range $\theta_0 < \theta < 180°$ - θ_0 for three values of x [95].

The LO ISR photon is preferably emitted at small polar angles with respect to the beam axis, which can be seen in the θ_γ distribution of the ISR photon, shown in Fig. 3.3.

The Radiator Function $H(s,x,\theta_\gamma)$ describes the probability, that a LO ISR photon is emitted in a symmetric θ_γ region around $\theta_\gamma = \pi/2$. It can be approximated for $\theta_\gamma \gg \frac{m_e}{\sqrt{s}}$ by the following expression [95]:

$$H(s,x,\theta_\gamma) = \int_{\theta_\gamma}^{\pi-\theta_\gamma} h_0(s,x,\theta)sin\theta d\theta \approx \frac{\alpha}{\pi x}\left[(2-2x+x^2)\ln\left(\frac{1+cos\theta_\gamma}{1-cos\theta_\gamma}\right) - x^2\cos\theta_\gamma\right]. \quad (3.3)$$

With $H(s,x,\theta_\gamma)$, it is possible to connect the non-radiative hadronic cross section $\sigma(m)$ with

the radiative one $\sigma_{ISR}(m)$ via [95]

$$\frac{d\sigma_{ISR}(m)}{dm} = \frac{2m}{s} \cdot \epsilon(s,m) \cdot H(s,x,\theta_\gamma) \cdot \sigma(m) \ , \tag{3.4}$$

whereas $\epsilon(s,m)$ is the detection efficiency.

The properties of a photon, emitted in the initial state, depend on the cms energy of the collider. This work deals with $e^+e^- \to \pi^+\pi^-\gamma$ events at $\sqrt{s} = 3.773$ GeV at BESIII. According to formula 3.1, high photon energies $E_\gamma > 1.8$ GeV are necessary to gain invariant $\pi^+\pi^-$ masses $m_{2\pi}$ below 0.9 GeV, which is the goal of this work. Two different measurement methods can be performed:

tagged measurement: the LO ISR photon is emitted in the direction of the fiducial volume of the EMC and can be detected. Its properties can be used in the event selection.

untagged measurement: the LO ISR photon is emitted with a small or large θ_γ, along the beam pipe. Hence, it cannot be detected and has to be predicted by calculating the missing momentum.

These two cases have to be studied separately. A MC study of $\pi^+\pi^-\gamma$ events is performed, using the PHOKHARA event generator, as described in section 2.6.

Figure 3.3 shows the polar angle of the LO ISR photon. The shaded areas display the acceptance regions of the BESIII EMC. The statistics in the tagged case are more than one order of magnitude lower than the untagged ones. However, the mass region of interest in this work, 0.6 GeV $< m_{2\pi} <$ 0.9 GeV, can not be studied in the untagged case. This is visible in Fig. 3.4, where the selection efficiency, determined with MC, of untagged ISR events is shown. The efficiency drops rapidly to zero below $m_{2\pi}$ masses below 0.9 GeV. The reason is a kinematical one. As explained, a high energetic ISR photon with $E_\gamma > 1.8$ GeV has to be emitted to reach these masses. In the untagged case, it is emitted along the beam axis. Hence, the produced $\pi^+\pi^-$ system is highly boosted back-to-back, also in the direction of the beam axis. Due to this boost, the opening angle of the two charged pions is small, supported by the fact that the energy of this system is not really high (< 0.9 GeV). Therefore, at least one of the generated hadrons do not fly in the direction of the fiducial volume of the MDC and can not be detected.

The conclusions for this work are:

- Exploiting ISR events $e^+e^- \to \pi^+\pi^-\gamma$, it is possible to measure $\sigma_{\pi\pi}$ at energies below 0.9 GeV, although data taken at $\sqrt{s} = 3.773$ GeV is used.

- LO ISR photons with energies $E_\gamma > 1.8$ GeV have to be emitted, to reach $m_{2\pi} < 0.9$ GeV.
- $\pi^+\pi^-\gamma$ events with $m_{2\pi} < 0.9$ GeV can only be studied with the tagged analysis approach.

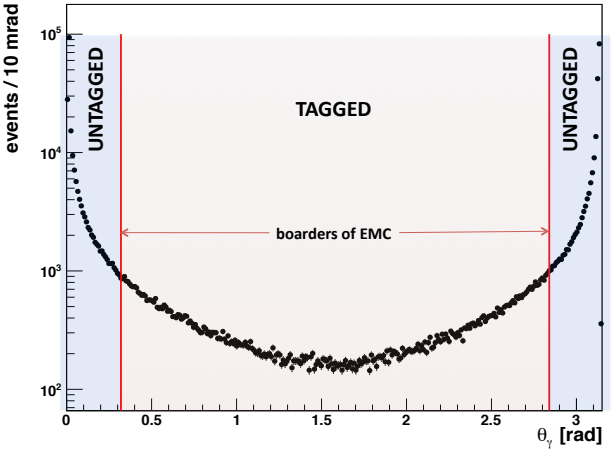

Figure 3.3: Number of $e^+e^- \to \pi^+\pi^-\gamma$ MC events versus their polar angle. The event number is arbitrary. The typically behavior of the radiator function can be seen, since most of the events are emitted along the beam axis at $\theta_\gamma = 0$ and $\theta_\gamma = \pi$. The shaded areas are the acceptance regions of the BESIII EMC and display, at which angles the tagged analysis can be performed.

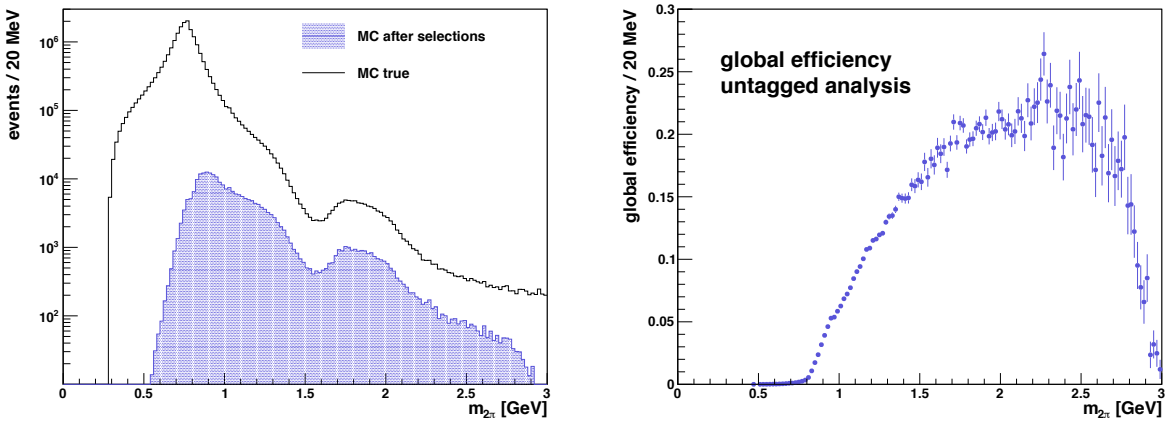

Figure 3.4: Left: MC distribution (black) for $\pi^+\pi^-\gamma$ events as a function of $m_{2\pi}$, without any requirements applied, compared to remaining events after applying an event selection for untagged events, which is not presented in this work and will be topic of further studies (blue shaded).
Right: ratio of these distributions, yielding the detection efficiency in the untagged case. The mass region below 0.9 GeV can not be studied in this case, since the efficiency drops rapidly to zero.

3.3 Next-to-leading order corrections

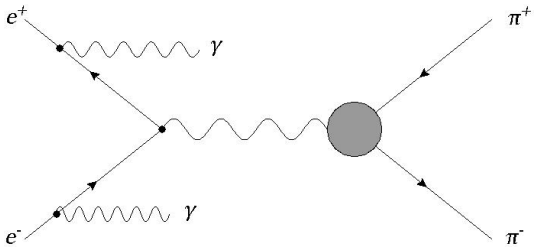

Figure 3.5: Next-to-leading order initial state radiation.

In addition to the LO ISR photon, a second one can be emitted in the initial state, too. This is called next-to-leading order (NLO). Figure 3.6 shows the energy distribution of ISR photons in case of NLO, simulated with the PHOKHARA generator. The distribution is symmetric, because the photons are not sorted by their order on generator level. The energy of the second photon is in most cases small compared to the one of the first photon. As expected, the cluster points are around 1.8 GeV and a small corresponding NLO energy.

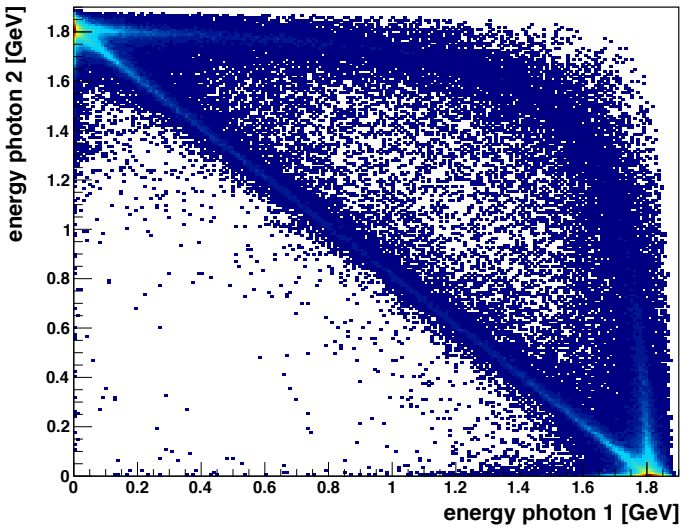

Figure 3.6: Energies of the two ISR photons in case of NLO $\pi^+\pi^-\gamma$ events, simulated with the PHOKHARA generator. The distribution is symmetric because the photons are not sorted by their order. The $\rho(770)$ resonance dominates the $\pi^+\pi^-$ cross section completely. According to formula(3.1), the sum of the photon energies have to be greater than 1.8 GeV to produce it. This leads to structures. A "band" with constant energy sum, clusters at the upper left and lower right edges, and a "bow" with one high and one low energetic photon.

The corresponding distribution for the polar angle can be seen in Fig. 3.7. In nearly all of the cases one photon has a very small angle. In many cases both photons have a small angle (clusters in the edges), which corresponds to the untagged case. The other ones correspond to the tagged case where the leading order ISR photon is emitted in the angular acceptance range

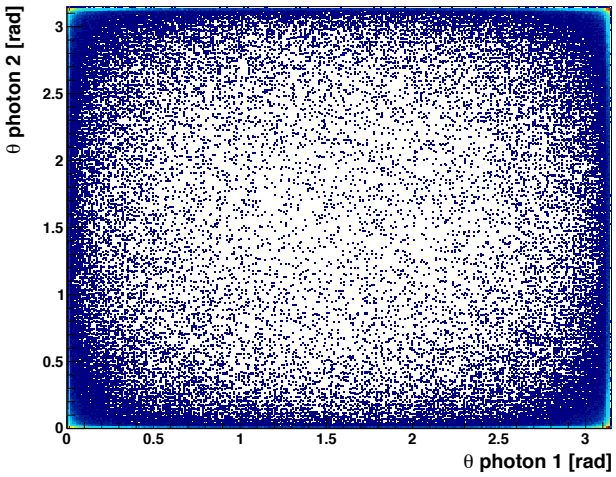

Figure 3.7: θ distribution in the NLO case. Shown is the angle of the first photon vs. the angle of the second one, simulated with the PHOKHARA event generator. Attend the clusters in the edges.

of the EMC. Only a very few events are such, that both photons can be detected in the EMC.

3.4 Final state radiation

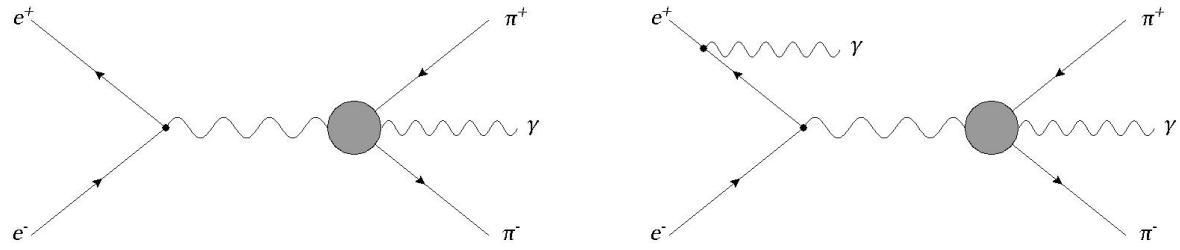

(a) leading order FSR (b) ISR + FSR

Figure 3.8: Final state radiation contributions.

Due to the fact that there are two charged pions in the final state, it is also possible, that a photon is emitted from the final state. This leads to a shift of the $m_{2\pi}$ distribution towards smaller masses. Final state radiation (FSR) and ISR photons can not be discriminated via their kinematics. Two different cases have to be distinguished.

On the one hand, only an FSR photon is emitted. In the $\pi^+\pi^-$ case this is very unlikely at $\sqrt{s} = 3773$ GeV, since the $\pi^+\pi^-$ cross section is nearly zero at this energy. Figure 3.9 shows the ratio of the cross section containing only LO ISR and the cross section containing LO ISR and LO FSR for $m_{2\pi}$ masses between 600 and 900 MeV and tagged photons. It is produced

with the PHOKHARA generator. A linear fit (p0) is performed to quantify the difference. As can be seen, the LO FSR contribution at $\sqrt{s} = 3.773$ GeV is extremely small in the kinematic configuration of BESIII. This FSR contribution on the level of $e^+e^- \to \pi^+\pi^-\gamma$ events, which means that the virtual photon has exactly the cms energy, is a background that needs to be corrected for. However, FSR on the level of $e^+e^- \to \pi^+\pi^-$ events, which means the virtual photon propagator has an energy between 600 and 900 MeV, is the desirable case. Indeed, by convention one uses the $\sigma(e^+e^- \to \pi^+\pi^-(\gamma_{\mathrm{FSR}}))$ cross section, including FSR, as input for the calculation of a_μ [16]. This FSR correction can be described with a calculation by Schwinger [96] (see section 10.5) assuming point-like particles.

On the other hand, ISR and FSR photons can be emitted simultaneously. This is a background, which shifts the invariant mass spectrum towards smaller values. In the extraction of the cross section, one needs to correct for this effect (see section 10.5).

The PHOKHARA event generator describes FSR up to NLO assuming point-like pions. As shown recently by the *BABAR* experiment [97], the assumption of point-like pions is reasonable at the energy scale of *BABAR* and BESIII. This is shown by studying the interference between ISR and FSR, which leads to a measurable forward-backward asymmetry, of the $\pi^+\pi^-$ final state and confronts the model of point-like pions in MC with data. No sizable effect beyond the point-like pion model is observed, which shows that this model is reasonable at the *BABAR* energy scale. We performed the same analysis at BESIII as well and, also, at the BESIII energy and with the BESIII geometry no indication for effects beyond point-like pions is visible (see section 11.4).

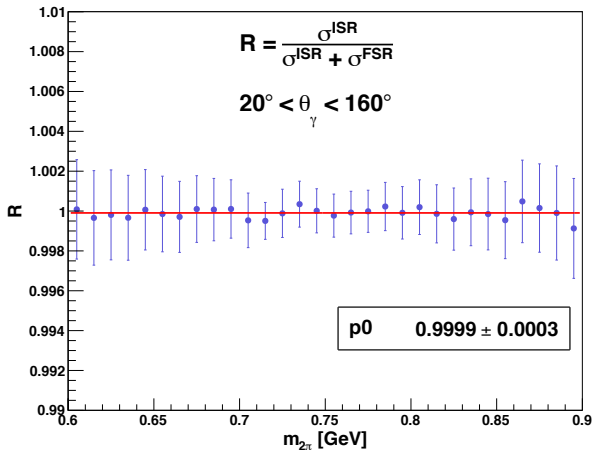

Figure 3.9: Ratio of the cross section containing only LO ISR and the cross section containing LO ISR and LO FSR for $m_{2\pi}$ masses between 600 and 900 MeV and tagged photons. A linear fit (p0) is performed to quantify the difference.

Chapter 4

Event Selection for $e^+e^- \to \pi^+\pi^-\gamma$ events

In this chapter the event selection for $e^+e^- \to \pi^+\pi^-\gamma$ events is presented. As motivated in the previous chapter, a tagged analysis is performed to study invariant masses between 0.6 and 0.9 GeV. The goal is to suppress as much background without losing too much signal events, by using kinematic and geometrical requirements. It turns out, that the $e^+e^- \to \mu^+\mu^-\gamma$ background can not be separated from the signal via kinematic criteria at BESIII, since the muon and pion masses are too similar. A different selection method is used, which is described in the next chapter.

4.1 Charged track selection

A charged track is defined as an entry in the MDC. The momentum can be measured via the curvature in the magnetic field. In $\pi^+\pi^-\gamma$ events, the pions are generated at the interaction point (IP) of the e^+e^- annihilation. Extrapolating the curvature information from the MDC, the point of closest approach to this IP is computed for each track. It has to be within a cylinder with length $|\mathrm{V}_z| < 10.0$ cm, along the beam axis, and a radius $|\mathrm{V}_r| < 1.0$ cm, perpendicular to the beam axis. To avoid edge effects in the MDC, the polar angle with respect to the beam axis, θ, has to satisfy 0.4 rad $< \theta < \pi -$ 0.4 rad. The number of charged tracks has to be two, with net charge zero. In case of three-track events, the contribution with net charge zero, which are closest to the IP, is chosen. In the magnetic field of 1T, charged pion tracks with a transverse momentum $p_t < 0.3$ GeV, spiral. They can enter and leave the MDC in a circle. This could create wrong information, like for example mimicking more than one track or a wrongly calculated momentum. Such tracks are rejected with the requirement $p_t < 0.3$ GeV,.

4.2 Photon selection

A photon is defined as neutral cluster in the EMC, without an associated hit in the MDC. The gaps between end caps and barrel part of the EMC are spared. Exactly one photon with a deposited energy $E_\gamma > 0.4$ GeV is required to select a tagged ISR event. According to formula (3.1) one expects photon energies greater than 1.8 GeV, in order to reach pion invariant masses below 1 GeV. Hence, this condition does not cause a large systematic uncertainty. In addition, the invariant mass of the hadronic system is in any case smaller than $m_{2\pi} < 3.35$ GeV. The background channel $e^+e^- \to \tau^+\tau^-\gamma$, where the τ leptons are decaying consecutively into pions and muons, is rejected by this requirement, since the threshold for this final state is at $2 \cdot m_\tau = 3.554$ GeV, whereas m_τ is the τ mass of (1776.82 $\pm$ 0.16) MeV [4].

4.3 Electron suppression using e-PID

The cross section of radiative Bhabha scattering events, $e^+e^- \to e^+e^-(n\gamma)$, is three orders of magnitude higher than the $\pi^+\pi^-\gamma$ one. A large number of electrons and positrons, respectively, survive the geometrical requirements, which needs to be suppressed. Therefore, the BESIII electron PID (e-PID), implemented in the BOSS software framework, is used, exploiting information from MDC, TOF and EMC. The probability p of a specific particle hypothesis is determined via a likelihood function, as described in section 2.5.

The probabilities for being a charged pion $p(\pi)$ and of being an electron, or positron, $p(e)$ are computed. The Double Logarithmic Likelihood (DLL) function

$$\mathrm{DLL}(\pi,\mathrm{e}) = 2 \cdot \log\left(\frac{\mathrm{p}(\pi)}{\mathrm{p}(\mathrm{e})}\right) \tag{4.1}$$

is calculated. If this quantity is positive, $p(\pi)$ is greater than $p(e)$. The distribution is shown in Fig. 4.1 for $\pi^+\pi^-\gamma$, $e^+e^-(n\gamma)$, and $\mu^+\mu^-\gamma$ events, determined with MC. One of the charged tracks is chosen randomly and its DLL value is filled into the histogram. For a better overview, the distributions are scaled to the same number of events between DLL values of -10 and 10. In reality, the electron distribution contains about a few hundred times more events. Both charged tracks have to fulfill the condition $\mathrm{DLL}(\pi,\mu) > 2$. This requirement suppresses 99.9% of all $e^+e^-(n\gamma)$ events.

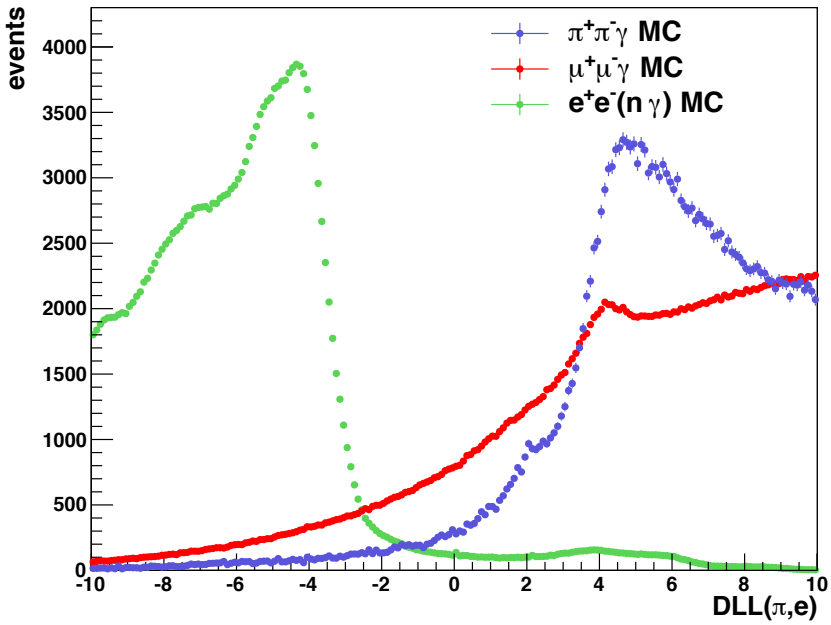

Figure 4.1: DLL(π,e) distribution for $\pi^+\pi^-\gamma$, $e^+e^-(n\gamma)$ and $\mu^+\mu^-\gamma$ MC events. One of the charged tracks is chosen randomly and its DLL value is filled into the histogram. For a better overview, the distributions are scaled to the same number of events between values of -10 and 10. In real the $e^+e^-(n\gamma)$ cross section is a few hundred times higher than the two others.

4.4 Kinematic fit

After the selections described so far a four constraint (4C) kinematic fit is performed, using the two charged tracks and the ISR photon candidate as input. The fit is performed under the hypothesis, that the charged particles found are pions, and that the four-momenta of these

tracks, together with the four-momentum of the ISR photon, fit to the four-momentum p_{CMS} of the initial e^+e^- system. Hence, the kinematic fit does not respect NLO effects. The e^+e^- beams have a crossing angle of 11 mrad, which yields to a boost. The boosted four-momentum is

$$p_{CMS} = \begin{pmatrix} 1 \\ 0.011 \\ 0 \\ 0 \end{pmatrix} \cdot \sqrt{s} \tag{4.2}$$

The fit has four constraints, the four entries of p_{CMS}. A χ^2 distribution with four degrees of freedom would be expected, if the errors are well-known. To quantify the goodness of the fit, this χ^2_{4C} variable is used. The distribution for $\pi^+\pi^-\gamma$ signal MC events is shown in Fig. 4.2, together with the main contributing background MC samples. They are scaled to the same luminosity. The histogram does not perfectly correspond to a χ^2 distribution. It is smeared due to the limited detector resolution, shifted to higher χ^2_{4C} values, and has a longer tail.

The main background in the present analysis is the channel $e^+e^- \to \mu^+\mu^-\gamma$. The pion and muon masses, $m_{\pi^\pm} = (139.57018 \pm 0.00035)$ MeV and $m_\mu = (105.6583715 \pm 0.0000035)$ MeV [4], are too close to each other for the performance of the BESIII MDC. The mass resolution of the MDC is not able to distinguish them. The χ^2_{4C} distribution is similar to the signal one and can not not be used to suppress the background by applying a requirement on this variable. The remaining $e^+e^-(n\gamma)$ events, too, have a similar χ^2_{4C} distribution. Other important backgrounds are $e^+e^- \to \pi^+\pi^-\pi^0\gamma$ and $e^+e^- \to K^+K^-\gamma$. Both have two charged particles in the final state and at least one photon, which can be misidentified as the signal channel.

A requirement on χ^2_{4C} shall reject background without loosing too much signal events. The distribution for $\mu^+\mu^-\gamma$ is similar to the signal one and, therefore, not taken into account for determining such a condition. One has to decide between two Hypothesis H_0 and H_1:

- H_0: the event is of the type $e^+e^- \to \pi^+\pi^-\gamma$
- H_1: the event is **not** of the type $e^+e^- \to \pi^+\pi^-\gamma$ (neglecting the $\mu^+\mu^-\gamma$ channel)

The χ^2_{4C} distributions between values of 0 and 200 are normalized to get a probability density in this range. The densities are called $f_0(\chi^2)$, corresponding to H_0, and $f_1(\chi^2)$, corresponding to H_1. They are displayed in Fig. 4.3. The hypothesis H_0 is accepted if

$$\frac{p_{2\pi} \cdot f_0(\chi^2)}{C_{01}} > \frac{p_{bg} \cdot f_1(\chi^2)}{C_{10}}\,, \tag{4.3}$$

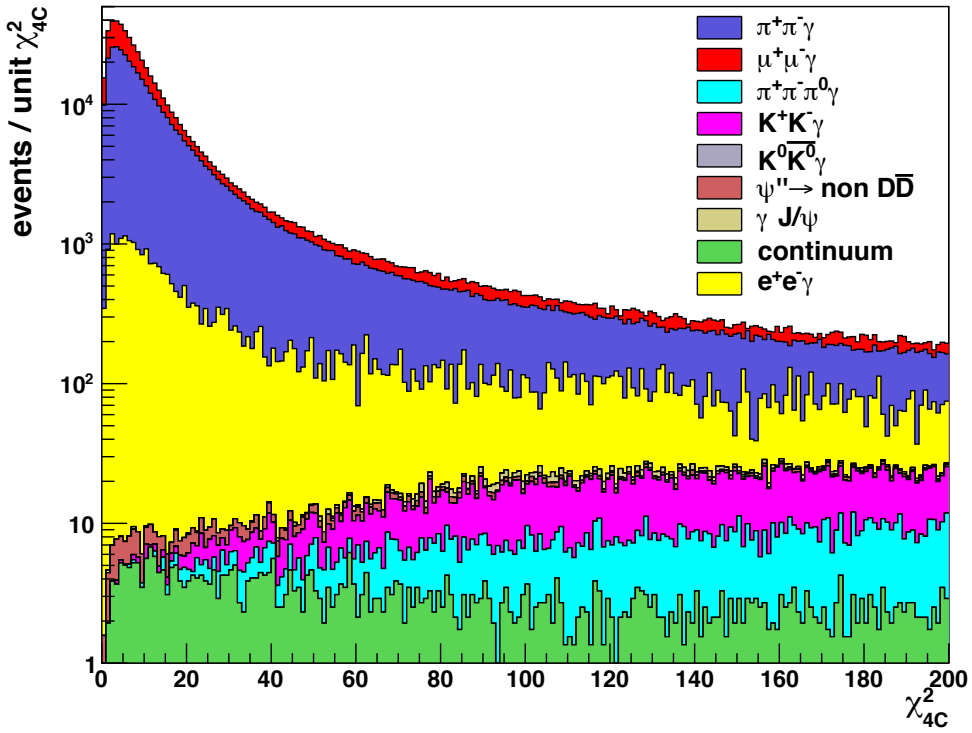

Figure 4.2: χ^2_{4C} distribution of the 4C kinematic fit with the hypothesis is $e^+e^- \rightarrow \pi^+\pi^-\gamma$. The blue histogram represents signal MC. The main contributing background channels are also shown. The distributions are scaled to the same luminosity. The distributions of signal MC and $\mu^+\mu^-\gamma$ background are nearly identical, since their masses are similar and, hence, the kinematic fit can not separate them due to the limited detector resolution.

where $p_{2\pi}$ and p_{bg} are the probabilities to have an event of the signal $\pi^+\pi^-\gamma$ or the background (bg) type. In other words, $p_{2\pi} = \frac{N_{2\pi}}{N_{2\pi}+N_{bg}}$ and $p_{bg} = 1 - p_{2\pi}$, with the number of signal events $N_{2\pi}$ and the number of summed background events (without the dimuon final state) N_{bg}, after scaling them to the same luminosity. Hence, the best requirement value χ^2_{cut} can be determined with the equation

$$\frac{p_{2\pi} \cdot f_0(\chi^2_{cut})}{C_{01}} = \frac{p_{bg} \cdot f_1(\chi^2_{cut})}{C_{10}} \,. \tag{4.4}$$

The constants C_{01} and C_{10} are Bayesian estimators. They describe the costs of accepting a hypothesis although the other one is true:

- C_{10}: costs for the acceptance of H_1 although H_0 is true (type 1 error)
- C_{01}: costs for the acceptance of H_0 although H_1 is true (type 2 error)

The subjective Bayesian probability comes into play at this point. In this case, a type 2 error

is worse than a type 1 error, since it is more important to reject background. The probabilities differ by an order of magnitude. Therefore, the costs can be set very high without losing too much signal. The costs are set to:

$$\frac{C_{01}}{C_{10}} = \frac{5}{1}, \tag{4.5}$$

yielding to the requirement $\chi^2_{4C} < 60$.

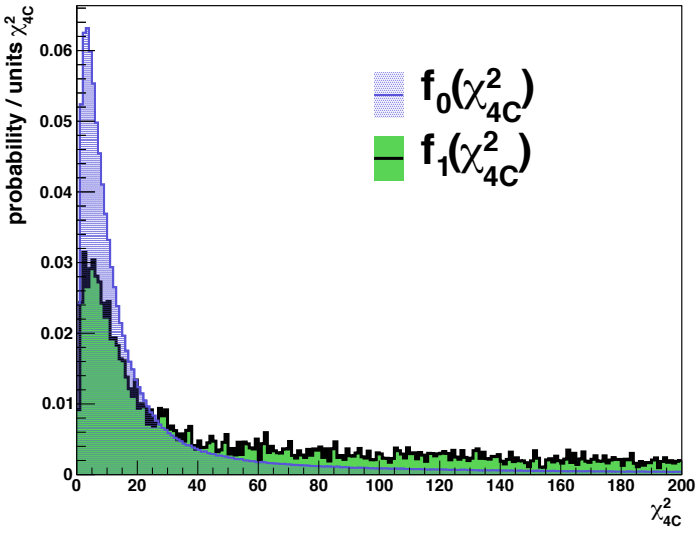

Figure 4.3: Probability densities $f_0(\chi^2_{4C})$ and $f_1(\chi^2_{4C})$ of the χ^2_{4C} distributions in the range $0 < \chi^2_{4C} < 200$.

4.5 Fraction of decaying pions before reaching the MDC

The charged pion has a mean lifetime of $\tau_\pi = (2.6033 \pm 0.0005) \cdot 10^{-8}$ s [4]. It decays in 99.99% [4] of all cases in a muon and the corresponding neutrino. If too many pions decay, before they reach the MDC, the measurement of $\pi^+\pi^-\gamma$ events might be affected by that. The probability, that a pion with momentum $|p|$ decays within a flight length x_0, is given by [4]:

$$\text{prob(decay)} = 1 - \exp\left(-\frac{\mathrm{m}_\pi \cdot \mathrm{x}_0}{\tau_\pi \cdot |\mathrm{p}|}\right). \tag{4.6}$$

The fraction of decaying pions in bins of the momentum is calculated using this formula. As flight length of $x_0 = 10.0$ cm is chosen, which is already 1.4 cm within the MDC. The result is the red curve displayed in Fig. 4.4. In blue, the momentum distribution of pions, originating from the $\pi^+\pi^-\gamma$ final state at $\sqrt{s} = 3.773$ GeV, with an invariant mass between 0.6 and 0.9 GeV is shown, determined with MC. About 0.2 - 0.5% of all generated pions decay into muons

before they reach the MDC and could be misidentified. This fraction is relatively small, and, in addition, this effect is simulated in MC. To conclude, the pion decay is negligible for the BESIII cms energy and can be neglected.

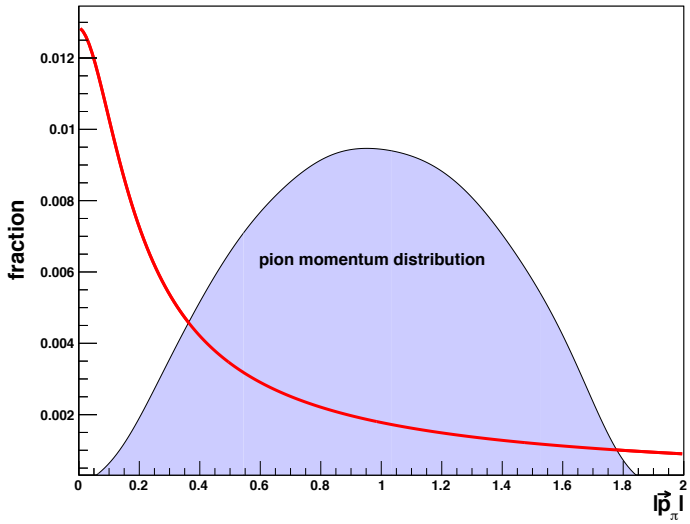

Figure 4.4: Fraction of decaying pions within the first 10 cm in bins of the momentum (red curve). In blue, the momentum distribution of pions, originating from the $\pi^+\pi^-\gamma$ final state at $\sqrt{s} = 3.773$ GeV, with an invariant mass between 0.6 and 0.9 GeV is shown, determined with MC.

4.6 Summary of the event selection

All requirements to select $\pi^+\pi^-\gamma$ events are listed in Tab. 8.1. They are ordered in the same order as they are performed in the analysis. The remaining distribution of the invariant mass $m_{2\pi}$ of the two charged tracks is shown in Fig. 4.5. Displayed is the data distribution after analyzing the full data set with a luminosity of 2.9 fb^{-1}. Also shown are the $\pi^+\pi^-\gamma$ and $\mu^+\mu^-\gamma$ MC samples, scaled to this luminosity. Obviously, the muon background dominates the whole spectrum apart from the ρ peak and needs to be suppressed by further study. A tool for that - an artificial neural network - is used and described in the next chapter. The global efficiency of the selections can be found in section 10.4. Two peaks are visible in the distribution. On the one hand the $\rho(770)$ resonance around 770 MeV. This is the most important region for $(g-2)_\mu$ and studied within this analysis. On the other hand the J/ψ resonance at 3.097 GeV [4] is visible, decaying into muons with a branching fraction of about 5% [4].

variable	**requirement**
MDC valid tracks	2 or 3
e-PID	DLL(π,e) > 2
$\lvert V_z \rvert$	< 10.0cm
$\lvert V_r \rvert$	< 1.0cm
acceptance	0.4 rad $< \theta <$ π - 0.4 rad
total charge	0
p_t charged tracks	> 0.3 GeV
photon energy E_γ	> 0.4 GeV
number photons with $E_\gamma > 0.4$ GeV	1
χ^2_{4C}	< 60

Table 4.1: Summary of the event selection for $\pi^+\pi^-\gamma$ events. The abbreviations are defined in the corresponding sections.

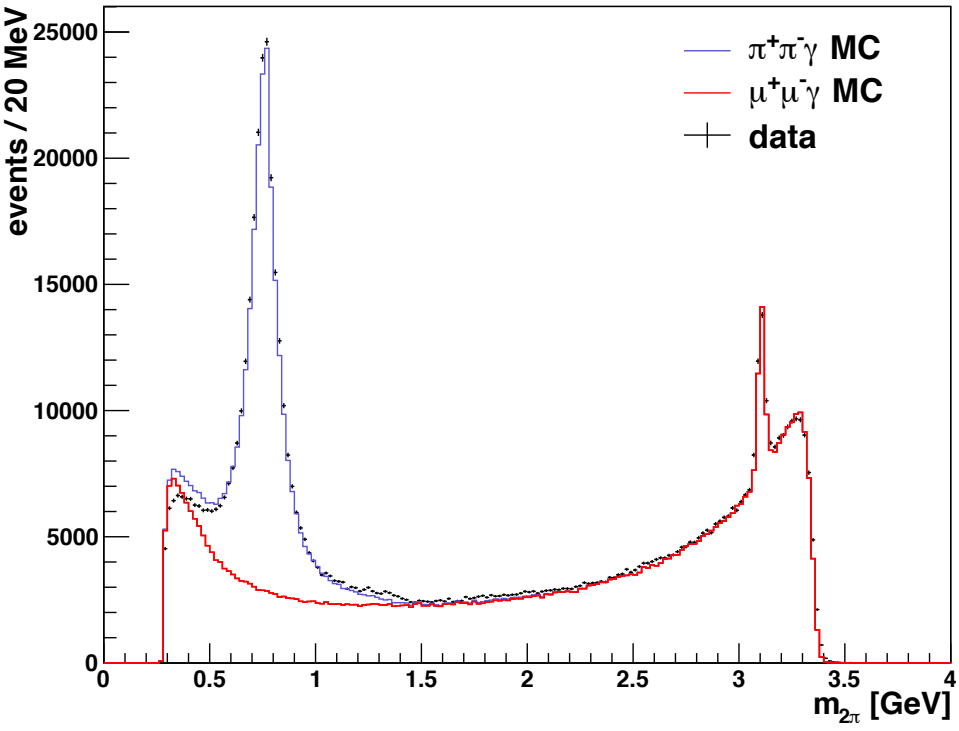

Figure 4.5: The invariant mass distribution of the two selected charged tracks. Shown is $\pi^+\pi^-\gamma$ MC, $\mu^+\mu^-\gamma$ MC, and data. The MC samples are scaled to the luminosity of data. No further muon PID is required.

Chapter 5

Developing a new μ/π separation by training an artificial neural network

---

As shown in chapter 4, the $e^+e^- \to \mu^+\mu^-\gamma$ channel is the most important background contribution for the measurement of $e^+e^- \to \pi^+\pi^-\gamma$ events. It is not possible to suppress it with linear requirements on kinematic variables. The pion and muon masses are too similar and cannot be resolved within the mass resolution of the MDC of BESIII. To separate pions from muons, a multivariate analysis method is trained and tested, more precisely an artificial neural network. This chapter presents the training results and how it is possible to suppress the muon background efficiently.

5.1 Multivariate analysis

Multivariate analysis (MVA) methods are a common tool in modern particle physics. In an MVA, several variables are examined parallel. The difference to bivariate statistics is, that, here, every variable is analyzed for its own. The $\mu^+\mu^-\gamma$ background can not be suppressed by applying requirements on single variables, like χ^2_{4C}, since the resolution of the MDC is not able to distinguish the similar pion and muon masses. However, using an MVA, several variables and their correlations can be exploited to calculate a likelihood y.

The goal is to develop a muon-pion separation method, using an MVA. Therefore, the Toolkit for Multivariate Analysis (TMVA) [98] package implemented in root is used. Several methods can be trained and tested with this package[1], like artificial neural networks (ANN), a boosted decision tree (BDT), or a multidimensional k-nearest neighbors (KNN) method. A detailed description of all implemented methods can be found in Ref. [98].

The package also provides visual output, which displays how effective the different methods are, like for example the signal efficiency vs. the background suppression. With this information one can select the MVA method, that fits best to the problem given. The MVA methods are trained and tested on a track basis, using $\pi^+\pi^-\gamma$ and $\mu^+\mu^-\gamma$ MC samples.

5.2 Usable variables

The first step is to find the optimal input variables for the MVA method. One criterium is, that the distributions for pions and muons separate as well as possible. The Fig. C.1 to C.5 in appendix C present the variables, which can be used. Shown are the MC distributions for pions (blue shaded) and muons (red shaded). The distributions are scaled to the same, arbitrary, luminosity.

These variables are tested according to their separation power. The TMVA package provides such a tool, which calculates the separation power of a set of input variables. The output is a number between 0 and 1. The greater this number, the better the separation between muons and pions. The ten best separating variables are summarized in Tab. 5.1. The five best variables from this ranking are selected as input. In addition, the dE/dx information from the MDC is used as input, too, to include a further sub detector beyond the EMC and MUC. As seventh and last variable the ϕ angle is chosen to describe the ϕ dependence of the

[1] see also www.tmva.sourceforge.net

muon chamber. The MuC contains eight resistive plate chambers. Between the connections a measurement is hindered, which produces a structure. It is illustrated in Fig. 5.1.

Rank	Variable	Separation
1	MuC depth	$4.74 \cdot 10^{-1}$
2	lateral moment	$3.13 \cdot 10^{-1}$
3	5×5 / 3×3	$3.03 \cdot 10^{-1}$
4	a20 moment	$2.81 \cdot 10^{-1}$
5	E/p	$2.80 \cdot 10^{-1}$
6	second moment	$2.76 \cdot 10^{-1}$
7	5×5 / Seed	$1.31 \cdot 10^{-1}$
8	3×3 / Seed	$8.97 \cdot 10^{-2}$
9	dE/dx	$3.87 \cdot 10^{-2}$
10	ϕ	$1.03 \cdot 10^{-2}$

Table 5.1: Ranked input variables (valid for all MVA methods). The variables are ordered descending by their separation power, which is a number between 0 and 1, calculated by TMVA. The variables are described in the text.

The input variables chosen for the ANN are:

- **Depth in the Muon Chamber:** range of a charged track in the MUC.
- **Lateral moment:** The lateral moment LAT is given by [99, Eq. (5)]:

$$LAT = \frac{\sum_{i=3}^{N} E_i \cdot r_i^2}{\sum_{i=3}^{N} E_i \cdot r_i^2 + E_1 \cdot r_0^2 + E_2 \cdot r_0^2} \qquad E_1 > E_2 > E_3 > \ldots > E_n \ , \tag{5.1}$$

  where n is the number of neutral clusters associated with the shower, r_0 is the averaged distanced between two clusters, E_i is the energy deposit in the i-th crystal, and r_i is the lateral distance between the i-th crystal and the center of the shower.
- **a20 moment:** "Zernike Momentum" [100], describing the shower shapes with an angular and a radial component.
- 5×5 / 3×3**:** energy deposition in the EMC in the 5×5 crystals around the central crystal where the main amount of energy is deposited, divided by the corresponding energy deposition in the 3×3 system around the center.
- **E/p:** energy deposition E in the EMC divided by the momentum p from the MDC.
- **dE/dx:** energy loss dE per interaction length dx from the MDC.
- ϕ **angle:** azimuthal angle.

The correlation matrices of these variables are presented in Fig. 5.2 for muon (background) and pion (signal) tracks, respectively. The remaining variables mentioned in Tab. 5.1 are not

used. They are too highly correlated with other variables. Hence, their inclusion do not yield to a better separating of the overall method.

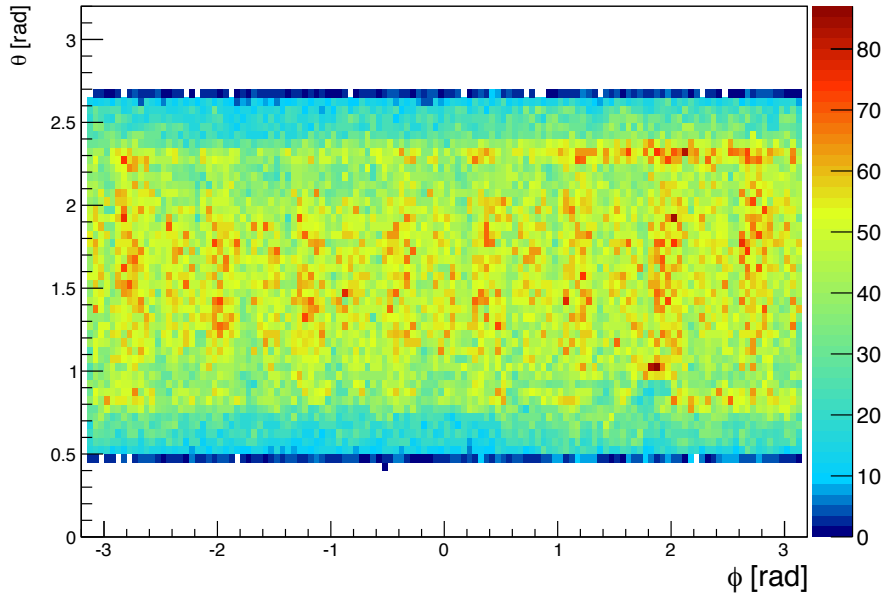

Figure 5.1: Angular distribution of muon tracks with a measurable depth in the MUC. A ϕ dependence is clearly visible, which is caused by the connection of the eight plate chambers.

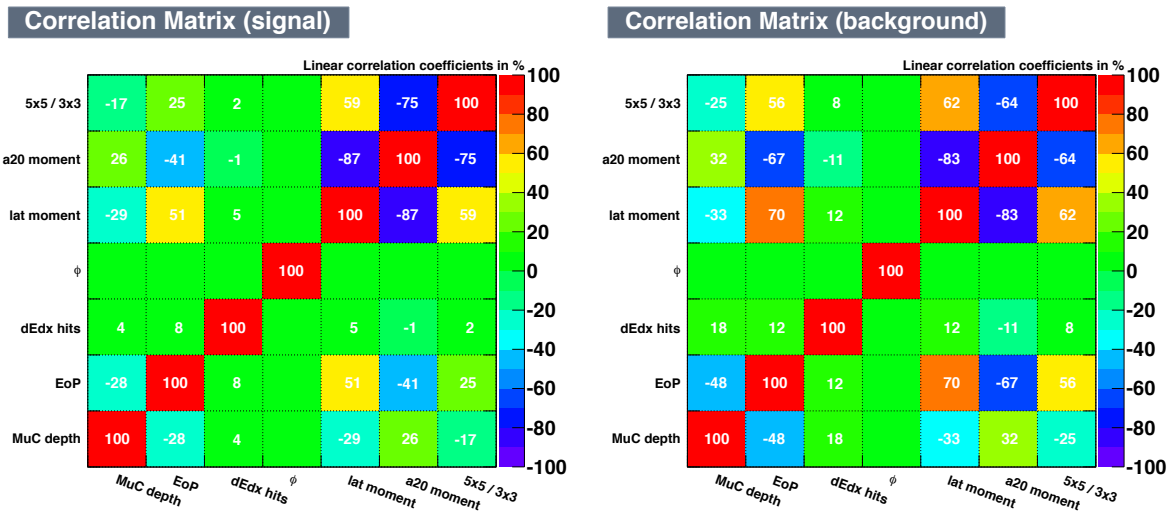

(a) pions (b) muons

Figure 5.2: Correlation matrix of the seven input variables for pion (signal) and muon (background) tracks.

5.3 Choice of the MVA method

The TMVA package provides a tool, which evaluates the optimal MVA method for the input variables given. The optimal method shall lead to the best signal efficiency and background rejection compared to the other methods.

It turns out, that an artificial neural network (ANN), a so-called multilayer perceptron (MLP), fits best to the problem given. Five different MLP's are implemented in TMVA [98]. Figure 5.3 shows their efficiency curve for the input variables given. The Clermont-Ferrand MLP ANN (CFMlpANN) provides the best signal efficiency vs. background rejection. Hence, this one is chosen for this analysis.

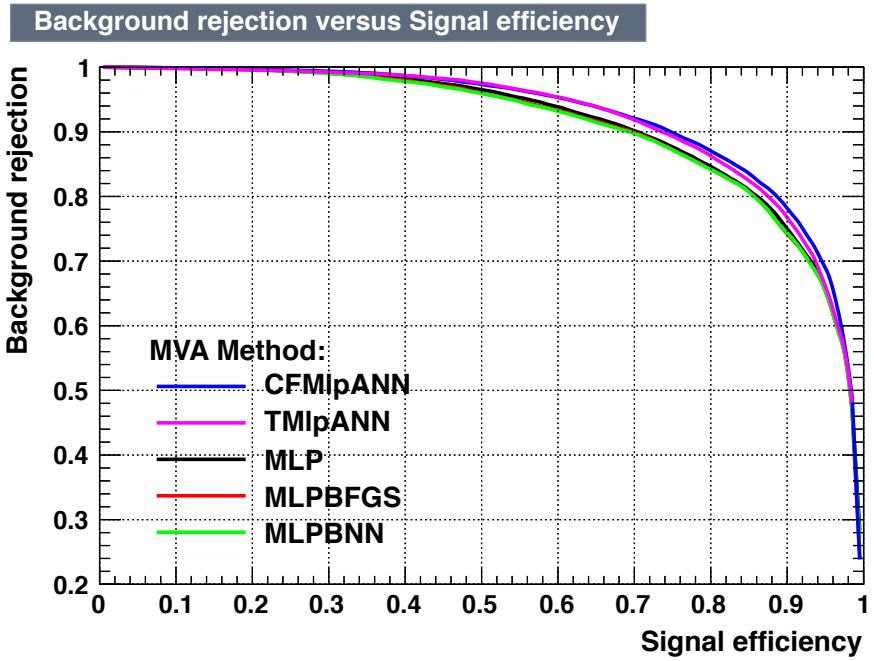

Figure 5.3: Background rejection versus signal efficiency for the five different Neural Network Methods implemented in the TMVA package. The best result is provided by the Clermont-Ferrand artificial neural network, which is represented by the blue line.

5.4 The multilayer perceptron

An ANN is a net of artificial neurons. The idea comes from the human brain structure. Several neurons are connected via a neurotransmission. An ANN is the mathematical description of such a natural network. The input variables are the input neurons, which are connected to an output neuron.

A neural network with n neurons can have n^2 connections. However, it can be simplified by

ordering the neurons in layers, and allowing only direct connections between neighbored layers. The first layer of the ANN is the input layer, the last one the output layer, and the layers in between are called hidden layers. Such a network is called multilayer perceptron (MLP). Figure 5.4 shows an MLP with one hidden layer.

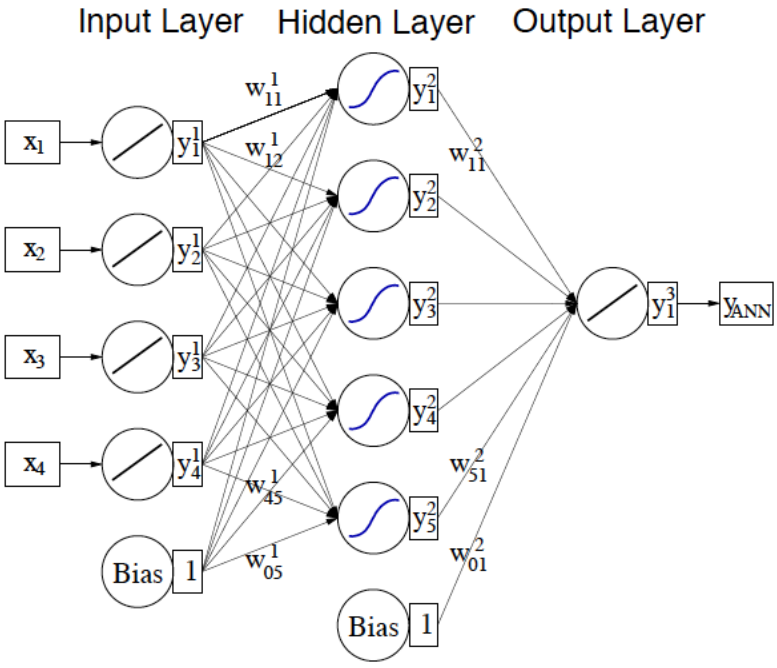

Figure 5.4: A multilayer perceptron with one hidden layer [98]. Four input variables x_i (i = 1,...,4) are translated to the four input neurons y_i^1, representing the input layer. These are connected to a hidden layer with five hidden nodes y_j^2 (j = 1,...,5), via weights w_{ij}^1. Their algorithms are connected to the output layer y_1^3 by probabilities w_{j1}^2. This incoming information is translated in the likelihood value y_{ANN}. Two additional nodes handle possible biases.

If n_{var} variables x_i are used as input to train the network, the input layer consists of n_{var} neurons y_i^1 and one bias node. One neuron y_1^{l+1} represents the output layer. It holds the neural net estimator y_{ANN}. This estimator is a probability between 1 and 0, whereas 1 corresponds to a signal, and 0 to a background event. A weight $w_{ij}^{(l-1)}$ is associated to each directional connection between the i-th neuron of layer $l-1$ and the j-th neuron of layer l. The input value for one neuron is calculated by multiplying the output values of all connected neurons with these weights, which is displayed in Fig. 5.5. The neuron input i_1 ... i_n is mapped by the neuron response function ρ on the neuron output y_j. It can be separated into an $\mathcal{R}^n \to \mathcal{R}$ synapse function κ and an $\mathcal{R} \to \mathcal{R}$ neuron activation function α. For an MLP, κ and α are [98]

$$\kappa : (y_1^l,\ldots,y_n^l|w_{0j}^l,\ldots,w_{nj}^l) \longmapsto w_{0j}^l + \sum_{i=1}^{n} y_i^l w_{ij}^l \ , \tag{5.2}$$

$$\alpha : x \longmapsto A(x) \ , \tag{5.3}$$

with a real function $A(x)$. The response function is $\rho = \alpha \circ \kappa$.

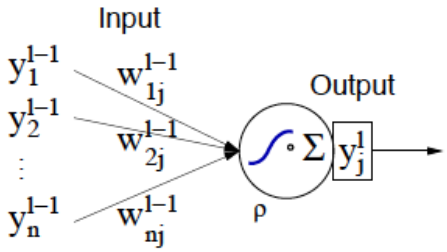

Figure 5.5: Neuron j in layer l connected to n nodes in layer $l-1$. The weight of an incoming connection is $w_{ij}^{(l-1)}$. The output values of each neuron y^{l-1} are weighted and multiplied to determine the output, mapped by the response function ρ [98].

The algorithm used to adjust the weights and to optimize the performance of the ANN is called back propagation. The network has to be trained with well known input, in this case $\pi^+\pi^-\gamma$ and $\mu^+\mu^-\gamma$ MC samples, so that the desired output for every event is well-known. The output of a network with a single hidden layer is [98]

$$y_{ANN} = \sum_{j=1}^{n_h} y_j^2 w_{j1}^2 = \sum_{j=1}^{n_h} A\left(\sum_{i=1}^{n_{var}} x_i w_{ij}^1 \right) \cdot w_{j1}^2 \,, \tag{5.4}$$

where n_h is the number of neurons in the hidden layer. The network is trained with N training events. The n_{var} input variables are stored in a vector $\mathbf{x}_k = (x_1,\ldots,x_{n_{var}})_a$. For each event k the desired output $\hat{y}_k$ is known, and the network output $y_{ANN,k}$ is computed. To find the optimal set of weights $\mathbf{w}$, the error function [98]

$$E(x_1,\ldots,x_N|\mathbf{w}) = \sum_{a=1}^{N} \frac{1}{2}(y_{ANN,a} - \hat{y}_a)^2 \tag{5.5}$$

has to be minimized.

The CFMlpANN is a special form of an MLP with the activation function [98]

$$\alpha : x \longmapsto \frac{1}{1+e^{-x}} \,. \tag{5.6}$$

5.5 Training the ANN

The network is trained with $\pi^+\pi^-\gamma$ and $\mu^+\mu^-\gamma$ MC samples on a track basis. The samples have a size of around 200 000 events. The efficiency differences between MC and data by using this network are determined with clean pion and muon data samples (as shown in sections 8.1.3 and 8.2.3).

The settings of the CFMlpANN, used in this study, are summarized in Tab. 5.2. It has seven input variables, as described in section 5.2, and two hidden layers with 27 and 17 nodes, respectively. A stochastic learning method with 6000 training cycles is performed.

number of input variables	7
number of hidden layers	2
number of hidden nodes	7+20 and 7+10
number of training cycles	6000
learning method	stochastic

Table 5.2: Settings of the CFMlpANN used in this study.

The output likelihood y_{ANN} is shown in Fig. 5.6 for charged pion (signal) and muon tracks. Hence, this network can be used as pion or as muon selector by applying different requirements on y_{ANN}. This likelihood value is required to be greater than 0.6 for both pion candidates in the $\pi^+\pi^-\gamma$ event selection. This condition reduces the $\mu^+\mu^-\gamma$ contribution in a way, that the systematic uncertainty, due to subtraction of this background, is smaller than a per mille.

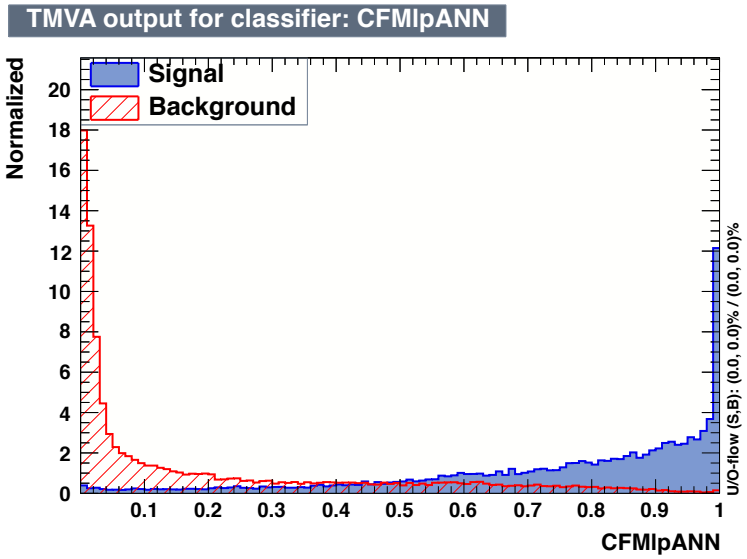

Figure 5.6: Likelihood output y_{ANN} of the Clermont-Ferrand artificial neural network.

If the training samples are too small, or the number of training cycles is too large, the network

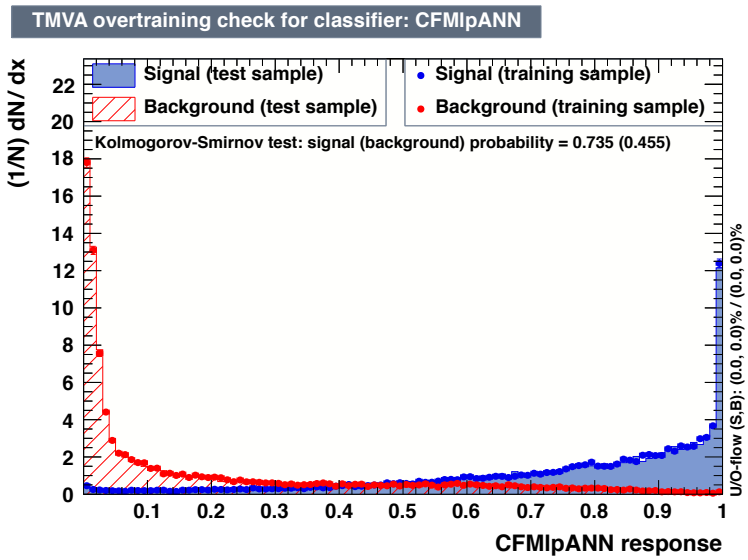

Figure 5.7: Comparison between the output of the training and the test samples. Also shown is the result of the Kolmogorov-Smirnov test, yielding a probability of 0.735 for signal and 0.455 for background. The results agree well, which allows the conclusion, that the network is not overtrained.

interprets the statistical fluctuations of these samples as characteristic of the corresponding particle types. This effect is called overtraining. To test whether the network is overtrained, the input samples are divided into a training and a test set. With the training set the Network is trained and the output likelihood y_{ANN} is calculated. The same is done with the test sample. Ideally, the training result of the two sets are the same. If this is not the case, the MVA method is overtrained. The statistical consistence of the outputs is quantified with a Kolmogorov-Smirnov test, yielding a probability of 0.735 for signal and 0.455 in case of background. These are acceptable values from a statistical point of view [98]. Figure 5.7 shows the comparison between training and test samples, for signal and background respectively.

To summarize, it is possible to develop a new μ/π separation method by training a CFMlpANN with $\pi^+\pi^-\gamma$ and $\mu^+\mu^-\gamma$ MC samples on a track basis. Both pion candidates have to fulfill the requirement $y_{ANN} > 0.6$, yielding a background rejection of more than 90% and a signal loss of less than 30%. The event yield after applying this requirement is shown in Fig. 5.8. Compared to Fig. 4.5, which shows the event yield before using the network, the $\mu^+\mu^-\gamma$ background can be highly suppressed. However, data-MC differences due to photon detection, track reconstruction, the usage of e-PID, and the described ANN method, need to be studied carefully. This is necessary, if one want to reach a high-precision result. This is done in the upcoming chapters.

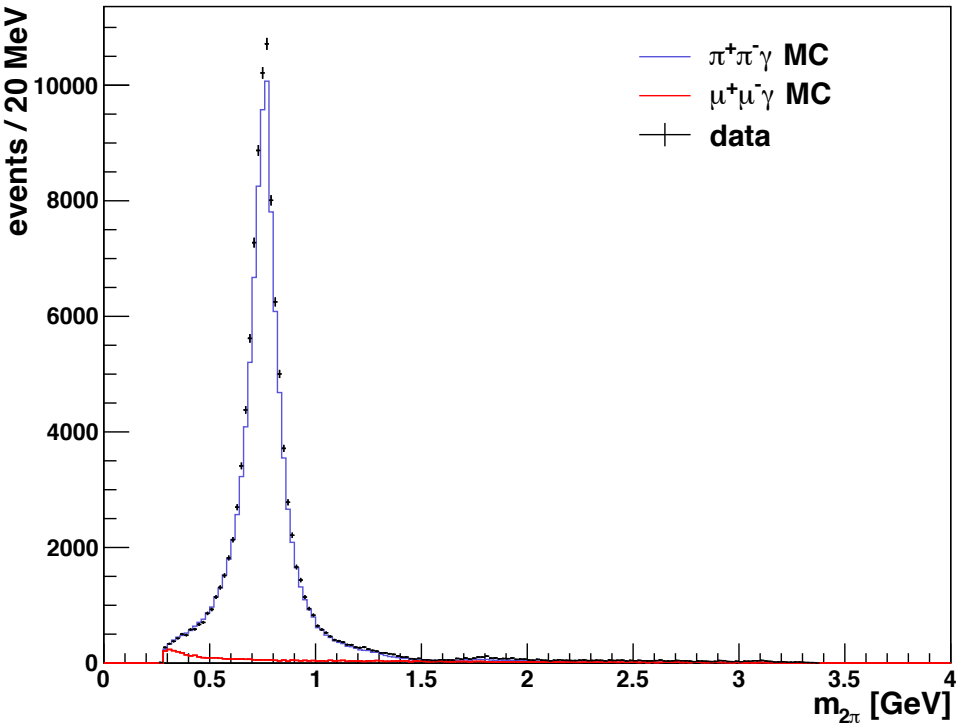

Figure 5.8: The invariant mass distribution of the two charged tracks identified as pions after applying the requirement on y_{ANN}. Shown is $\pi^+\pi^-\gamma$ MC, $\mu^+\mu^-\gamma$ MC, and data. Compared to Fig. 4.5 the muonic background can be suppressed efficiently.

Chapter 6

Photon detection efficiency study

The study of efficiency differences between data and MC due to imperfections of the detector simulation is necessary to determine the efficiency of the event selection with high precision. Therefore, the deviations between MC and data have to be corrected in the MC sample. In the following chapter, the photon detection efficiency data-MC differences are studied and a correction is developed. The matching of predicted and real photons is done via a 4C kinematic fit requirement, $\chi^2_{4C} < 60$, as in the ISR measurement of the $\pi^+\pi^-$ cross section. Hence, the efficiency differences due to this condition are corrected as well.

6.1 Event selection

The photon detection efficiency is studied with $e^+e^- \to \mu^+\mu^-\gamma$ events. They are easy to select and the statistic is large. The strategy is, to detect the two charged muons and to predict the kinematics of the ISR photon by exploiting momentum conservation. The matching of the predicted photon and the detected photon in the EMC is described in section 6.5. The detection efficiency is the ratio of detected photons and all predicted measurable ones. This efficiency is studied for photon energies greater than 0.3 GeV. Hence, a much wider energy range is covered than needed for this work.

The selection of $\mu^+\mu^-\gamma$ events is straight-forward. Exactly two charged tracks are required, with an entry in the MDC and EMC. They have to originate from the IP and have to be detected in the same acceptance region of the MDC, as in the $\pi^+\pi^-\gamma$ event selection. Furthermore, the ratio E/p has to be smaller than 0.5 for both tracks to reduce electron background, whereas p is the momentum of the charged track, and E the associated energy deposition in the EMC. This condition yields to a suppression of 99.9% of all $e^+e^-(n\gamma)$ events by losing only 0.9% of signal events. The distribution can be found in Fig. 6.2. To be sure that these two charged tracks are muons, at least one of the tracks must have a depth in the MUC greater than 35.0 cm. The corresponding distribution can be seen in Fig. 6.2 for muon and charged pion MC tracks, respectively. A negative value denotes for insufficient information, and, hence, the depth in the MUC cannot be determined. This requirement on the depth guaranties for a low background contamination due to pions. There is no entry required for the second track, to enhance statistics and not to be biased by efficiency differences in the MUC or a possible momentum - depth correlation. After that, a one constraint (1C) kinematic fit is performed taking into account two charged tracks, to predict the angular direction θ_{fit} and ϕ_{fit}, and the energy E_{fit} of the missing photon. The constraint is a missing photon, hence, a massless track. The χ^2_{1C} distribution can be seen in Fig. 6.1. The requirement $\chi^2_{1C} \leq 10$ is applied to reject background events and to enhance the accuracy of the predicted variables. To compare the data and MC prediction the MC samples are scaled to the luminosity of data.

By using this selection criteria, it is possible to find nearly 450 000 events in data. With these events, the differences in the photon detection efficiency, between data and MC, can be studied. A summary of the requirements applied is given in Tab. 6.1.

6.2 Background contamination

The result of the efficiency study can be falsified due to a possible background contamination in data which might not be considered. If the mass of the background tracks differs from

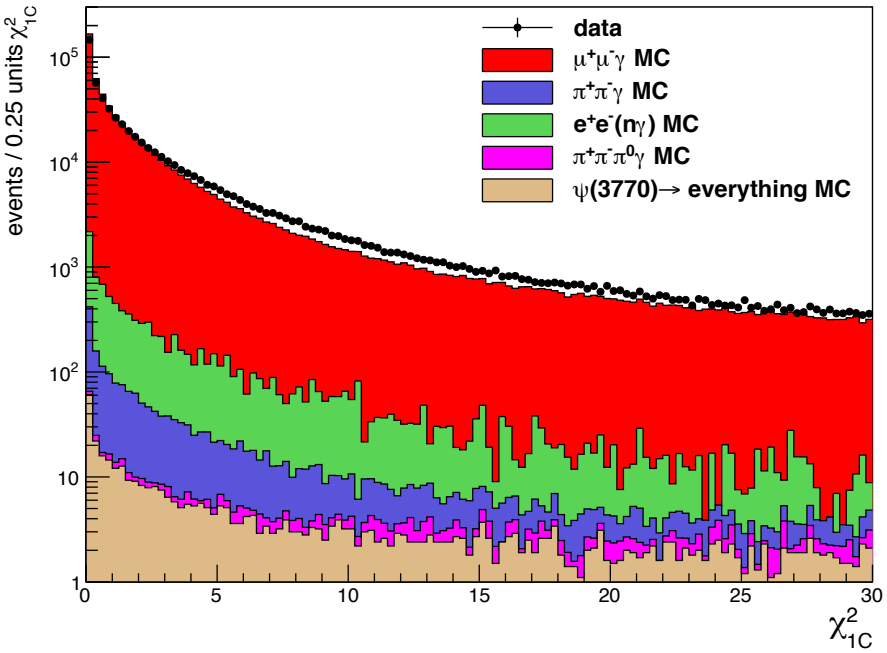

Figure 6.1: χ^2 distribution of the 1C kinematic fit to predict the kinematic variables of the ISR photon. The distribution is broader for real data.

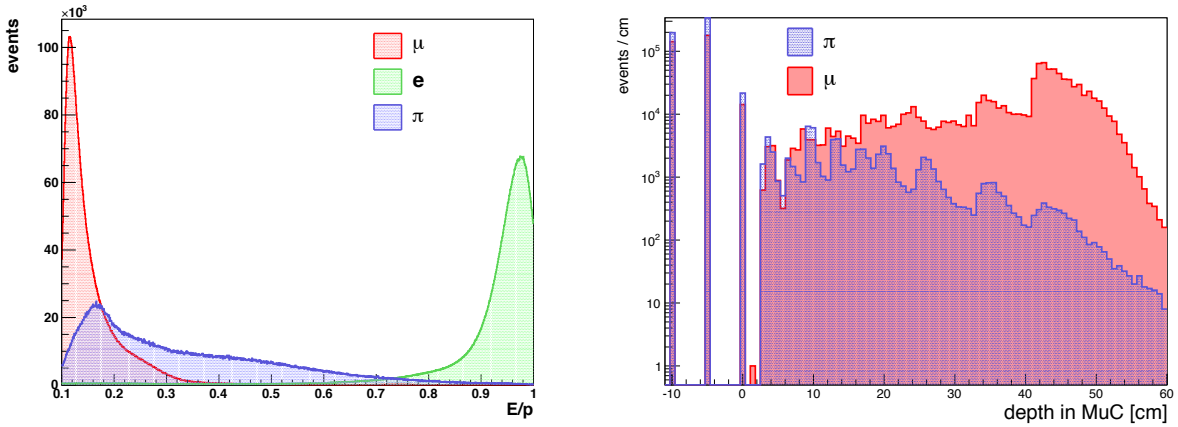

Figure 6.2: Left: E/p ratio for muon, electron and pion MC tracks.
Right: Depth in the MUC of muon and charged pion MC tracks. A negative value denotes for insufficient information, and, hence, the depth in the MUC can not be determined. A requirement of $\geq$ 35 cm is chosen to to select muon tracks.
The distributions are scaled to the same number of events.

cut variable	**cut value**
MUC valid tracks	≥ 1
$\|V_z\|$	< 10.0cm
$\|V_r\|$	< 1.0cm
E/p	< 0.5
acceptance	0.4 rad $< \theta <$ π - 0.4 rad
depth in MuC of one track	≥ 35 cm
# charged tracks with entry in EMC	2
total charge tracks	0
χ^2_{1C}	≤ 10
$\|\vec{p}\|$	< 1.85 GeV

Table 6.1: Summary of the $\mu^+\mu^-\gamma$ event selection for the photon detection efficiency studies. The requirement on $|\vec{p}|$ is explained in section 6.2.

the muon mass, the prediction of the kinematics of the ISR photon, like angular direction or energy deposition, is not correct. This might affect the results. The most serious background is $e^+e^- \to e^+e^-(n\gamma)$. The cross section is three orders of magnitude higher than the one for $\mu^+\mu^-\gamma$ events. Hence, it is very probable that such kind of events survive the event selection, although requirements on the depth in the MUC and on E/p are applied. Figure 6.3 shows the momentum distribution $|\vec{p}|$ of the charged tracks selected for data, signal MC, and the most relevant background MC samples. The MC samples are scaled to the luminosity of data. The distribution of the electron background rises towards high momenta, since high momenta tracks can achieve a large depth in the MUC. The dip before the steep rising is due to the fact, that only photon energies above 0.3 GeV are considered in this efficiency study. To reduce the $e^+e^-(n\gamma)$ background the condition $|\vec{p}| < 1.85$ GeV is required.

The fraction of remaining $e^+e^-(n\gamma)$ events is shown in Fig. 6.4 in bins of the predicted photon energy by the 1C fit. It is smaller than 0.3%. The MC prediction is subtracted from the data distribution to remove this background. Bhabha scattering is a QED process. Hence, the accuracy of the MC prediction is much below one percent. However, efficiency differences between data and MC are not considered, which reduces the accuracy. An uncertainty of 3% is assumed, yielding a systematic uncertainty of $0.3\% \cdot 3\% < 0.1\%$ due to the subtraction of this background MC sample.

The $\pi^+\pi^-\gamma$ contribution rises up to 3% at the highest reachable photon energies above 1.8 GeV. With ISR energies greater than 1.6 GeV, it is possible to produce the $\rho(770)$ resonance, where the $\pi^+\pi^-$ cross section has its maximum. Hence, the pion contamination is largest in this energy region. As shown in section 4.4, muons and pions can not be resolved by a kinematic fit, due to their similar masses. Therefore, this final state does not have to be subtracted. In

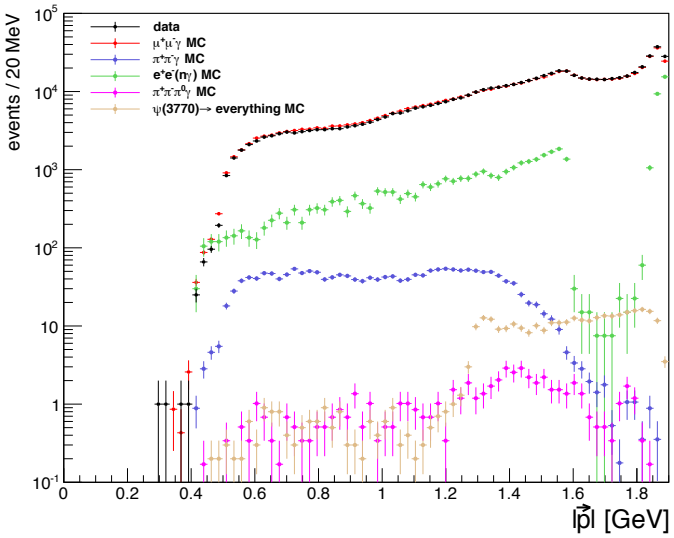

Figure 6.3: Momentum distribution of the charged tracks. The distribution of the electron background rises towards very high momenta. This is exploited to suppress such kind of events.

contrast it can be treated as signal.

Another dangerous background is $\pi^+\pi^-\pi^0\gamma$. The charged pions fake the $\mu^+\mu^-$ final state, but due to the additional π^0, the kinematics of the ISR photon are predicted wrongly. However, the background fraction is everywhere below half a per mille, as can be seen in Fig. 6.4, and thus, negligible.

The resonant decay of the $\psi(3770)$, which corresponds to the cms energy of the data set used, has a large cross section. For photon energies around 600 MeV, the fraction of these events is around two per mille. This leads to a larger systematic error for photon energies below 1 GeV, as explained in section 6.6. Also studied are the $K^+K^-\gamma$, $p\bar{p}\gamma$, $\pi^+\pi^-\pi^+\pi^-\gamma$, $\pi^+\pi^-\pi^0\pi^0\gamma$, and the non-ISR continuum MC samples. However, all of these final states are suppressed efficiently and their contribution is negligible.

In summary, only the $e^+e^-(n\gamma)$ final state is subtracted in data, which leads to a systematic uncertainty smaller than 0.1%. The $\pi^+\pi^-\gamma$ channel is treated as signal. The resonant $\psi(3770)$ decays are considered as systematic uncertainty in section 6.6. All other background channels can be neglected.

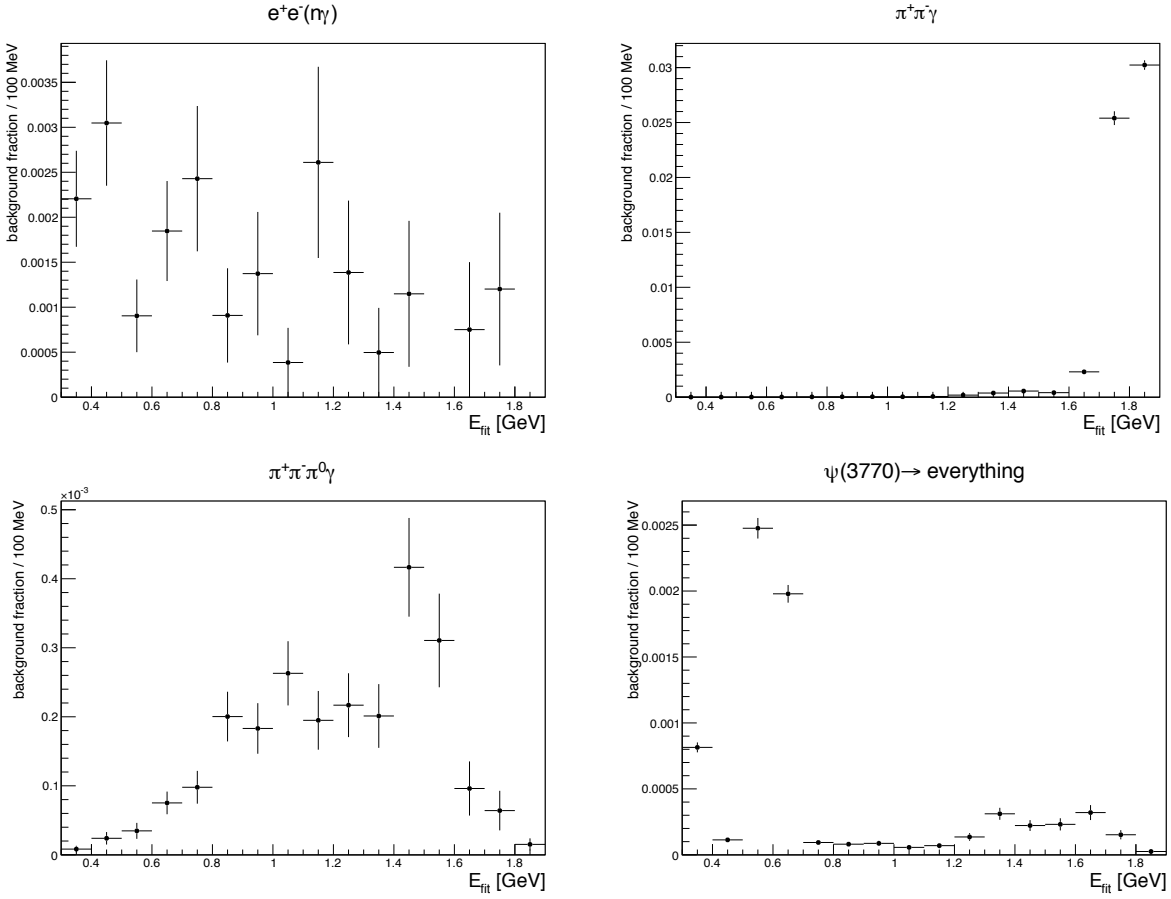

Figure 6.4: Fraction of remaining background events in the photon efficiency study.

6.3 Accuracy of the 1C kinematic fit

The following terminology is used for variables determined with MC simulation: Simulated values on the generator level are called **true** values. If the detector simulation by the GEANT-4 framework is applied on these true variables, they are called **reconstructed** values. If the 1C kinematic fit is used, to predict the kinematics missing track, the information is named **fitted**, or **predicted** values.

To study the accuracy of the 1C kinematic fit, MC events are used. Here, a matching between true and reconstructed values is possible. In addition, the true and the predicted values can be compared, too. In this way, the accuracy of the predicted photon kinematics can be quantified.

Figure 6.5 shows the true ISR photon energy compared to the prediction of the 1C fit in case of $\mu^+\mu^-\gamma$ events. Both, LO and NLO MC samples can be seen, as well as the ratio of the true and predicted distribution. In the LO case, predicted and true energies are consistent, instead

of energies around 0.6 GeV. Here, the narrow charmonium resonance J/ψ is produced. The energy resolution of the fit is larger than the width of the resonance, yielding to a resolution difference. The 1C fit considers only LO ISR. Hence, the predicted energy is higher than the true energy of the LO photon, if a NLO photon is emitted. The predicted distribution is shifted towards higher energies, as can be seen in the left picture of Fig. 6.5.

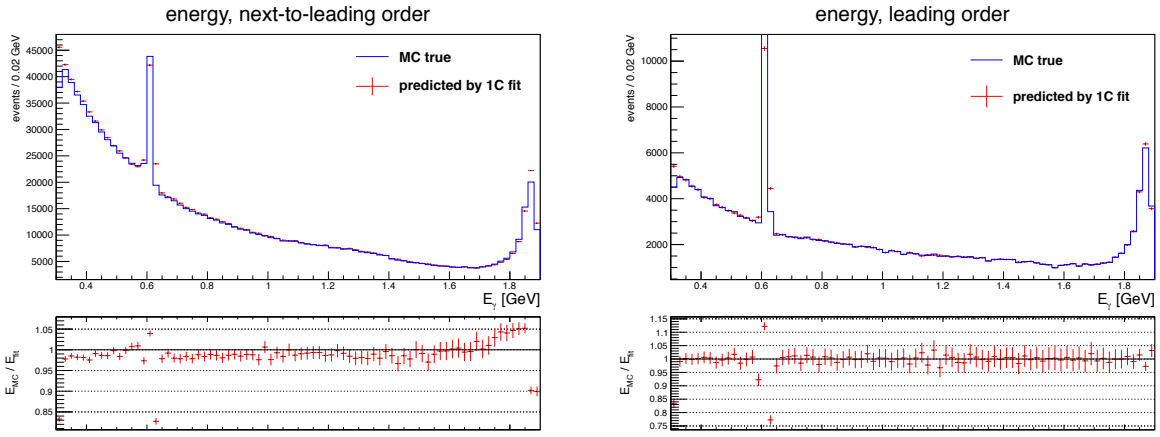

Figure 6.5: Left: True NLO energy distribution in comparison to the predicted one of the 1C fit. Right: Same distribution for LO ISR events.

Figure 6.6 shows the same for the polar angle θ. A deviation for small and large angles can be observed, too. As well, it is caused by NLO photon radiation, as can be approved by an optimal agreement in the LO ISR case. A LO ISR photon is preferably emitted at small θ angles. Hence, the predicted angular distribution is stretched outwards in case of NLO ISR events.

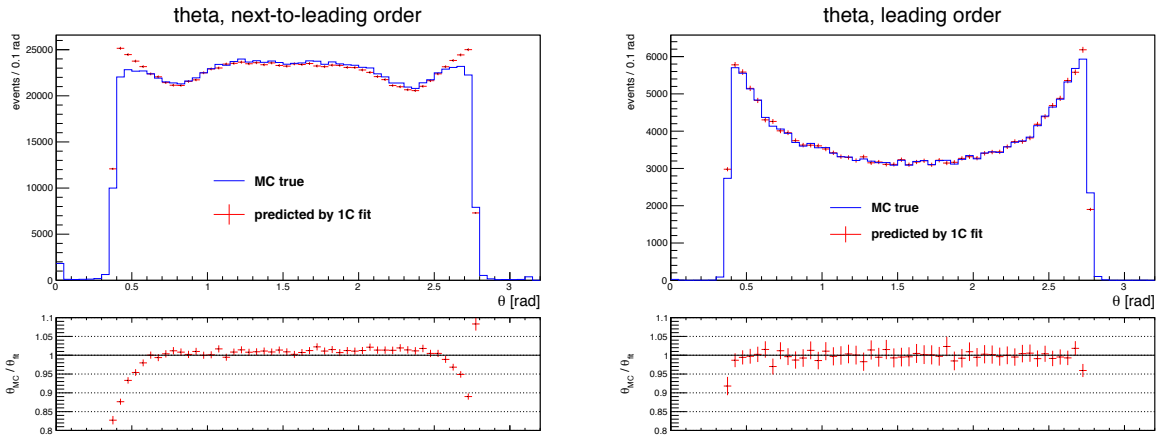

Figure 6.6: Left: True NLO theta distribution in comparison to the one of the kinematic fit. Right: Same distribution only in LO. Notice the better agreement and the changed shapes.

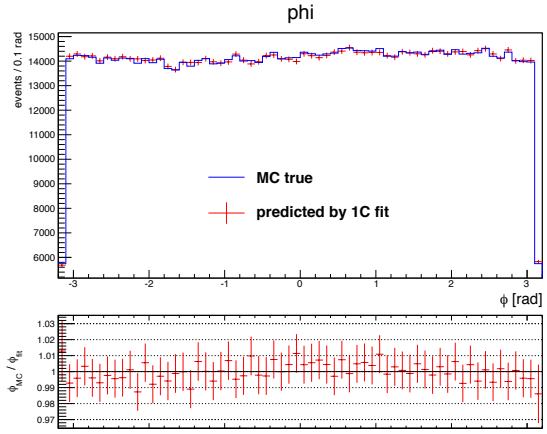

Figure 6.7: True ϕ distribution in comparison to the one of the kinematic fit. Shown are NLO ISR events.

Finally, one can find the ϕ distributions for true and fitted values in Fig. 6.7. Shown are NLO ISR events. Both distributions agree well, as expected. The emission of an ISR photon is symmetric in ϕ direction. Hence, the ϕ distribution is flat and not affected strongly by NLO ISR corrections.

The spatial resolution $\Delta\phi$ and $\Delta\theta$ of the EMC reconstruction and of the 1C kinematic fit is examined by comparing the true ϕ and θ position of the ISR photon with the corresponding reconstructed, as well as, the fitted values. Figure 6.8 shows the difference between the MC true value and the fitted, respectively the reconstructed one. The results are slightly shifted. This is affected by the MDC, since the charged tracks are used as input for the kinematic fit.

The root mean square (rms) value of these distributions, σ_ϕ and σ_θ, is a quantification of the spatial resolution in ϕ and θ direction. The rms is calculated for different energy bins with a width of 200 MeV, presented in Fig. 6.8. The dots are placed at the center of the energy intervals. The resolution of the reconstructed ISR photons in the EMC is better at energies below 1.4 GeV, than the one for the fit. Only for very high energies, the situation turns around. However, the resolution is better than 0.03 radian in the whole energy range in both cases. This is smaller than the spatial resolution chosen of 0.1 rad in the efficiency study.

As a last check, the prediction of the 1C fit is compared to the calculation of the missing LO photon four momentum p_{miss}, using the four momentum of the initial e^+e^- system $p_{initial}$, and the two muon tracks p_{μ^+} and p_{μ^-} as input:

$$p_{miss} = p_{initial} - p_{\mu^+} - p_{\mu^-} \,. \tag{6.1}$$

Figure 6.9 shows the result in bins of the true energy E_γ. The prediction and the simple

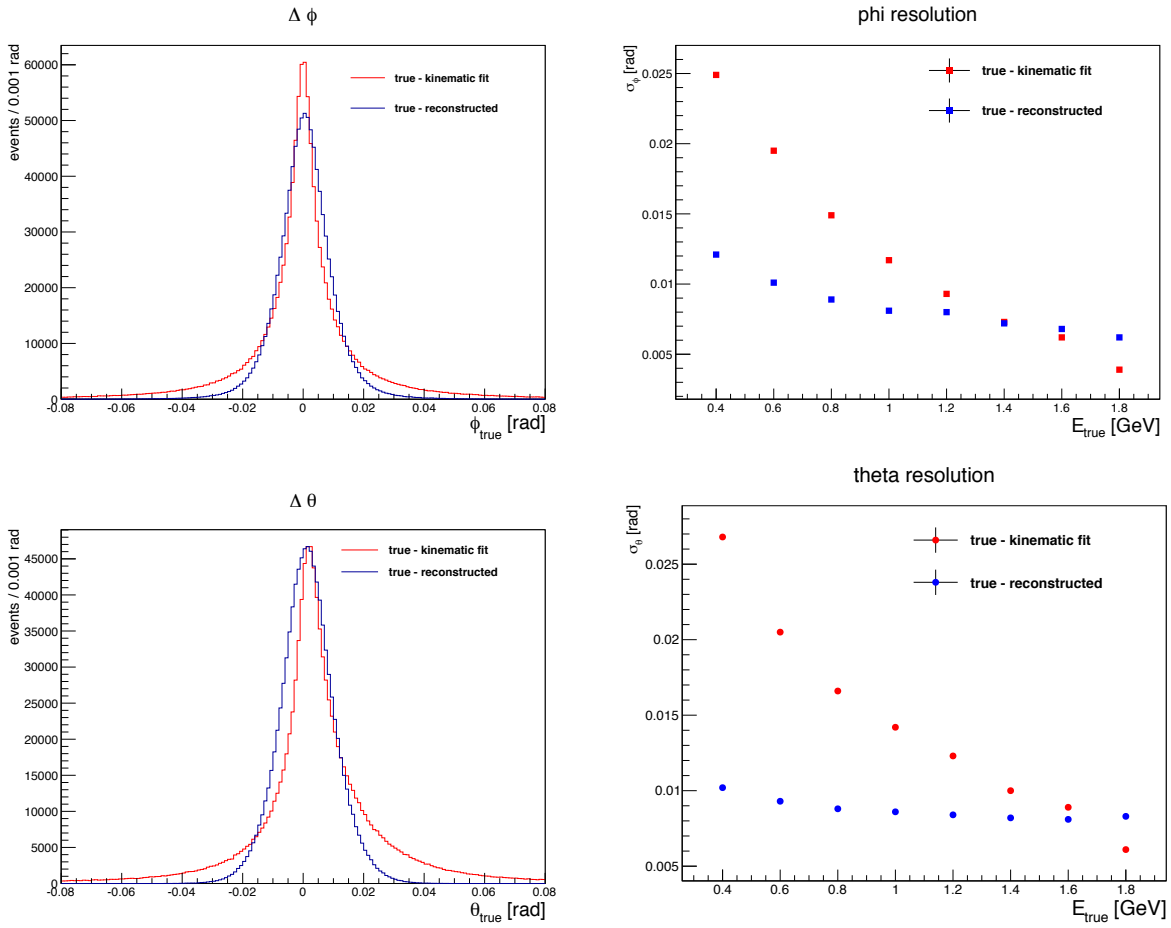

Figure 6.8: Left: True value minus fitted, respectively reconstructed, value, $\Delta\phi$ and $\Delta\theta$. Shown is the situation for 0.3 GeV $<$ E$_{true}$ $\leq$ 0.5 GeV.
Right: Spatial resolution in ϕ and θ direction. The resolution is defined as *rms* value, so-called σ_ϕ and σ_θ, of the corresponding $\Delta\phi$ and $\Delta\theta$ distributions. The dots are placed at the center value of the 200 MeV intervals.

calculation agree well. This shows that there is no bias by using the 1C kinematic fit, in order to predict the kinematics of the ISR photon. In conclusion, the kinematic fit does not respect NLO effects. However, it achieves reliable and adequate results to predict the kinematics of an ISR photon. It is a good tool for the following efficiency studies.

6.4 EMC Alignment

By comparing the fitted and reconstructed energy, θ, and ϕ values of the ISR photon for MC and data, it is possible to analyze the EMC calibration differences between data and MC. It is studied, whether the position of the EMC and its energy measurement differs in MC and data.

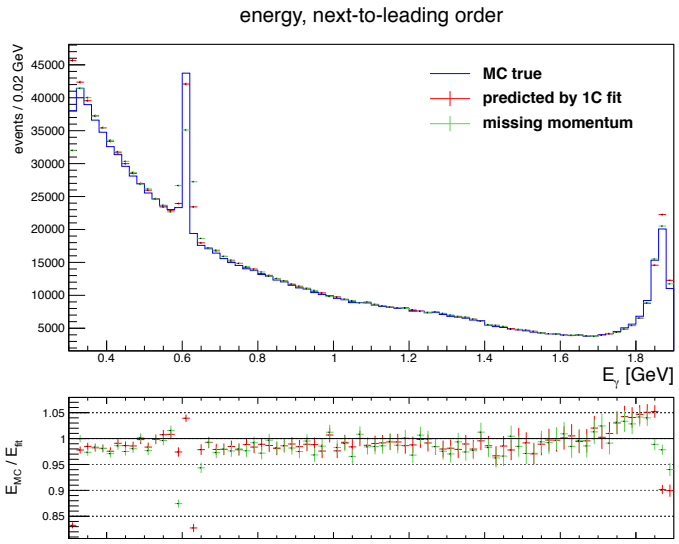

Figure 6.9: Comparison of true photon energy E_γ, prediction of the 1C kinematic fit, and the calculation of the missing momentum.

In Fig. 6.10, one can see the difference between the fitted and the reconstructed value, called EMC value in that case, for energy, θ, and ϕ respectively. Both, data and MC are shown.The energy distribution has a tail towards positive differences. This is a well known effect. The deposited energies of the photons are smaller than the predicted ones. One reason for this are NLO effects. In most of the cases, not the whole energy of the photon is deposited in the detector material. However, this effect is well-simulated in MC. In MC, the energy distribution is slightly shifted towards higher energies with respect to data. This means, that the reconstructed energies in data are a little bit smaller than in MC. The shift is in the order of 3 MeV, as can be seen in Fig. 6.10 for barrel and end caps separately. The exact values for both data taking runs and detector parts, can be found in Tab. 6.2. Shown are the mean values of the energy distributions, including all photons with an energy > 0.3 GeV. The systematic uncertainties are estimated by varying the energy of the photons used between > 0.2 GeV and > 1.5 GeV systematically. This leads to the fact that a MC photon with E > 0.3 GeV deposits, in average, around 2 MeV more in the EMC than a photon in data. The results for run 1 and 2 agree. This has to be considered in the photon correction, i.e. the bin size of the correction matrix must not be chosen narrower than 2 MeV.

The ϕ and θ distributions are, too, shifted a little bit in data compared to MC. This means that the EMC is rotated around and shifted along the beam axis. The deviation in ϕ describes the rotation and the deviation in θ the shift between data and MC. To have an idea of the order of magnitude of these deviations, the mean value of the distributions are calculated for

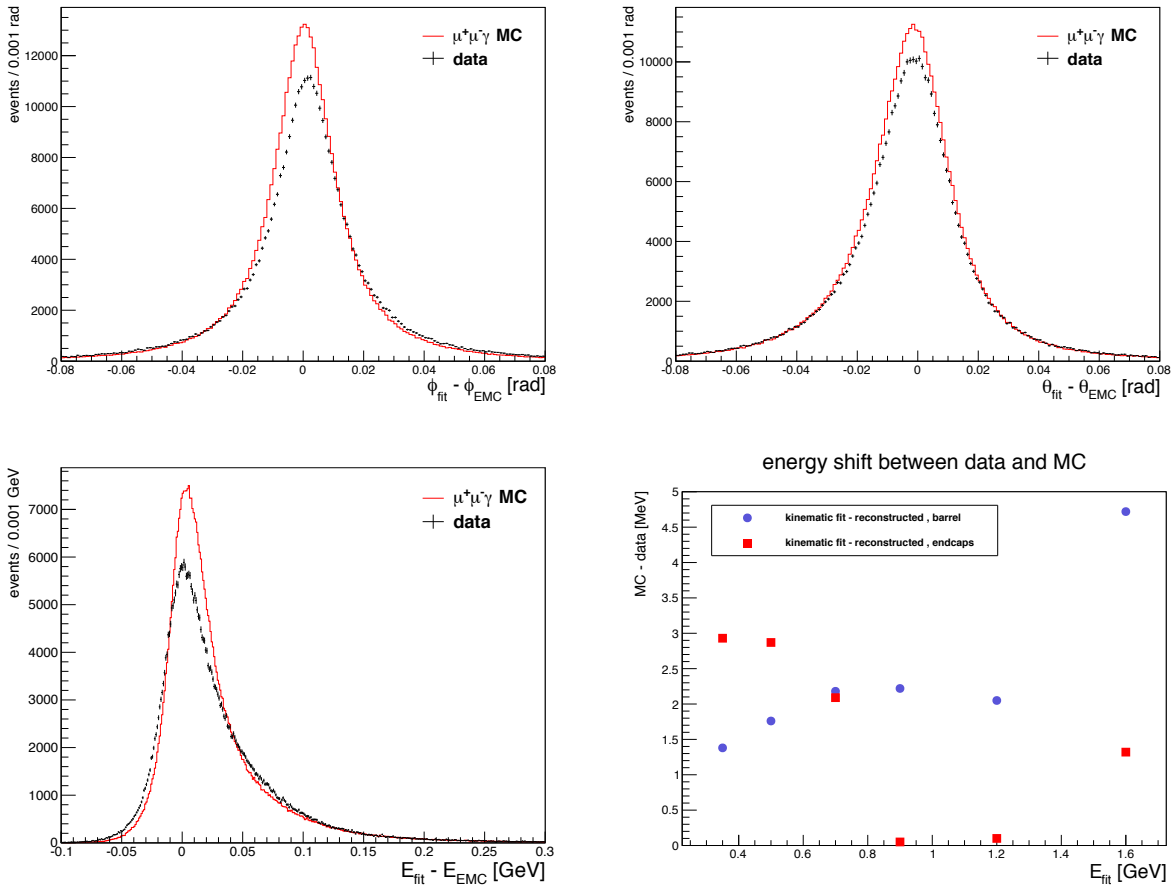

Figure 6.10: Fitted value minus reconstructed value in the EMC parts. Shown are the distributions for ϕ, θ and energy for MC and data, respectively. Also shown is the difference between MC and data of the mean value of the energy distribution, which displays the energy shift in the photon energy deposition between data and MC.

data and MC, for the different detector parts and run periods, respectively. The results are summed up in Tab. 6.3 for ϕ and 6.4 for θ. The systematic uncertainties are even estimated by varying the photon energies used between > 0.2 GeV and > 1.5 GeV. In the end cap parts, the differences between data and MC are compatible with zero, in case of ϕ. The deviation in the barrel is about 1 mrad, and, thus, smaller than the spatial resolution of 0.03 rad. The same is the case, if one looks at the θ angle. Figure 6.11 sketches the differences between MC and data for the two run periods. To conclude, the description of the EMC in MC by the GEANT-4 simulation is feasible. The data MC difference of deposited energies is about 2 MeV in average. With respect to ϕ, the data-MC difference in the end caps is compatible with zero and smaller than the resolution in the barrel part. With respect to θ, the difference is, also, smaller than the spatial resolution.

part	runs	MC [MeV]	data [MeV]	MC - data [MeV]
barrel	whole data	19.64 ± 0.05	17.35 ± 0.07	$2.29 \pm 0.09_{stat} \pm 0.64_{sys}$
	run 1	19.39 ± 0.08	17.49 ± 0.14	$1.90 \pm 0.16_{stat} \pm 0.41_{sys}$
	run 2	19.75 ± 0.06	17.28 ± 0.09	$2.47 \pm 1.08_{stat} \pm 0.73_{sys}$
endcaps	whole data	$46{,}76 \pm 0.16$	44.92 ± 0.25	$1.85 \pm 0.33_{stat} \pm 0.50_{sys}$
	run 1	$46{,}77 \pm 0.28$	45.80 ± 0.46	$0.97 \pm 1.12_{stat} \pm 0.69_{sys}$
	run 2	$46{,}76 \pm 0.19$	44.53 ± 0.30	$2.23 \pm 0.10_{stat} \pm 0.41_{sys}$

Table 6.2: Mean value of the distributions from E_{fit} - E_{true}, and difference between MC and data. The mean value is calculated including all photons with an energy > 0.3 GeV.

part	runs	MC [mrad]	data [mrad]	MC - data [mrad]
barrel	whole data	0.52 ± 0.02	1.65 ± 0.03	$-1.13 \pm 0.04_{stat} \pm 0.04_{sys}$
	run 1	0.51 ± 0.04	1.75 ± 0.07	$-1.24 \pm 0.08_{stat} \pm 0.11_{sys}$
	run 2	0.53 ± 0.03	1.60 ± 0.04	$-1.07 \pm 0.05_{stat} \pm 0.03_{sys}$
end cap 1	whole data	0.37 ± 0.10	0.58 ± 0.18	$+0.21 \pm 0.21_{stat} \pm 0.02_{sys}$
	run 1	0.69 ± 0.19	0.36 ± 0.33	$+0.38 \pm 0.38_{stat} \pm 0.73_{sys}$
	run 2	0.22 ± 0.12	0.68 ± 0.21	$+0.24 \pm 0.24_{stat} \pm 0.08_{sys}$
end cap 2	whole data	0.35 ± 0.11	0.93 ± 0.18	$+0.21 \pm 0.21_{stat} \pm 0.51_{sys}$
	run 1	0.41 ± 0.20	0.12 ± 0.34	$+0.39 \pm 0.39_{stat} \pm 0.32_{sys}$
	run 2	0.32 ± 0.13	0.08 ± 0.02	$+0.13 \pm 0.13_{stat} \pm 0.66_{sys}$

Table 6.3: Mean value of the distributions from ϕ_{fit} - ϕ_{true} and difference between MC and data. The mean value is calculated with all photons with an energy > 0.3 GeV.

part	runs	MC [mrad]	data [mrad]	MC - data [mrad]
whole EMC	whole data	-3.07 ± 0.03	-2.96 ± 0.04	$-0.11 \pm 0.05_{stat} \pm 0.14_{sys}$
	run 1	-4.10 ± 0.04	-2.44 ± 0.07	$-1.66 \pm 0.08_{stat} \pm 1.29_{sys}$
	run 2	-2.61 ± 0.03	-3.18 ± 0.05	$+0.57 \pm 0.06_{stat} \pm 0.29_{sys}$

Table 6.4: Mean value of the distributions from θ_{fit} - θ_{true} and difference between MC and data. The mean value is calculated using all photons with an energy > 0.3 GeV.

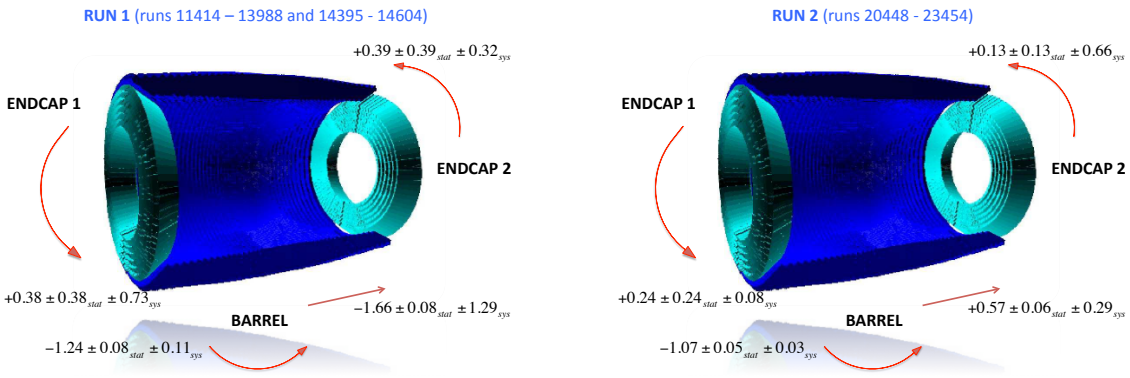

Figure 6.11: Sketch of the differences in the EMC position between MC and data. The values are in mrad.

6.5 Photon efficiency differences and corrections

To study the photon efficiency differences between data and MC, the following condition needs to be fulfilled, in order to match the predicted photon and a reconstructed one. If the prediction by the 1C fit is such, that the ISR photon hits the fiducial volume of the EMC, a 4C kinematic fit is performed. As input, the two charged tracks and one photon are used, exactly as performed in the $\pi^+\pi^-\gamma$ event selection. As photon candidate all neutral clusters in the EMC are used, successively. The combination of the two charged tracks and one photon with the best χ^2_{4C} value is matched to the predicted photon. The χ^2_{4C} distribution of the best combination is displayed in Fig. 6.12 for data and MC events, whereas the MC is scaled to the data luminosity. An event is efficient, if it has a $\chi^2_{4C} < 60$. This is the same requirement as in the $\pi^+\pi^-\gamma$ case. Hence, in addition to photon detection data-MC differences, also data-MC differences due to the χ^2_{4C} requirement are studied. The photon efficiency is defined as:

$$\epsilon_{photon} = \frac{\text{events}(\chi^2_{4C} < 60)}{\text{all events}}\,, \tag{6.2}$$

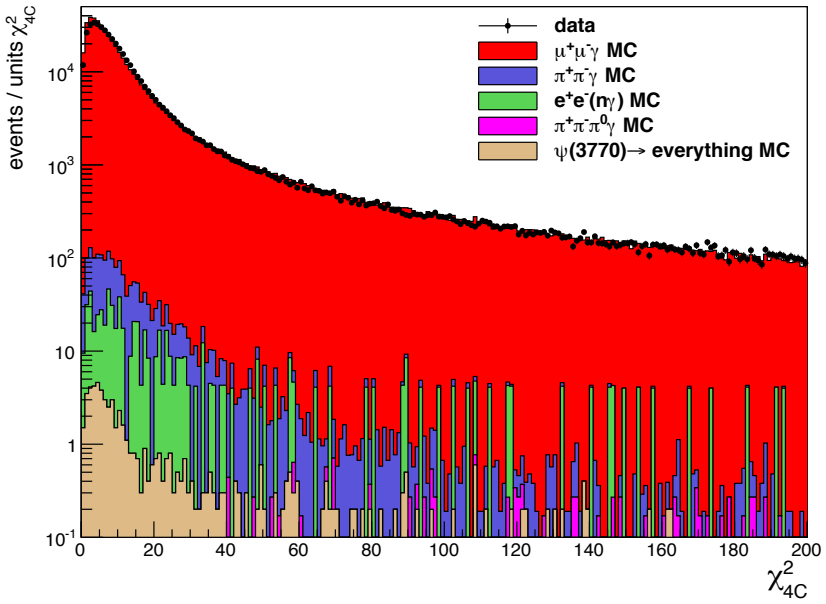

Figure 6.12: χ^2_{4C} distribution to match predicted and reconstructed tracks. A photon is treated as efficient if this value is smaller than 60.

where "all events" stands for the remaining ones after applying the selection requirements described in section 6.1. This efficiency is studied for energies above 0.3 GeV in 20 MeV bins, and the full angular acceptance of the EMC in 0.1 rad bins. Photon energies above 1.6 GeV are of special interest, since an ISR photon emission of this energy yields to an invariant mass below 1 GeV, in the $\pi^+\pi^-\gamma$ case. The photon efficiency in bins of the energy can be seen

in Fig. 6.13, for the barrel and the end caps, respectively. Shown is the data (black) of the whole data sample, taken at $\sqrt{s} = 3.773$ GeV, the MC sample (red), and the same MC sample after applying the efficiency corrections (green), as explained in the following. After applying these corrections, the MC describes the data much better. The same can be seen in 6.14 for the θ angle. Displayed are two cases: using photons with energies greater than 0.3 GeV and restricting to photons with energies above 1.6 GeV. The drop around 0.5 and 2.5 rad is the connection between barrel and end cap part, where no energy deposition can be measured, since there is a small gap for technical support and cooling. Figure 6.15 shows the situation for the ϕ angle. As expected, the efficiency, in bins of ϕ, is flat. It drops twice, where also small gaps for technical support are located in the EMC.

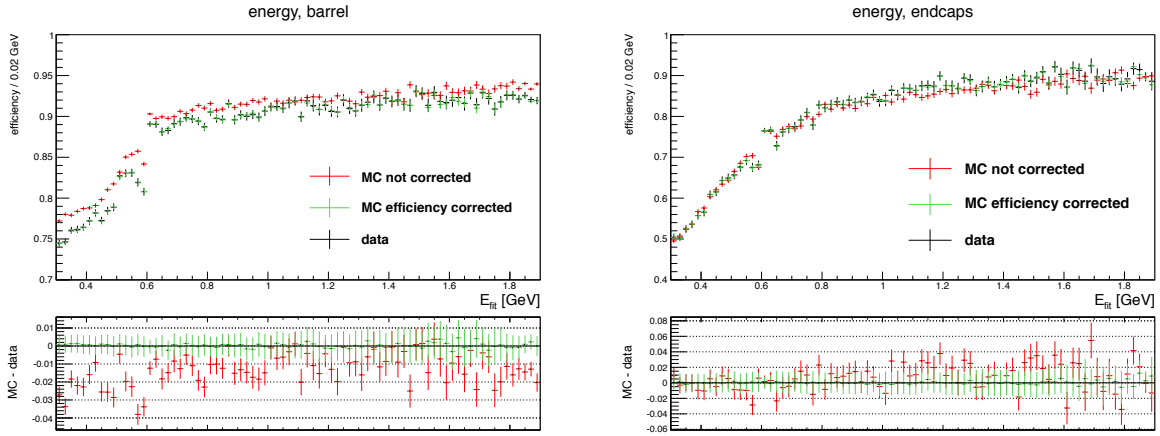

Figure 6.13: Photon detection efficiency for photon energies between 0.3 GeV and 1.9 GeV for barrel and end cap parts, separately. Displayed are the distributions for barrel and end caps of the EMC, respectively. Shown is data (black), MC (red), and the same MC sample (green), after applying the correction factors, as explained in the text. The lower panels display the difference between data and MC. In red the difference with respect to the not corrected MC, and in green with respect to the corrected one.

In the energy dependence a structure around 0.6 GeV can be seen. This is the ISR photon energy yielding to J/ψ production. A pure photon efficiency should be independent of the final state. This is an indication that not only the pure photon efficiency is studied by this technique, but also the efficiency of the 4C kinematic fit. The decay of the J/ψ to $\mu^+\mu^-$ has a different kinematic than the non-resonant QED production. Hence, the efficiency of the kinematic fit is different and causes a structure as the one seen in Fig. 6.13.

The MC photon detection efficiency correction, in order to adjust data-MC differences, is performed on a track basis in bins of energy E and θ. In MC, an event is multiplied with a scaling factor depending on the difference between MC and data in energy and θ. The scaling

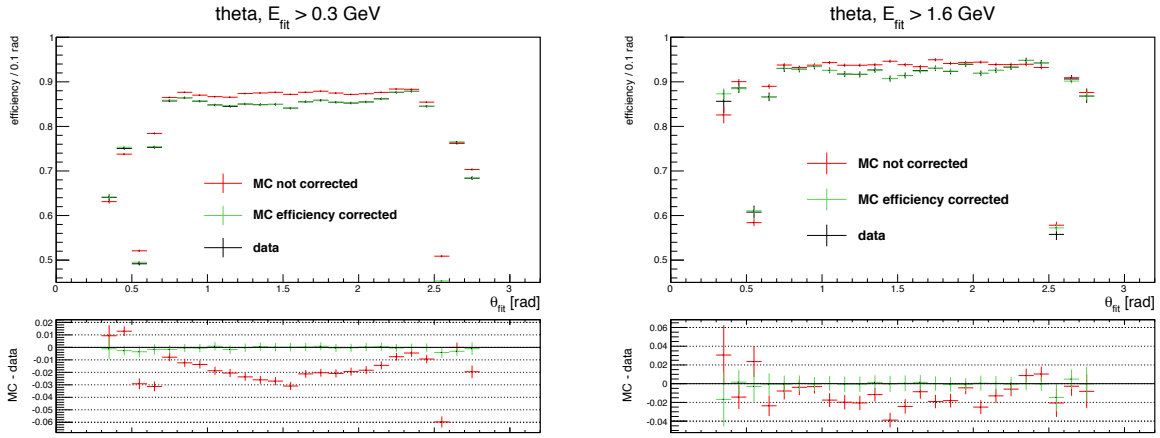

Figure 6.14: Same as explained in Fig. 6.13 in bins of θ. In the left case, photons with energies greater 0.3 GeV are used to calculate the efficiency. In the right case, it is restricted to photons with energies greater than 1.6 GeV.

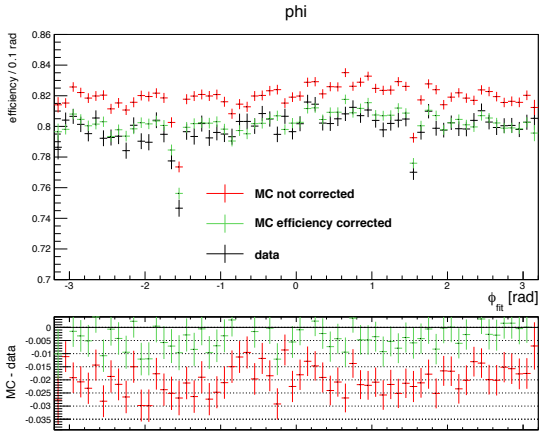

Figure 6.15: Same as explained in Fig. 6.13 in bins of ϕ.

factor is determined via:

$$scaling = \frac{\epsilon_{data}(E,\theta)}{\epsilon_{MC}(E,\theta)} \,, \tag{6.3}$$

where ϵ_{data} is the efficiency in data and ϵ_{MC} is the MC efficiency, in dependence of E and θ. Figure 6.16 displays the resulting scaling matrix in bins of E and θ. The bin size in this figure is larger than in the actual calculated matrix, to be able to display the entries. The actual used matrix has bin sizes of 20 MeV and 0.1 radians. The error shown is the statistical one. Figures 6.13, 6.14, and 6.15 show the MC sample, after applying these correction factors on each track, displayed in green. The systematic uncertainties of this correction method are estimated for different energy and angular regions in section 6.6.

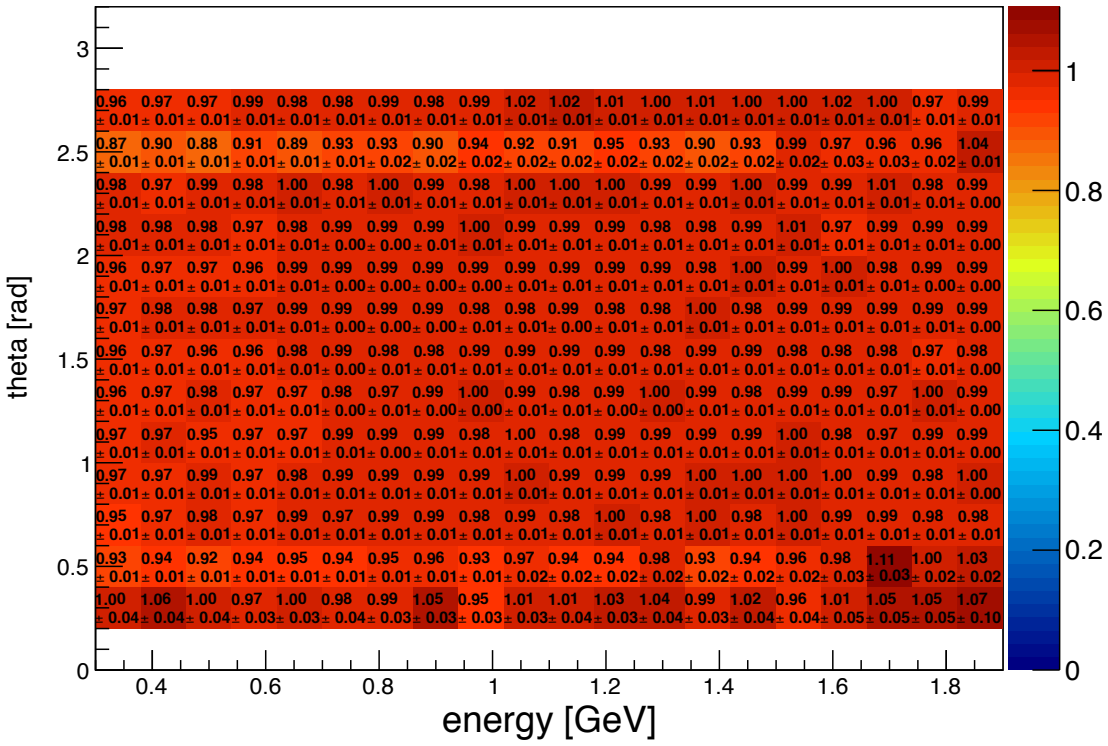

Figure 6.16: Correction factors in bins of energy and θ to adjust data MC difference in case of photon detection. The corrections are applied on a track basis on MC events. The errors are the statistical ones. For illustration, the bin sizes shown are larger than the ones of the actual used correction matrix.

6.6 Systematic uncertainties

The systematic uncertainties of the track-based photon detection efficiency correction has three different sources. First, a potential bias between the selection of $\mu^+\mu^-\gamma$ events and the correction factors obtained. Second, how well the MC describes data after applying the corrections. Third, the uncertainty due to background contamination.

(1) The bias of the event selection requirements on the correction factors is estimated by varying the criteria used on the depth of the charged tracks in the MUC, E/p, χ^2_{1C}, and momentum $|\vec{p}|$. All other selection requirements applied are left equal to the ones used in the $\pi^+\pi^-\gamma$ event selection and, thus, do not effect the efficiency correction. To find a meaningful variation range of these parameters, the efficiencies of the requirements applied are evaluated in data and in MC, separately. The **efficiency** ϵ is defined as the number of remaining events after applying the requirement, divided by the number before applying it. The **resolution** of a variable is defined as the maximum variation range, either in data or MC, where a requirement has to be varied such, that the efficiencies in data and MC agree to each other. For example: in the

standard selection of $\mu^+\mu^-\gamma$ events, the requirement $E/p < 0.5$ is applied. For this criterium, one finds an $\epsilon(E/p)$ of (99.64±0.01)% in MC and (99.44±0.01)% in data. On the one hand, one has to change this requirement to $E/p < 0.46$ only in MC, to force an agreement in $\epsilon(E/p)$ between MC and data. On the other hand, one can also change it to $E/p < 0.53$ only in data, to achieve the same result. The maximum variation range is 0.04 units in E/p, which is chosen as **resolution** of the E/p variable. The numbers are summarized in Tab. 6.6. The resolutions χ^2_{1C} and for the depth in MUC are determined in the same way and are listed in Tab. 6.5 and 6.7, which are found to be 1.5 χ^2_{1C} units and 1.0 cm for the depth. The criterium on the momentum is $|\vec{p}| < 1.85$ GeV. The resolution for charged tracks with momenta greater than 1.0 GeV is better than 0.5% [74]. Thus, the resolution is chosen as 0.1 GeV. As a meaningful variation range for each variable, three times its resolution is chosen. This leads to a "**tight**" and "**loose**" event selection, as shown in Tab. 6.8. The photon detection correction factors are determined using the "tight" and "loose" selection requirements, separately, and are applied on the $\pi^+\pi^-\gamma$ MC event numbers between 0.6 and 0.9 GeV. The relative difference between using these correction factors to the ones determined with the standard event selection, is shown in Fig. 6.17 in bins of $m_{2\pi}$, between 600 and 900 MeV. It turns out, that the "loose" selection yields to the largest deviation, which is claimed as the systematic error. This is what one would expect, because more background events pass the selection criteria. It is determined by performing a linear fit on the relative difference in bins of $m_{2\pi}$, which yields to (0.13±0.2)%. It is compatible with zero. However, a systematic uncertainty of 0.2% is claimed as systematic uncertainty due to the choice of the selection requirements.

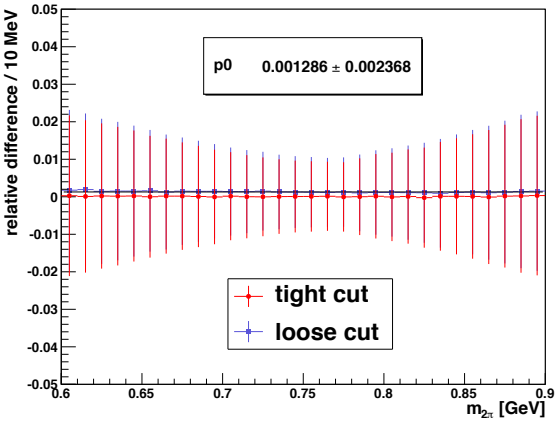

Figure 6.17: Relative difference of $\pi^+\pi^-\gamma$ MC events when applying the standard photon detection correction factors from section 6.5 and using either the "loose", or the "tight", requirements from Tab. 6.8 to determine them. Shown is the case for $m_{2\pi}$ between 0.6 and 0.9 GeV. The largest difference can be observed when applying the "loose" selection and is claimed as systematic uncertainty due to the choice of the selection requirements. It is determined by performing a linear fit, called p_0. Its result is shown in the upper part of the figure.

		standard cut	data corrected	MC corrected
MC	χ^2_{1C}	< 10	< 10	< 8.5
	$\epsilon(\chi^2_{1C})$ [%]	93.13 ± 0.04	93.13 ± 0.04	91.51 ± 0.04
data	χ^2_{1C}	< 10	< 11.5	< 10
	$\epsilon(\chi^2_{1C})$ [%]	91.47 ± 0.04	93.11 ± 0.04	91.47 ± 0.04

Table 6.5: χ^2_{1C} requirement and its efficiency in data and MC.

		standard cut	data corrected	MC corrected
MC	E/p	< 0.5	< 0.5	< 0.46
	ϵ(E/p) [%]	99.64 ± 0.01	99.64 ± 0.01	99.44 ± 0.01
data	E/p	< 0.5	< 0.53	< 0.5
	ϵ(E/p) [%]	99.44 ± 0.01	99.63 ± 0.01	99.44 ± 0.01

Table 6.6: E/p requirement and its efficiency in data and MC.

		standard cut	data corrected	MC corrected
MC	depth [cm]	> 35.0	> 35.0	> 34.0
	ϵ(depth) [%]	81.50 ± 0.06	81.50 ± 0.06	82.99 ± 0.06
data	depth [cm]	> 35.0	> 36.0	> 35.0
	ϵ(depth) [%]	83.05 ± 0.06	81.27 ± 0.06	83.05 ± 0.06

Table 6.7: Depth in MUC requirement and its efficiency in data and MC.

	standard cut	tight cut	loose cut
χ^2_{1C}	< 10	< 5.5	< 14.5
E/p	< 0.5	< 0.41	< 0.59
depth [cm]	> 35.0	> 38.0	> 32.0
$\lvert\vec{p}\rvert$ [GeV]	< 1.85	< 1.82	< 1.88

Table 6.8: Criterias of the standard event selection used in the photon detection efficiency study and the "loose" and "tight" selections, found as described in the text. The variation ranges are three times the estimated resolutions of the variables.

(2) The goodness of the photon detection correction is estimated by comparing the efficiency of the photon efficiency in MC, after applying the corrections, and data, in bins of the predicted photon energy. Figure 6.18 shows this difference for barrel and end cap, separately. A linear fit is performed, to estimate the difference over the whole available energy range from 0.3 to 1.85 GeV. The result is a difference of 0.04% for the barrel and 0.03% for the end caps. It is in both cases smaller than 0.1%, and thus, negligible.

(3) As described in section 6.2 the $e^+e^-(n\gamma)$ background is subtracted, yielding to a neglectable uncertainty smaller than 0.1%. The $\pi^+\pi^-\gamma$ final state can be treated as signal. Thus, no

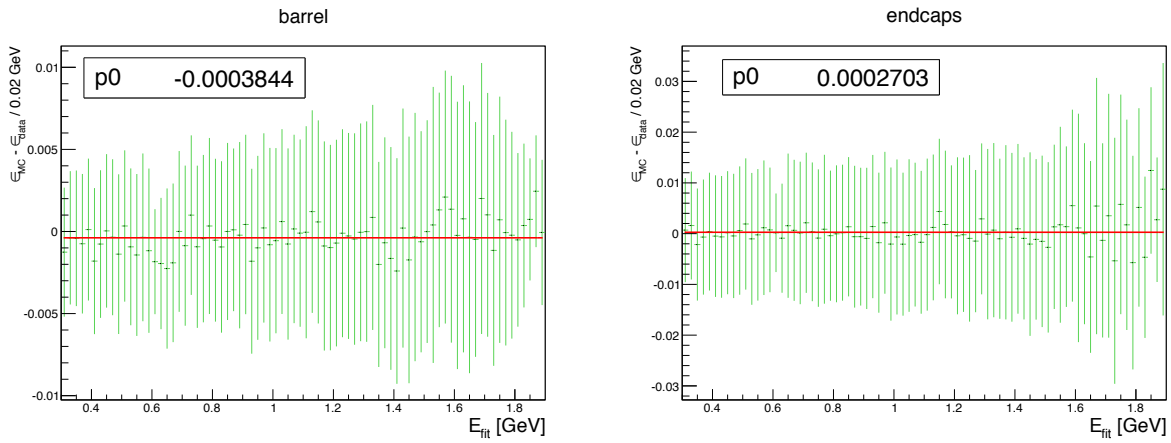

Figure 6.18: Difference of the Photon detection efficiency in MC after applying the correction factors and data. A linear fit p0 is performed to estimate the global shift for barrel and end caps, separately. It is in both cases below 0.1%.

systematic error has to be claimed here. All other background MC samples, scaled to the luminosity of data, are not subtracted. They are summed and their fraction with respect to the number of data events in bins of the predicted photon energy is claimed as systematic error. This fraction, or uncertainty, is shown in Fig. 6.19. For relevant photon energies above 1.5 GeV (or $m_{2\pi}$ masses smaller than 1 GeV in $\pi^+\pi^-\gamma$ events), it is smaller than 0.05% and, thus, negligible.

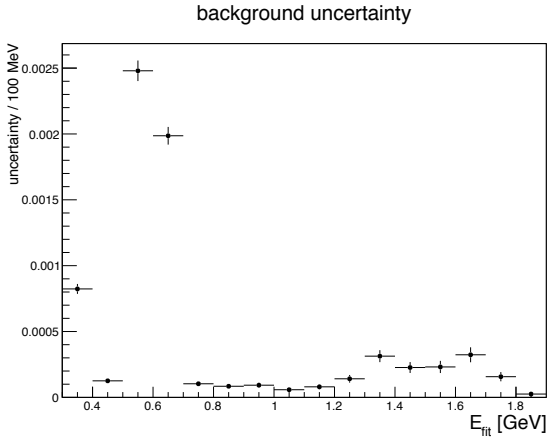

Figure 6.19: Fraction, also treated as uncertainty, of summed background MC samples, which are scaled to the luminosity of data and are not of the type $e^+e^-(n\gamma)$ or $\pi^+\pi^-\gamma$, with respect to events in data. Shown is the dependence on the predicted photon energy.

In summary, a systematic uncertainty of 0.2% is claimed, when applying the photon detection efficiency corrections on MC. The treatment of statistical errors, caused by limited statistics in data, is described in section 9.1.

Chapter 7

Tracking efficiency studies

As in the case of photon detection, also differences between data and MC in the detection of charged pion and muon tracks in the MDC have to be studied. The corrections are developed on a track basis for muons and pions, separately. Events of the kind $e^+e^- \to \pi^+\pi^-\pi^+\pi^-\gamma$ are used to study the reconstruction of charged pion tracks, and $e^+e^- \to \mu^+\mu^-\gamma$ events in case of muon tracking.

7.1 Pion tracking efficiency studies

7.1.1 Event selection

The pion tracking efficiency study as presented here was performed in collaboration with the $e^+e^- \to \pi^+\pi^-\pi^0$ ISR analysis performed by Yaqian Wang[1] [101]. A $e^+e^- \to \pi^+\pi^-\pi^+\pi^-\gamma$ control sample is used. In this case, one has to select tagged events. By selecting three tracks only and predicting one of the charged pion tracks with a 1C kinematic fit, similar to what has been done for the ISR photon in the last chapter, one can study, whether this track is reconstructed in the MDC.

The presence of three or four charged tracks in the MDC is required. The points of closest approaches from the interaction point for these two tracks have to be within a cylinder with V_r = 1.0 cm radius in the transversal direction and $|V_z|$ = 10 cm of length along the beam axis. At least one good photon with an energy $E_\gamma > 1.2$ GeV is required in the EMC, treated as the ISR photon. Its distribution for data and MC, generated with the PHOKHARA event generator, can be found in Fig. 7.1. Other good photons are required to have an energy < 0.07 GeV. A 1C kinematic fit is performed with the ISR photon, three charged tracks and one missing charged track, in the hypothesis of an $e^+e^- \to \pi^+\pi^-\pi^+\pi^-\gamma$ event. The χ^2_{1C} distribution is shown in in Fig. 7.1 for data and MC events, $\chi^2_{1C} < 5$ is required. In case of three track events, only one configuration as input for the fit is possible. In case of four track events, four configurations are possible, which are all exploited to enhance statistics, and thus, four entries per event can be used. All performed selection requirements are listed in Tab. 7.1.

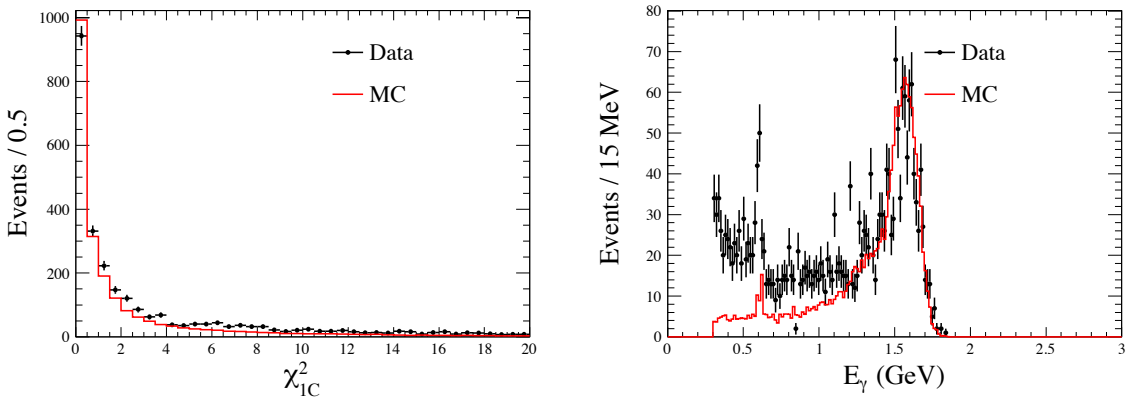

Figure 7.1: χ^2_{1C} distribution of the 1C kinematic fit (left) and energy distribution of the measured photon (right). Requirements of $\chi^2_{1C} \leq 5$ and $E_\gamma > 1.2$ GeV are applied to suppress background events.

[1]Postdoc at the Institute for Nuclear Physics Mainz.

7.1.2 Background rejection

Three vetoes are performed, to reduce background:
(1) π^0 **veto:** the ISR photon candidate could originate from a $\pi^0 \to \gamma\gamma$ decay, most likely in $\pi^+\pi^-\pi^+\pi^-\pi^0(\gamma)$ events. The combinatorics of all good photons and the ISR photon are determined, and their invariant masses $m_{\gamma\gamma}$ are calculated. If one of the combinations has an invariant mass around the π^0 mass of $m_{\pi^0} = 0.13498$ GeV [4], 0.12 GeV $< m_{\gamma\gamma} <$ 0.145 GeV, the event is rejected.

(2) K_s **veto:** Another contributing background is $K_sK^\pm\pi^\mp\gamma \to \pi^+\pi^-K^\pm\pi^\mp\gamma$. In order to suppress it, the invariant masses $m_{\pi^+\pi^-}$ of all possible pion pair combinations with net charge zero are calculated. If one of the combinations has a mass around the K_s mass of $m_{K_s} =$ 0.4976 GeV [4], 0.487 GeV $< m_{\pi\pi} <$ 0.507 GeV, the event is rejected.

(3) $\overline{n}$ **veto:** A quite high contamination comes from $e^+e^- \to \pi^+\pi^-\pi^+\pi^-n\overline{n}$ events. Neutrons n affect neutral clusters in the EMC and, hence, can fake an ISR photon. To reject these kind of events, the second moment of the neutral cluster $P = \sum_i E_i r_i^2$ is exploited, where E_i is the deposited energy in the ith crystal and r_i the radial distance of this crystal to the central cluster [102]. P has to be smaller than 14 cm^2. Figure 7.2 shows the second moment of data, signal MC and the above mentioned background channel. With this requirement the background contamination due to these kind of events can be scaled down to 0.11%.

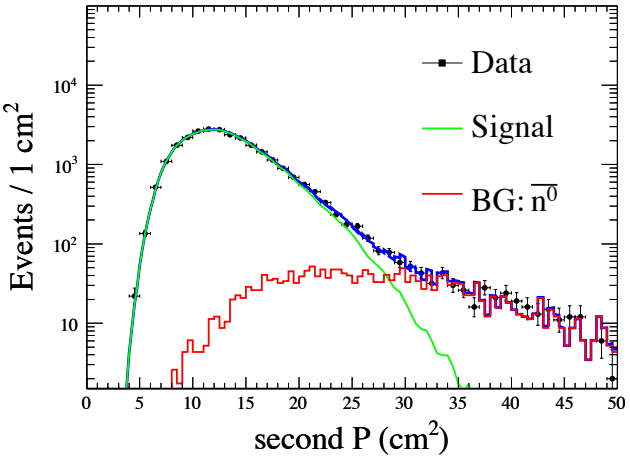

Figure 7.2: Second moment P of the measured neutral track in the EMC, which is treated as ISR photon. Shown is data, signal MC and the $e^+e^- \to \pi^+\pi^-\pi^+\pi^-n\overline{n}$ MC sample. The requirement $P <$ 14 cm^2 is performed, to reduce this background.

Table 7.2 summarizes the main background channels after applying the described selection requirements, studied with the KKMC event generator. Their fraction with respect to the

expected number of signal events from MC is shown, too. A total background fraction of 3.1% is observed. These channels are subtracted from data, using the inclusive continuum $q\bar{q}$ MC sample, containing $61{\cdot}10^6$ events and provided by the BESIII collaboration. The scaling factor for the MC sample of the main background channel, $\pi^+\pi^-\pi^+\pi^-\pi^0\gamma$, is determined with the latest cross section measurement of this exclusive final state by the *BABAR* collaboration [103]. This leads to a scaling factor of (0.6 ± 0.18). All other MC samples are scaled to the luminosity of data.

cut variable	**cut value**
V_z	< 10.0 cm
V_r	< 1.0 cm
acceptance	$21.6^\circ < \theta < 158.4^\circ$
# charged tracks	3 or 4
χ^2_{1C}	≤ 5
E_γ	> 1.2 GeV
π^0 veto	0.12 GeV $< m_{\gamma\gamma} <$ 0.145 GeV
K_s veto	0.487 GeV $< m_{\pi\pi} <$ 0.507 GeV
$\overline{n}$ veto	second moment < 14 cm^2

Table 7.1: Summary of the selection requirements to select a clean $\pi^+\pi^-\pi^+\pi^-\gamma$ sample for the pion tracking efficiency study.

background	**background fraction**	**total fraction**
$\pi^+\pi^-\pi^+\pi^-\pi^0\gamma$	51.6 %	1.60 %
$\pi^+\pi^-\pi^+\pi^-\pi^0$	15.7 %	0.49 %
$\pi^+\pi^-\pi^+\pi^-\pi^+\pi^-\gamma$	10.8 %	0.33 %
$K_sK^\pm\pi^\mp\gamma$	7.7 %	0.24 %
$\eta \to \gamma\gamma$	4.9 %	0.15 %
$\pi^+\pi^-\pi^+\pi^-\pi^0\pi^0(\pi^0)$	4.8 %	0.15 %
$\pi^+\pi^-\pi^+\pi^-n\overline{n}(\pi^0)$	3.5 %	0.11 %
$\pi^0 \to e^+e^-\gamma$	1.0 %	0.03 %
total	100.0 %	3.1 %

Table 7.2: Contributing background channels in the pion tracking efficiency study, studied with MC and simulated with the KKMC generator. Shown is the fraction on the whole background of 3.1% and the total fraction with respect to the number of signal events.

7.1.3 Pion tracking efficiency differences

The pion tracking efficiency is defined as

$$\epsilon_\pi^{tracking} = \frac{events(\#\ charged\ tracks = 4)}{events(\#\ charged\ tracks = 3) + events(\#\ charged\ tracks = 4)}\ , \tag{7.1}$$

whereas charged tracks are the measured pion candidates in the MDC. The tracking efficiency is studied as a function of the polar angle θ and the transversal momentum p_T. The systematic uncertainties, defined as the ratio of the efficiency in data and in MC per bin, are shown in Fig. 7.3. They are studied for π^+ and π^- tracks separately. They are flat in θ and p_T and, thus, a linear fit is performed to quantify the average differences between data and MC.

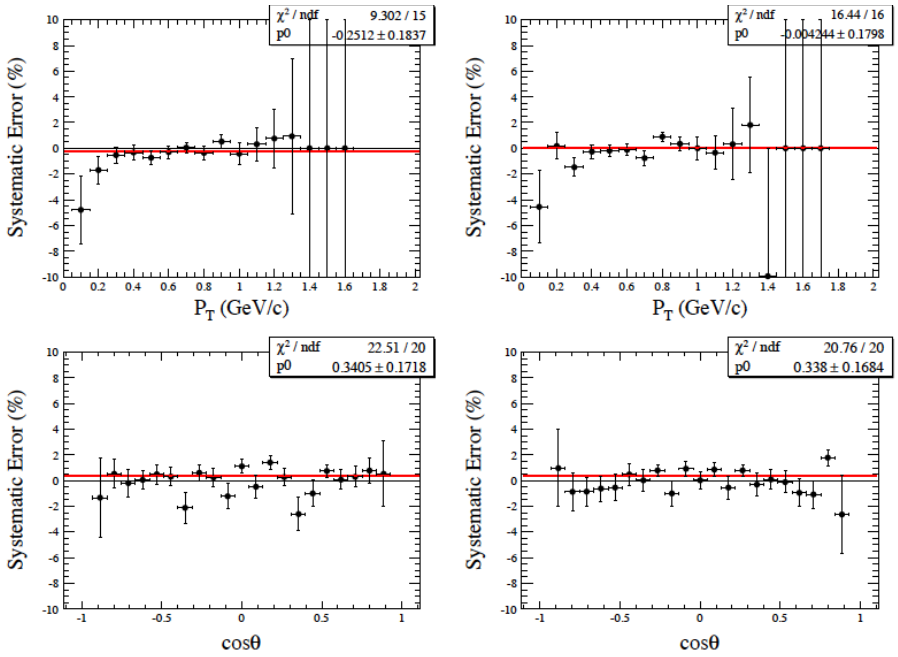

Figure 7.3: Data-MC differences (systematic errors) of the pion tracking efficiency study, defined as the ratio of efficiency in data and MC. They are studied as functions of p_T and θ. The left side displays the result for π^+ tracks, the right side for π^- tracks. A linear fit is performed to quantify the average error.

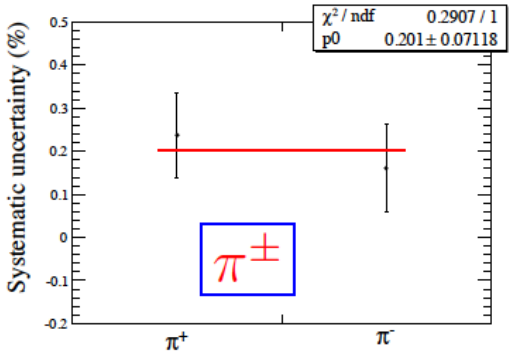

Figure 7.4: Combined statistics of π^+ and π^- tracks. A linear fit is performed to quantify the average systematic uncertainty due to charged pion detection. This leads to $(0.201 \pm 0.071)\%$.

The combination of the available statistics is displayed in Fig. 7.4. Again, a linear fit is performed to quantify the average difference between data and MC, yielding to $(0.201 \pm$

0.071)%. The statistics are much smaller, compared to the photon detection study. Hence, a correction matrix in bins of p and θ would not deliver proper results, since the statistical uncertainties of the correction factors would be too large. Thus, it is resigned in this case, and a systematic uncertainty of 0.2% is claimed as systematic uncertainty in case of charged pion tracking detection in the MDC. Thus, the systematic uncertainty is 0.3% in bins of $m_{2\pi}$, when adding the uncertainty of two pion tracks quadratically.

7.1.4 High momenta tracks

The selection requirement $E_\gamma > 1.2$ GeV is essential to suppress background events when studying the $\pi^+\pi^-\pi^+\pi^-\gamma$ final state, but limits the analysis to p_T values smaller than 1.2 GeV. As can be seen in Fig. 7.3, the statistics at higher momenta are nearly zero. However, the data-MC differences of high momenta tracks should be smaller than for low momenta tracks, because they can be better reconstructed. To proof this, the non-radiative control sample $e^+e^- \to \pi^+\pi^-\pi^+\pi^-$ is used. The same event selection as described in 7.1.1 is applied, without taking an ISR photon into account. The 1C fit is also performed without a photon. The tracking efficiency is defined as in formula (7.1). The result for momenta greater 1.2 GeV is shown in Fig. 7.5. Presented is the absolute efficiency in data and MC, simulated with the KKMC generator, together with their ratio. Again, a linear fit is performed to quantify the average data-MC difference for this momentum region, yielding to (0.04 ± 0.25)% and, thus, compatible with zero. Hence, the systematic uncertainty assumed of 0.3% for the pion tracking detection in the MDC, is feasible for the whole momentum range.

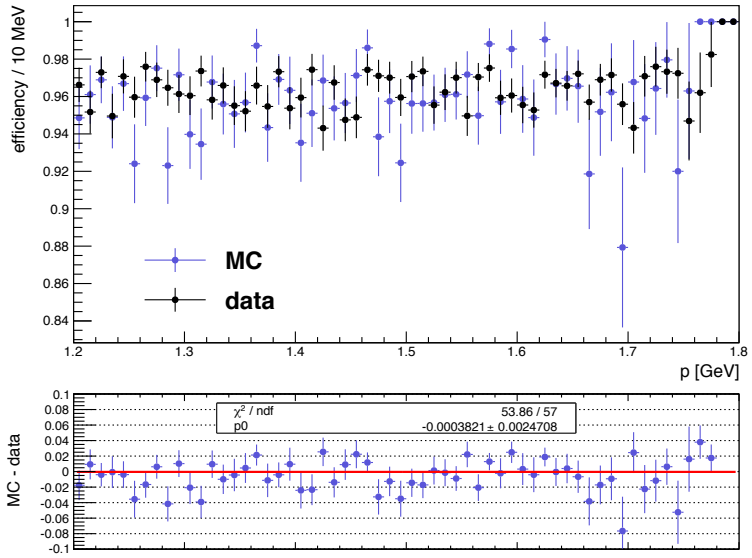

Figure 7.5: Pion tracking efficiency in the case of non-radiative $e^+e^- \to \pi^+\pi^-\pi^+\pi^-$ events. Shown is the absolute efficiency for data and MC, simulated with the KKMC generator. The lower panel displays the data-MC ratio, which is flat. A linear fit is performed to quantify the average data-MC difference for momenta greater than 1.2 GeV, yielding to (0.04 ± 0.25)%.

7.2 Muon tracking efficiency studies

7.2.1 Method

To study the muon tracking efficiency the control sample $\mu^+\mu^-\gamma$ is used, as in the case of the photon detection study. The difference to the photon study is that, here, one muon track and the ISR photon are measured, and the second muon is predicted by a 1C kinematic fit.

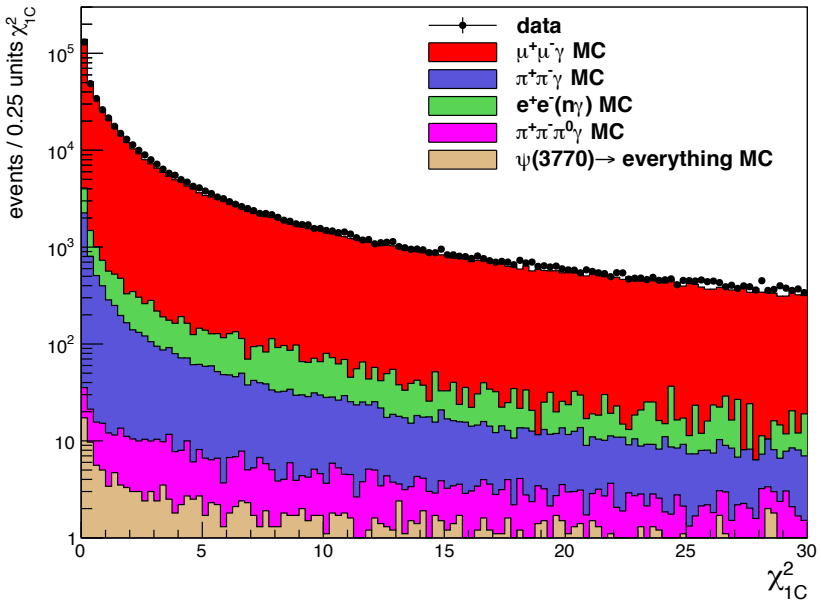

Figure 7.6: χ^2_{1C} distribution of the 1C kinematic fit to predict the kinematics of the missing muon track.

The selection requirements are similar to the ones described in section 6.1. They are listed in Tab. 7.3. Figure 7.6 shows the χ^2_{1C} distribution of the 1C kinematic fit. MC and data agree very well. The requirement $\chi^2_{1C} \leq 10$ has to be fulfilled to reduce background and to achieve a good prediction of the missing track. In Fig. 7.7 one can see the transverse momentum p_t of the predicted charged track after applying the selection requirements for data and MC respectively. The whole momentum range can be studied with the event sample selected. For this study only events with less or equal two charged tracks are considered, where the direction of the missing track is such, that it would leave a signature in the MDC. An event is treated as efficient, if it contains exactly two charged tracks, i.e. the missing track is measured in the MDC. It also must achieve that the total charge of the two tracks is zero. Thus, the definition of efficiency is the following:

$$\epsilon_\mu^{tracking} = \frac{events(\#\ charged\ tracks = 2\ \&\&\ total\ charge = 0)}{events(\#\ charged\ tracks = 1) + events(\#\ charged\ tracks = 2)}\ , \tag{7.2}$$

whereas *events* mean, that the missing track would hit the fiducial volume of the MDC.

variable	requirement
MDC and EMC valid tracks	≥ 1
MuC valid tracks	≥ 1
$\|\vec{p}\|$	< 1.8 GeV
V_z	< 10.0cm
V_r	< 1.0cm
E/p	< 0.6
acceptance	0.4 rad $< \theta < \pi$ - 0.4 rad
depth in MuC of one track	≥ 35 cm
# charged tracks	≤ 2
χ^2_{1C}	≤ 10

Table 7.3: Summary of the event selection to select a clean $\mu^+\mu^-\gamma$ sample for the muon tracking efficiency study.

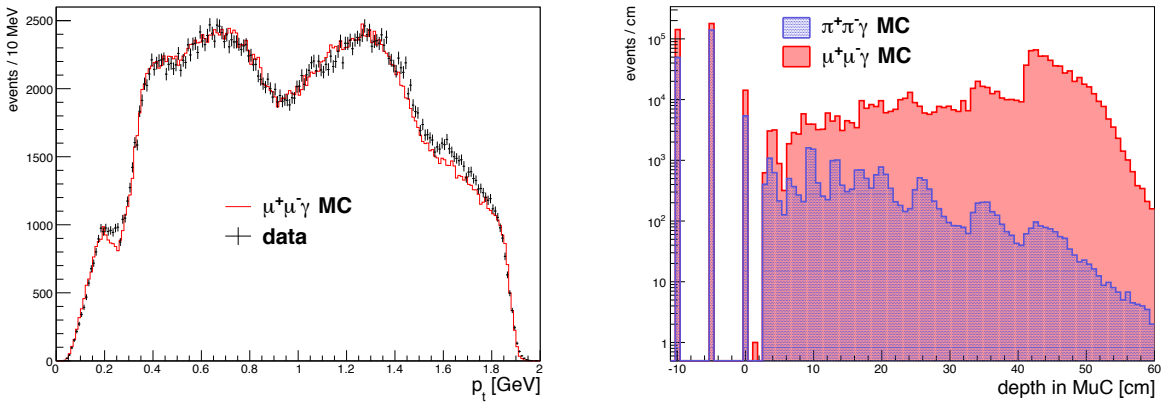

Figure 7.7: Left: Transverse momentum of the predicted muon track after applying the selection requirements. Shown is data and MC.
Right: Depth in the MUC from MC. The requirement ≥ 35 cm is chosen to achieve a low background contamination from charged pion tracks. A value smaller than 0 is gained, if the depth can not be computed, either to the missing of a signature (value of -10) or insufficient information (value of -5).

7.2.2 Background contamination

The background contamination is higher than in the photon detection efficiency study, since only one charged track is measured. Figure 7.8 presents the momentum $|\vec{p}|$ of this measured charged track. As in the photon detection study, the $e^+e^-(n\gamma)$ background MC peaks at high momenta above 1.8 GeV. The requirement $|\vec{p}| < 1.8$ GeV is applied, to reject more than 99% of all Bhabha events. This background, as well as the final states $\pi^+\pi^-\gamma$ and $\pi^+\pi^-\pi^0\gamma$, are subtracted. Their fraction with respect to data can be seen in Fig. 7.9. The accuracy of the MC samples is taken into account in the estimation of the systematic uncertainties in section 7.2.4.

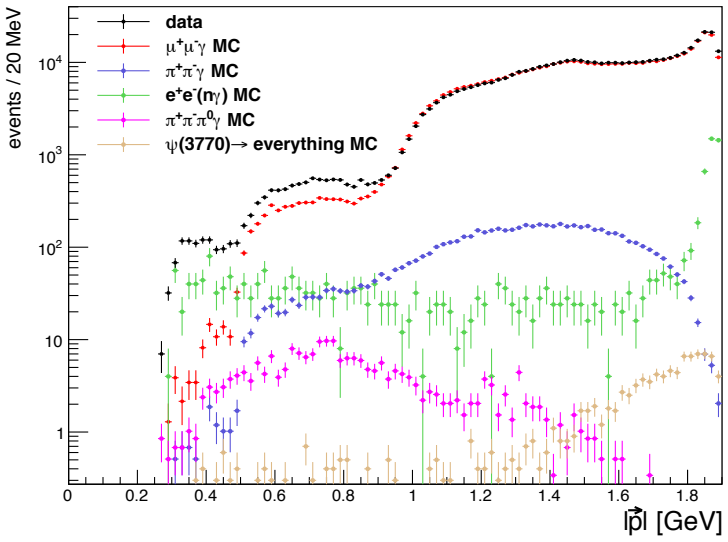

Figure 7.8: Momentum distribution of the measured charged track. A cut at $|\vec{p}| < 1.8$ GeV is performed to reject the steep rising election background.

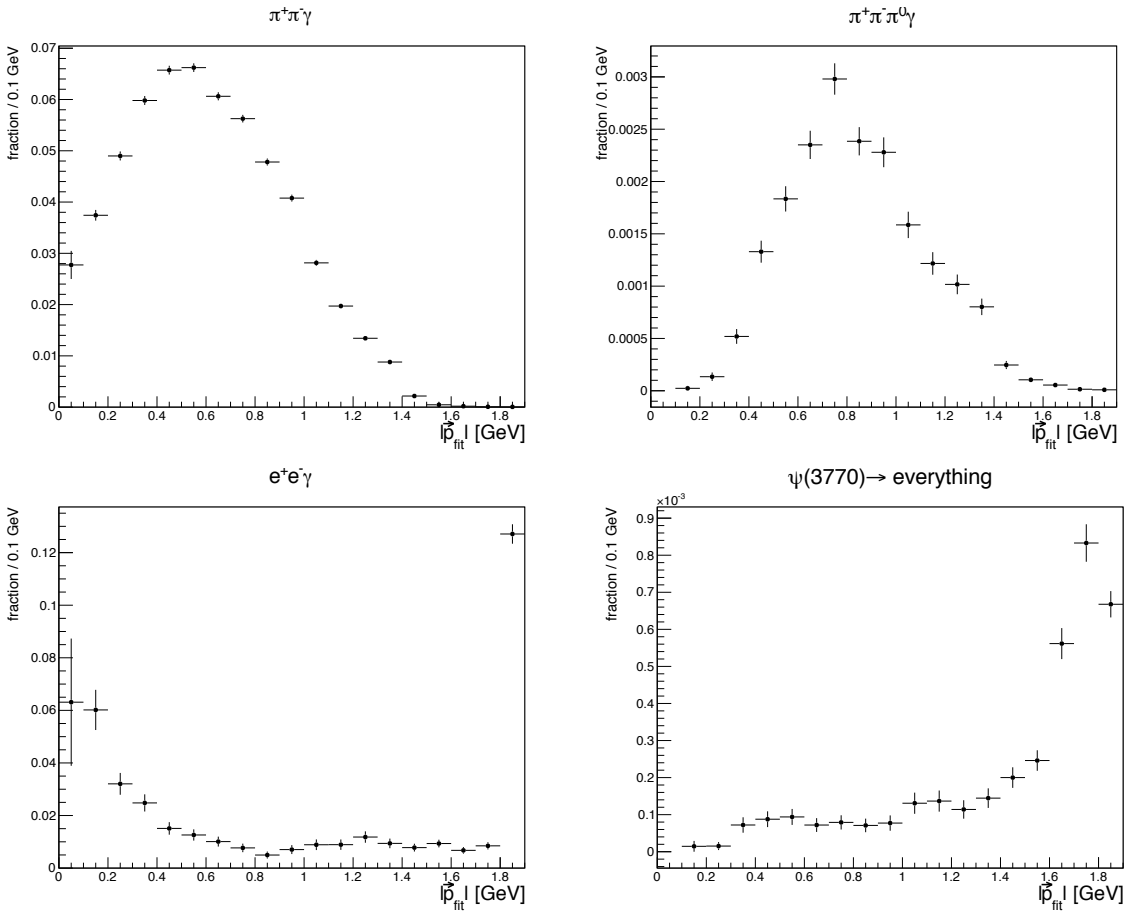

Figure 7.9: Background fractions of the main contributing final states.

The resonant $\psi(3770)$ decay, for example, is smaller than 0.1%, as shown in Fig. 7.9. It is not subtracted but, however, taken into account in the systematic uncertainties. Other backgrounds besides the ones presented here are found to be negligible after studying them with MC samples.

7.2.3 Muon tracking efficiency differences and corrections

The efficiency $\epsilon_{\mu}^{tracking}$ is studied in bins of the predicted momentum $|\vec{p}_{fit}|$, and the predicted angles θ_{fit}, and ϕ_{fit}, of the missing charged track, for data and MC, respectively. Differences between data and MC are studied and MC correction factors on a charged track basis are developed, as explained in section 6.5.

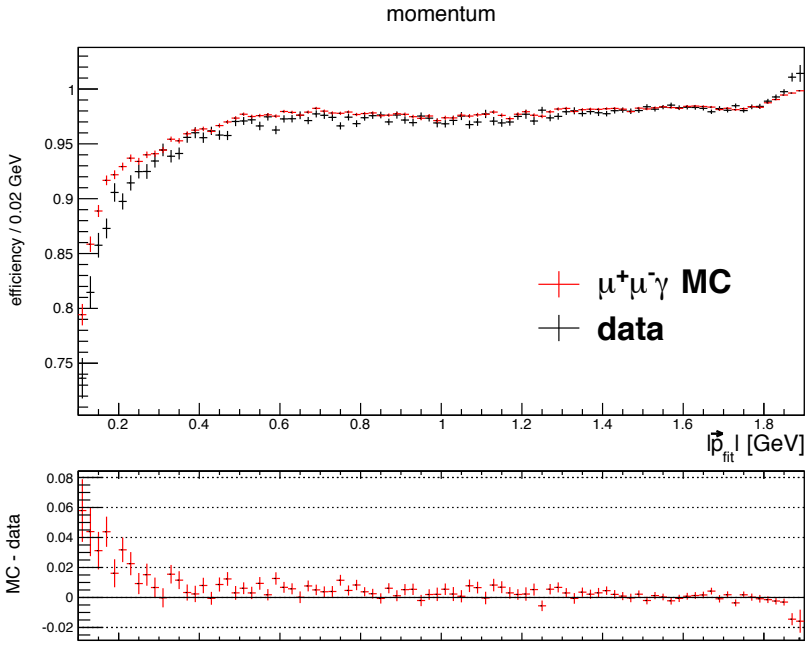

Figure 7.10: Muon tracking efficiency in bins of the predicted momenta of the missing charged track. Shown is data and MC, respectively The lower panel displays the difference between MC and data.

Figures 7.10 and 7.11 show these efficiencies for MC and data. The lower panels display the difference between MC and data. The efficiency differences are also studied for positive and negative charged tracks, separately. Figure 7.12 shows the efficiency in bins of the predicted momentum for negative and positive charged tracks. Within the statistical uncertainties, no significant asymmetry is visible. To reduce the statistical error of the efficiency correction factors, they are not separated by the charge in the final result.

The muon tracking efficiency correction is performed in bins of $|\vec{p}|$ and θ on a MC track basis. Thus, a MC muon track is multiplied with a scaling factor, which depends on its $|\vec{p}|$ and θ

values. This scaling factor is calculated as:

$$scaling(|\vec{p}|,\theta) = \frac{\epsilon_{data}(|\vec{p}|,\theta)}{\epsilon_{MC}(|\vec{p}|,\theta)} \ . \tag{7.3}$$

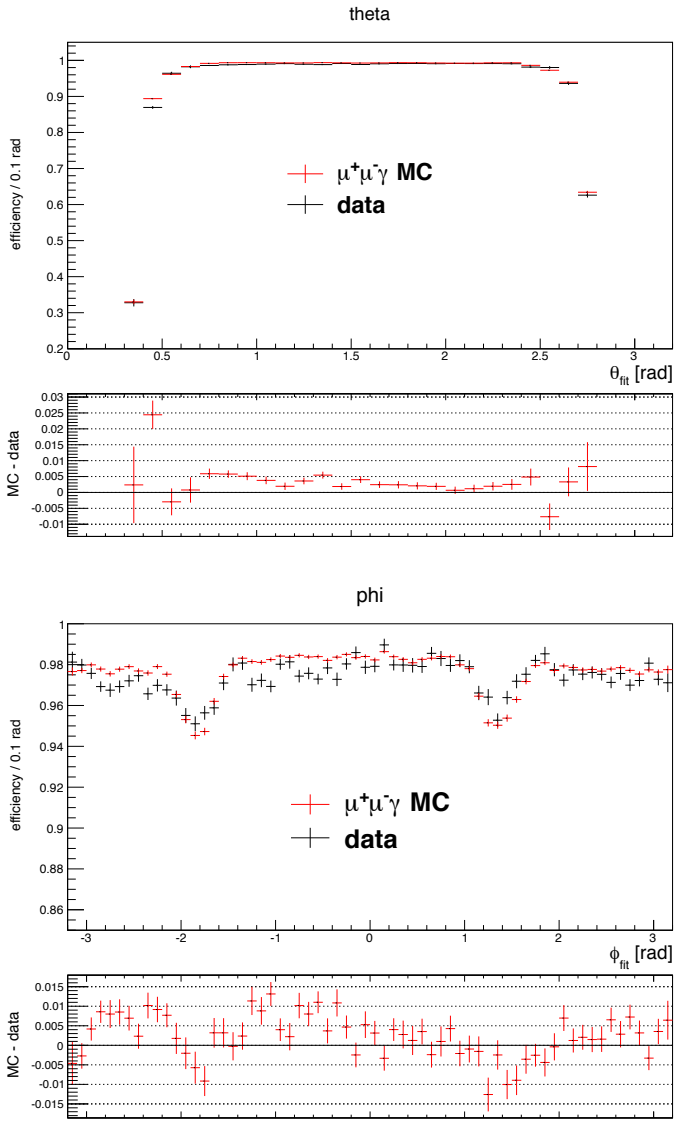

Figure 7.11: Muon tracking efficiencies in bins of the predicted angles θ and ϕ of the missing charged track. Shown is data and MC, respectively The lower panel displays the difference between MC and data.

The scaling matrix, which is a function of $|\vec{p}|$ and θ, is shown in Fig. 7.14. For better illustration, it is shown in wider bins than the actual used one, which is in bins of 0.1 radians in θ and 0.02 GeV in $|\vec{p}|$. The error shown is the statistical one, caused by limited statistics in data. Above 0.1 GeV and between 0.5 and 2.5 radians the matrix is stable. At the edges of the MDC and

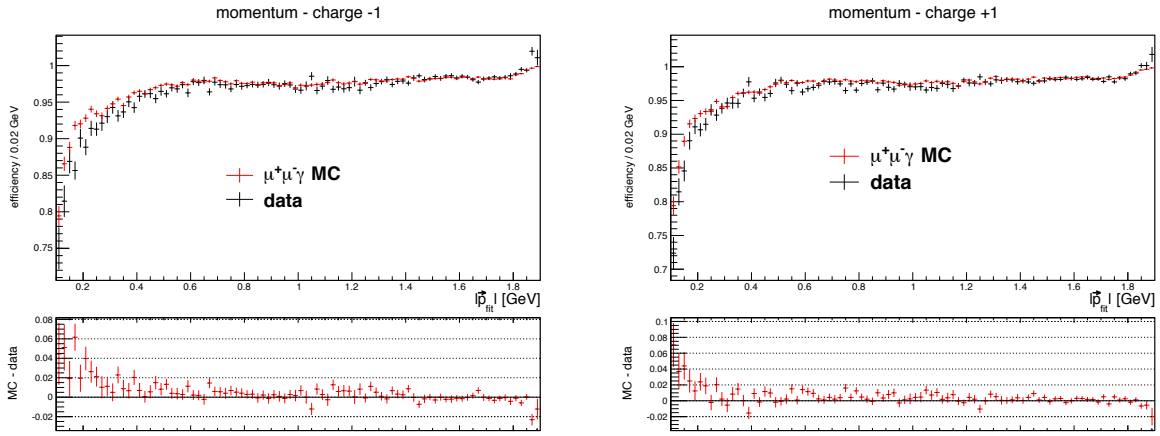

Figure 7.12: Efficiency for positive and negative charged tracks. No significant difference can be observed.

for low momenta the scaling factors are significantly different from 1.

The corrected MC distributions, compared to data, can be found in Fig. 7.13. Shown are the predicted $|\vec{p}|$ and θ variables. In comparison to the not corrected distributions (Fig. 7.10 and 7.11) the MC fits now much better to data.

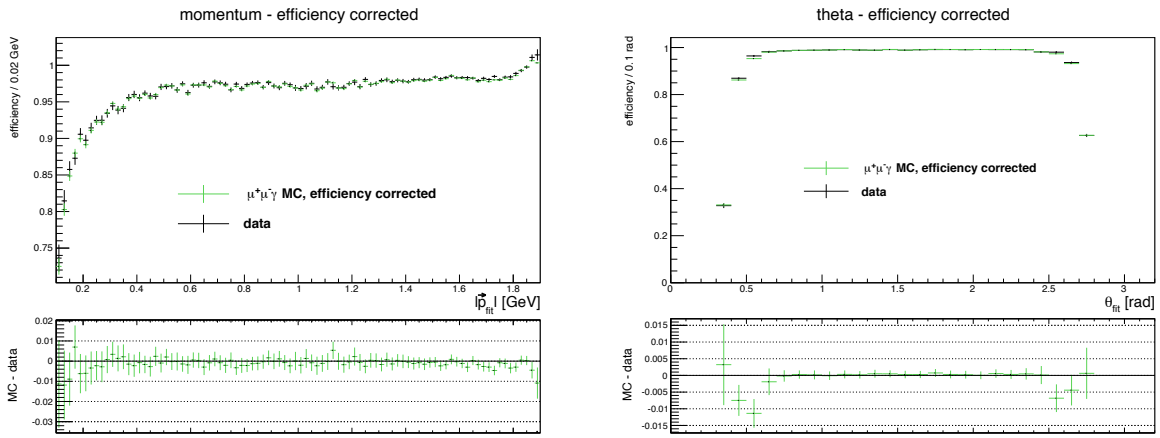

Figure 7.13: Momentum and angular distributions after efficiency corrections. The MC is corrected to the real data. The distributions look more similar now than before the correction which is shown in Fig. 7.10 and 7.11.

7.2.4 Estimation of the systematic uncertainties

The estimation of the systematic uncertainties is similar to the one of the photon detection efficiency study. Also here, three different sources of systematic errors are considered: A

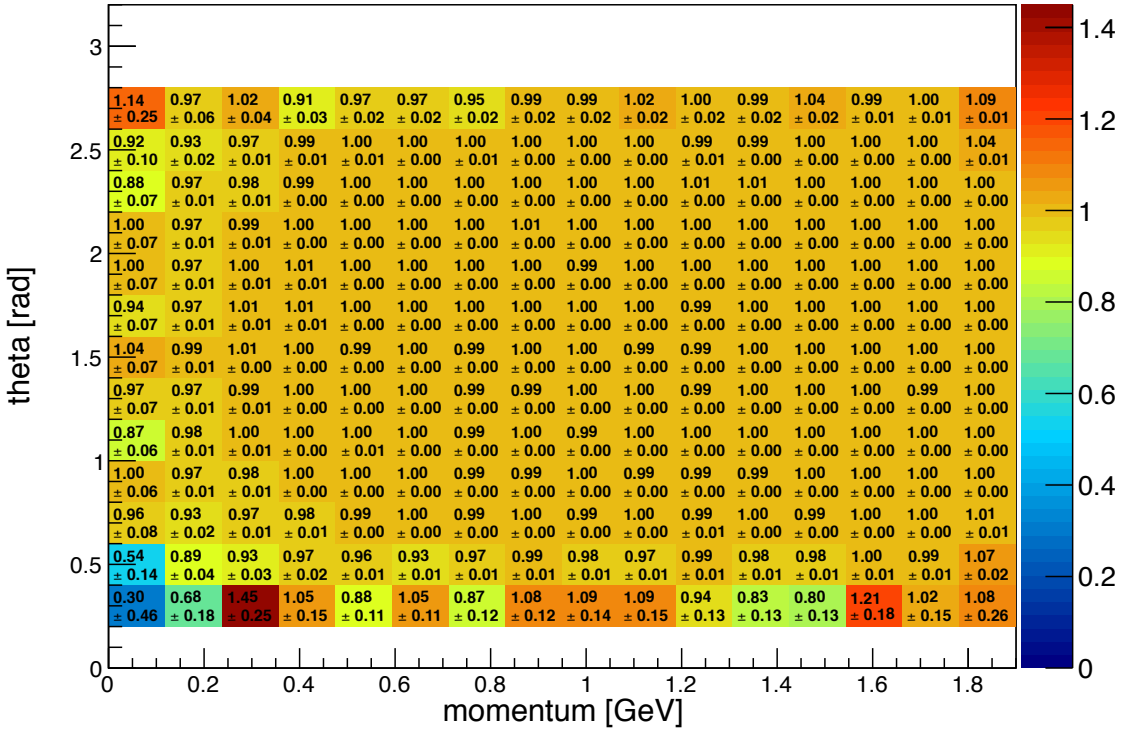

Figure 7.14: Tracking efficiency scaling matrix. The MC is corrected to real data by using the momentum and theta information. Shown is the scaling factor and the statistical error.

systematic shift due to the event selection, the accuracy of the correction, and the background uncertainty.

(1) The systematics due to the choice of the selection requirements are studied in the same way as described in the photon detection efficiency study in section 6.6, yielding the "loose" and "tight" event selections, as listed in Tab. 7.4.

	standard cut	**tight cut**	**loose cut**
χ^2_{1C}	< 10	< 5.5	< 14.5
E/p	< 0.60	< 0.51	< 0.69
depth [cm]	> 35.0	> 38.0	> 32.0
$\|\vec{p}\|$ [GeV]	< 1.80	< 1.77	< 1.83

Table 7.4: Cut values of the standard event selection used in the tracking efficiency study and the defined loose and tight selections. The variation ranges are three times the estimated resolution of the specific cut values.

The relative differences of applying the standard tracking efficiency corrections on the $\mu^+\mu^-\gamma$ MC sample and applying the ones, gained with the "loose" or "tight" event selection, are shown in Fig. 7.15. One can see the results for the ρ peak region between 0.6 and 0.9 GeV, as

well as for the whole invariant mass range between 0.3 and 3.3 GeV. A linear fit is performed to estimate the difference and the largest value is claimed as systematic uncertainty. The numbers can be found in Fig. 7.15. It is compatible with zero in the ρ peak region. However, a systematic uncertainty of 0.2% is claimed for the whole mass range.

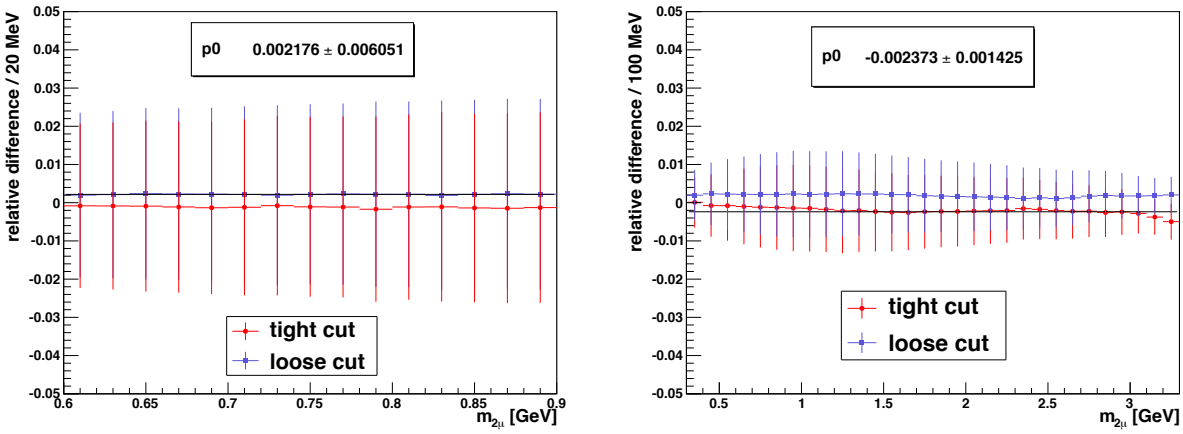

(a) ρ peak regin (b) whole spectrum

Figure 7.15: Relative difference of events between the standard event selection and the cut values varied as mentioned in Tab. 7.4. The largest difference is taken as systematic uncertainty. Shown is the case in the ρ peak region and for the whole spectrum. Also shown is the result of the linear fit of the largest difference.

(2) As in the photon efficiency study in section 6.6, the difference between data and MC, after applying the corrections for muon tracking, is negligible small. No uncertainty is claimed in this case.

(3) The uncertainty of the background contamination is also estimated as in the photon efficiency study in section 6.6. The $e^+e^-(n\gamma)$, $\pi^+\pi^-\gamma$, $\pi^+\pi^-\pi^0\gamma$ MC samples are subtracted from data. For $e^+e^-(n\gamma)$ MC events, again, an uncertainty of 3% is claimed, considering the scaling to the data luminosity and possible, not corrected data-MC differences. The same is claimed for $\pi^+\pi^-\gamma$ MC events. Data-MC differences due to tracking and photon detection are small in case of these events. In addition, the PHOKHARA event generator has an accuracy better than 0.5%. For the $\pi^+\pi^-\pi^0\gamma$ MC sample a conservative error of 5% is chosen. All other background MC samples are not subtracted. Their fraction with respect to data is used as uncertainty. This yields to Fig. 7.16, which shows the uncertainty due to background subtraction and contamination in bins of the predicted momentum. Momenta below 0.3 GeV are not used in the $\pi^+\pi^-\gamma$ analysis and can be neglected. This uncertainty is below 0.2%, instead for momenta greater than 1.8 GeV, where it rises up to 0.45%. Hence, when applying the muon tracking corrections on $\mu^+\mu^-\gamma$ events, one has to weight the systematic uncertainty

with the momentum distribution.

When doing so, invariant masses below 1.5 GeV have a total systematic uncertainty $< 0.3\%$, when taking all described sources from this section into account and summing them up in quadrature. For higher masses, one has to claim an uncertainty of 0.45%, obtained by taking the momentum distribution of the muon tracks into account.

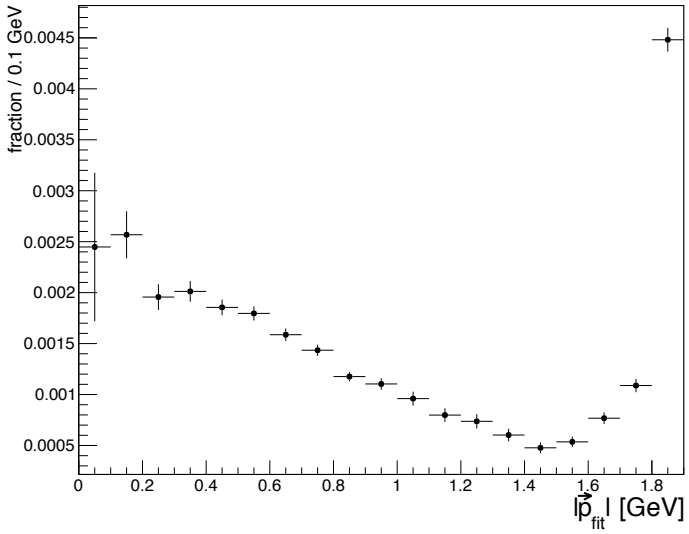

Figure 7.16: The total estimated background uncertainty for the muon tracking efficiency study.

Chapter 8

PID efficiency studies

For the selection of pion tracks and background suppression, two different particle identification methods are used. The trained artificial neural network to separate muons from pions and the electron PID provided by the BOSS framework to reject the large $e^+e^-(n\gamma)$ background. The usage of both methods leads to efficiency differences between data and MC, which have to be corrected. Especially the differences due to the neural network method applied are large and a precise study is needed.

8.1 PID efficiency studies for pion tracks

8.1.1 Selection of untagged $\pi^+\pi^-\pi^+\pi^-\gamma$ events

The PID efficiency studies for pion tracks is performed with $e^+e^- \to \pi^+\pi^-\pi^+\pi^-\gamma$, as in the pion tracking efficiency study. However, in this case it is possible to use untagged ISR events, since a pion track has to have a signature in the detector, in order to study its ANN and e-PID likelihoods. This enhances the statistics compared to the tracking efficiency study, which allows to develop correction matrices.

Exactly four charged tracks in the MDC are required. The points of closest approaches from the interaction point (IP) for these four tracks have to be within a cylinder with $V_r = 1.0$ cm radius in the transversal direction and $|V_z| = 10$ cm of length along the beam axis. To reject kaons and protons in the final state, the BESIII PID system is used (see section 2.5), exploiting information from MDC, TOF, and EMC. The calculated particle probability of a charged track being a pion, $p(\pi)$ has to be greater than being a kaon $p(K)$ or proton $p(P)$. There might be a correlation between PID probability and the variables used in the ANN or e-PID, respectively. To avoid this, the track, which is used to determine the efficiency, does not need to fulfill these requirements on the probability. This is only applied on the three other tracks. After that a 1C kinematic fit with the four charged tracks and a missing photon is performed. The corresponding χ^2_{1C} distribution is shown in Fig. 8.1 for data and MC. The requirement $\chi^2_{1C} \leq 10$ is applied. The selection criteria are summarized in Tab. 8.1.

cut variable	**cut value**
MDC valid tracks	4
$\|V_z\|$	< 10.0cm
V_r	< 1.0cm
p(π)	$>$ p(K) and $>$ p(P)
acceptance	$21.6° < \theta < 158.4°$
# charged tracks	4
total charge tracks	0
χ^2_{1C}	≤ 10

Table 8.1: Summary of the event selection to select $\pi^+\pi^-\pi^+\pi^-\gamma$ events for the PID efficiency studies.

8.1.2 Background rejection

Table 8.2 lists the main contributing backgrounds for the $4\pi\gamma$ channel, studied with MC. All other background MC samples are found to be negligible.

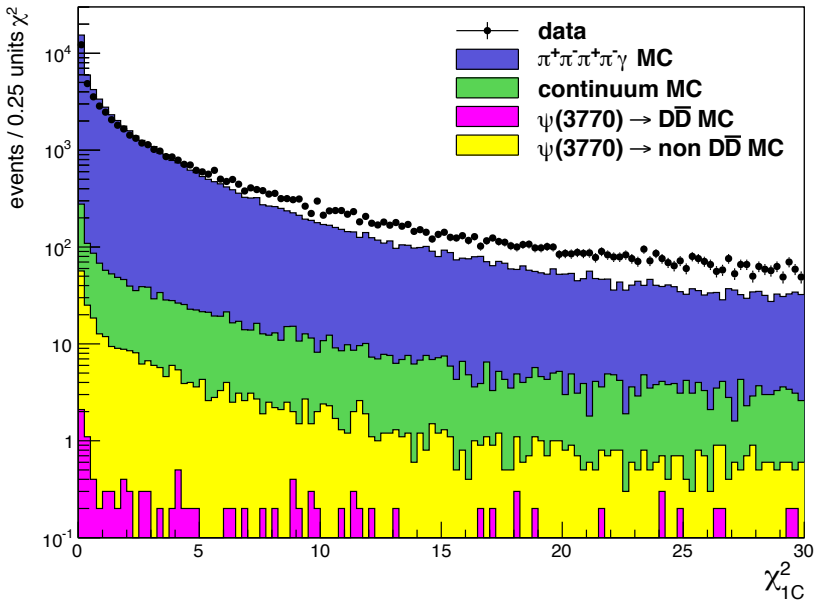

Figure 8.1: χ^2_{1C} distribution of the 1C kinematic fit to select $\pi^+\pi^-\pi^+\pi^-\gamma$ events. Shown is data, signal MC, and the main background MC samples.

background contributions	rejection
$\psi(3770) \to J/\psi\ \pi^+\pi^- \to \mu^+\mu^-\pi^+\pi^-$	$E_\gamma > 0.2$
$K^+K^-\pi^+\pi^-\gamma$	kaon PID
$K^0_s K^\pm\pi^\mp \to \pi^+\pi^- K^\pm\pi^\mp$	kaon PID
$\pi^+\pi^-\pi^+\pi^-\pi^0\gamma$	not neccessary
$\pi^+\pi^-\pi^+\pi^-\pi^0\pi^0\gamma$	not neccessary
$\pi^+\pi^-\pi^+\pi^-\pi^+\pi^-\gamma$	not neccessary

Table 8.2: Summary of main contributing background channels in $e^+e^- \to \pi^+\pi^-\pi^+\pi^-\gamma$ event selection. and how they are rejected. If there are only pions in the final state a rejection is not necessary, since the goal is to find a clean sample of charged pions. Additional neutral or charged pions do not play a role.

The most critical background is $\psi(3770) \to J/\psi\ \pi^+\pi^- \to \mu^+\mu^-\pi^+\pi^-$, since there are two muons in the final state. The two muons originate from a J/ψ decay. Hence, their invariant mass is the J/ψ mass of 3.096 GeV [4]. Figure 8.2 shows the $\pi^+\pi^-$ invariant mass in data and in signal MC. All combinations of the four pion candidates are considered, hence four entries per event. The J/ψ peak is clearly visible in data. It is missing in MC, as expected. To reject the muons in the final state, one can use a requirement on the ISR photon energy E_γ, which is predicted by the 1C fit. Thus, the J/ψ resonance can not be produced. By requiring $E_\gamma > 0.2$ GeV the J/ψ peak vanishes, as visible in the right panel of Fig. 8.2.

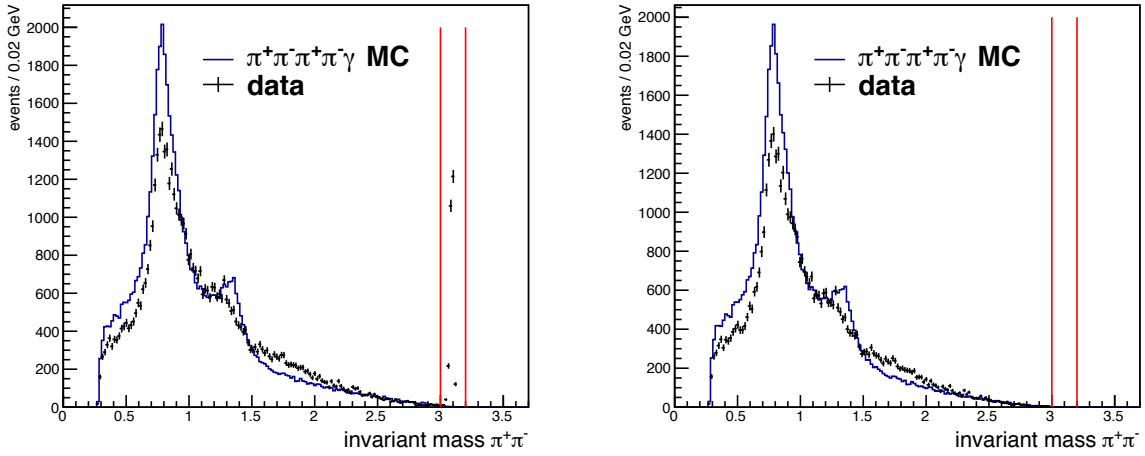

(a) without cut on E_γ

(b) $E_\gamma > 0.2$ GeV

Figure 8.2: Invariant mass of a positively and negatively charged pion candidate. In the left figure, the J/ψ peak is visible in data. This is a result of the decay $J/\psi \to \mu^+\mu^-$. On the right hand side, a requirement on the photon energy of $E_\gamma > 0.2$ GeV is applied. The peak vanishes. The MC distribution is scaled arbtitrary.

Further contamination comes from $K_s^0 K^\pm \pi^\mp \to \pi^+\pi^- K^\pm \pi^\mp$ events. There is a kaon in the final state and, thus, these events should be rejected by the requirement on the probability, $p(\pi) > p(K)$. To proof this, also here the invariant mass of a pion pair with net charge zero is considered. The $K_s^0 \to \pi^+\pi^-$ decay causes a peaking structure around the K_s^0 mass of 497.6 MeV [4]. Figure 8.3 shows this invariant mass spectrum in this mass region. No significant peak is visible in data. Hence, this background is suppressed efficiently. The fact that a final state with only one kaon is rejected efficiently, shows, that the requirement on the kaon probability works well. The background channel $K^+K^-\pi^+\pi^-\gamma$ has two kaons in the final state. Thus it is also rejected efficiently.

The ISR background channels with only pions in the final state, like $e^+e^- \to \pi^+\pi^-\pi^+\pi^-\pi^0\gamma$, $e^+e^- \to \pi^+\pi^-\pi^+\pi^-\pi^0\pi^0\gamma$, or $e^+e^- \to \pi^+\pi^-\pi^+\pi^-\pi^+\pi^-\gamma$ do not need to be rejected. All charged tracks found are pions and, thus, their PID efficiency can be studied. The kinematics might be different from the $\pi^+\pi^-\pi^+\pi^-\gamma$ MC sample selected, however, this is not a problem, since only ratios are studied. Table 8.3 displays the remaining number of events from the continuum and $\psi(3770) \to$ everything MC samples. All charged particles of the remaining events are pions which means they can be treated as signal. A clean pion sample is found in data, with nearly 50,000 events. Due to the fact, that there are four charged pions in the final state, four entries per event can be investigated. Hence, the ANN and e-PID efficiency can be studied with a sample of 200,000 charged pion tracks.

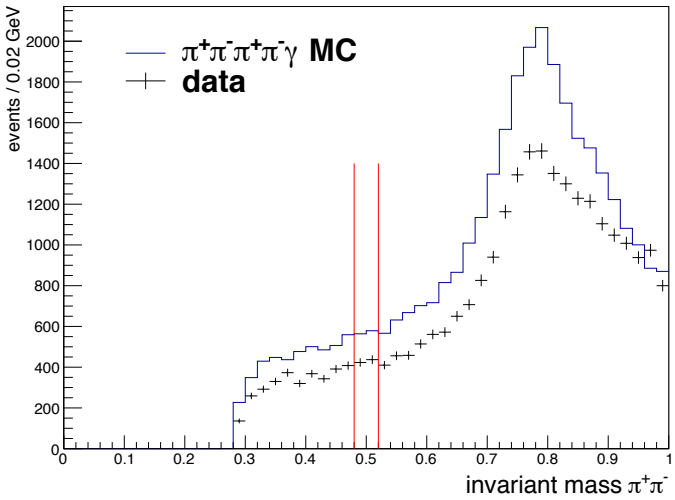

Figure 8.3: Invariant mass of a a positive and a negative charged pion candidate. The two red lines show the K_s^0 mass region around 497.6 MeV. No peak is visible in data. The MC is scaled arbitrary.

	continuum	$\psi(3770) \to D\overline{D}$	$\psi(3770) \to$ non $D\overline{D}$
background events in MC	978 ± 31	9 ± 3	231 ± 15
events with 4π in final state	961 ± 31	9 ± 3	231 ± 15
difference	17 ± 44	0 ± 4	0 ± 21

Table 8.3: The estimation of left background events from the continuum and $\psi(3770) \to$ everything MC samples. Mostly all of the remaining events have only charged particles, which are pions, in the final state. Hence, they can be treated as signal.

8.1.3 ANN efficiency differences and corrections for pion tracks

With the pion sample selected, the efficiency differences between MC and data can be studied by using the ANN. Figure 8.4 shows the calculated likelihood of the ANN for data and MC pions. Huge differences are observed. One of the main reasons for this are the deviations for hadronic showers in descriptions of the MUC and EMC. These differences have to be studied and corrected in MC.

The data-MC efficiency differences are studied for two different requirements on y_{ANN}. On the one hand, $y_{ANN} > 0.6$, which is applied to select charged pion tracks in the $\pi^+\pi^-$ cross section measurement. On the other hand, $y_{ANN} < 0.4$, which is used to select μ^+ and μ^- tracks in sections 9.2 and 9.3. The ANN efficiency is defined as

$$\epsilon^{\pi}_{ANN} = \frac{\text{events}(\text{y}_{\text{ANN}} > 0.6)}{\text{all events}} \text{, or} \tag{8.1}$$

$$\epsilon^{\mu}_{ANN} = \frac{\text{events}(\text{y}_{\text{ANN}} < 0.4)}{\text{all events}} \text{.} \tag{8.2}$$

The absolute efficiencies for data and MC as functions of $|\vec{p}|$, θ, and ϕ are shown in Fig. 8.5, 8.6, and 8.7 for the two requirements on y_{ANN}. With these information, the scaling factors, which are applied on MC, are developed, as defined in formula (7.3). Again, a track based correction in bins of $\vec{p}$ and θ are calculated. Their systematic uncertainty is estimated in section 8.1.5.

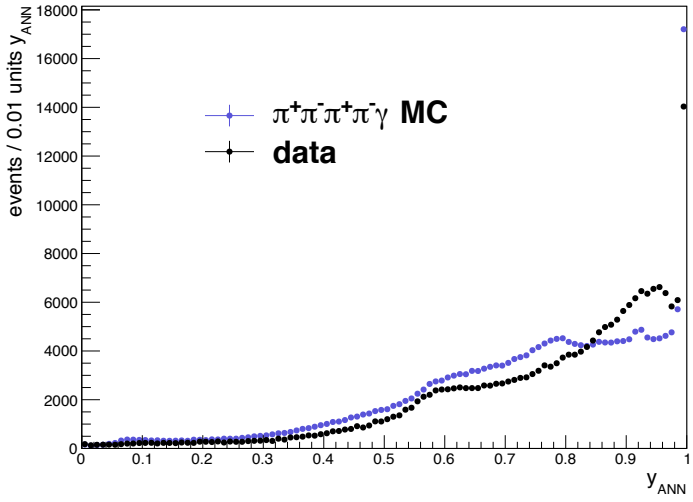

Figure 8.4: Output y_{ANN} of the artificial neural network for MC and data.

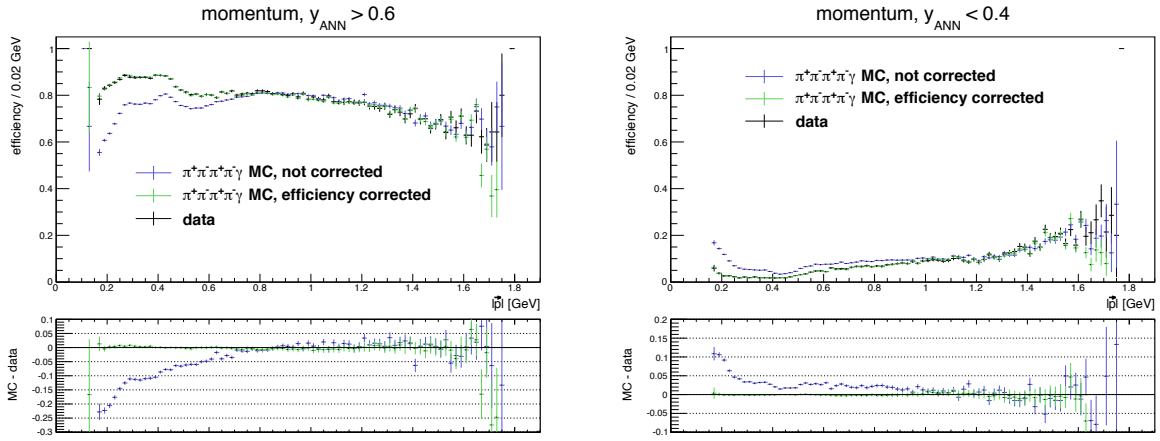

Figure 8.5: Efficiency differences between data and MC by using the artificial neural network cut. Shown is the case for using the ANN as muon selector (right) and for using it as pion selector (left).

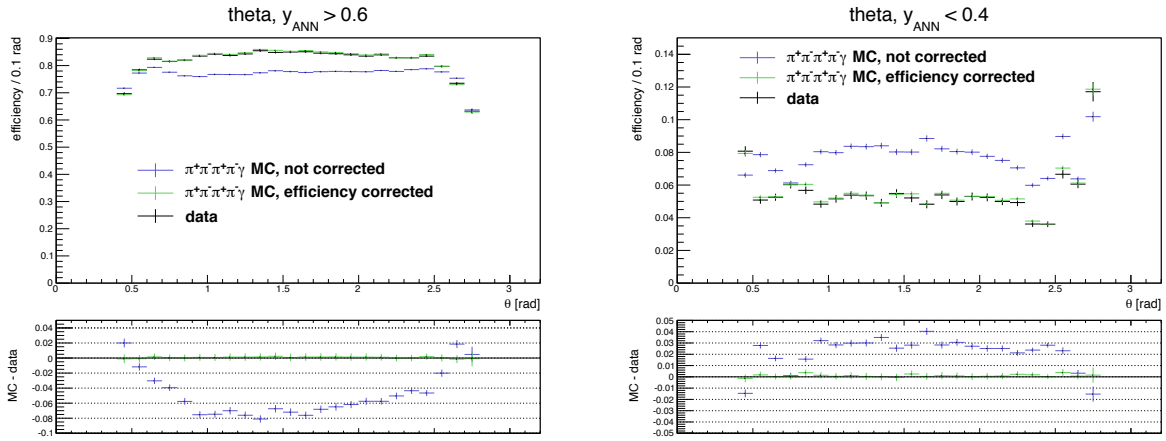

Figure 8.6: Efficiency differences between data and MC by using the artificial neural network cut. Shown is the case for using the ANN as muon selector (right) and for using it as pion selector (left).

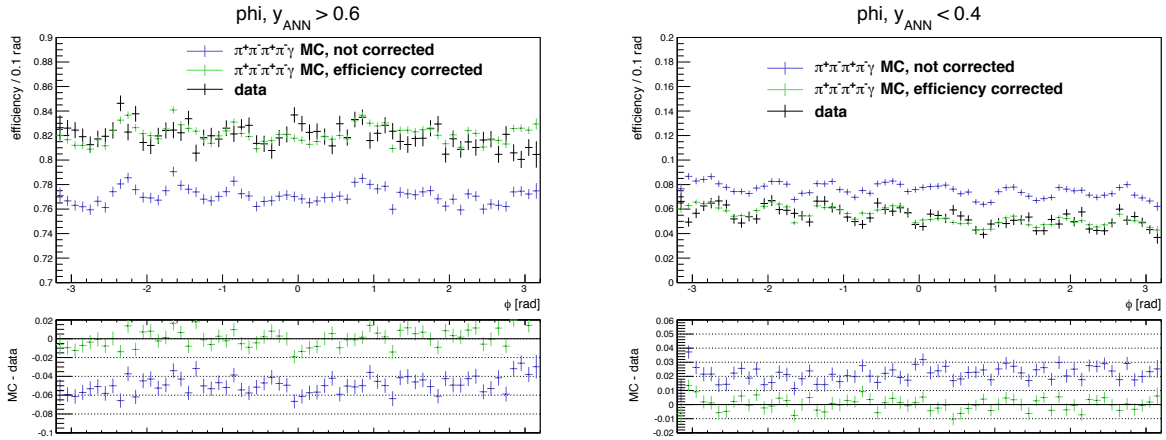

Figure 8.7: Efficiency differences between data and MC by using the artificial neural network cut. Shown is the case for using the ANN as muon selector (right) and for using it as pion selector (left).

8.1.4 e-PID efficiency studies for pion tracks

The efficiency by using the requirement on the e-PID, $DLL(\pi,e) > 2$, is defined as

$$\epsilon_{\mathrm{e-PID}} = \frac{\mathrm{events(DLL(\pi,e) > 2)}}{\mathrm{all\,events}} \,. \tag{8.3}$$

The absolute efficiency for data and MC can be seen in Fig. 8.8, as function of $\vec{p}$, θ, and ϕ. also shown are the data-MC difference, which are very small in this variable. However, also here a correction on a track basis, in bins of $\vec{p}$, θ, is determined according to formula (7.3). Fig. 8.8 shows also the MC sample after applying these corrections. It agrees to data much better in this case. The systematic uncertainties of this correction is estimated in the next chapter.

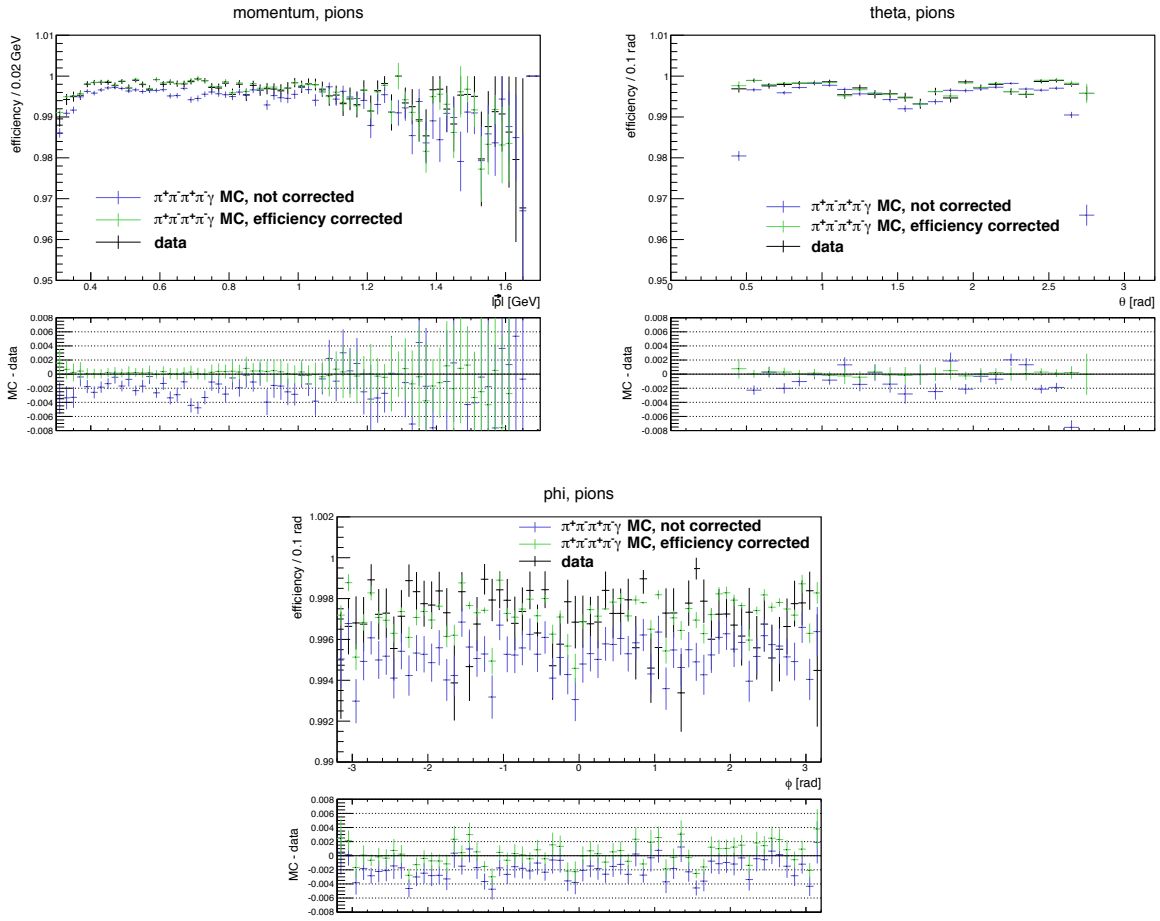

Figure 8.8: Efficiency differences between data and MC after using the e-PID requirement. Also shown is the corrected MC distribution in green.

8.1.5 Systematic uncertainties

The systematic uncertainty of the ANN and the e-PID efficiency corrections can be estimated at once, since they are using the same event sample. It has to be investigated whether there is an uncertainty due to the event selection applied or due to background contamination.

As shown in section 8.1.1 the remaining background contains as charged tracks only pions. The pion sample used is, thus, nearly background free, and no systematic uncertainty is considered in this case.

The only systematic shifts are caused by the event selection applied. Two requirements are applied, which differ from the event selection in the $\pi^+\pi^-\gamma$ analysis. The criteria $\chi^2_{1C} < 10$, $p(\pi) > p(K)$ and $p(\pi) > p(K)$. In the case of χ^2_{1C} the systematic uncertainty is estimated as

in section 6.6. As described there, a "tight" and a "loose" selection is defined as mentioned, see Tab. 8.4. The result of the different event selections in bins of $m_{2\pi}$ is displayed in Fig. 8.9 (a). Shown is the difference between the standard selection and the "loose" and "tight" one. The difference is much below 0.1% over the whole mass spectrum, and, hence, the systematic uncertainty of the χ^2_{1C} requirement is negligible.

	standard cut	**tight cut**	**loose cut**
χ^2_{1C}	< 10	< 5.5	< 14.5

Table 8.4: Requirements on χ^2_{1C} of the standard event selection used in the e-PID efficiency study for pions, and the "loose" and "tight" values found, as described in section 6.6.

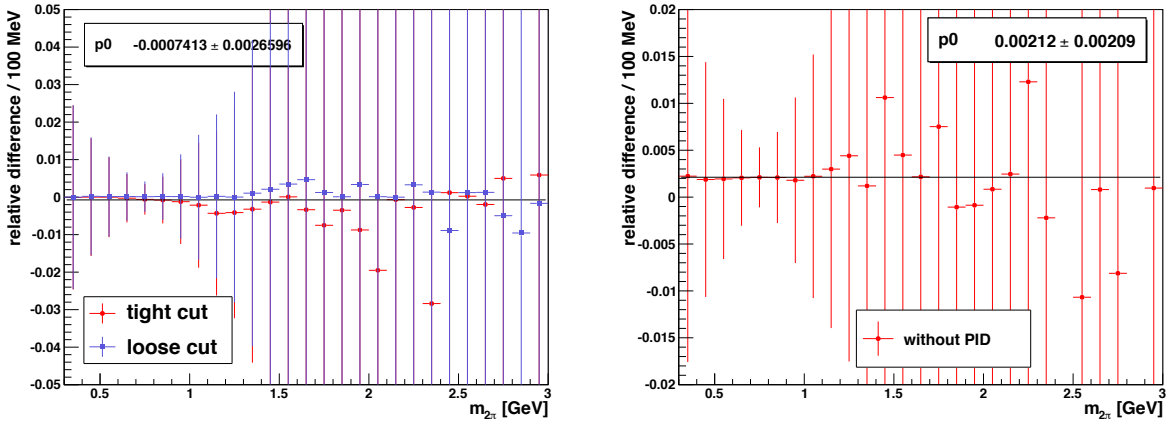

(a) Variation of χ^2_{1C}

(b) without requirement on $p(k)$ and $p(P)$

Figure 8.9: Sytsematic uncertainties due to the requirement on χ^2_{1C} (a) and on the kaon and proton PID used (b). Shown is the difference between the standard selection and the "loose" and "tight" one. To estimate the uncertainty, the shift is calculated via a linear fit.

The kaon- and proton-PID used could be correlated to the e-PID. For example, the same shower shape variables could be used. To check, whether this is the case, the efficiency correction factors are also determined with a data and MC sample, where the requirements $p(\pi) > p(K)$ and $p(\pi) > p(K)$ are not applied. Figure 8.9 (b) shows the difference between applying the correction factors from section 8.1.4 and these new ones, applied on a $\pi^+\pi^-\gamma$ MC sample. The systematic is estimated with a linear fit. The deviation is in the order of 0.2%. However, doing the efficiency study without the kaon-PID is very rigid, since the kaon background is not taken into account in the MC. The difference found overestimates the systematic uncertainty.

However, a conservative systematic uncertainty of 0.2% is estimated, as well for the ANN efficiency correction, as for the e-PID efficiency correction, in order to cover all described sources.

8.2 PID efficiency studies for muons

8.2.1 Event selection

As control sample to study PID efficiency differences for muon tracks, the same $\mu^+\mu^-\gamma$ sample is used as in the study of the muon tracking efficiency. The only difference is, that the predicted muon track has to be measured in the MDC, in order to calculate its y_{ANN} and $DLL(\pi,e)$ value. Since there are no further conditions on this clear muon track, it is perfectly suitable to determine the efficiency differences between data and MC by using the ANN and the e-PID.

8.2.2 Background subtraction

The background contamination from electrons is not as high as for the tracking efficiency study, since the second charged track is measured in the detector. Hence, no cut on the momentum is performed, to enhance statistics. The $e^+e^-(n\gamma)$ background is simply subtracted in data.

The largest and most dangerous background is the $\pi^+\pi^-\gamma$ final state, which has been treated as signal in the muon tracking efficiency study. The ANN was developed to distinguish between muon and pion tracks. Hence, pion tracks will fake the results for the muon efficiency study. The fraction of this background is up to 5%, as displayed in Fig. 8.10. However, it can not be suppressed by kinematic cuts. Therefore, it is subtracted in data. The fact that the MC prediction from PHOKHARA has a very high accuracy will still lead to a quite low systematic uncertainty.

As in the muon tracking efficiency study, the two other notable backgrounds are $\pi^+\pi^-\pi^0\gamma$ and $\psi(3770) \rightarrow everything$. The first one has a fraction of 1 - 2 per mille and is subtracted in data. The second one is below everywhere smaller than 0.1% and only taken into account as systematic uncertainty.

8.2.3 ANN efficiency differences and corrections for muon tracks

The output of the ANN, y_{ANN}, for muons is presented in Fig. 8.11 for data and MC. Large differences between data and MC can be observed, especially for high and low y_{ANN} values.These differences have to be corrected to enhance the accuracy of the MC prediction after using the requirement on y_{ANN}.

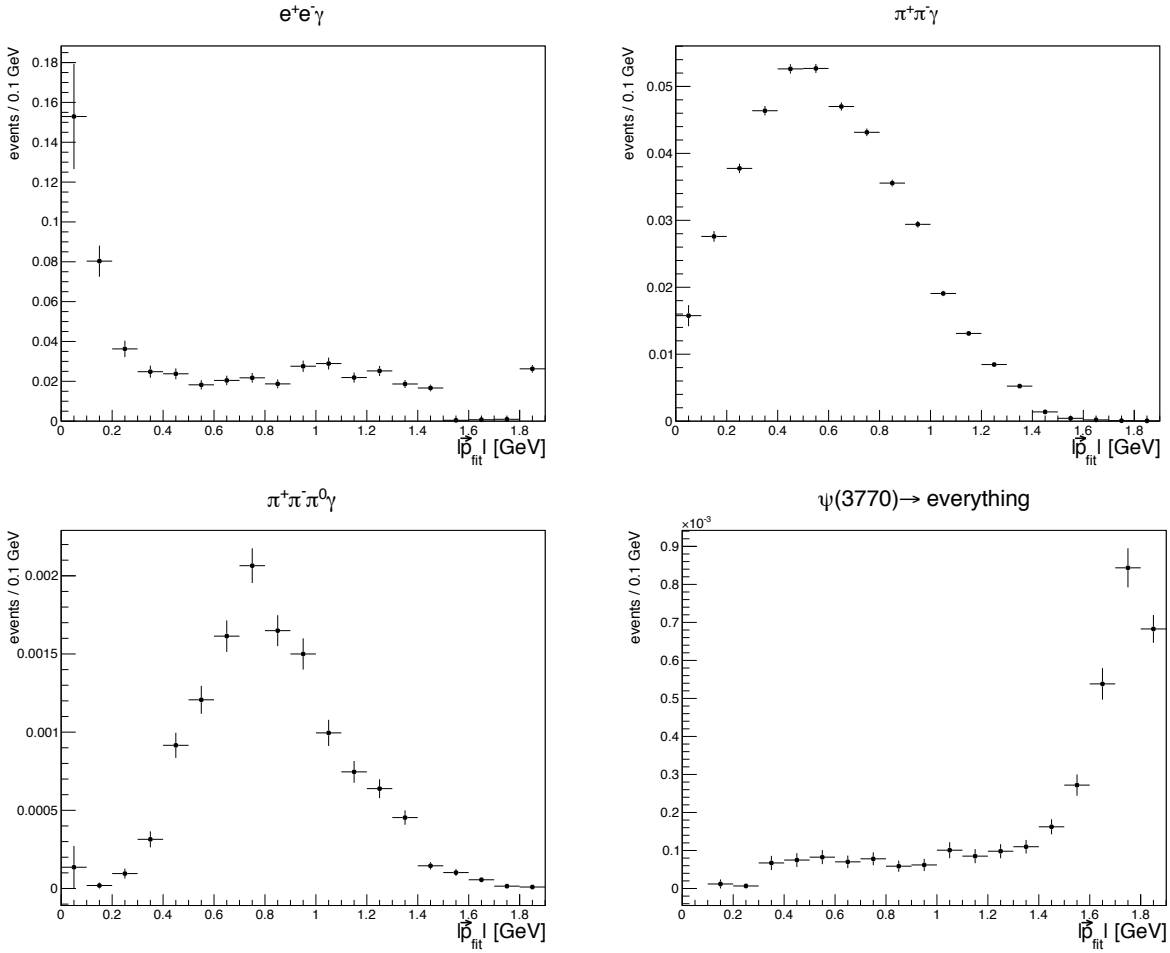

Figure 8.10: Background fractions of the most contributing final states for the muon PID efficiency study.

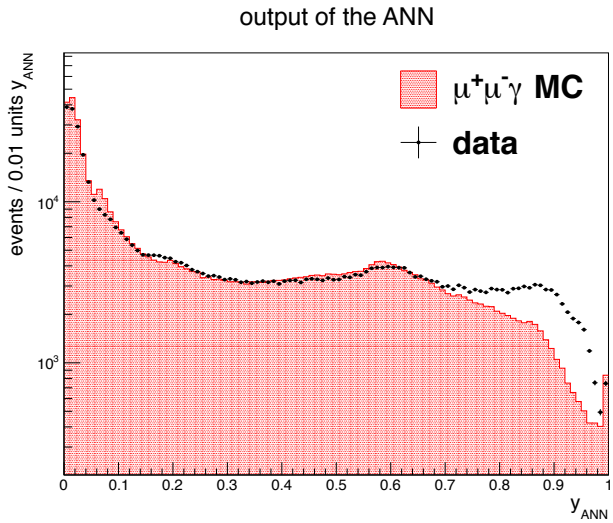

Figure 8.11: Output of the ANN, y_{ANN}, for data and MC.

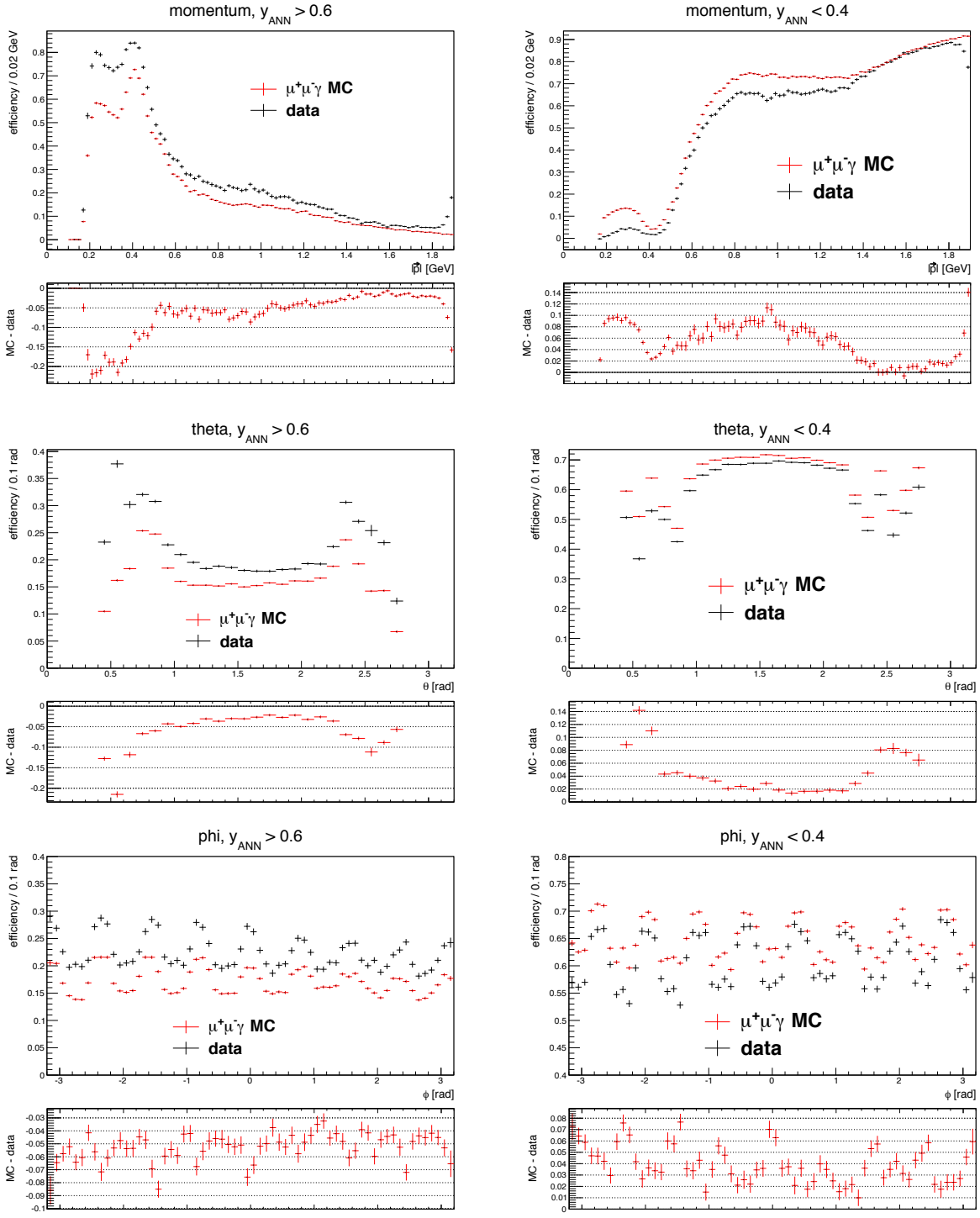

Figure 8.12: Efficiency differences between data and MC by using the artificial neural network cut. Shown is the case for using the ANN as pion selector (left) and for using it as muon selector (right).

The data-MC efficiency differences are studied for two different requirements on y_{ANN}. On the one hand, $y_{ANN} > 0.6$, which is applied to select charged pion tracks in the $\pi^+\pi^-$ cross

section measurement. On the other hand, $y_{ANN} < 0.4$, which is used to select μ^+ and μ^- tracks in sections 9.2 and 9.3.

The absolute efficiencies for data and MC, as well as their differences, are shown in Fig. 8.12, as functions of $\vec{p}$, θ, and ϕ. In case of $y_{ANN} > 0.6$, the efficiency in data is greater for lower momenta. The reason is, that low momenta muon tracks are more often wrongly identified as pions, since they have a smaller range in the MUC. For $y_{ANN} < 0.4$, the situation turns around, as expected. The structures in ϕ dimension are caused by the structure of the MUC. The RPC's are arranged in an octagon. The efficiency drops at their connections, where the sensitivity is systematically lower.

The efficiencies are defined as in formula (8.2). The correction factors are calculated according to formula (7.3), also here in bins of $\vec{p}$ and θ. Their systematic uncertainty is estimated in section 8.2.5.

8.2.4 e-PID efficiency studies for muon tracks

The efficiency in case of the requirement on the e-PID, $DLL(\pi,e) > 0$, is defined as in formula (8.3). The absolute efficiencies for data and MC, as well as their differences, are shown in Fig. 8.13, as functions of $\vec{p}$, θ, and ϕ. As in the pion case, the differences are small. However, corrections are calculated for the MC sample according to formula (7.3), also here in bins of $\vec{p}$ and θ. Their systematic uncertainty is estimated in section 8.2.5.

8.2.5 Systematic uncertainties

The systematic uncertainty by using the ANN and the e-PID efficiency correction on muon tracks, is absolutely the same, since the same event samples are used. As sources for systematic shifts, background contamination and events selection are studied, which is very similar to section 7.2.4.

(1) The systematics due to the choice of the selection requirements can be adopted from section 7.2.4, since the event selection is the same. There, an uncertainty of 0.2% is found.

(2) As explained in section 8.2.2 the background contamination differs towards section 7.2.4. In addition, pion and electron background might affect the study of ANN and e-PID significantly. To cover this, the uncertainties assumed on the MC samples are conservatively tripled, compared to section 7.2.4 are assumed on the background MC samples. 9% in the cases of $\pi^+\pi^-\gamma$

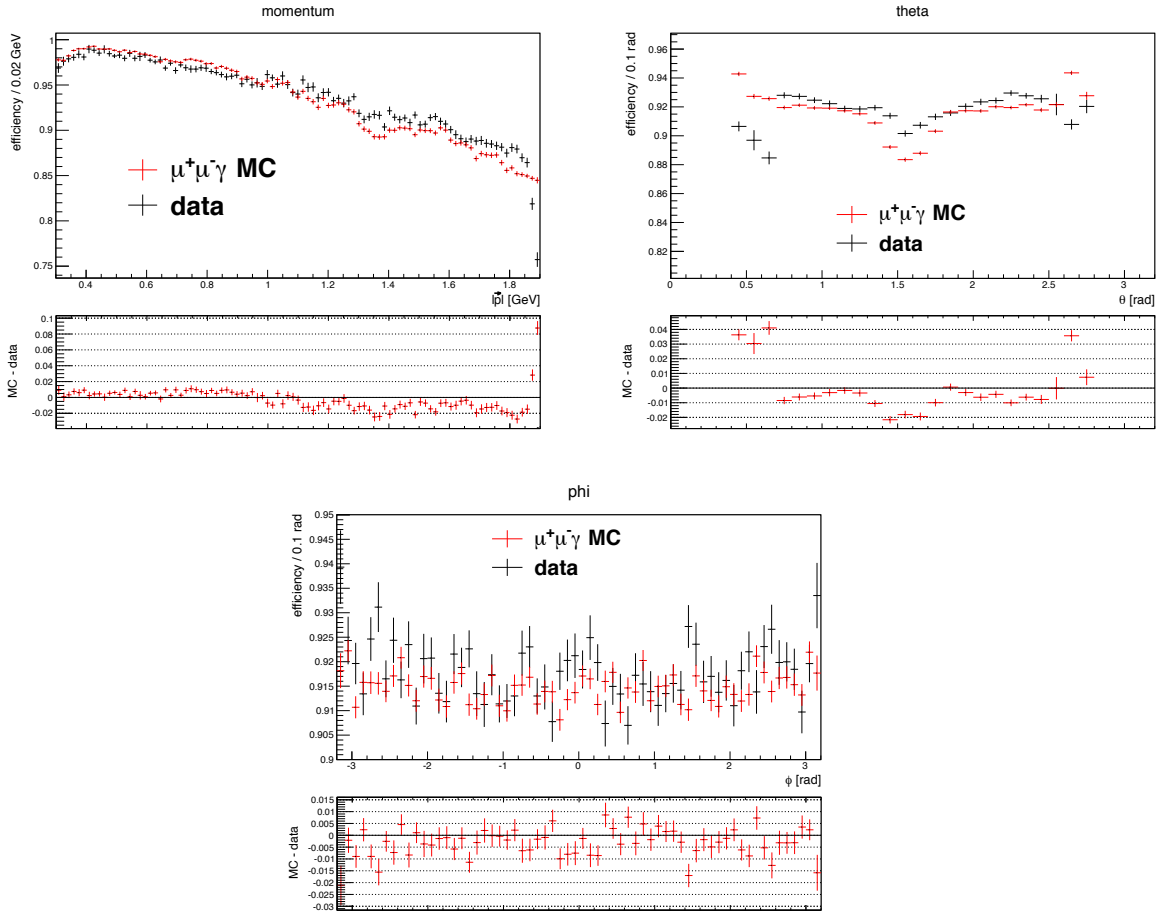

Figure 8.13: Efficiency differences between data and MC for muons after using the electron PID.

and $e^+e^-(n\gamma)$, and 15% on $\pi^+\pi^-\pi^0\gamma$. The background fractions are shown in Fig. 8.10. As in section 7.2.4, they are combined with the corresponding uncertainty assumed on the several channels, to account for the uncertainty when subtracting them from data. The $\psi(3770) \rightarrow$ everything MC sample is not subtracted from data, as explained. Its fraction is treated as uncertainty directly. Considering all this, one finds a systematic uncertainty of 0.45% due to background subtraction.

Thus, the total systematic uncertainty of the ANN and e-PID corrections is 0.5%, when adding the above 0.2% and 0.45% in quadrature.

Chapter 9

Systematic studies and cross checks

Systematic shifts can occur due to efficiency differences between data and MC by applying a selection requirement. They shift the result in a specific direction, which is not the case for statistical errors. One possibility to estimate the scale of these uncertainties is to vary the requirements and to analyze the differences with respect to the standard requirements. Another approach is, to use completely different methods, like it is done to obtain the systematics of the artificial neural network under use in the upcoming chapter.

Further, two more cross checks of the efficiency corrections used, which are obtained in the previous chapters, are performed. On the one hand, the integrated luminosity of the data set is obtained using $\mu^+\mu^-\gamma$ events. On the other hand, an absolute comparison between data and efficiency corrected $\mu^+\mu^-\gamma$ MC is made.

9.1 Uncertainties of the efficiency corrections

The efficiency corrections, studied in the previous chapters, are applied on a track basis. Every event is weighted with a total scaling factor $C_{tot}(|\vec{p}|,E_\gamma,\theta)$, which depends on the momentum $|\vec{p}|$ of the charged tracks, the energy E_γ of the ISR photon, and the θ angle of the charged tracks and the ISR photon. The assumption is made that the charged tracks and the photon are not correlated. On this account, $C_{tot}(|\vec{p}|,E_\gamma,\theta)$ is the product of several efficiency correction factors, i.e. tracking, e-PID, ANN and photon efficiency corrections:

$$C_{tot}(|\vec{p}|,E_\gamma,\theta) = C_{photon}^{detection} \cdot C_{track1}^{tracking} \cdot C_{track2}^{tracking} \cdot C_{track1}^{ANN} \cdot C_{track2}^{ANN} \cdot C_{track1}^{e-PID} \cdot C_{track2}^{e-PID} \; . \quad (9.1)$$

The statistical error of $C_{tot}(|\vec{p}|,E_\gamma.\,\theta)$ is calculated via the Gaussian error propagation, since the individual contributions are assumed to be statistically independent:

$$\Delta C_{tot} = \sqrt{\sum_i \left(\frac{\partial C_{tot}}{\partial C_i} \Delta C_i \right)^2} \; . \quad (9.2)$$

ΔC_i is the statistical error of each correction factor. For each bin of the invariant mass spectrum, the weighted events are summed. The events are statistically independent and, hence, the statistical errors of each event are added in quadrature. The total statistical error of one mass bin ΔN, is the counting error $\sqrt{N}$ added in quadrature with the quadratic sum of the statistical uncertainties of the global correction factors of the contributing events:

$$\Delta N = \sqrt{\left(\sqrt{N}\right)^2 + \sum_{j=1}^{N} (\Delta C_{tot,j})^2} \; , \quad (9.3)$$

where N is the weighted number of events. The systematic errors due to the usage of these corrections have already been estimated in bins of $m_{2\pi}$ in the previous chapters. Table 9.1 lists all the uncertainties and where they can be found.

correction	uncertainty	see section
photon efficiency	0.2%	6.6
pion tracking efficiency	0.3%	7.1.3
muon tracking efficiency	0.3%	7.2.4
ANN efficiency for pion tracks	0.2%	8.1.5
e-PID efficiency for pion tracks	0.2%	8.1.5
ANN efficiency for muon tracks	0.5%	8.2.5
e-PID efficiency for muon tracks	0.5%	8.2.5

Table 9.1: Summary of systematic uncertainties of the efficiency corrections in bins of $m_{2\pi}$.

9.2 Cross check: QED test using $\mu^+\mu^-\gamma$ events

The yield of events in data of the channel $e^+e^- \to \mu^+\mu^-\gamma$ as a function of the two-muon invariant mass $m_{2\mu}$ can be compared to a precise MC prediction by QED, which is provided by the PHOKHARA event generator. Muon events are selected according to the ANN method described previously, and $y_{ANN} < 0.4$ is required for both tracks. All other requirements are identical to the $\pi^+\pi^-\gamma$ analysis. The remaining pion background after the selection is small, reaching only 10% in the $\rho(770)$ peak region. The comparison between data and MC is shown in Fig. 9.1. Here, the same data sample have been analyzed as in the main analysis, but a much larger mass range as in the $\pi^+\pi^-\gamma$ case is presented.

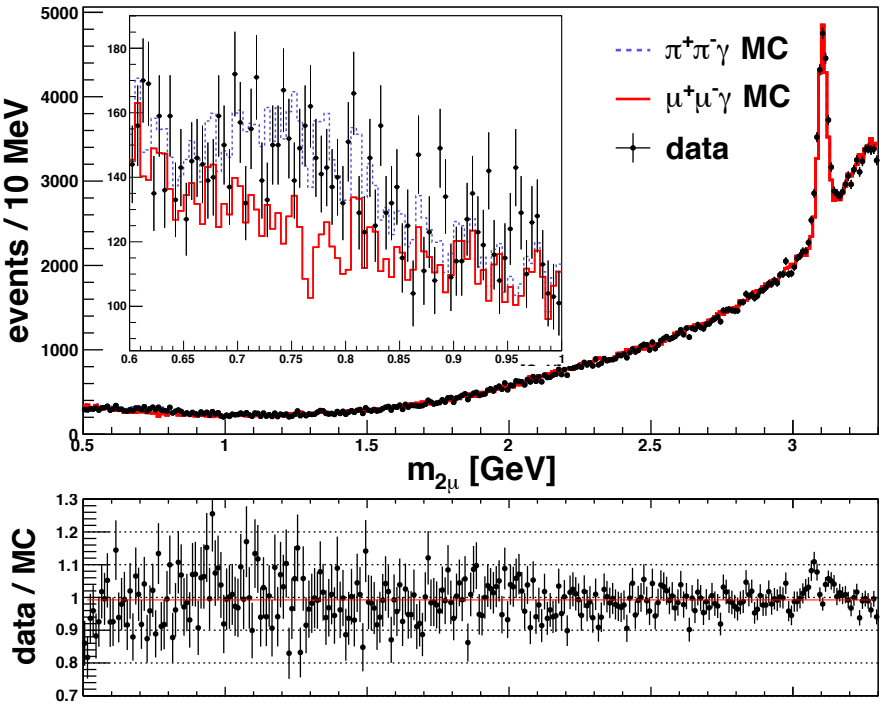

Figure 9.1: Comparison of data and $\mu^+\mu^-\gamma$ MC after using the ANN as muon selector and applying the efficiency corrections in bins of the dimuon invariant mass on the MC events. The upper panel presents the absolute comparison of the number of events found in data and MC. The MC sample is scaled to the luminosity of the data set. The lower one shows the fraction of these two histograms. A linear fit is performed to quantify the data-MC difference, which gives a difference of $(0.49 \pm 0.30)\%$, where the error is the statistical one. The inlay shows the same situation for invariant masses between 0.6 and 1.0 GeV/c^2.

The efficiency corrections described in the previous chapters have been applied to MC on a charged track and photon candidate basis. The lower panel of Fig. 9.1 shows the relative discrepancy between data and MC. An excellent agreement over the full $m_{2\mu}$ mass range on the level of $(0.49 \pm 0.30)\%$ with a χ^2 per degrees of freedom $\chi^2/\text{ndf} = 134/139$ is found, where the uncertainty is of statistical nature only. A fit in the mass range 600 MeV/c^2 $< m_{2\mu} <$

1000 MeV/c^2, which is approximately the mass range studied in the main analysis, results in a relative discrepancy of (0.9 ± 1.4)%. It is illustrated in the inlay of the upper panel of Fig. 9.1. The theoretical uncertainty of the PHOKHARA event generator is below 0.5% [87], while the uncertainty of this measurement is 0.9% and is dominated by the normalization to the luminosity of the data set and the efficiency corrections applied. This result can be considered as a valuable check of the pion-muon separation realized by the ANN, as well as the accuracy of the efficiency corrections applied. It also can be seen as a precise test of the QED prediction.

With the neural network and efficiency corrections developed in the analysis presented we performed further studies, which are not part of this thesis (see also section 11.4). Amongst others, we searched for a dark photon signal and measured the electronic width $\Gamma_{ee}(J/\psi)$ of the J/ψ resonance with unraveled precision. Both results will be published in two separate papers, an overview is given in appendices F and G.

9.3 Cross check: measurement of the integrated luminosity using untagged $\mu^+\mu^-\gamma$ events

By comparing simulation and data of the reaction $e^+e^- \to \mu^+\mu^-\gamma$, it is also possible to determine the integrated luminosity $\mathcal{L}$ of the data set used in the main analysis. Here, untagged events are used, where the ISR photon is not detected in the fiducial volume of the EMC. Thus, an independent $\mu^+\mu^-\gamma$ control sample with respect to the ones used in the efficiency studies is used. The event selection is performed similarly to the cross check described in section 9.2. In contrast, a photon is not required in the EMC. Instead of a 4C kinematic fit, a 1C fit with a missing photon is performed, as already described in the previous chapters 6, 7, and 8. The requirement $\chi^2_{1C} < 10$ is applied, as well as $\theta_{\gamma,miss} < 0.1$ rad or $\theta_{\gamma,miss} > \pi$ - 0.1 rad. Again, the efficiency corrections are applied on the MC sample. The integrated luminosity is the ratio of the number of events N and the corresponding cross section σ

$$\mathcal{L} = \frac{N}{\sigma} \, . \tag{9.4}$$

It can be calculated based on the number of events obtained from data and simulation for each $m_{2\mu}$ bin i via

$$\mathcal{L}^{\mu\mu\gamma}_{data}(m_{2\mu}) = \frac{N_i^{data}(m_{2\mu})}{N_i^{MC}(m_{2\mu})} \cdot \mathcal{L}^{\mu\mu\gamma}_{MC} \, , \tag{9.5}$$

where N_i is the number of found events in data and MC per bin, and $\mathcal{L}_{MC}^{\mu\mu\gamma}$ the integrated luminosity of the produced MC sample. The latter one can be obtained with the event generator.

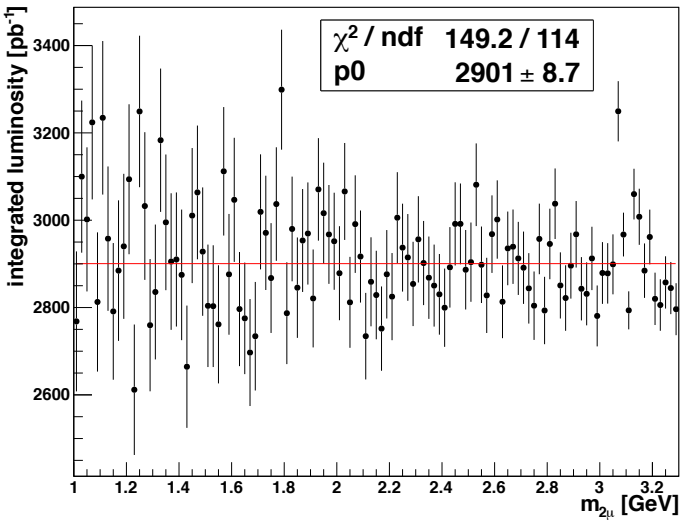

Figure 9.2: Calculated integrated luminosity for each invariant mass bin.

The luminosity $\mathcal{L}_{data}^{\mu\mu\gamma}(m_{2\mu})$ is determined with events that have $m_{2\mu} > 1$ GeV. In this region the contamination by the background channel $e^+e^- \to \pi^+\pi^-\gamma$ is negligible. The result is shown in Fig. 9.2. A linear fit is performed to determine the average luminosity, yielding $(2901.0 \pm 8.7_{\text{stat}})$ pb^{-1} with a $\chi^2/\text{ndf} = 149/114$.

Sources of systematic uncertainties are background subtraction, which is found to be smaller than 0.1%, the event selection, and the efficiency corrections. The systematic uncertainty of the event selection contains contributions from the requirements on χ^2_{1C} and $\theta_{\gamma,miss}$, studied as before in the context of the efficiency studies[1] (chapters 6, 7, and 8.). The values are listed in Tab. 9.2. They are added in quadrature, yielding to a total systematic uncertainty of 1.3%. Hence, the result of the luminosity measurement using untagged $\mu^+\mu^-\gamma$ events is

$$\mathcal{L}_{\mu\mu\gamma} = (2901.0 \pm 8.7_{\text{stat}} \pm 37.7_{\text{sys}})\text{pb}^{-1} ,$$

where the statistical error is the uncertainty of the linear fit. There are two different luminosity measurements for the $\psi(3770)$ data set: The published result [86] with an uncertainty of 1.0%, and the refined analysis, performed in the course of this work, with an uncertainty of 0.5% (for details see section 10.6.2). Both exploit Bhabha scattering events. Their results are listed for

[1] Because of the available space, these studies are not described in detail, here. They are a main part of the measurement of the electronic width of the J/ψ resonance, which is a side product of this thesis and briefly described in appendix G.

comparison in Tab. 9.3. The result obtained from $e^+e^- \to \mu^+\mu^-\gamma$, as described in this section, agrees well with the others within the errors.

source	**uncertainty**
background subtraction	$< 0.1\%$
event selection	0.9%
muon tracking efficiency	0.3%
muon ANN efficiency	0.5%
muon e-PID efficiency	0.5%
sum	1.3%

Table 9.2: The estimated systematic uncertainty of the luminosity measurement using $\mu^+\mu^-\gamma$ events.

To stress this again, an untagged $\mu^+\mu^-\gamma$ sample is used here, which is independent of the ones used to determine the efficiency corrections. Thus, this section shows that the efficiency corrections are applicable in general. In conclusion, this result is another valuable check of the performance of the ANN and the applicability of the developed efficiency corrections.

final state	**can be found in**	$\mathcal{L}$ **[**pb^{-1}**]**
e^+e^-	[86]	$2916.94 \pm 0.18_{\text{stat}} \pm 29.17_{\text{sys}}$
e^+e^-	section 10.6.2	2925 ± 15
$\mu^+\mu^-\gamma$	this section	$2901.0 \pm 8.7_{\text{stat}} \pm 37.7_{\text{sys}}$

Table 9.3: Summary of performed luminosity measurements of the $\psi(3770)$ data set at BESIII.

9.4 Systematic uncertainty of the ANN

Three different checks are performed, to verify the performance of the implemented ANN with respect to reliability and correctness of the results. First, two alternative MVA methods are trained and their data-MC corrections are determined. The cross section of $e^+e^- \to \pi^+\pi^-\gamma$, resulting from the application of these methods in the main analysis, is compared to the actual result, obtained with the ANN. Second, the requirement applied on y_{ANN} is varied generously in order to study shifts introduced by remaining differences of simulation and data. Third, the two-pion production cross section is extracted without further pion-muon separation based on MVA algorithms, but by subtracting the $\mu^+\mu^-\gamma$ background.

(1) Comparisons to alternative MVA methods

Two other MVA methods, provided by the TMVA package [98], are trained, and implemented in this analysis to extract the $\pi^+\pi^-$ cross section: The k-nearest neighbors method (KNN) and a boosted decision tree (BDT), which provide nearly as good signal efficiency and background rejection as the ANN used in this work. The training is done with the same samples of $\pi^+\pi^-\gamma$

and $\mu^+\mu^-\gamma$, used for the ANN training, described in Section 5.5. The same input variables, which are exploited for training the ANN, are considered.

The KNN algorithm searches for k events (placed in the training phase), which are closest to the tested one. To this end, a metric function is used, for example a simple euclidian metric. The method looks for the k nearest events, n of them are signal events and $k - n$ are background ones (with $n < k$). This leads to a discrete probability density, which is shown in Fig. 9.3 (a). A BDT is a binary classifier. Yes or no decisions are taken for one variable, until a stop criterium is reached. In this way, the phase space is split into many regions, which can be allocated to signal or background. This concept is extended by boosting, which means that several trees are used and form a forest. For a more detailed description of the KNN and BDT methods see Ref. [98].

The cross section is extracted (see section 10.6.1) using these independent PID methods. The efficiency corrections, as described in sections 8.1.3 and 8.2 are also determined for the KNN and BDT methods, and applied on the $\pi^+\pi^-\gamma$ and $\mu^+\mu^-\gamma$ MC samples in the analysis. The requirements on y_{KNN} and y_{BDT} are selected such that the respective signal efficiencies are the same as for the $y_{ANN} > 0.6$ and $y_{ANN} < 0.4$ requirements. The result for the number of $\pi^+\pi^-\gamma$ data events in the ρ peak region using the KNN as well as the ANN, is shown in Fig. 9.3. The relative difference between the respective results is estimated with a linear fit on their bin-by-bin calculated ratio, yielding to $(0.63 \pm 0.59)\%$. The error is only the statistical one. Figure 9.4 shows the BDT case. Here, $\mu^+\mu^-\gamma$ events are selected and the $e^+e^- \to \mu^+\mu^-$ cross section is extracted from data. The difference between using the ANN and the BDT method is found to be $(0.04 \pm 0.38)\%$ over the mass range $0.3 < m_{2\mu} < 3.3$ GeV.

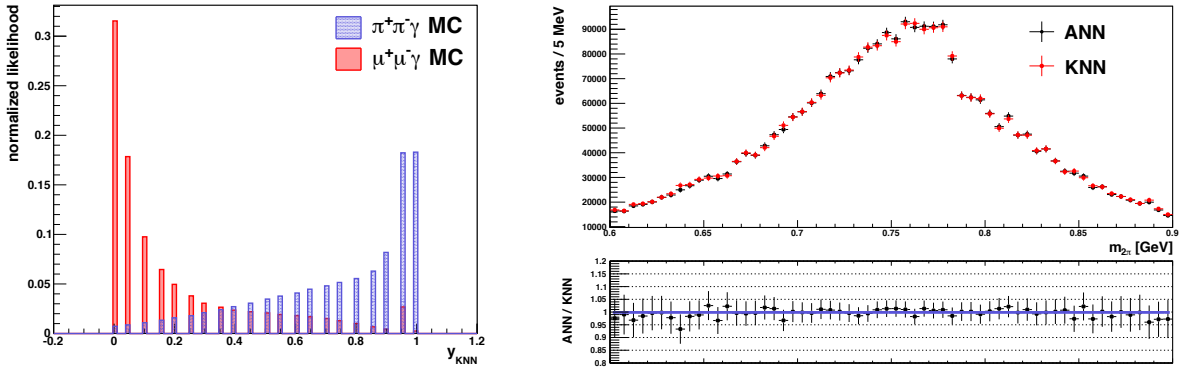

(a) likelihood KNN

(b) ANN vs. KNN

Figure 9.3: Likelihood (a) and output (b) after using of the KNN method. It is compared with the number of $\pi^+\pi^-\gamma$ events from data by using the ANN.

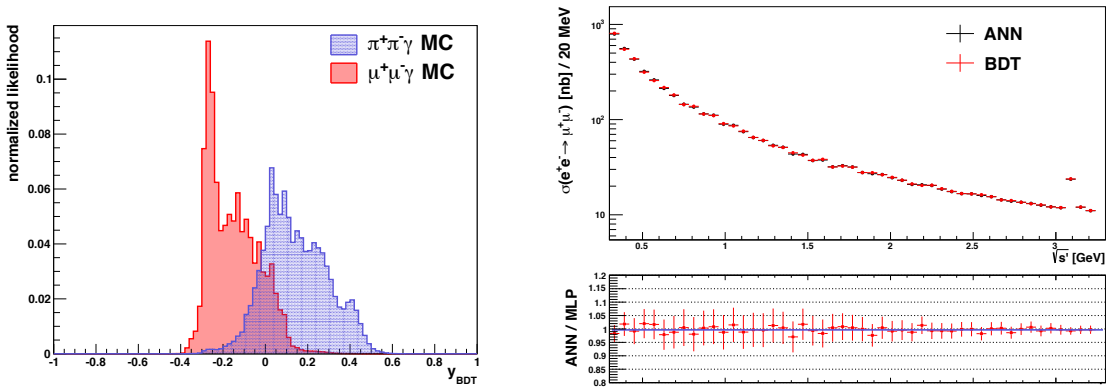

(a) likelihood BDT

(b) ANN vs. BDT

Figure 9.4: Likelihood (a) and output (b) of the usage of the BDT method. It is compared with the $\mu^+\mu^-\gamma$ cross section derived from data by using the ANN.

Two conclusions can be drawn: First, there is no systematic shift between the different MVA methods within the TMVA software. Second, the efficiency corrections work very well, since the results agree with each other although different PID methods and therefore different corrections have been used. This is an important finding, as it demonstrates that the final result does not depend on the PID method.

(2) Variation of y_{ANN}

The condition on y_{ANN} is varied arbitrarily by $\pm$ 0.1 units to estimate its contribution to the systematic uncertainty, i.e between $0.7 > y_{ANN} > 0.5$ for $\pi^+\pi^-\gamma$ events and $0.3 < y_{ANN} < 0.5$ for $\mu^+\mu^-\gamma$ events. For the different y_{ANN} requirements, the efficiency corrections of the ANN are adapted to the new value. The fraction of remaining background differs also, which is considered. Figure 9.5 shows the the number of events in data, using the different requirements on y_{ANN}. The differences are quantified with a linear fit on their ratios. The largest difference is $(0.5 \pm 0.4)\%$, where the error is statistical only. The fact that the outcomes after applying different requirements on y_{ANN} agree with each other, is another valuable cross check, that the data-MC efficiency corrections, which depend on the requirement on y_{ANN}, work well.

(3) $\mu^+\mu^-\gamma$ background subtraction without using the ANN

The $\pi^+\pi^-$ cross section is also determined without using the ANN. The significant $\mu^+\mu^-\gamma$ background is subtracted based on MC simulation. Here, the ANN data-MC efficiency corrections must not been used on the MC samples. The other corrections, i.e. for photon detection, tracking, and e-PID still have to be applied. The comparison of the $\pi^+\pi^-$ cross section obtained from an analysis with and without additional pion-muon separation by an

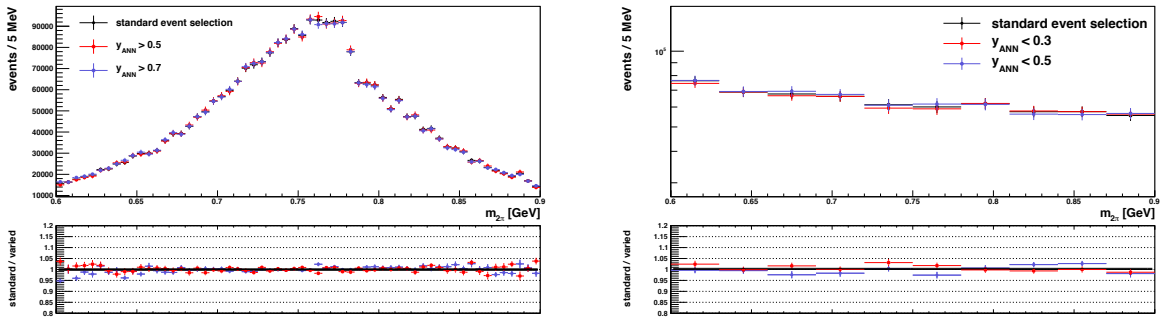

Figure 9.5: Number of events in data for various y_{ANN} requirements. The difference is estimated via a linear fit to evaluate a shift. The fit result shown is the one of the largest deviation.

ANN is shown in Fig. 9.6. Again, a linear fit to the fraction of both results is performed, to quantify their difference, yielding $(0.27 \pm 0.58)\%$. Thus, it is compatible with zero.

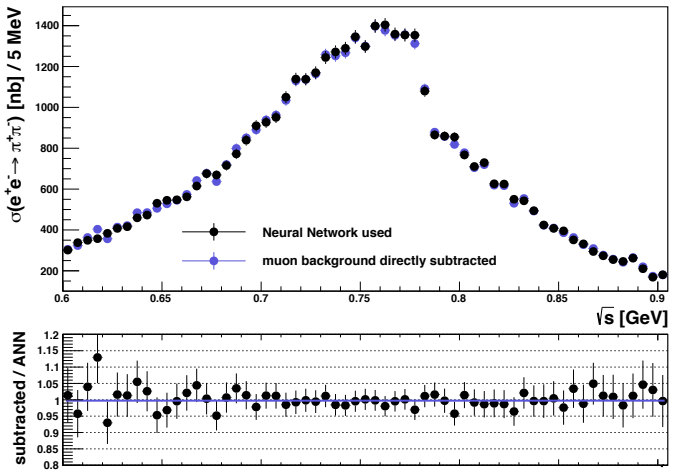

Figure 9.6: Comparison of the $e^+e^- \to \pi^+\pi^-$ cross sections derived from data by using the ANN and subtracting the muon background without using a PID method.

As conclusion, the ANN method delivers reliable results. The three cross checks performed, as described in this section, are successful and their outcomes are compatible with zero. Hence, no additional uncertainty is taken into account.

9.5 4C kinematic fit and electron PID

Data-MC differences due to the requirements $\chi^2_{4C} < 60$ and $DLL(\pi,e) > 2$, are corrected. The first one by the photon detection efficiency correction, and the second one by the e-PID efficiency correction. To proof this, these requirements are varied in a wide range, while the

efficiency corrections are determined with the new χ^2_{4C} and $DLL(\pi,e)$ values.

The χ^2_{4C} value is varied between 30 and 200 with a step size of 10 χ^2_{4C} unites between values of 30 and 100, and a step size of 25 above. The requirement on $DLL(\pi,e)$ in a region between 0 and 10 with a step size of 2. The number of events in data is compared. The changes are all within the systematic uncertainties assumed for this specific quantity. This shows the stability of these corrections. Hence, also here additional contributions to the systematic error are not accounted for. Only in the extreme case of $\chi^2_{4C} < 200$ a not with zero compatible difference of $(0.41 \pm 0.13)\%$ is found, where the error is statistical only. If one considers, that in this case much more background has to be considered in a systematic study, the result is reasonable.

9.6 Angular acceptance, photon energy requirement and point of closest approach

To avoid edge effects where the detector simulation might not be reliable, a charged track has to be in the angular acceptance region between 0.4 rad $< \theta <$ π - 0.4 rad. The systematic uncertainties due to this requirement are studied by varying this acceptance region in a meaningful range, which is determined with the angular resolution. The angular resolution of the MDC is estimated based on the the $\mu^+\mu^-\gamma$ sample discussed in section 7.2.1. The difference between scattering angles of tracks predicted by a 1C kinematic fit and their scattering angles as measured by the MDC is determined. The resolution σ_θ is determined as the root mean square of this difference, which is shown in Fig. 9.7. It is determined for MC and data. The resolution obtained from data is $\sigma_\theta = 0.024$ radians. It is is greater than the MC determined value by about 5% and, thus, taken as resolution in θ. The acceptance region of charged tracks is varied in a $3\sigma_\theta$ range, i.e. between 0.4 rad $\pm$ $3\sigma_\theta < \theta <$ π - 0.4 rad $\pm$ $3\sigma_\theta$.

The number of $\pi^+\pi^-\gamma$ and $\mu^+\mu^-\gamma$ events in data are extracted using these different acceptance regions, and are compared to the standard requirement. Also here, the systematic uncertainty is quantified by a linear fit on their ratio, yielding to a maximum difference of $(0.1 \pm 0.1)\%$. A a conservative estimate an uncertainty of 0.1% is obtained.

Also requirements on the measured ISR photon energy $E_\gamma > 0.4$ GeV, as well as on the distance to the IP, $|V_z| < 10.0$ cm and $V_r < 1.0$ cm, are applied in the analysis. To study their contribution to the systematic uncertainty, these requirements are varied and the impact on the final result is investigated. The requirement on E_γ is varied between 0.2 and 1.0 GeV with a step size of 0.1 GeV, and data and simulation are compared as above. As expected, the

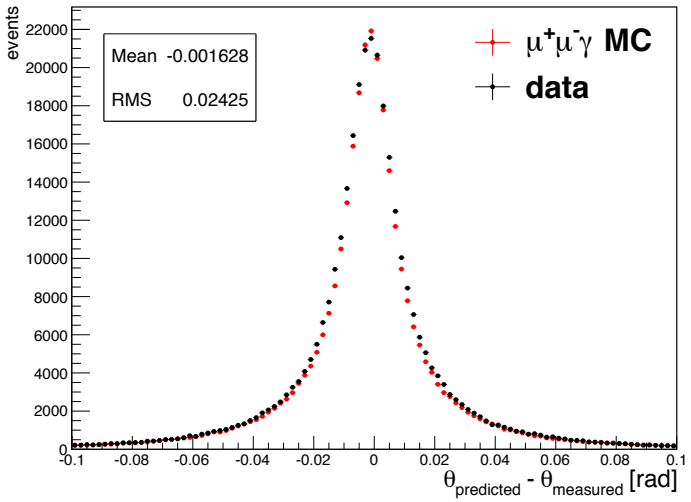

Figure 9.7: θ resolution of the MDC. Shown is the difference between predicted direction and real measured one. As resolution the root mean square of this difference is chosen. The values shown are the ones from data.

impact on the final result is negligible small, since photon energies of 1.8 GeV are needed, to produce $m_{2\pi}$ masses below 0.9 GeV. The requirements on $|V_z|$ and V_r are varied by a factor of 2. Also here, the impact on the final result is determined as above and is found to be negligible small. No further uncertainty has to be accounted for.

Chapter 10

Extraction of $\sigma^{bare}(e^+e^- \to \pi^+\pi^-(\gamma_{\mathrm{FSR}}))$

The bare cross section, i.e. neglecting vacuum polarization effects, of the process $e^+e^- \to \pi^+\pi^-(\gamma_{\mathrm{FSR}})$ in the energy region between 0.6 GeV $< \sqrt{s} <$ 0.9 GeV, is the most important input for the standard model prediction of the hadronic content of the muon anomaly a_μ^{had}.

This chapter deals with the extraction of this cross section, performed in two different ways. First, the number of $\pi^+\pi^-\gamma$ events is normalized to the luminosity and the radiator function. Second, the R ratio is calculated.

In both cases, an FSR correction needs to be applied, as well as an unfolding procedure, which is also presented in the upcoming sections.

10.1 Analysis overview

As pointed out in Ref. [16] the bare $\sigma^{\rm bare}(e^+e^- \to \pi^+\pi^-(\gamma_{\rm FSR}))$ cross section is needed as input for the calculation of $a_\mu^{\rm had}$, whereas "bare" describes the cross section without taking vacuum polarization corrections into account (see section 10.6.4). An overview of the analysis steps performed, which are performed to extract this cross section, are displayed in Fig. 10.1. After applying the event selection, described in chapter 4 and 5, and after subtracting the remaining background determined with MC, one gains the event yield of the $\pi^+\pi^-\gamma$ final state. Afterwards, the two-pion invariant mass spectrum is unfolded and corrected for the detection efficiency, to counterbalance detector smearing and loss due to detector acceptance and analysis requirements. This efficiency is determined with a MC sample, whereas the efficiency corrections obtained in sections 6, 7, and 8 have to be applied to reduce the systematic uncertainty as much as possible. This is crucial for a high precision measurement. An FSR correction is performed to remove final state radiation, which shifts the invariant mass spectrum towards lower values. Two different normalizations are applied to extract $\sigma^{\rm bare}(e^+e^- \to \pi^+\pi^-(\gamma_{\rm FSR}))$. One method is to normalize the number of $\pi^+\pi^-\gamma$ events to the radiator function, the luminosity, and perform a vacuum polarization correction. This approach has been used in the KLOE 08 [60] and 10 [61] measurements. In a second method one can normalize it to the number of $\mu^+\mu^-\gamma$ events, with other words one can calculate the R ratio [4]. This approach has been obtained at the KLOE 12 [62] and BaBar [64] analysis. Finally, an FSR correction on the level of $e^+e^- \to \pi^+\pi^-$ events has to be applied, which is a calculation by Schwinger, to gain $\sigma^{\rm bare}(e^+e^- \to \pi^+\pi^-(\gamma_{\rm FSR}))$.

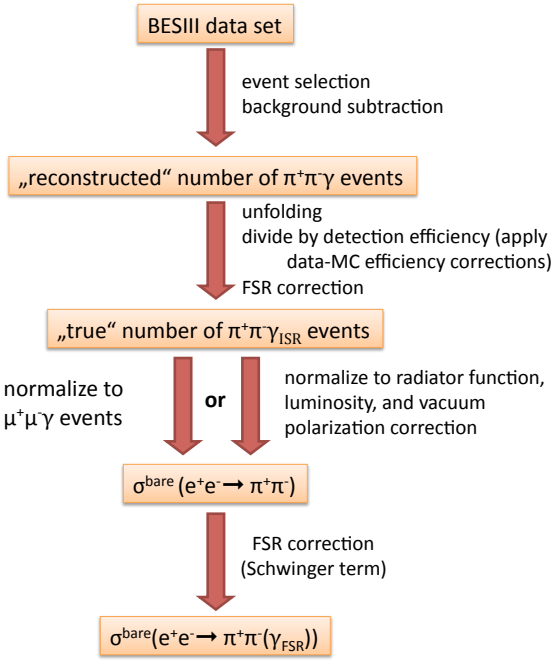

Figure 10.1: Flow chart of the ISR analysis to extract the $\sigma^{\rm bare}(e^+e^- \to \pi^+\pi^-(\gamma_{\rm FSR}))$ cross section.

10.2 Background subtraction

The background remaining in data after applying the event selection is estimated from the MC samples listed in Tab. 2.9, and is subtracted from data. The dominating contribution, stemming from the $\mu^+\mu^-\gamma$ final state, is treated separately from the other sources of background.

Figure 10.2 (left) shows the remaining $\mu^+\mu^-\gamma$ MC contribution, scaled to the luminosity of data, together with the data sample, after applying the event selection. The efficiency corrections for photon detection, muon tracking, e-PID and ANN, are applied to the MC sample. This provides the best possible prediction of the remaining background. The uncertainties are listed in Tab. 10.1, yielding a 0.9% systematic uncertainty. In Fig. 10.2 (right), the fraction of $\mu^-\mu^-\gamma$ MC and data is shown in a larger binning of 100 MeV. The MC distribution is subtracted from data to remove the remaining muon background. Hence, the systematic uncertainty of 0.9% has to be multiplied with the background fraction, which is smaller than 7.4% in the mass range investigated. This yields to a systematic uncertainty of $0.9\% \cdot 7.4\% < 0.05\%$, when subtracting the $\mu^+\mu^-\gamma$ background.

source	**uncertainty**	**cited from**
photon efficiency correction	0.2%	section 6.6
muon tracking efficiency correction	0.3%	section 7.2.4
e-PID efficiency correction	0.5%	section 8.2.5
ANN efficiency correction	0.5%	section 8.2.5
luminosity	0.5%	section 10.6.2
accuracy of PHOKHARA	0.5%	[88]
sum	0.9%	

Table 10.1: Systematic uncertainties of the $\mu^+\mu^-\gamma$ background MC sample.

The non-muon background is estimated with the MC samples listed in Tab. 10.2. They are scaled with the calculated cross sections from the MC generators to the luminosity of data. Table 10.2 summarizes the total estimated numbers of events in the invariant mass range between 0.6 and 0.9 GeV. Figure 10.3 shows the sum of the non-muon background MC samples together with data. Also, the fraction of the non-muon MC and data can be seen. The three spikes at 0.64, 0.67, and 0.72 GeV originate from the $e^+e^-(n\gamma)$ MC sample, which has a statistics of only 25% of data. Scaling the distribution according to the integrated luminosity results in the artifacts observed. Apart from these outliers, the background contamination is well below 0.1%.The MC is subtracted from data, whereas a conservative 50% uncertainty for the well-known $e^+e^-(n\gamma)$ sample, and a 200% uncertainty on all other samples, is applied. This has to be multiplied with the non-muon background fraction, yielding to a systematic uncertainty smaller than 0.03% when taking the exact numbers of the background fraction into account.

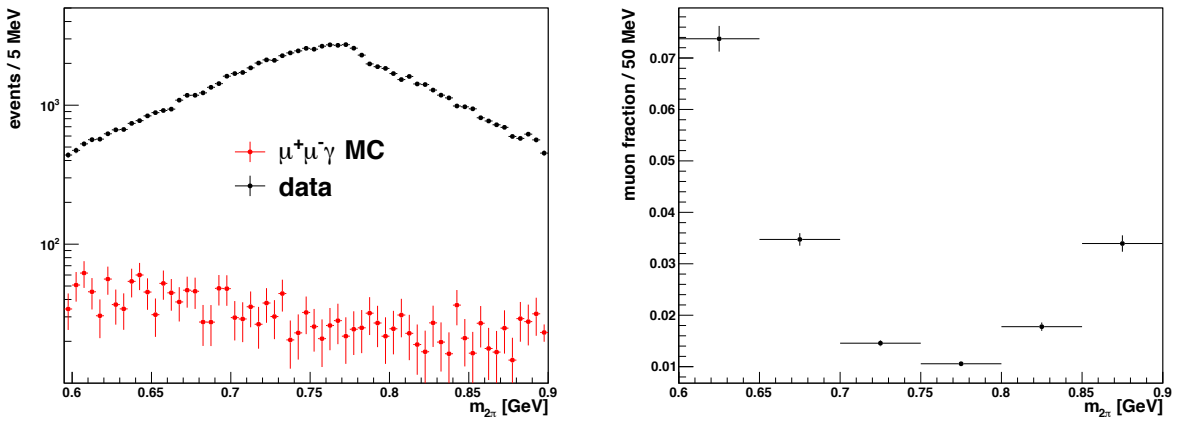

Figure 10.2: Left: remaining $\mu^+\mu^-\gamma$ MC background, after applying all determined efficiency corrections, together with data. The MC is scaled to the luminosity of data.
Right: fraction of $\mu^+\mu^-\gamma$ and data events. The uncertainty of the MC has to be multiplied with this value when subtracting the muon background.

final state	background events
$e^+e^-(n\gamma)$	12 ± 3.5
$\pi^+\pi^-\pi^0\gamma$	3.3 ± 1.8
$\pi^+\pi^-\pi^0\pi^0\gamma$	0
$\pi^+\pi^-\pi^+\pi^-\gamma$	0
$K^+K^-\gamma$	2 ± 1.5
$K^0\overline{K^0}\gamma$	0.4 ± 0.6
$p\overline{p}\gamma$	0
continuum	3.9 ± 1.9
$\psi(3770) \to D^+D^-$	0
$\psi(3770) \to D^0\overline{D^0}$	0
$\psi(3770) \to non\ D\overline{D}$	3.1 ± 1.8
$\psi(3770) \to \gamma\ J/\psi$	0.6 ± 0.8

Table 10.2: MC non-muon background estimation for $600 < m_{2\pi} < 900$ MeV.

The event yield after the background subtraction procedure described above, is shown in Fig. 10.4 as a function of $m_{2\pi}$. Within the estimated systematic uncertainties, these selected $\pi^+\pi^-\gamma$ events are assumed to be background free now.

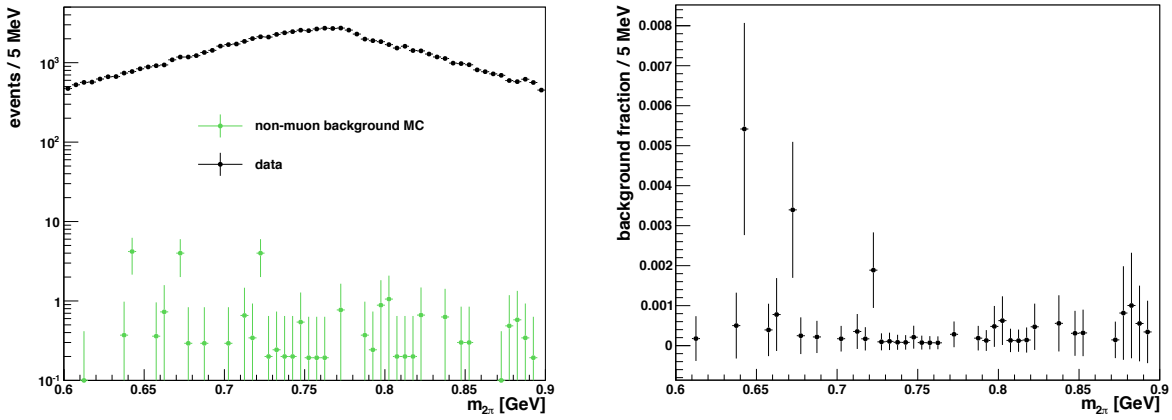

Figure 10.3: Left: total estimated non-muon background. The estimation is done by using the MC samples listed in Tab. 10.2.
Right: non-muon background fraction.

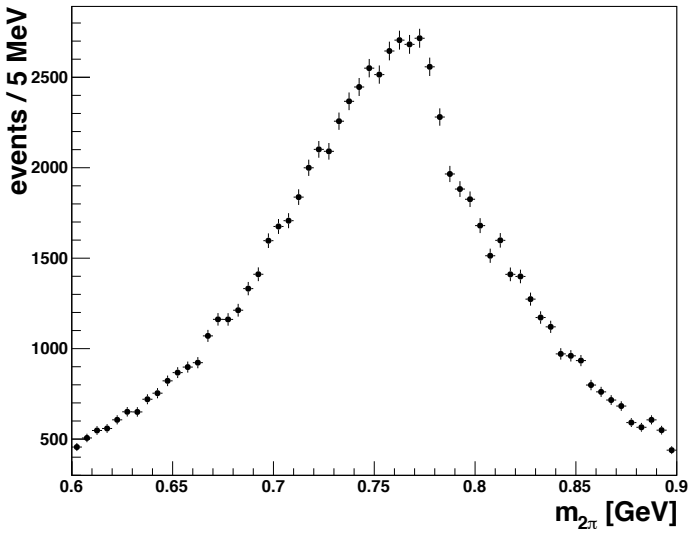

Figure 10.4: Event yield after applying the event selection and subtracting the background, estimated with MC.

10.3 Unfolding

Due to the interaction with the detector material and a limited detector resolution, the $m_{2\pi}$ invariant mass distribution is smeared. In order to investigate the underlying physics, the results of the data analysis need to be unfolded from these detector effects. As unfolding method the Singular Value Decomposition (SVD) method is used, which is tested and optimized for the energy range investigated. It is described in detail in Ref. [104]. Two input parameters are needed for this procedure - the response matrix and the regularization parameter τ.

The response Matrix is determined from a $\pi^+\pi^-\gamma$ PHOKHARA MC sample, by comparing the MC true $m_{2\pi}$ distribution with the reconstructed one after applying the event selection. The settings of the PHOKHARA generator to produce this MC sample are summarized in Tab. 2.8. To recall the terminology: the distribution on the generator level is called "true", the distribution after taking the detector environment into account is called "reconstructed". The response matrix for $m_{2\pi}$ between 0.6 and 0.9 GeV and for the invariant mass spectrum up to 3.0 GeV, is displayed in Fig. 10.5. About 43% of events are found to be on the diagonal axis, choosing a bin width of 5 MeV.

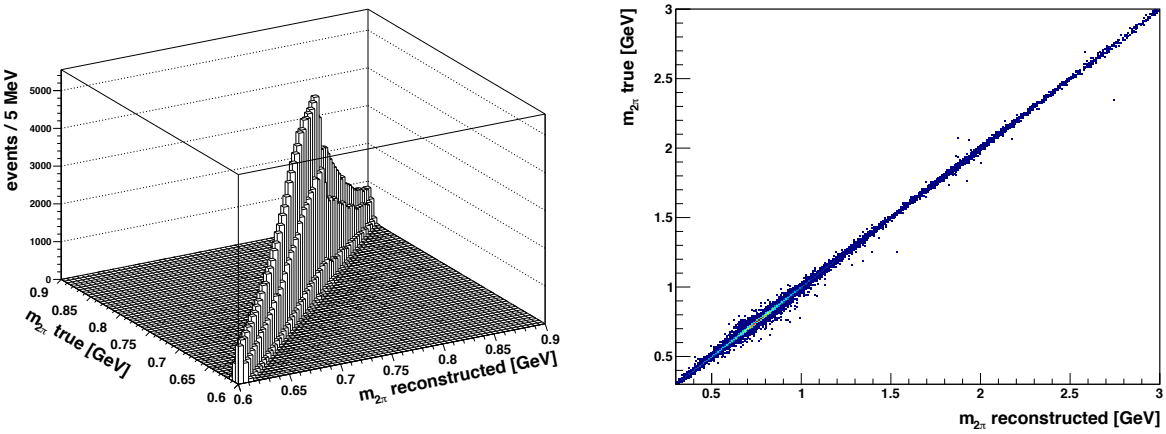

(a) ρ peak region (b) whole spectrum

Figure 10.5: Response matrix determined with a $\pi^+\pi^-\gamma$ MC sample. Shown is the $m_{2\pi}$ region between 0.6 and 0.9 GeV as 3-dimensional histogram, as well as for the mass spectrum up to 3.0 GeV as 2-dimensional projection.

In the technical execution of the SVD method, a regularization term is added in order to minimize the equations [104], which are needed to calculate the singular values. The regularization term features a free parameter τ. The optimal value of this parameter is problem dependent. However, if it is chosen too small, it biases the result towards the MC sample, which is used to compute the response matrix. If it is too large, it will lead to large fluctuations in the unfolded mass spectrum. Two independent procedures are suggested in Ref. [104], to find the best value for τ.

(1) The optimal choice of τ can be determined via the distribution of a vector $\vec{d}$, with length n. This vector is a rotation of the reconstructed spectrum, in order to make the matrix equations diagonal. The behavior of its components d_i, i = 1,2,...,n, should depend exponentially on i and should become constant for large values of i. According to Ref. [104], the optimal choice of τ is the square of the ith singular value s_i^2, where the distribution $log(d_i)$ becomes constantly

smaller than 1. This distribution is presented in Fig. 10.6 as red histogram. The statistical fluctuations are large and, hence, the right choice can not be made by eye. A solution to find the right parameter is also given in Ref. [104]. If the correct value $\tau = s_k^2$ is found, the distribution

$$d_i^{(\tau)} = d_i \cdot \frac{s_i^2}{s_i^2 + \tau} \tag{10.1}$$

falls constantly below 1, for the correct $\tau = s_k^2$ at $i > k$. Iteratively, a good choice of τ can be found. The result is the blue histogram from Fig. 10.6. The value $\tau = s_k^2 = 72.4$ corresponds to $k = 94$. For $i > k = 94$ the distribution becomes constantly smaller than one. Hence, a good regularization parameter, $\tau \approx 72$, has been found.

(2) Another possible approach to find an acceptable τ value, is to calculate it based on a test sample [104]. As test sample a $\pi^+\pi^-\gamma$ MC with the Kühn-Santamaria (KS) parametrization of the pion form factor and neglecting vacuum polarization corrections (see section 10.6.4) is used. Thus, it is statistically and partly systematically independent from the MC sample, used to derive the response matrix, which uses the Gounaris-Sakurai parametrization and takes vacuum polarization corrections into account. The reconstructed invariant mass of the test spectrum is unfolded with different τ parameters and compared with the MC true value of the test distribution. The parameter τ is optimized by minimizing the difference between the MC true test distribution and the unfolded one, quantified with a linear fit to their difference. The result can be seen in Fig. 10.7. A value of $\tau \approx 72$ is found again. Hence, two independent methods arrive to the same regularization parameter, $\tau \approx 72$. Such an independent check is suggested in Ref. [104].

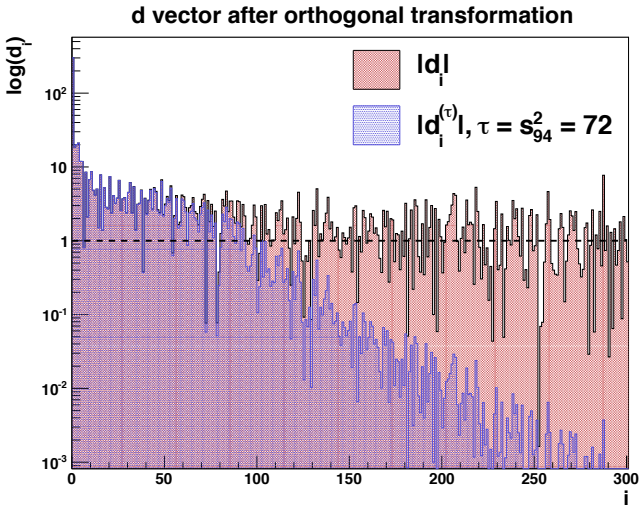

Figure 10.6: Entries d_i and $d_i^{(\tau)}$ of the vector $\vec{d}$ as explained in the text and in Ref. [104].

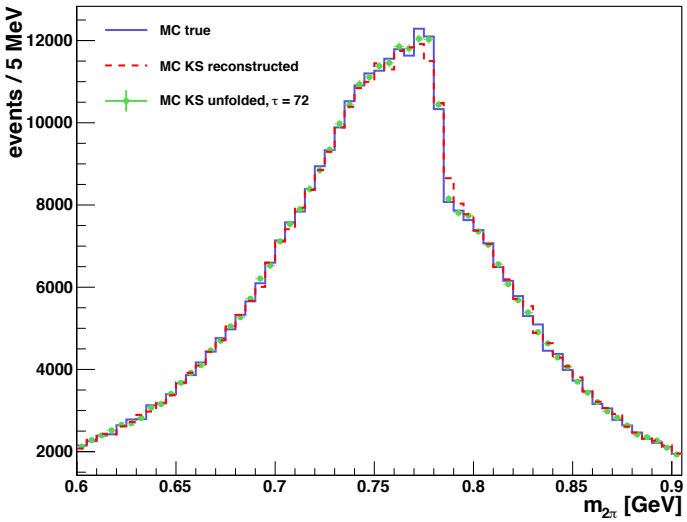

Figure 10.7: The MC true distribution (blue histogram) of a $\pi^+\pi^-\gamma$ sample using the Kühn-Santamaria form factor parametrization and neglecting vacuum polarization effects. The corresponding reconstructed distribution including detector effects (red dotted line) is unfolded with different regularization parameters τ. This parameter is optimized by minimizing the difference between the unfolded spectrum and the true one, quantified with a linear fit on this difference. The value found is $\tau = 72$ (green dots).

It has to be tested, how well the SVD method works, which corresponds to its systematic uncertainty determination. Two issues have to be tested. First, whether the method is correctly implemented in the analysis. Second, how large possible systematic shifts using this method are. This is done in the following.

To check, whether the method is correctly implemented, the same reconstructed MC distribution, which is used as input for the response matrix, is unfolded. If the method is correct, it should deliver the corresponding MC true distribution. Figure 10.8 shows the MC true and reconstructed distributions before (a) and after applying the unfolding algorithm (b). Before using the SVD method, a randomly scattered difference due to detector smearing can be seen. After the unfolding, the two distributions fit perfectly to each other. This is exactly what one would expect, if the method is correctly implemented in the analysis, which is obviously the case.

To estimate the systematics of the SVD method used, three different checks are performed:

(a) The MC test sample, using the KS parametrization and neglecting vacuum polarization effects, is unfolded[1] and compared with the true test distribution via a linear fit to their difference. The result can be seen in Fig. 10.9. The result is a difference of $(0.04 \pm 0.24)\%$

[1]Note: the response matrix is in all cases the same. It is shown in Fig. 10.5.

and, thus, compatible with zero.

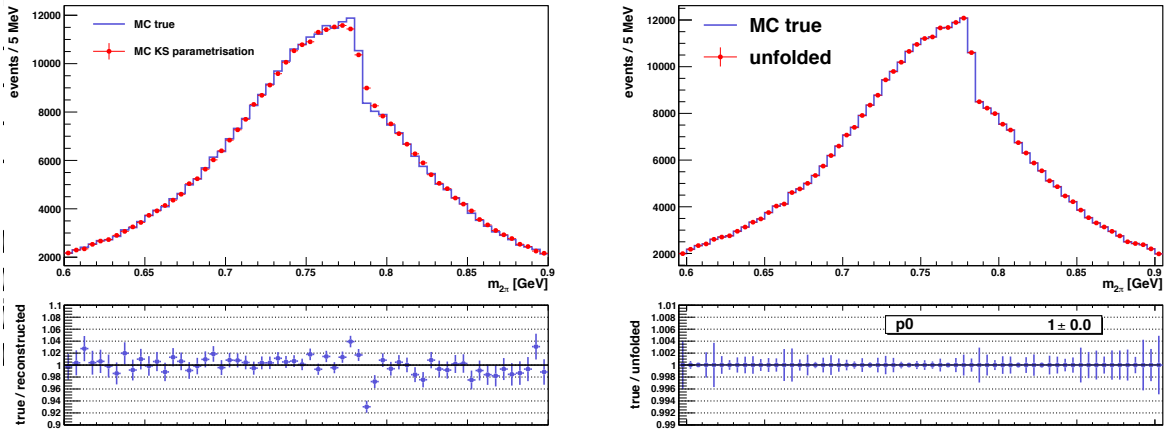

(a) MC reconstructed (b) MC unfolded

Figure 10.8: The MC true and reconstructed distributions used in the SVD response matrix (a). Also shown is the reconstructed spectrum after the unfolding (b). It fits perfectly to the MC true distribution.

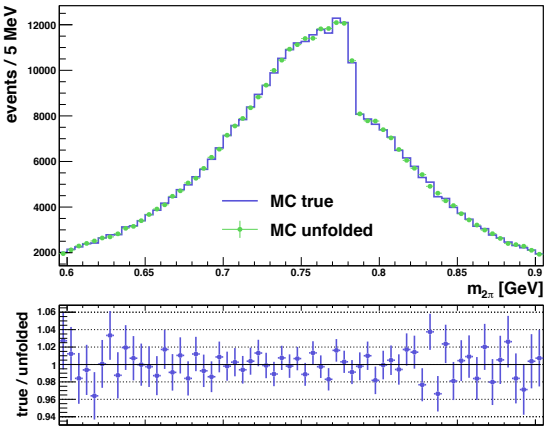

Figure 10.9: Smeared, reconstructed, and unfolded MC distribution compared to the MC true one using the KS form factor and neglecting vacuum polarization effects in the MC production.

(b) The $m_{2\pi}$ distribution of the reconstructed test MC sample, is smeared with a large additional Gaussian error of 20%, to simulate a larger detector smearing than expected from MC. Also in this case the unfolding is successful. A possible difference is estimated with a linear fit on the ratio of MC true and unfolded distribution. The result is a deviation of $(0.2 \pm 0.2)\%$ and, hence, compatible with zero.

(c) As a third test, the mass of the ρ-resonance of 770 MeV is shifted to different values within the simulation. Four different MC samples are generated with ρ masses according to 750, 760,

780, and 790 MeV. Figure 10.10 shows the ρ peak of these MC samples and how it is shifted towards the new mass setting.

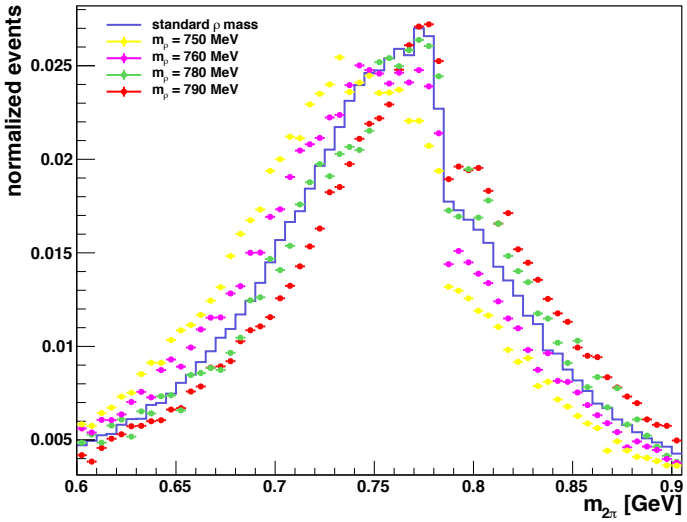

Figure 10.10: ρ peak region of the MC samples, simulated with different ρ masses.

These reconstructed MC samples are unfolded, while the response matrix is the same as in Fig. 10.5 in each case. The result is presented in Fig. 10.11, where the unfolded mass spectra (green dots) are compared to the corresponding MC true distributions (blue histograms). They agree well with each other, quantified by a linear fit to their difference. A maximum difference of $(0.011 \pm 0.005)\%$ is observed. One can conclude that the unfolded result is not biased by the input MC sample, which is used to calculate the response matrix.

A conservative systematic uncertainty of 0.2% is estimated, which represents the largest deviation that is found in the checks performed. To conclude and summarize this section:

- The Singular Value Decomposition Method from Ref. [104] is used to unfold the $m_{2\pi}$ invariant mass spectrum.
- The needed response matrix is determined with a MC sample, the needed regularization parameter is found to be $\tau = 72$.
- The SVD method is correctly implemented in the analysis.
- The unfolded result is not biased by the input MC sample.
- The results of all performed checks is compatible with zero.
- A conservative systematic uncertainty of 0.2% is estimated, which represents the largest found deviation.

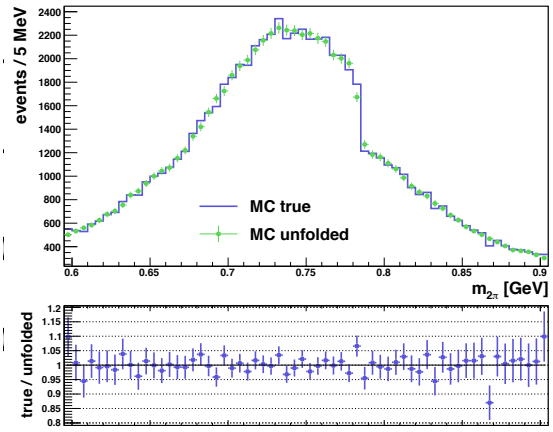

(a) $m_\rho = 750$ GeV

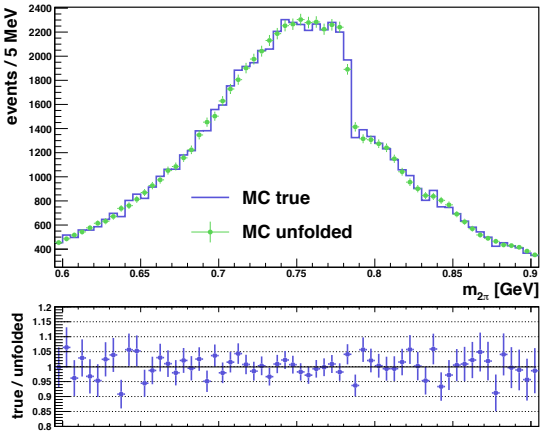

(b) $m_\rho = 760$ GeV

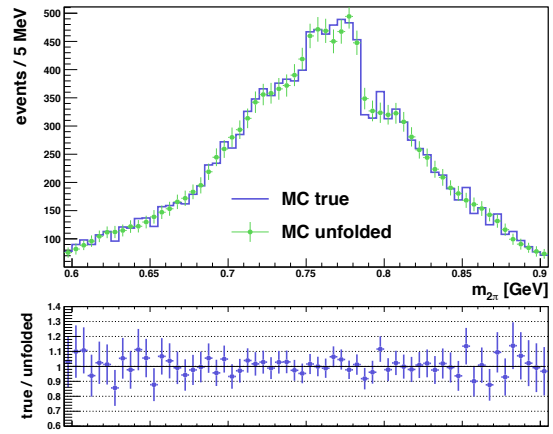

(c) $m_\rho = 780$ GeV

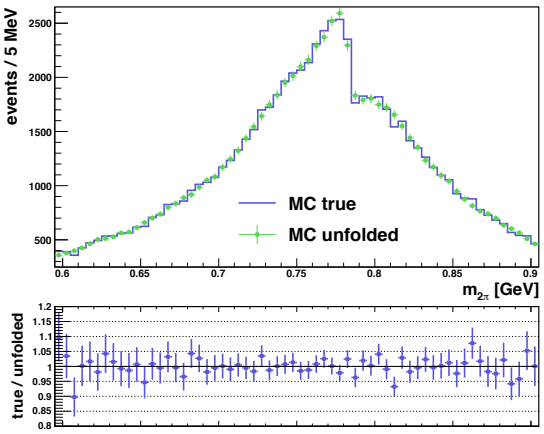

(d) $m_\rho = 790$ GeV

Figure 10.11: Unfolded distributions (green dots) and the corresponding MC true ones (blue histograms) of the MC samples, simulated with shifted ρ-masses. They agree very well with each other, which shows the stability of the unfolding method chosen.

10.4 Selection efficiency

The selection efficiency as a function of $m_{2\pi}$, $\epsilon(m_{2\pi})$, is determined with a $\pi^+\pi^-\gamma$ MC sample. The true invariant mass spectrum after applying the event selections described in chapters 4 and 5 is divided by the MC true distribution before any selections. The result is the efficiency of the imposed requirements in bins of $m_{2\pi}$. The MC sample after applying the selections is corrected for the data-MC differences, described in chapters 6, 7.1, and 8.1. I.e. for photon detection, pion tracking, e-PID of pion tracks, and pion ANN-PID differences. The left panel of Fig. 10.12 shows the MC true distribution before and after applying the selection conditions. The selection, or global efficiency can be seen in the right panel of Fig. 10.12, which is the ratio

of these two distributions. In the mass range between 600 and 900 MeV it is flat between 2.8% and 3.0%. The event yield in data after applying the event selection, background subtraction, unfolding, and normalizing to $\epsilon(m_{2\pi})$ is shown in Fig. 10.13.

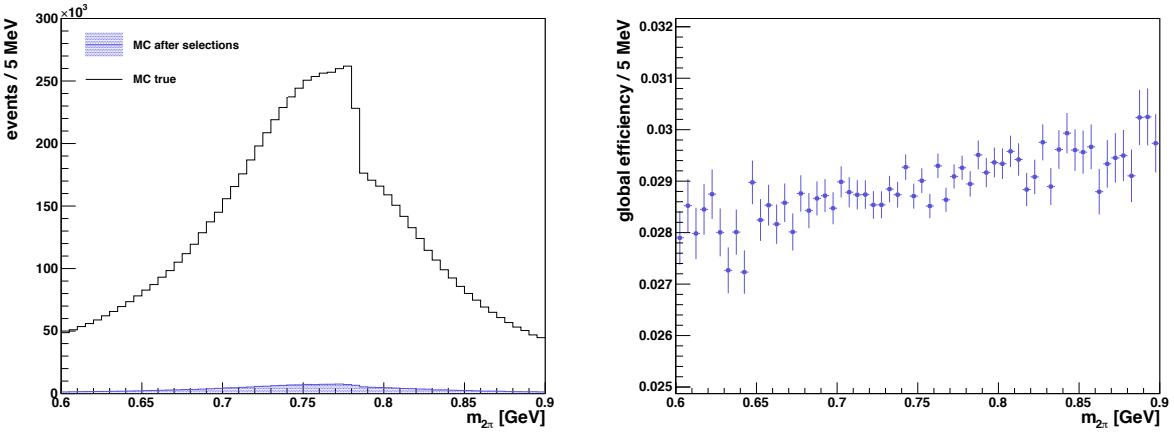

Figure 10.12: Left: true $\pi^+\pi^-\gamma$ MC after applying event selections and efficiency corrections (blue shaded) compared to corresponding MC true distribution.
Right: global detection efficiency $\epsilon(m_{2\pi})$.

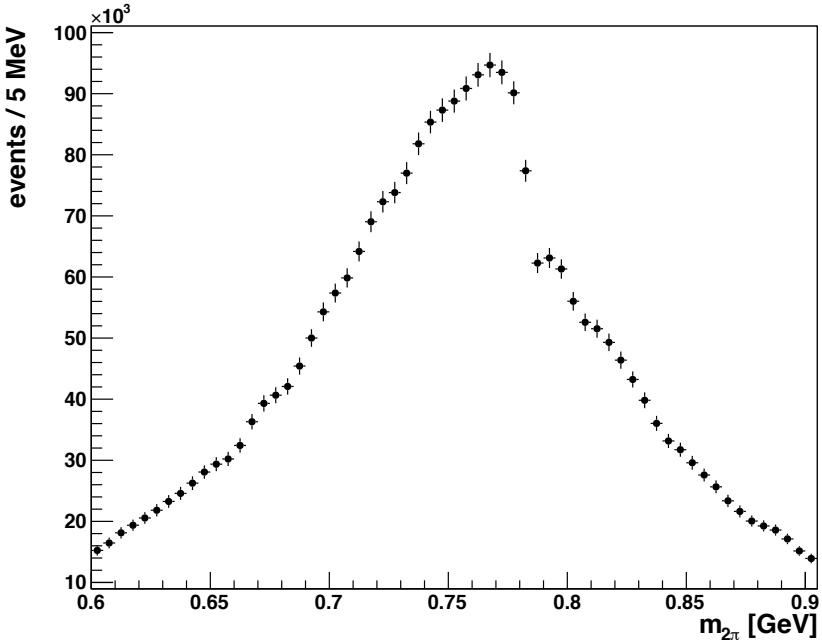

Figure 10.13: Event yield in data after applying the event selection, background subtraction, unfolding, and normalizing to $\epsilon(m_{2\pi})$.

10.5 FSR correction $\delta^{2\pi}_{\rm FSR}$

As pointed out in Ref. [16] and already described in section 3.4, in order to consider radiative effects in the dispersion integral for a_μ, an FSR correction has to be performed.

On the one hand, the FSR correction for two pion production $\delta^{2\pi}_{\rm FSR}$ accounts for FSR effects in events on the level $e^+e^- \to \pi^+\pi^-\gamma$, where a photon is emitted in the initial and final state, as shown in the right Feynman diagram in Fig. 10.14. In this case, $m_{2\pi}$ does not correspond to the mass of the virtual photon propagator, but it is shifted towards smaller masses, leading to a shifted cross section. On the other hand, as input for $a_\mu^{\rm had,VP}$, the $\pi^+\pi^-(\gamma_{\rm FSR})$ cross section is needed, including LO FSR on the level of $e^+e^- \to \pi^+\pi^-$ events and, thus, for 600 MeV $< \sqrt{s'} <$ 900 MeV, as shown in Fig. 10.14 (left).

Hence, $\delta^{2\pi}_{\rm FSR}$ shall correct the $m_{2\pi}$ distribution for NLO FSR and higher orders on the level $e^+e^- \to \pi^+\pi^-\gamma$, while LO FSR contributions on the level of $e^+e^- \to \pi^+\pi^-$ events need to be retained. Two independent methods are performed and compared, to evaluate $\delta^{2\pi}_{\rm FSR}$.

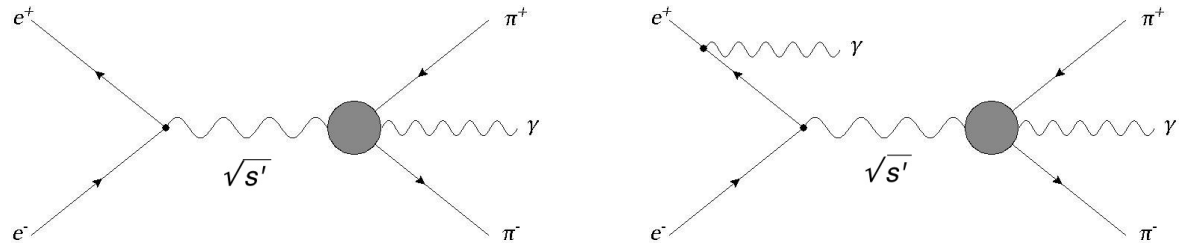

(a) LO FSRon the level of $e^+e^- \to \pi^+\pi^-$ events (b) ISR + FSR

Figure 10.14: Left: LO FSR contribution. This one has to be retained on the level of $e^+e^- \to \pi^+\pi^-$ events (thus, for 600 MeV $< \sqrt{s'} <$ 900 MeV), since the $\pi^+\pi^-(\gamma_{\rm FSR})$ cross section is needed as input for $a_\mu^{\rm had,VP}$.
Right: NLO FSR contribution, one has to correct the mass spectrum for.

Method 1

The whole FSR contribution, LO as well as NLO, on the level of $e^+e^- \to \pi^+\pi^-\gamma$ events, is adjusted. After that, the LO FSR contribution on the level of $e^+e^- \to \pi^+\pi^-$ is added, using a theoretical calculation by Schwinger.

The whole FSR correction, $\delta^{2\pi}_{\rm LO+NLO}$, is determined with the PHOKHARA event generator. The $e^+e^- \to \pi^+\pi^-\gamma$ cross sections are generated with NLO ISR only, called $\sigma_{MC}^{NLO\ ISR}(m)$, and also including LO and NLO ISR, as well as LO and NLO FSR, called $\sigma_{MC}^{all}(m)$. The FSR

correction as function of $m_{2\pi}$ can then be calculated as

$$1 + \delta^{2\pi}_{\rm LO+NLO} = \frac{\sigma^{all}_{MC}(m_{2\pi})}{\sigma^{NLO\ ISR}_{MC}(m_{2\pi})} \ . \tag{10.2}$$

In Fig. 10.15 the $m_{2\pi}$ distributions and the $(1+\delta^{2\pi}_{\rm LO+NLO})$ distribution are shown. As explained, the invariant mass is shifted towards lower values, due to FSR.

Afterwards, a theoretical calculation from Schwinger is applied to add LO FSR on the level of $e^+e^- \to \pi^+\pi^-$ events, and to obtain $\delta^{2\pi}_{\rm FSR}$ [96]:

$$\sigma(e^+e^- \to \pi^+\pi^-(\gamma_{\rm FSR})) = \sigma(e^+e^- \to \pi^+\pi^-) \cdot \left[1 + \eta(s)\frac{\alpha}{\pi}\right] , \tag{10.3}$$

$$1 + \delta^{2\pi}_{\rm FSR} = \frac{1 + \delta^{2\pi}_{\rm LO+NLO}}{1 + \eta(s)\frac{\alpha}{\pi}} \ , \tag{10.4}$$

where $\eta(s)$ is the theoretical energy dependent LO FSR correction factor taken from Ref. [70] and α the fine structure constant taken from [4]. It is shown in Fig. 10.16 as a function of $\sqrt{s}$ in the ρ peak region, where $\eta(s)\frac{\alpha}{\pi}$ is between 0.9% and 0.7%. This calculation assumes point-like pions in the final state. This is a valid assumption in the kinematical configuration of BESIII, as discussed in sections 3.4 and 11.4.

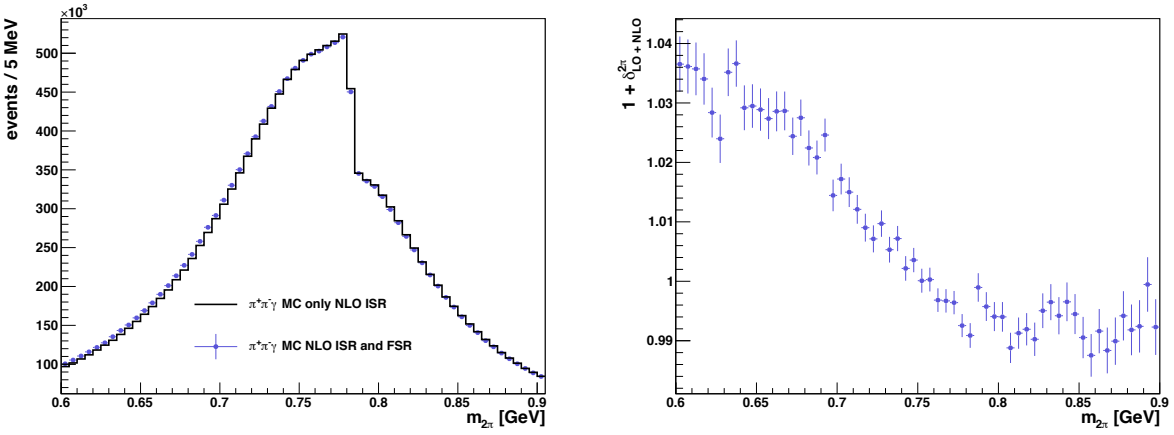

Figure 10.15: Left: $m_{2\pi}$ distributions in case of only NLO ISR and NLO ISR and FSR. The distribution of the latter one is shifted towards smaller masses.
Right: $1 + \delta^{2\pi}_{\rm LO+NLO}$ as function of $m_{2\pi}$.

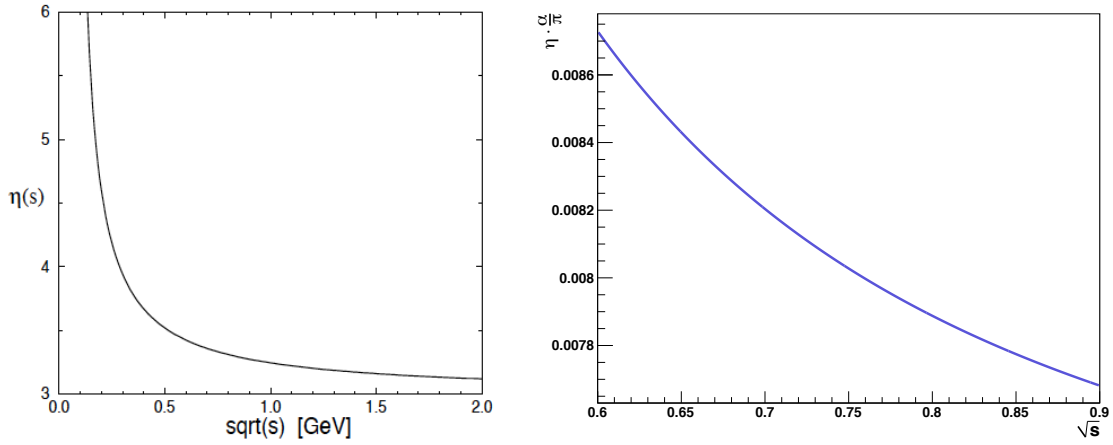

Figure 10.16: Left: LO FSR correction function $\eta(s)$ as a function of the center of mass energy $\sqrt{s}$ [70]. Right: $\eta \cdot \frac{\alpha}{\pi}$ in the ρ peak region investigated. The correction is between 0.9% and 0.7%.

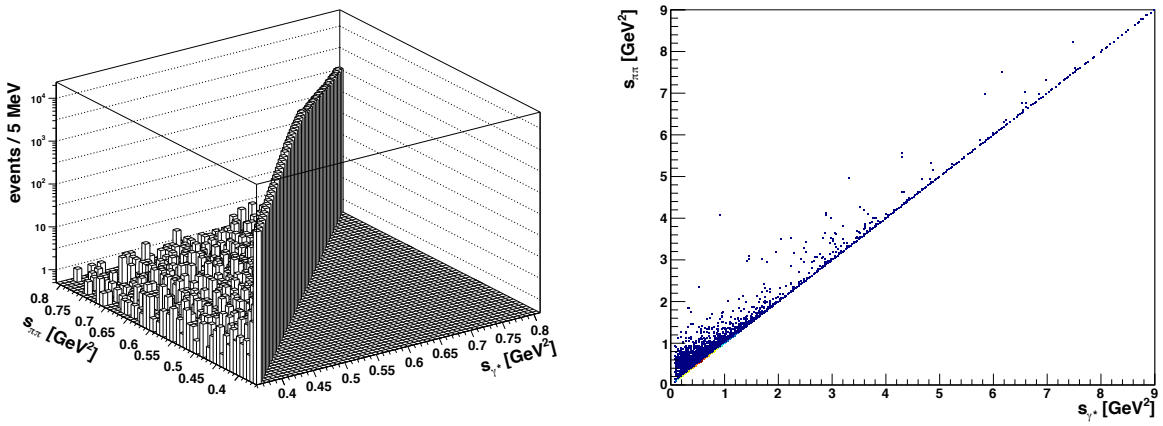

Figure 10.17: Response matrix of the unfolding procedure, to gain the $\pi^+\pi^-(\gamma_{\text{FSR}})$ cross section. $s_{\gamma*}$ corresponds to the four momentum squared of the virtual photon, $s_{\pi\pi}$ to the four momentum squared of the $\pi^+\pi^-$ system, which is equal to $m_{2\pi}$

Method 2

A special version of PHOKHARA, called PHOKHARA Omega [145], is used. With this version, it is possible to distinguish, whether a photon is emitted in the initial or the final state. The momentum transfer of the virtual photon s_{γ^*} is equal to the invariant of the two pions $m^2_{2\pi}$, in case of ISR. If an additional FSR photon is emitted, $m_{2\pi}$ is lowered and, thus, $m^2_{2\pi} < s_{\gamma*}$. The invariant mass $m_{2\pi}$ is shifted towards smaller values. This effect can be handled by an unfolding procedure using the SVD method [104] as described in section 10.3. Correcting for this, one obtains the $\pi^+\pi^-(\gamma_{\text{FSR}})$ cross section, including FSR on the level of $e^+e^- \to \pi^+\pi^-$ events, di-

rectly. Figure 10.17 shows the response matrix used for the unfolding, determined with a $\pi^+\pi^-\gamma$ MC sample, including NLO ISR and FSR, simulated with PHOKHARA Omega. It is $s_{\gamma*}$ vs. $m^2_{2\pi}$.

The difference between using the results of method 1 and method 2 on the $m_{2\pi}$ distribution in data, which is shown in Fig. 10.13, can be seen in Fig. 10.18. It is quantified by a linear fit, yielding to a difference of (0.18 ± 0.13), and, hence, both complementary methods agree well with each other. However, the rounded difference of 0.2% is taken into account as the systematic uncertainty of $\delta^{2\pi}_{\rm FSR}$.

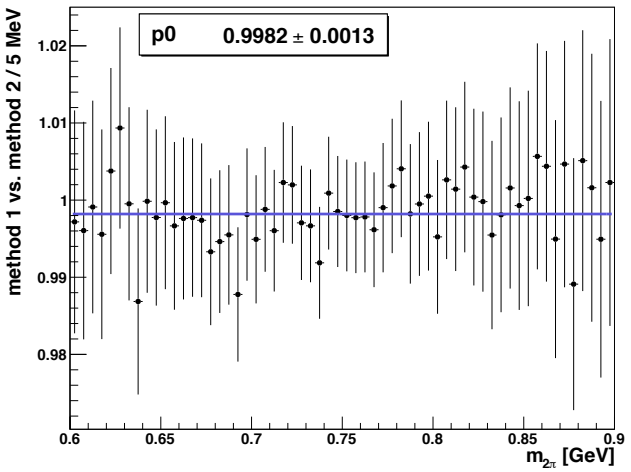

Figure 10.18: Fraction of the $m_{2\pi}$ distribution in data after applying either the $\delta^{2\pi}_{\rm FSR}$ correction from method 1 or method 2. The difference is quantified by a linear fit, yielding $(0.18 \pm 0.13)\%$.

10.6 Extraction of $\sigma^{\text{bare}}(e^+e^- \to \pi^+\pi^-(\gamma_{\text{FSR}}))$: Normalization to $\mathcal{L}$, H, and δ_{VP}

10.6.1 Method

The cross section $\sigma^{\text{bare}}(e^+e^- \to \pi^+\pi^-(\gamma_{\text{FSR}}))$ can be calculated as [105]

$$\sigma^{bare}(e^+e^- \to \pi^+\pi^-(\gamma_{\text{FSR}})) = \frac{N_{2\pi\gamma}}{\mathcal{L} \cdot \epsilon \cdot \frac{2m_{2\pi}}{s} \cdot H \cdot \delta_{VP} \cdot (1 + \delta^{2\pi}_{\text{FSR}})} , \tag{10.5}$$

whereas $N_{2\pi\gamma}/\epsilon$ is the $\pi^+\pi^-\gamma$ event yield after unfolding and after dividing by the efficiency ϵ, as shown in Fig. 10.13, H is the radiator function, $\mathcal{L}$ the luminosity of the data set, and δ_{VP} the vacuum polarization correction in case of $\pi^+\pi^-$ events. This is the approach that has been used at the KLOE 08 [60] and KLOE 10 [61] measurements of this cross section. The luminosity, radiator function, and the vacuum polarization correction are derived in the following, so that finally the cross section can be extracted.

10.6.2 Luminosity measurement using Bhabha scattering events

The luminosity $\mathcal{L}$ of the data taken at $\sqrt{s} = 3.773$ GeV was determined by a measurement of radiative Bhabha scattering and is published in Ref. [86] with an uncertainty of 1.0%. However, this uncertainty turns out to be the limiting factor, if one wants to reach a total systematic uncertainty in $\sigma^{\text{bare}}(e^+e^- \to \pi^+\pi^-(\gamma_{\text{FSR}}))$ in the order of 1%. Some of the estimated uncertainties in this study can be improved. The largest contributions were identified as the uncertainty of the MC event generator used, BABAYAGA 3.5, especially the systematics of the polar angle requirement on charged tracks. It is possible to reduce these two by a better choice of the event generator an a careful reevaluation of the condition on polar angles. Hence, $\mathcal{L}$ is determined again, using Bhabha scattering events, $e^+e^- \to e^+e^-(\gamma)$ [109].

For the new determination of $\mathcal{L}$, the event generator BABAYAGA 3.5, with a claimed uncertainty of 0.5% [92], is replaced by BABAYAGA@NLO, which has an improved uncertainty of 0.1% [93]. The event selection requires two charged tracks emitted close to the IP, within a cylinder with 1 cm radius in the transversal direction and ±10 cm of length along the beam axis. In addition, these tracks are required to be reconstructed in the fiducial volume of the MDC and the barrel EMC, $cos(\theta) < 0.8$. In order to select a clean sample, background needs to be rejected, namely $e^+e^- \to \mu^+\mu^-\gamma$ and ISR production of $e^+e^- \to J/\psi\gamma \to e^+e^-\gamma$. A requirement on the deposited energy of the tracks in the EMC is sufficient to reject the muonic contribution, $E_{EMC} > 0.73 \cdot \sqrt{s} = 1.37$ GeV. Electrons emitted from the J/ψ decay have a maximum momentum of 1.55 GeV. Thus, the requirement for the absolute value of the track momentum, $p_{tr} > 0.93 \cdot$

$E_{beam} = 1.77$ GeV, where E_{beam} is the beam energy, eliminates these events, taking also into account the momentum resolution due to track reconstruction uncertainties.

The luminosity is calculated as

$$\mathcal{L} = \frac{N_{data} - N_{bg}}{\epsilon_{MC} \cdot \sigma_{MC}} = \frac{N_{data}}{\epsilon_{MC} \cdot \sigma_{MC}} \,, \tag{10.6}$$

whereas N_{data} is the event yield in data after applying the above described selection requirements, ϵ_{MC} the selection efficiency determined with MC, and σ_{MC} the $e^+e^- \to e^+e^-(\gamma)$ cross section calculated with the BABAYAGA@NLO event generator. The number of background events N_{bg} is found to be negligible.

source	uncertainty (%)
$cos(\theta) < 0.8$	0.2
E_{EMC}	0.2
$\|p_{tr}\|$	0.2
track reconstruction in MDC	0.3
MC statistics	0.1
Trigger	0.1
Energy calibration	0.1
Generator	0.1
sum	**0.5**

Table 10.3: Systematic uncertainties of the luminosity measurement [109].

The following systematic studies are performed:
(1) The requirements on $cos(\theta)$, E_{EMC}, and $|p_{tr}|$ are varied in meaningful range. The uncertainties found are smaller than 0.2% for each criterium.
(2) The beam energy calibration is studied by assuming a large uncertainty of 2 MeV on E_{beam}. The value of σ_{MC} is determined with the BABAYAGA@NLO generator within $\sqrt{s} \pm 2$ MeV, which corresponds to the beam energy spread. The same seed is used in each simulation to avoid differences due to statistical fluctuations, leading to a systematic uncertainty smaller than 0.1%.
(3) The impact of vacuum polarization corrections on σ_{MC} can be studied with BABAYAGA@NLO. Varying its size by one standard deviation of its uncertainty, the cross section changes by only 0.01%. This effect is, thus, negligible.
(4) Data-MC differences from track reconstruction and trigger information have been studied in Ref. [86] and are found to be 0.3% and 0.1%, respectively.
The uncertainties are listed in Tab. 10.3 and are added in quadrature, yielding a total systematic

uncertainty of 0.5%. This results a final value of

$$\mathcal{L} = (2925 \pm 15)\text{pb}^{-1} \,,$$

where the statistical uncertainty of 0.1% of the MC sample is included in the error.

10.6.3 Radiator function

The radiator function H is described in section 3.2. It is taken from PHOKHARA using the NLO corrections [90]. This is done by producing a bare $\mu^+\mu^-\gamma$ MC sample, i.e. neglecting vacuum polarization effects, with NLO ISR photon emittance, $\sigma^{bare}(e^+e^- \to \mu^+\mu^-\gamma(\gamma))$. This is divided by the exact QED prediction of the bare $e^+e^- \to \mu^+\mu^-$ cross section, which can be expressed as [106]

$$\sigma^{bare}(e^+e^- \to \mu^+\mu^-)(s') = \frac{4\pi\alpha^2}{3s'} \cdot \frac{\beta(3-\beta^2)}{2} \,, \tag{10.7}$$

where $\beta = \sqrt{1 - \frac{4m_\mu^2}{s'}}$, with the muon mass m_μ from [4]. According to formula (3.4) one obtains the radiator function:

$$\frac{2m}{s} \cdot H_{NLO} = \frac{\sigma^{bare}(e^+e^- \to \mu^+\mu^-\gamma(\gamma))}{\sigma^{bare}(e^+e^- \to \mu^+\mu^-)} \,. \tag{10.8}$$

To check whether this procedure is correct, also the LO radiator function is extracted from PHOKHARA and is compared with the exact theoretical LO formula [95]. Both are illustrated in Fig. 10.19 by red data points and the black curve, respectively. As expected, they agree with each other. Also shown is the extracted NLO radiator function from PHOKHARA in green. It is slightly higher than the leading order one, which means that the radiative cross section is enhanced in this energy region, due to NLO soft photon radiation.

10.6.4 Vacuum polarization correction

To obtain the *bare* cross section, which is needed as input for the calculation of $(g-2)_\mu$, vacuum polarization (VP) effects have be corrected. This can be achieved by adjusting the dressed cross section, including vacuum polarization, for the running of the coupling constant α [70]. Bare and dressed cross section are related as [47, Eq. 2]

$$\sigma^{\text{bare}} = \sigma^{\text{dressed}} \cdot \left(\frac{\alpha(0)}{\alpha(s)}\right)^2 \,. \tag{10.9}$$

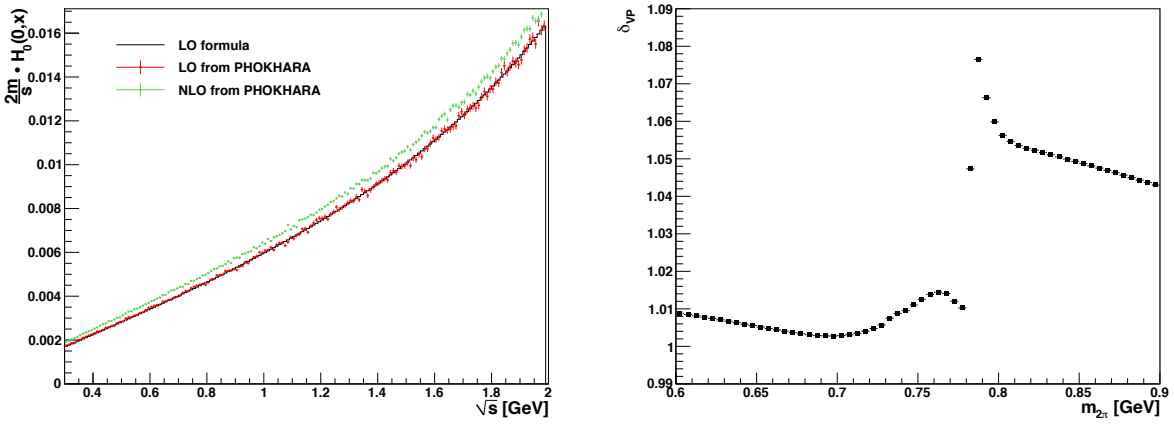

Figure 10.19: Left: The extracted radiator function from PHOKHARA in NLO (green). Also shown is the LO function compared with the exact theoretical formula [95] (red crosses and solid line). Right: Vacuum polarization correction δ_{VP} taken from Ref. [107].

The running of α can be expressed as [70]

$$\alpha(s) = \frac{\alpha(0)}{1 - \Delta\alpha_{lep}(s) - \Delta\alpha_{had}(s)} \,. \tag{10.10}$$

The leptonic part $\Delta\alpha_{lep}(s)$ can be calculated analytically, but the hadronic part $\Delta\alpha_{had}(s)$ comes from a dispersion integral, which includes the R ratio $R(s)$ itself [70]:

$$\Delta\alpha_{had}(s) = -\frac{\alpha(0)\cdot s}{3\pi}\,\Re\int_{4m_\pi^2}^{\infty} ds' \frac{R(s')}{s'(s'-s-i\epsilon)}\,, \tag{10.11}$$

where $\Re$ stands for the real part of the integral, and ϵ a rational number greater than 0. A calculation by Fred Jegerlehner is used for the correction [107]. The effect of the VP in the ρ peak region is presented in Fig. 10.19. The correction is up to 8% at the ρ-ω interference, up to 2% before the interference, and between 4% and 6% after it. This calculation is consistent with calculations by Thomas Teubner (HLMNT11)[2] [108] and Fedor Ignatov (Novosibirsk)[3] within 0.1% [105]. Thus, a conservative systematic uncertainty of 0.2% is used in this analysis.

10.6.5 Extraction of the cross section

After extracting the radiator function H (section 10.6.3) and using the vacuum polarization correction δ_{VP} (10.6.4) from Ref. [107], one can extract the bare $e^+e^- \to \pi^+\pi^-(\gamma_{\rm FSR})$ cross section according to formula (10.5). The result between 600 and 900 MeV is presented in Fig. 10.20. The numerical values are given in appendix A. One can see the broad $\rho(770)$ and

[2] provided by authors, standalone fortran code vp_hlmnt_v2_2.f
[3] http://cmd.inp.nsk.su/~ignatov/vpl

the sharp negative $\rho - \omega$ interference around 780 MeV. The errors shown are statistical only. The sources of systematic uncertainties are listed in Tab. 10.4. They are summed in quadrature, yielding a total uncertainty of 0.9%, which is still dominated by the experimental uncertainty of the luminosity measurement and the theoretical uncertainty of the radiator function.

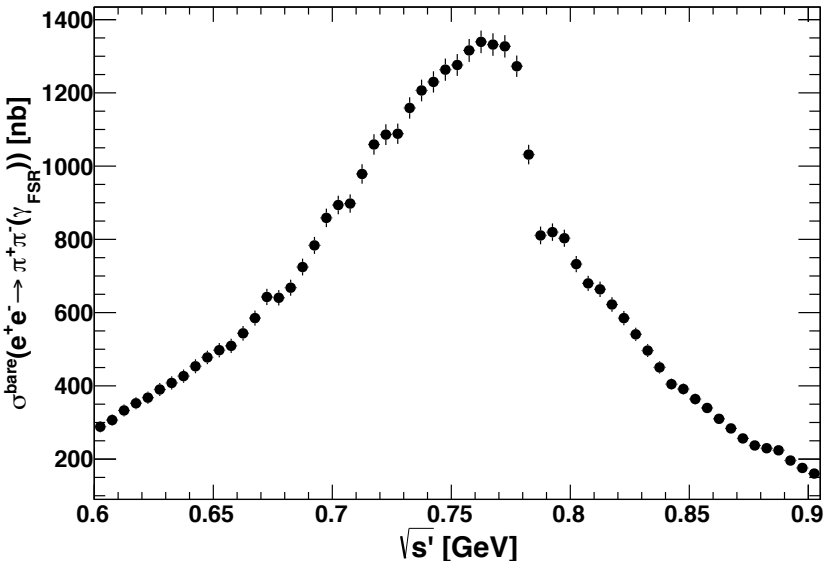

Figure 10.20: Bare $e^+e^- \to \pi^+\pi^-(\gamma_{\text{FSR}})$ cross section, extracted according to formula (10.5), using the $\psi(3770)$ data set from BESIII. The errors are statistical only. The estimated systematic uncertainty in this region is 0.9%.

source	uncertainty (%)
photon efficiency correction	0.2
pion tracking efficiency correction	0.3
pion ANN efficiency correction	0.2
pion e-PID efficiency correction	0.2
ANN	negl.
angular acceptance	0.1
muon background subtraction	0.06
non-muon background subtraction	0.03
unfolding	0.2
FSR correction δ_{FSR}	0.2
vacuum polarization correction δ_{VP}	0.2
radiator function	0.5
Luminosity $\mathcal{L}$	0.5
sum	**0.9**

Table 10.4: Summary of systematic uncertainties of $\sigma^{\text{bare}}(e^+e^- \to \pi^+\pi^-(\gamma_{\text{FSR}}))$.

10.7 Extraction of $\sigma^{\rm bare}(e^+e^- \to \pi^+\pi^-(\gamma_{\rm FSR}))$: Normalization to $\mu^+\mu^-\gamma$ events

One can extract $\sigma^{\rm bare}(e^+e^- \to \pi^+\pi^-(\gamma_{\rm FSR}))$, by normalizing the $\pi^+\pi^-\gamma$ event yield (after unfolding and after division by the efficiency $\epsilon^{2\pi\gamma}$) to the number of $\mu^+\mu^-\gamma$ events. It can be calculated as [105]

$$R = \frac{\sigma^{bare}(e^+e^- \to \pi^+\pi^-(\gamma_{\rm FSR}))}{\sigma^{bare}(e^+e^- \to \mu^+\mu^-)} = \frac{N_{2\pi\gamma}}{N_{2\mu\gamma}} \cdot \frac{\epsilon^{2\mu\gamma} \cdot (1 + \delta^{2\mu}_{\rm FSR,LO+NLO})}{\epsilon^{2\pi\gamma} \cdot (1 + \delta^{2\pi}_{\rm FSR})}\,, \tag{10.12}$$

whereas $N_{2\mu\gamma}$ is the number of $\mu^+\mu^-\gamma$ events from data, $\epsilon^{2\mu\gamma}$ the selection efficiency of $\mu^+\mu^-\gamma$ events, and $\delta^{2\mu}_{\rm FSR,LO+NLO}$ the FSR correction for the two muon production. The bare non-radiative muon cross section is a QED process with point like leptons in the final state. Its cross section is described by equation (10.7). This is the approach that have been exploited at the KLOE 12 [62] and the BaBar [64] measurements of the $\pi^+\pi^-$ cross section. The advantage of this method, compared to the one described in section 10.6.1, is that H, $\mathcal{L}$, and δ_{VP} cancel in the ratio.

The factor $\delta^{2\mu}_{\rm FSR,LO+NLO}$ is the LO and NLO FSR correction for the $\mu^+\mu^-\gamma$ final state. In contrast to $\delta^{2\pi}_{\rm FSR}$ it is not adjusted with the Schwinger calculation (see section 10.5), since the $\mu^+\mu^-$ cross section without any FSR contribution is required in equation (10.12). It is determined, as described in method 1, in section 10.5 using a MC simulation of $e^+e^- \to \mu^+\mu^-\gamma$ instead of $e^+e^- \to \pi^+\pi^-\gamma$ events, without applying the Schwinger term. The result is shown in Fig. 10.21. Shown are the $\mu^+\mu^-$ dimuon invariant mass $m_{2\mu}$ distributions with and without FSR up ton NLO, along with the resulting $(1 + \delta^{2\mu}_{\rm FSR,LO+NLO})$ correction. Muons are point like charged particles and, hence, the FSR correction can be calculated exactly. For $m_{2\mu}$ between 0.6 and 0.9 GeV it is around 1%. For higher masses, it rises strongly up to 20%, however, this has no impact on this work.

The event number $N_{2\mu\gamma}$ is determined in data by using the artificial neural network as a muon selector. The requirement $y_{ANN} < 0.4$ is applied. The result is shown in Fig. 10.22, together with the remaining $\pi^+\pi^-\gamma$ background, estimated with the $\pi^+\pi^-\gamma$ MC from PHOKHARA. Presented is also the fraction of these background events. It is found to be as large as 22%, since the $\pi^+\pi^-$ cross section dominates the $\mu^+\mu^-$ one between 0.6 and 0.9 GeV. This $\pi^+\pi^-\gamma$ background is subtracted from data using a MC distribution. The pion MC is corrected for data MC differences in the photon detection, the pion tracking, the e-PID, and the ANN-PID. The ANN-PID correction is determined, as described in section 8.1.3, applying the

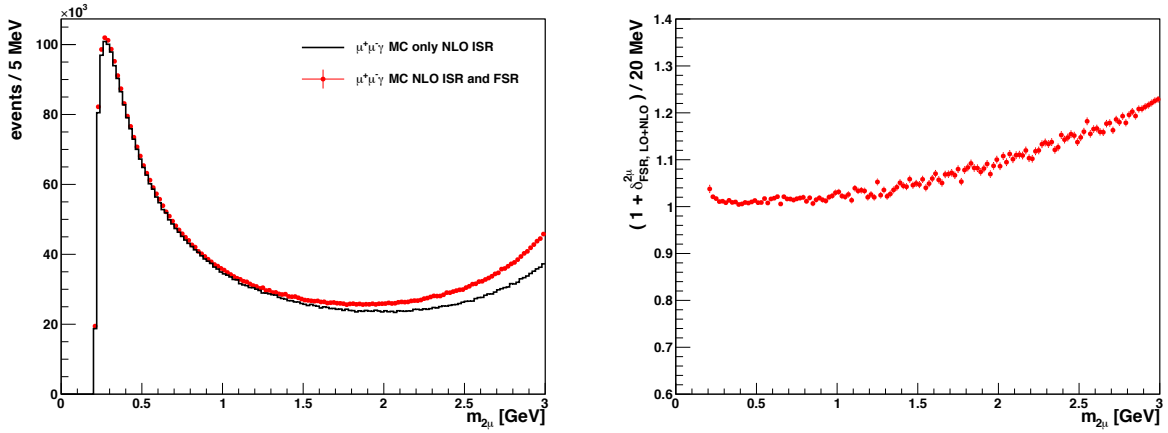

Figure 10.21: Left: MC true distribution of $\mu^+\mu^-\gamma$ events with only ISR events (black line) and including also FSR (red dots).
Right: FSR correction $\delta^{2\mu}_{\text{FSR,LO+NLO}}$ for muon events.

requirement $y_{ANN} < 0.4$. Sources for systematic uncertainties of this MC sample are listed in Tab. 10.5. The contribution of the generator depends mainly on the uncertainty of the radiator function (0.5%) and the form factor model. A conservative error of 2% is estimated for the total uncertainty attributed to the PHOKHARA generator. The various sources are added in quadrature, yielding an uncertainty of 2.2%. Multiplying it with the pion background fraction of 22%, leads to an uncertainty of 0.5%, when subtracting it from data. The sum of other background MC samples is found to be much smaller than 0.1% over the whole mass spectrum, and is, thus, negligible.

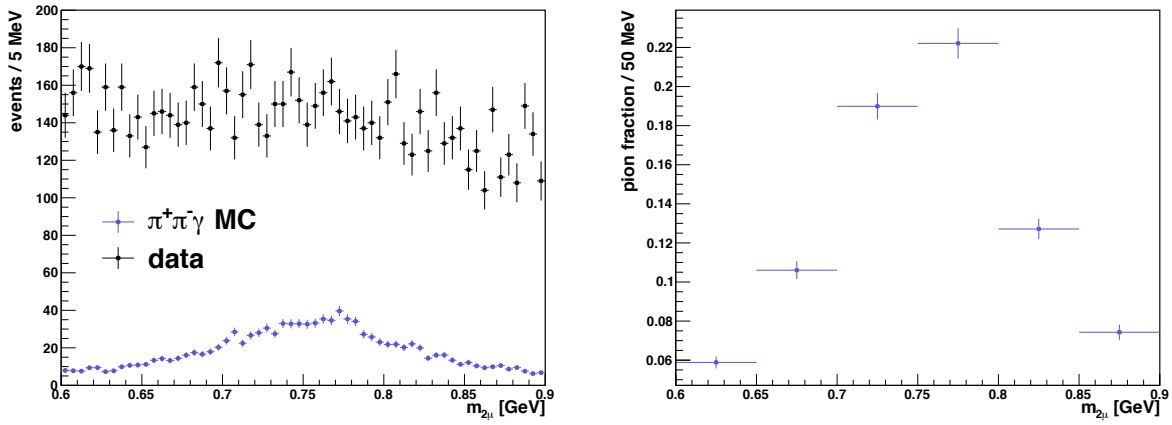

Figure 10.22: Left: Extracted number of $\mu^+\mu^-\gamma$ events from data by using the ANN as muon selector, together with the remaining $\pi^+\pi^-\gamma$ background estimated with MC.
Right: corresponding $\pi^+\pi^-\gamma$ background fraction.

source	uncertainty	cited from
luminosity	0.5%	section 10.6.2
photon efficiency correction	0.2%	section 6.6
muon tracking efficiency correction	0.3%	section 7.1.3
e-PID efficiency correction	0.2%	section 8.1.5
ANN efficiency correction	0.2%	section 8.1.5
accuracy of PHOKHARA	2.0%	[88]
sum	2.2%	

Table 10.5: Systematic uncertainties of the $\pi^+\pi^-\gamma$ MC background sample.

The efficiency $\epsilon^{2\mu\gamma}$ is determined as described in section 10.4, using a $\mu^+\mu^-\gamma$ MC sample instead of a $\pi^+\pi^-\gamma$ one. The data MC efficiency corrections for photon detection (chapter 6), muon tracking (section 7.2), e-PID (section 8.2.4), and ANN-PID (section 8.2) are applied. The ANN-PID correction is determined, as described in section 8.1.3, applying the requirement $y_{ANN} < 0.4$. Since the $m_{2\mu}$ distribution is smooth between 0.6 and 0.9 GeV, the unfolding can be omitted.

The resulting number of $\pi^+\pi^-\gamma$ and $\mu^+\mu^-\gamma$ events can be seen in Fig. 10.23, together with their ratio $R(\sqrt{s})$ from equation (10.12). From this, the bare $e^+e^- \to \pi^+\pi^-(\gamma_{\mathrm{FSR}})$ cross section, using formula (10.12) is computed. The result is presented in Fig. 10.24. The statistical errors are large due to the limited $\mu^+\mu^-\gamma$ statistics. The sources of systematic uncertainties between 0.6 and 0.9 GeV are listed in Tab. 10.6 and are added in quadrature. The photon efficiency correction cancels in the ratio. The final systematic uncertainty is 1.1% and, thus, larger than the normalization to H, $\mathcal{L}$, and δ_{VP}.

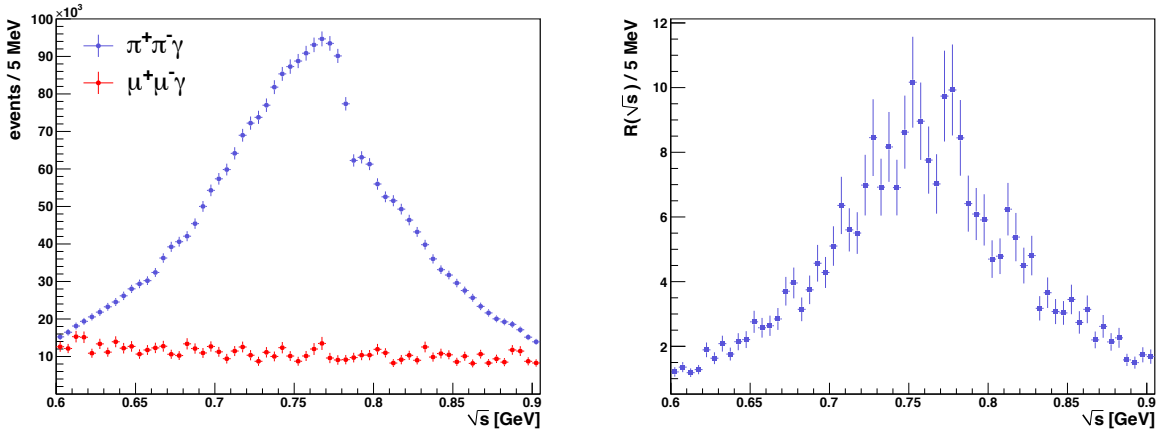

Figure 10.23: Left: Number of measured $\pi^+\pi^-\gamma$ and $\mu^+\mu^-\gamma$ events from data, after normalizing them to the corresponding efficiency and FSR correction.
Right: R ratio from formula (10.12).

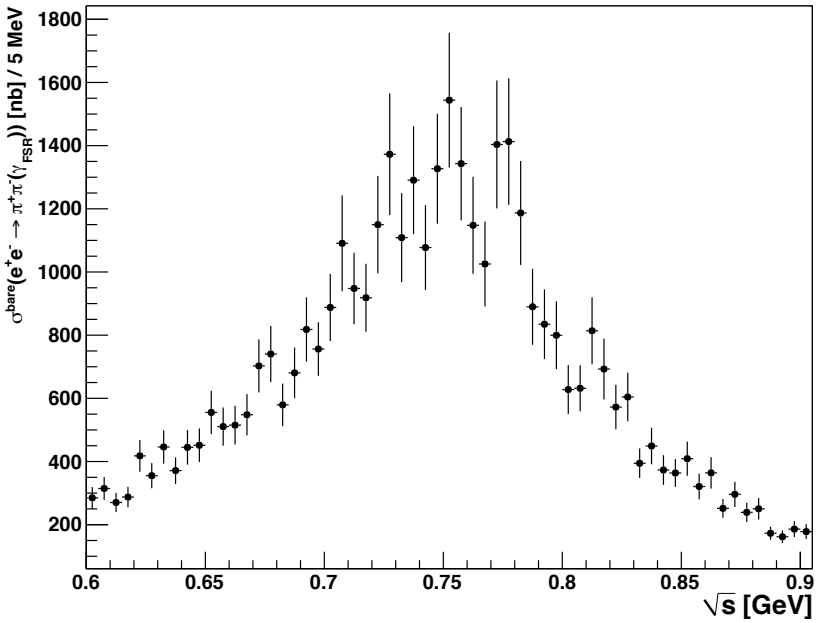

Figure 10.24: Bare $e^+e^- \to \pi^+\pi^-(\gamma_{\mathrm{FSR}})$ cross section extracted from the R ratio. The errors are statistical only.

source	uncertainty (%)
pion tracking efficiency correction	0.3
pion ANN efficiency correction	0.2
pion e-PID efficiency correction	0.2
muon tracking efficiency correction	0.3
muon ANN efficiency correction	0.5
muon e-PID efficiency correction	0.5
ANN	negl.
angular acceptance	0.1
pion background subtraction	0.5
unfolding of $m_{2\pi}$ distribution	0.2
$\delta^{2\pi}_{\mathrm{FSR}}$	0.2
sum	**1.1**

Table 10.6: Summary of systematic uncertainties of $\sigma^{\mathrm{bare}}(e^+e^- \to \pi^+\pi^-(\gamma_{\mathrm{FSR}}))$, extracted from the R ratio.

10.8 Comparison of the normalization methods

The bare $e^+e^- \to \pi^+\pi^-(\gamma_{\rm FSR})$ cross section has been extracted, using two different normalization schemes, as presented in sections 10.6 and 10.7. In the first method, the number of $\pi^+\pi^-\gamma$ events is normalized to $\mathcal{L}$, H, and δ_{VP}, yielding to a systematic uncertainty of 0.9%. This is the approach used at the KLOE 08 and 10 measurements of the $\pi^+\pi^-$ cross section. In the second method, the number of $\pi^+\pi^-\gamma$ events is normalized to $\mu^+\mu^-\gamma$ events, yielding to a systematic uncertainty of 1.1%. This is the approach used at the KLOE 12 and *BABAR* measurements. Besides the better systematic accuracy, the statistical uncertainties of the first method are much smaller, since the second method is limited by the $\mu^+\mu^-\gamma$ statistics. Therefore, the computation of $a_\mu^{\pi\pi,\rm LO}$ as well as the calculation of the pion form factor will performed in chapter 11 based on the first normalization method. Its numerical values can be found in appendix A.

Fig. 10.25 shows the comparison of these two normalization schemes. Their relative difference is quantified by a linear fit to their ratio. It yields a difference of $(0.85 \pm 1.68)\%$, where the error is statistical, with a χ^2 per degrees of freedom of 51/60. They agree within the uncertainty. Since both normalization methods are independent, this is an important cross check for the analysis performed.

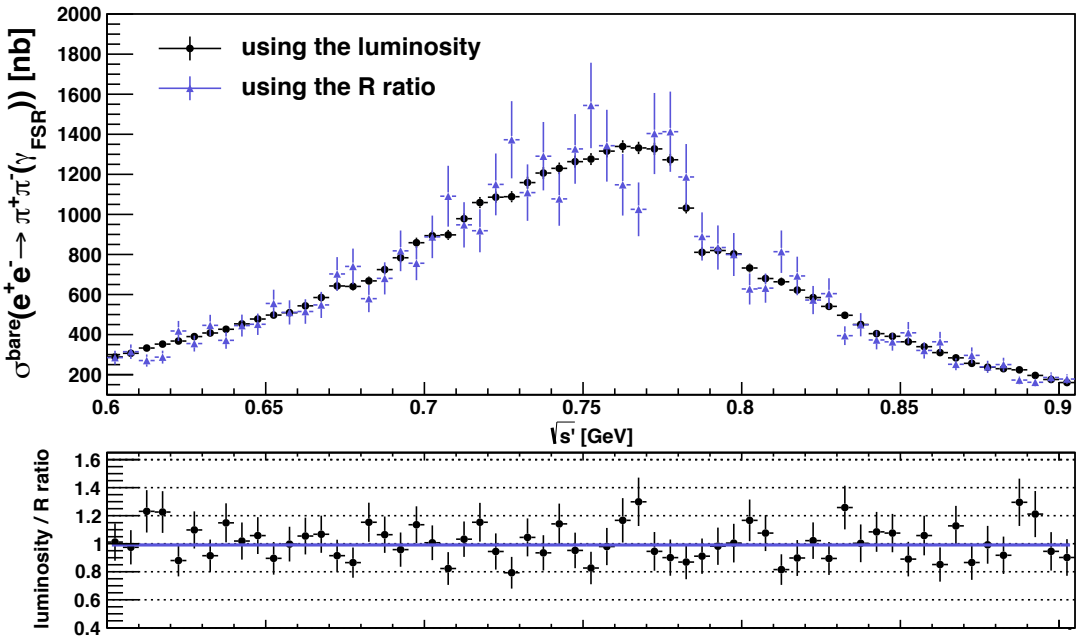

Figure 10.25: Comparison between the two normalization methods, to extract $\sigma^{\rm bare}(e^+e^- \to \pi^+\pi^-(\gamma_{\rm FSR}))$. The normalization to $\mathcal{L}$ and H is shown in black, the normalization to $\mu^+\mu^-\gamma$ events in blue. The lower panel displays their ratio, their difference is quantified by a linear fit with the parameter p0. The errors are statistical.

Chapter 11

Results, comparisons and outlook

After the extraction of $\sigma^{\text{bare}}(e^+e^- \to \pi^+\pi^-(\gamma_{\text{FSR}}))$, the pion form factor squared, $|F_\pi|^2$, can be computed. A fit using the Gounaris-Sakurai parametrization is performed.

The main motivation of this work is to perform a competitive and independent measurement of the $e^+e^- \to \pi^+\pi^-(\gamma_{\text{FSR}})$ cross section. Hence, the outcome of this work is compared with the results from BABAR , KLOE, CMD2, and SND.

Finally, the contribution to $a_\mu^{\pi\pi,\text{LO}}$ is computed for the energy range investigated and compared to the corresponding calculations using the BABAR and KLOE data. It follows a conclusion and an outlook.

11.1 Pion form factor

With the extracted $\pi^+\pi^-$ cross section, one can calculate the pion form factor squared $|F_\pi|^2$ as [70]

$$|F_\pi(s)|^2 = \frac{3s}{\pi\alpha\beta_\pi^3(s)}\sigma^{\text{dressed}}(e^+e^- \to \pi^+\pi^-)(s) \,, \tag{11.1}$$

with the pion velocity $\beta_\pi(s') = \sqrt{1 - 4m_\pi^2/s'}$, and the charged pion mass m_π from Ref. [4]. Here, the dressed cross section σ^{dressed} is required, which means that one needs to include VP effects. Hence, δ_{VP} must not be applied in this extraction of the cross section. In addition, LO FSR has to be corrected for. This is achieved by using $\delta^{2\pi}_{\text{LO+NLO}}$ instead of $\delta^{2\pi}_{\text{FSR}}$ in the extraction of the cross section, i.e. without applying the Schwinger calculation (see section 10.5).

$|F_\pi|^2$ is shown in Fig. 11.1 together with a fit to the data, using the Gounaris-Sakurai (GS) parametrization of the pion form factor [110]. The numerical values are given in appendix A. The function can be found in appendix B. Is has been used as a fit also at the *BABAR* experiment [64]. Free parameters of the fit function are the mass m_ρ and width Γ_ρ of the $\rho(770)$ resonance, the mass m_ω of the $\omega(782)$ resonance, as well as the amplitude $|c_\omega|$ of the Breit-Wigner function, describing the narrow ω resonance, and the phase ϕ_ω of the ρ-ω interference. The width Γ_ω of the ω resonance is fixed to the PDG value [4]. The masses, widths, amplitudes, and phases of higher resonances ρ', ρ'', and ρ''' are taken from Ref. [64], since these are the most precise experimental values and the mass range covered in this work has no sensitivity for these high-mass states. The resulting parameters of the fit to the BESIII form factor data are listed in Tab. 11.1, together with the PDG [4] and *BABAR* [64] results for comparison. As can be seen, the resonance parameters are in agreement with the PDG values [4] within uncertainties, except for Γ_ρ, which shows a 3.4σ deviation. The systematic uncertainty in Γ_ρ due to the assumptions described above has not been quantitatively evaluated. The fit of the ω mass is a cross check within 0.6 MeV, that there is no systematic mass shift in the final result.

The fit describes the data well, yielding a χ^2/ndf = 49.1 / 56. Figure 11.2 shows the normalization of the BESIII pion form factor data to the fit function. Here, the data points show the statistical uncertainties only, while the shaded error band of the fit shows the systematic uncertainty only. The data points are correlated after unfolding the mass spectrum. Hence, they scatter less around the fit result, as one would expect from Gaussian distributed values.

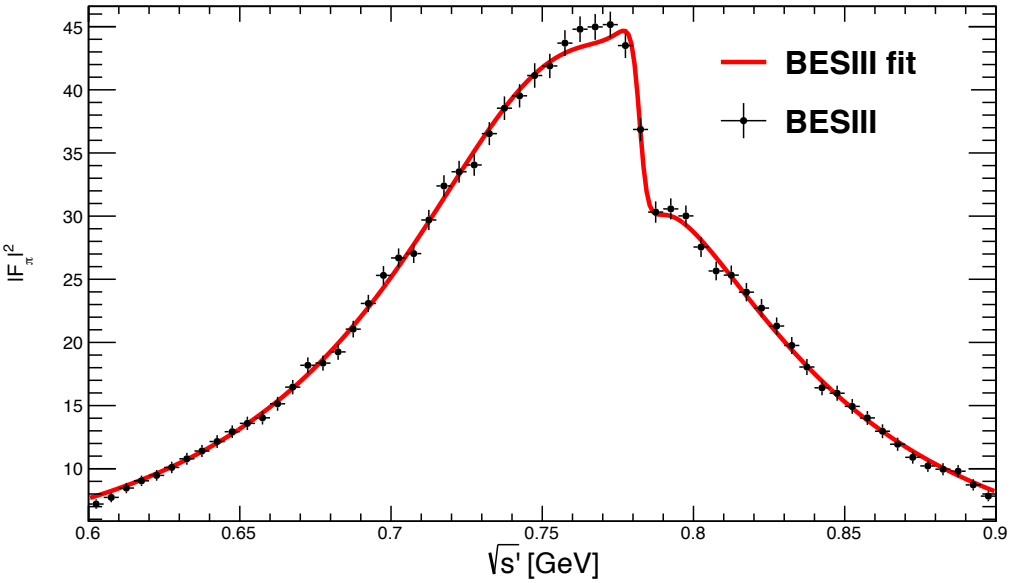

Figure 11.1: The measured squared pion form factor $|F_\pi|^2$. Only statistical errors are shown. The red line represents the fit using the Gounaris-Sakurai parametrization as given in appendix B.

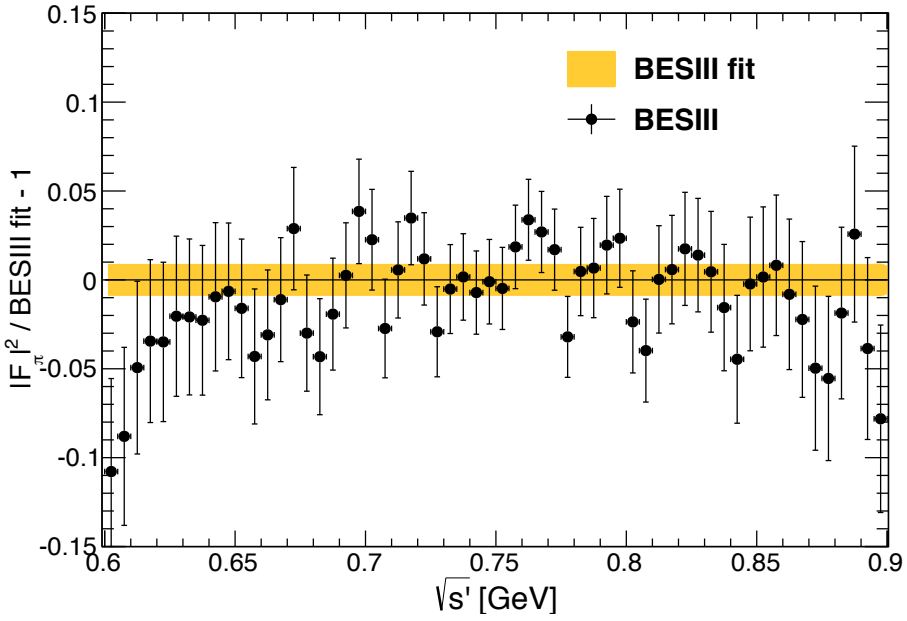

Figure 11.2: Relative difference of the form factor squared from BESIII data and BESIII fit. Statistic uncertainties are included in the data points. The width of the BESIII band shows the systematic uncertainty of 0.9%.

parameter	BESIII	*BABAR*	PDG
m_ρ [MeV/c^2]	776.0 ± 0.4	775.02 ± 0.31	775.49 ± 0.34
Γ_ρ [MeV]	151.7 ± 0.7	149.59 ± 0.67	149.1 ± 0.8
m_ω [MeV/c^2]	782.2 ± 0.6	781.91 ± 0.18	782.65 ± 0.12
$\lvert c_\omega \rvert$ [10^{-3}]	1.7 ± 1.644	0.061 ± 0.2	-
$\lvert \phi_\omega \rvert$ [rad]	0.04 ± 0.13	-0.011 ± 0.037	-

Table 11.1: Fit parameter and statistical errors of the Gounaris-Sakurai fit of the pion form factor, together with the *BABAR* [64] and PDG 2014 [4] values.

11.2 Comparisons to other experiments

The absolute comparison of $\sigma^{\text{bare}}(e^+e^- \to \pi^+\pi^-(\gamma_{\text{FSR}}))$ of this work with the results from *BABAR*, KLOE and CMD2-2006 is shown in Fig. 11.3. The BESIII pion form factor data and the fit result is confronted with the results from *BABAR* and KLOE in Fig. 11.4.

In order to compare the result with previous measurements, the relative difference of the BESIII fit and data from *BABAR* [64], KLOE [60, 61, 62], CMD2 [55, 56], and SND [57] is investigated. The individual comparisons are illustrated in Figs. 11.5, 11.6, and 11.7. Please note that for all comparisons presented in this chapter, the same VP correction [107] is used and hence the KLOE 08, 10, 12, and BaBar data sets have been modified accordingly[1]. The comparisons are presented in Fig. 11.5, 11.6, and 11.7. Here, the shaded error band of the fit includes the systematic uncertainty only, while the uncertainties of the data points include both, the statistical and systematic errors.

A good agreement with *BABAR* above approximately 0.8 GeV is observed, while below this energy a systematic shift is visible, with the *BABAR* data points being systematically higher of about 1-3%. This deviation is, however, not exceeding 1 to 2 standard deviations. All three KLOE spectra for the form factor values are below the BESIII fit on the level of 2-5% in the mass range above the ω mass, while they agree very well below the ρ-ω interference, where a resolution effect is visible. We have also compared our results in the ρ peak region with data from Novosibirsk. The spectra from SND and from the 2006 publication of CMD-2 are found to be in very good agreement with BESIII in the ρ peak region, while the 2004 result of CMD-2 shows a systematic deviation of a few percent. At lower and higher masses, the statistical uncertainties of the Novosibirsk results are too large to draw definite conclusions.

[1] A comparison to the actual published results can be found in appendix D.

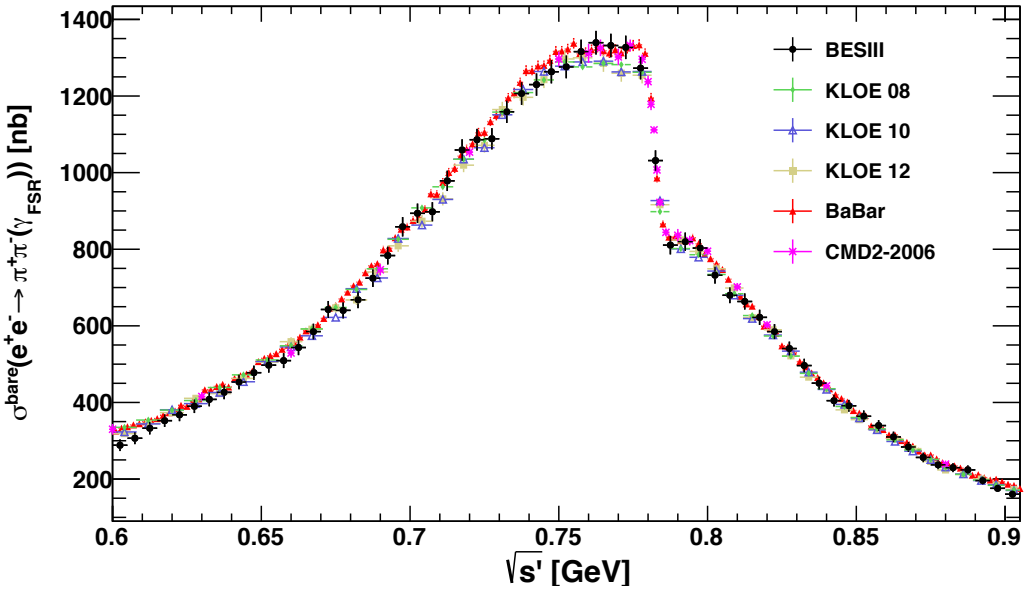

Figure 11.3: $\sigma^{\text{bare}}(e^+e^- \to \pi^+\pi^-(\gamma_{\text{FSR}}))$ from this work, compared to the results from *BABAR* [64], KLOE [60, 61, 62], and CMD2-2006 [56]. The errors are statistical only for the BESIII result, the other ones include statisticcal and systematic uncertainies.

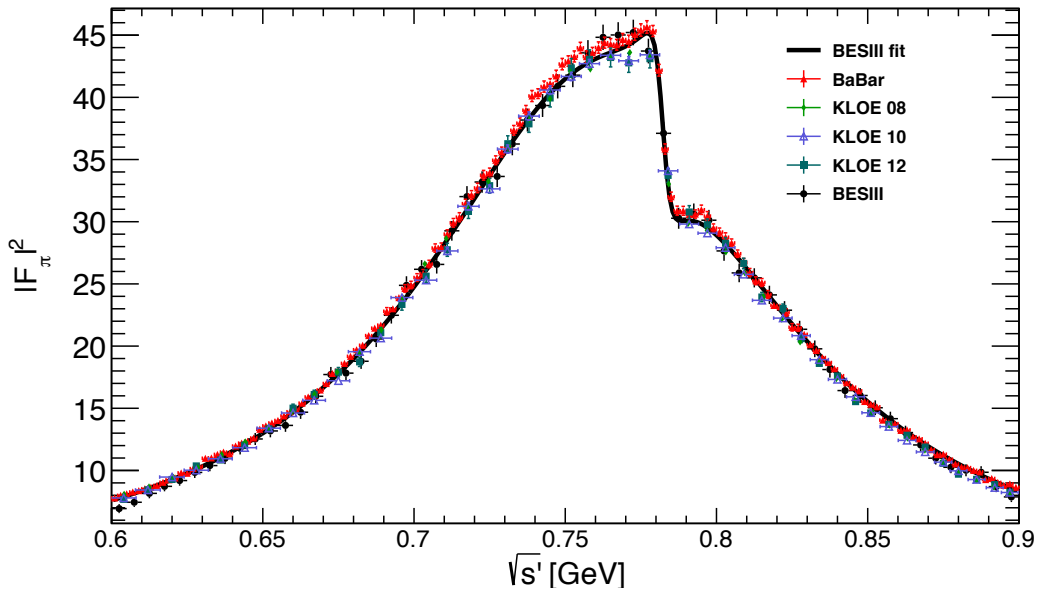

Figure 11.4: $|F_\pi|^2$ data and fit result from this work compared to the results from *BABAR* [64] and KLOE [60, 61, 62]. The errors are statistical only for the BESIII result, the other ones include statistical and systematic uncertainties.

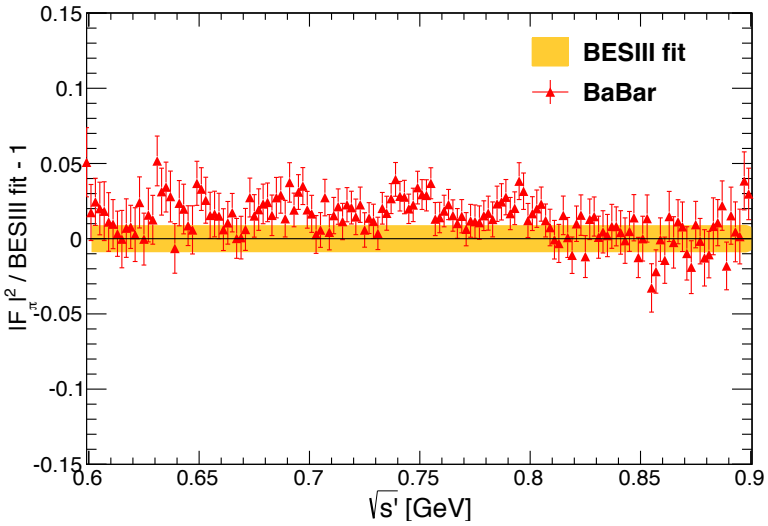

Figure 11.5: Relative difference of the form factor squared from *BABAR* [64] and BESIII fit. Statistic and systematic uncertainties are included in the data points. The width of the BESIII band shows the systematic uncertainty only.

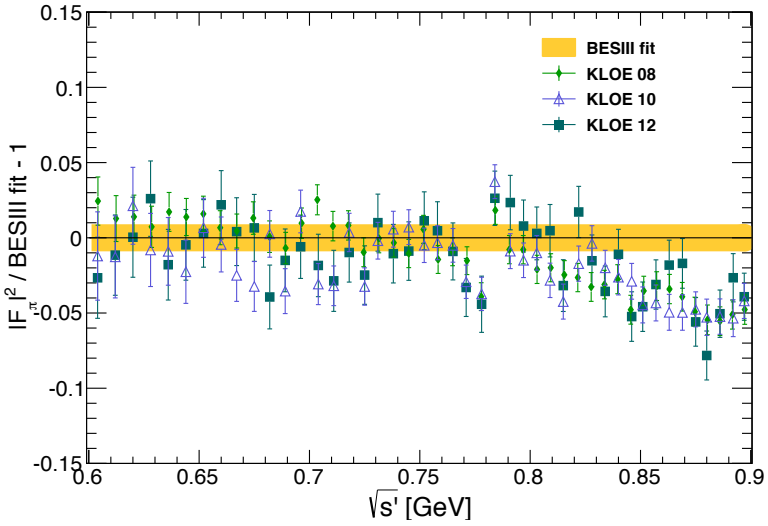

Figure 11.6: Relative difference of the form factor squared from KLOE [60, 61, 62] and BESIII fit. Statistic and systematic uncertainties are included in the data points. The width of the BESIII band shows the systematic uncertainty only.

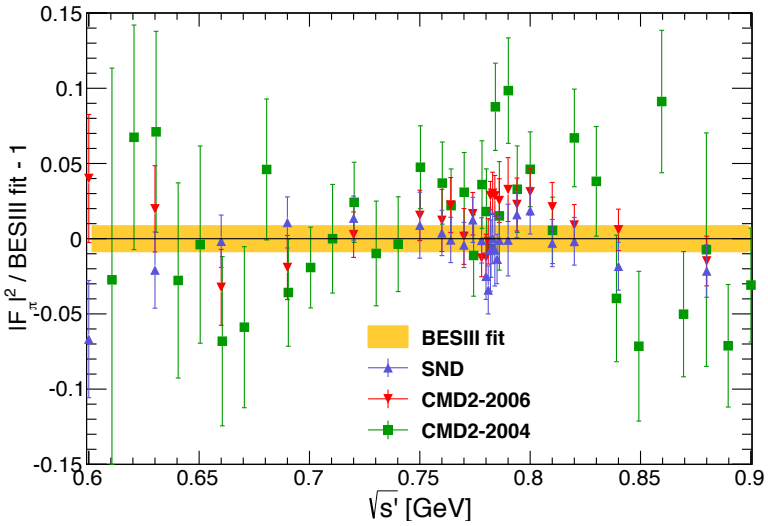

Figure 11.7: Relative difference of the form factor squared from CMD2, SND [55, 56, 57], and BESIII fit. Statistic and systematic uncertainties are included in the data points. The width of the BESIII band shows the systematic uncertainty only.

11.3 Calculation of $a_\mu^{\pi\pi,\mathrm{LO}}$

The contribution of the BESIII cross section measurement $\sigma^{\mathrm{bare}}(e^+e^- \to \pi^+\pi^-(\gamma_{\mathrm{FSR}}))$ to the hadronic contribution of $(g-2)_\mu$ can be computed as [16] (see formula (1.13))

$$a_\mu^{\pi\pi,\mathrm{LO}}(600-900\,\mathrm{MeV}) = \frac{1}{4\pi^3}\int_{(0.6\mathrm{GeV})^2}^{(0.9\mathrm{GeV})^2} \mathrm{ds'K(s')}\sigma^{\mathrm{bare}}(\mathrm{e^+e^-} \to \pi^+\pi^-(\gamma_{\mathrm{FSR}}))\,, \qquad (11.2)$$

where $K(s')$ is the Kernel function [47]. For the calculation of the statistical uncertainty, the correlation of the data points has to be taken into account, as described in appendix E. As summarized in Tab. 11.2 and Fig. 11.8 the BESIII result, $a_\mu^{\pi\pi,\mathrm{LO}}(600-900\ \mathrm{MeV}) = (368.2 \pm 2.5_{\mathrm{stat}} \pm 3.3_{\mathrm{sys}}) \cdot 10^{-10}$, is found to be in favor of the corresponding values of KLOE, while there is a discrepancy of about 1.7 standard deviations to the *BABAR* outcome. The dispersion integral has been evaluated in the energy range between 600 and 900 MeV for KLOE and *BABAR* as well. Please note that for the calculations presented in this section, the same VP correction [107] is used and hence the KLOE 08 and 10 data sets have been modified accordingly[2].

By averaging the KLOE, *BABAR*, and BESIII values of $a_\mu^{\pi\pi,\mathrm{LO}}$ and assuming that the five data sets are independent, a deviation of more than 3σ between the SM prediction of $(g-2)_\mu$ and its direct measurement is confirmed. For the low mass region < 600 MeV$/c^2$ and the high

[2] A comparison to the actual published results can be found in appendix D.

mass region > 900 MeV/c^2, the *BABAR* data was used in this calculation.

experiment	$a_\mu^{\pi\pi,\mathrm{LO}}$ (600 - 900 MeV) $[10^{-10}]$
BABAR	$376.7 \pm 2.0_{\mathrm{stat}} \pm 1.9_{\mathrm{sys}}$
KLOE 08	$368.1 \pm 0.4_{\mathrm{stat}} \pm 2.3_{\mathrm{sys,exp}} \pm 2.2_{\mathrm{sys,theo}}$
KLOE 10	$365.3 \pm 0.9_{\mathrm{stat}} \pm 2.3_{\mathrm{sys,exp}} \pm 2.2_{\mathrm{sys,theo}}$
KLOE 12	$366.7 \pm 1.2_{\mathrm{stat}} \pm 2.4_{\mathrm{sys,exp}} \pm 0.8_{\mathrm{sys,theo}}$
BESIII	$368.2 \pm 2.5_{\mathrm{stat}} \pm 3.3_{\mathrm{sys}}$

Table 11.2: The leading-order (LO) hadronic vacuum polarization 2π contributions to $(\mathrm{g\text{-}2})_\mu$ in the energy range 600 - 900 MeV from BESIII and other e^+e^- experiments [64, 60, 61, 62] with the statistical and systematic errors. Please note that for the calculations presented in this table, the same VP correction [107] is used and hence the KLOE 08 and 10 data sets have been modified accordingly.

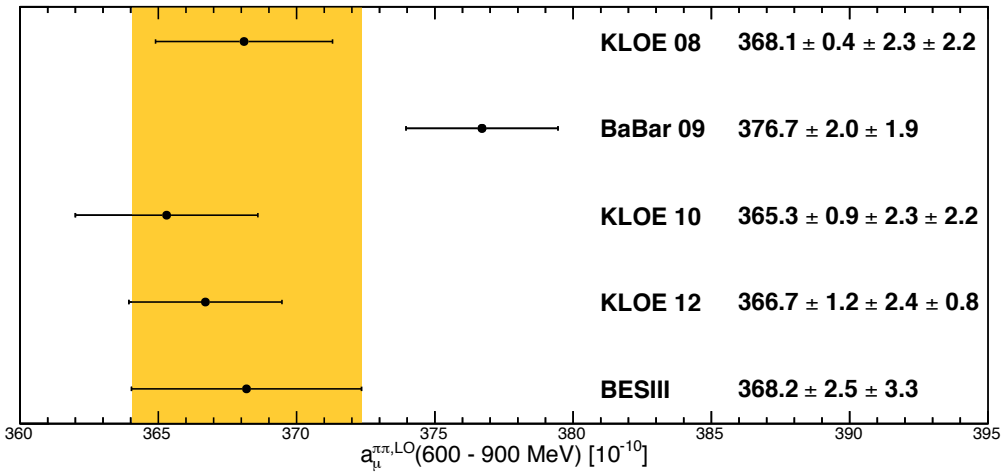

Figure 11.8: Calculation of the leading-order hadronic vacuum polarization 2π contributions to $(\mathrm{g\text{-}2})_\mu$ in the energy range 600 - 900 MeV from BESIII and other e^+e^- experiments [64, 60, 61, 62] with the statistical and systematic errors. The statistic and systematic errors are added quadratically. The band shows the 1σ range of the BESIII result. Please note that for the calculations presented in this figure, the same VP correction [107] is used and hence the KLOE 08 and 10 data sets have been modified accordingly.

11.4 Conclusion, summary and outlook

Using a data set with an integrated luminosity of 2.92 fb^{-1} taken at $\sqrt{s} = 3.773$ GeV with the BESIII detector at the BEPCII facility in Beijing, a new measurement of the $e^+e^- \to \pi^+\pi^-(\gamma_{\mathrm{FSR}})$ cross section, as well as the pion form factor $|F_\pi|^2$, has been performed with an accuracy of 0.9%. The energy range between 600 MeV and 900 MeV, which includes about 70% of the $a_\mu^{\pi\pi,\mathrm{LO}}$ and nearly 50% of the whole $a_\mu^{\mathrm{had,LO}}$ contribution to $(g-2)_\mu$, has been studied with the ISR method. The contribution $a_\mu^{\pi\pi,\mathrm{LO}}$, resulting from the cross section measurement presented here, is:

$$a_\mu^{\pi\pi,\mathrm{LO}}(600-900\ \mathrm{MeV}) = (368.2 \pm 2.5_{\mathrm{stat}} \pm 3.3_{\mathrm{sys}}) \cdot 10^{-10}\ .$$

It is still dominated by the systematic uncertainty. Further and more detailed investigations are planned to achieve a significant improvement. One of the largest contributions to the systematic uncertainty, as listed in Tab. 10.4, stems from the radiator function. A more precise description is one of the most promising options for a reduction of the total systematic uncertainty. From the point of view of statistics, more than twice the integrated luminosity is already available at BESIII, taken at higher cms energies between 4 and 4.4 GeV. More data is added in each running period. Analyzing this, the statistical error can be reduced significantly, which might lead to a competitiveness of the normalization method to R ratio, if the corresponding systematic uncertainty can also be reduced when performing the efficiency studies with larger data samples.

The BESIII result of $a_\mu^{\mathrm{had,LO}}$ is found to be in good agreement with the corresponding values of KLOE and shows a difference of about 1.7σ with respect to the *BABAR* outcome. By averaging the KLOE, *BABAR* and BESIII values of $a_\mu^{\pi\pi,\mathrm{LO}}$ and assuming that the five data sets are independent, a deviation of more than 3σ between the SM prediction of $(g-2)_\mu$ and its direct measurement is confirmed. Including the BESIII result from this work in the theoretical computation of $a_\mu^{\pi\pi,\mathrm{LO}}$, Thomas Teubner was able to reduce its uncertainty from $3.1 \cdot 10^{-10}$ to $2.6 \cdot 10^{-10}$ [111] and, thus, by nearly 20% [3]. This shows the impact that this analysis can have.

The analysis presented in this thesis is published in Ref. [112]. With the artificial neural network and efficiency corrections developed in this work, we performed further studies, which are not topic of this thesis:

- We performed a dark photon γ' search, exploiting its possible ISR production and decay into an e^+e^- or $\mu^+\mu^-$ pair. An exclusion limit on the mixing parameter ϵ^2, describing

[3] This is a preliminary calculation using the *BABAR*, the three KLOE, and the BESIII data sets. The dispersion integral for $a_\mu^{\pi\pi,\mathrm{LO}}$ is calculated in the energy range between 0.305 and 2.0 GeV, using the HLMNT11 vacuum polarization correction [108, 111].

the strength of the dark photon coupling to standard model matter, is set in the dark photon mass range between 1.5 and 3.4 GeV, which supersedes all previous measurements in this mass range [113]. This measurement will be published in a separate paper. A short overview of this work is given in appendix F.

- We measured the electronic width of the J/ψ resonance, $\Gamma_{ee}(J/\psi)$, with unrivaled precision, by using its ISR production and its muonic decay $e^+e^- \to J/\psi\gamma \to \mu^+\mu^-\gamma$. The result is $\Gamma_{ee}(J/\psi) = (5.58 \pm 0.05_{\text{stat}} \pm 0.08_{\text{sys}})$ keV. This work will also be published in a separate paper. A short overview of this analyses is given in appendix G.

- In e^+e^- annihilations only $J^{PC} = 1^{--}$ states can be produced due to quantum number conservation. In this case J is the total angular momentum, P the parity, and C the charge conjugation. Only the neutral gauge bosons γ and Z^0, and the vector resonances ρ, ϕ, ω etc. can be produced via one production vertex. Therefore, the direct production of the χ_{c1}, which is a 1^{++} state [4], via e^+e^- annihilation is forbidden by the quantum numbers. However, it can be created via a two photon exchange (see figure 11.9). This is a second order process and, thus, highly suppressed. This process is so rare that it has never been observed at an e^+e^- facility, yet. Within this thesis we have developed the optimal tools to search its direct ISR production: $e^+e^- \to \gamma_{ISR}\chi_{c1} \to \gamma_{ISR}\gamma J/\psi \to \gamma_{ISR}\gamma\mu^+\mu^-$. The result from data is shown in Fig. 11.9 together with the signal and the background MC samples.

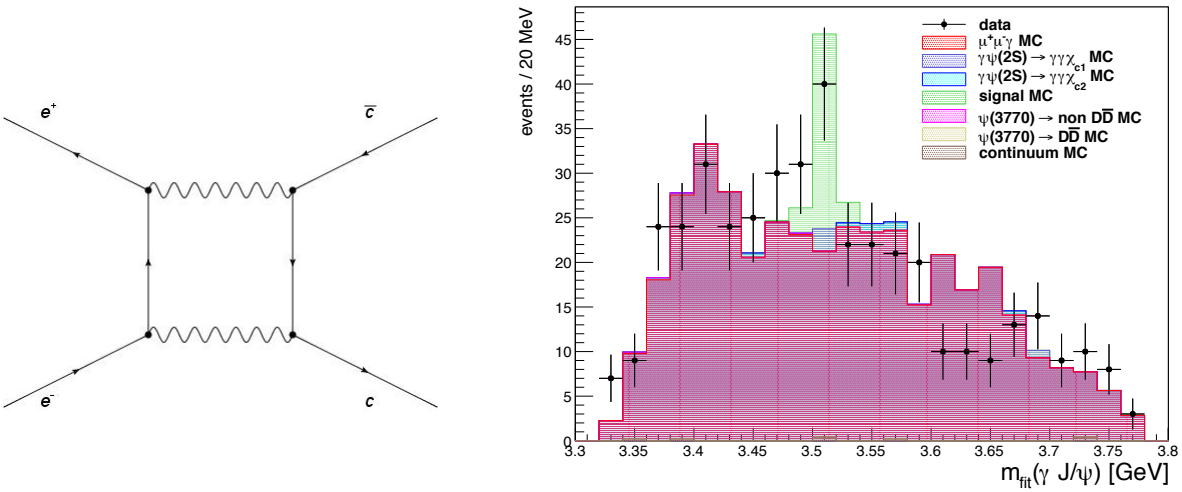

Figure 11.9: Left: Feynman diagram of the direct production of a $J^{PC} = 1^{++}$ state (charmonium in this case) via e^+e^- annihilation. This is only possible via a highly suppressed two photon exchange.
Right: Event yield in data after selecting the ISR production of the χ_{c1} resonance, $e^+e^- \to \gamma_{ISR}\chi_{c1} \to \gamma_{ISR}\gamma J/\psi \to \gamma_{ISR}\gamma\mu^+\mu^-$, together with signal MC (green) and background MC samples in bins of the $\gamma J/\psi$ invariant mass.

Indeed, we observed an enhancement in data at the predicted position of the signal phase space MC. Unfortunately, this enhancement has a significance of 2σ only and, thus, too less to claim an observation. However, based on these results we applied for beam time at BESIII for a scan around the χ_{c1} resonance. With this data, the direct χ_{c1} production could be observed and, maybe, an observation can be made in the future.

- As already shown in Fig. 3.4, the untagged measurement of the $e^+e^- \to \pi^+\pi^-$ cross section is possible at energies greater than 900 MeV. We did first studies and a detailed analysis will be performed in the near future. The event yield from data is presented in Fig. 11.10. The negative interferences with the $\rho(1450)$ and $\rho(1700)$ resonances can be seen. The energy region above 1 GeV is less important for the calculation of a_μ^{had}. However, The only ISR measurement in this energy range has been performed by *BABAR* [64] but due to their detector geometry this measurement was limited to tagged ISR events. Exploiting untagged ISR events we can achieve a so far unrivaled statistical precision above 1 GeV at BESIII. Interesting spectroscopy analyses and a search for a possible dark photon decay into pions, $e^+e^- \to \gamma' \to \pi^+\pi^-$, will be possible in the near future with the developed tools in this thesis.

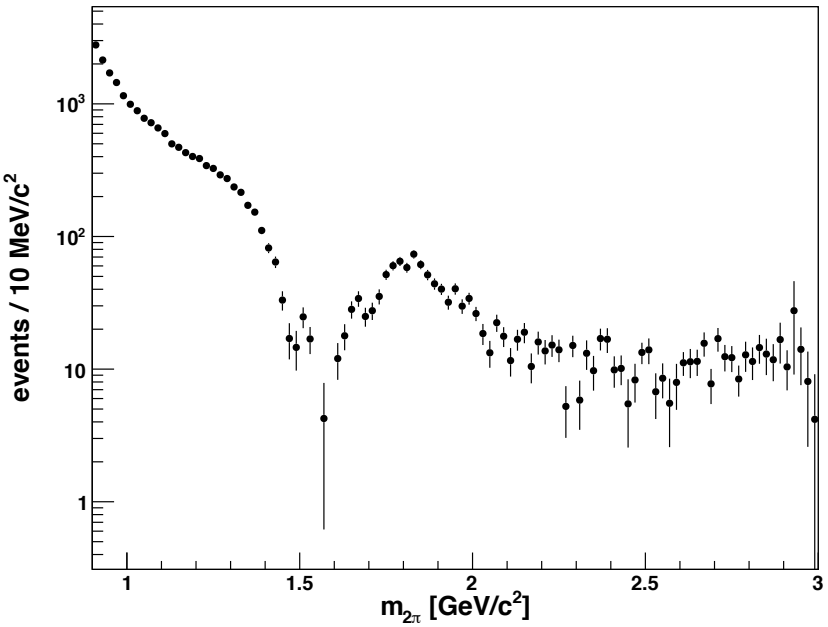

Figure 11.10: Event yield from 2.9 fb^{-1} data after selecting untagged $\pi^+\pi^-\gamma$ events.

- As discussed in section 3.4, the PHOKHARA generator describes FSR assuming point-like pions. We confronted this model with data in a preliminary measurement of the forward-backward asymmetry of the $e^+e^- \to \pi^+\pi^-$ cross section. The preliminary result

is presented in Fig. 11.11. No sizable effect beyond the point-like pion model is observed at the moment. A precise analysis will be performed in the near future using the tools and knowledge gained in this thesis.

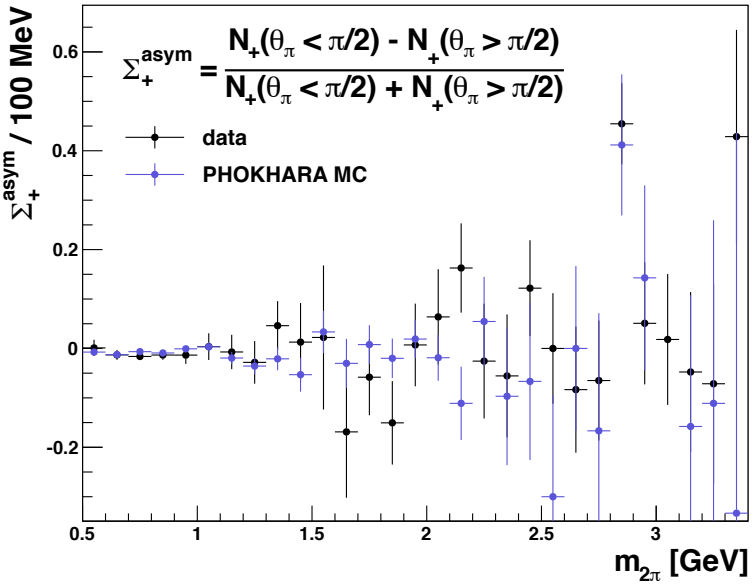

Figure 11.11: Forward-backward asymmetry Σ^{asym} of $e^+e^- \to \pi^+\pi^-\gamma$ events N. Shown is the result for positively charged pions and a tagged ISR photon in data and MC.

The next decade will be crucial as well as interesting for the $(g-2)_\mu$ puzzle. On the experimental side, two independent measurements of a_μ^{exp} will be performed in the USA [23] and Japan [24]. Both aim to reduce the current uncertainty on the experimental value by a factor of 4 or more. This shows the necessity to improve also the SM prediction. On the theoretical side, the ISR program at BESIII will continue with investigations of hadronic cross sections of the final states $\pi^+\pi^-\pi^0$ [114] and $\pi^+\pi^-\pi^0\pi^0$ [115], which will give a significant impact on the uncertainty of $a_\mu^{\text{had,LO}}$. The error of the SM prediction is still dominated by the hadronic Light-by-Light contribution $a_\mu^{\text{had,LBL}}$ [16]. Experimental input from the BESIII $\gamma\gamma$ physics program, investigating the π^0 [116, 117], η [118, 119], η' [118, 119] and $\pi^+\pi^-$ [117] $\gamma\gamma$ production, will contribute significantly to this important topic. With all this new, interesting results, it will hopefully be possible to judge, whether our current knowledge of Δa_μ is only a statistical fluctuation or the first observation of New Physics beyond the Standard Model.

Appendix A

Cross section and form factor values

$\sqrt{s'}$ [MeV]	$\sigma^{bare}_{\pi^+\pi^-(\gamma_{\rm FSR})}$ [nb]	$\lvert F_\pi\rvert^2$	$\sqrt{s'}$ [MeV]	$\sigma^{bare}_{\pi^+\pi^-(\gamma_{\rm FSR})}$ [nb]	$\lvert F_\pi\rvert^2$
602.5	288.3 ± 15.2	6.9 ± 0.4	752.5	1276.1 ± 29.8	41.8 ± 1.0
607.5	306.6 ± 15.5	7.4 ± 0.4	757.5	1315.9 ± 31.3	43.6 ± 1.0
612.5	332.8 ± 16.3	8.2 ± 0.4	762.5	1339.3 ± 30.9	44.8 ± 1.0
617.5	352.5 ± 16.3	8.7 ± 0.4	767.5	1331.9 ± 30.8	45.0 ± 1.0
622.5	367.7 ± 16.6	9.2 ± 0.4	772.5	1327.0 ± 30.6	45.2 ± 1.0
627.5	390.1 ± 17.7	9.8 ± 0.4	777.5	1272.7 ± 29.2	43.7 ± 1.0
632.5	408.0 ± 18.0	10.4 ± 0.5	782.5	1031.5 ± 26.7	37.1 ± 0.9
637.5	426.6 ± 18.1	11.0 ± 0.5	787.5	810.7 ± 24.2	30.3 ± 0.8
642.5	453.5 ± 19.0	11.8 ± 0.5	792.5	819.7 ± 23.8	30.6 ± 0.8
647.5	477.7 ± 18.5	12.5 ± 0.5	797.5	803.1 ± 23.3	30.1 ± 0.8
652.5	497.4 ± 19.5	13.2 ± 0.5	802.5	732.4 ± 22.1	27.7 ± 0.8
657.5	509.2 ± 19.4	13.6 ± 0.5	807.5	679.9 ± 20.6	25.9 ± 0.7
662.5	543.4 ± 19.9	14.7 ± 0.5	812.5	663.6 ± 21.0	25.5 ± 0.8
667.5	585.0 ± 20.5	16.0 ± 0.6	817.5	622.2 ± 19.9	24.1 ± 0.7
672.5	642.7 ± 22.2	17.7 ± 0.6	822.5	585.0 ± 19.5	22.9 ± 0.7
677.5	640.5 ± 21.0	17.8 ± 0.6	827.5	540.8 ± 18.1	21.4 ± 0.7
682.5	668.0 ± 21.9	18.8 ± 0.6	832.5	496.4 ± 17.7	19.8 ± 0.7
687.5	724.4 ± 22.9	20.6 ± 0.6	837.5	450.4 ± 16.8	18.1 ± 0.6
692.5	783.5 ± 23.2	22.5 ± 0.7	842.5	404.7 ± 15.2	16.4 ± 0.6
697.5	858.6 ± 25.3	24.9 ± 0.7	847.5	391.3 ± 15.4	16.0 ± 0.6
702.5	893.8 ± 25.4	26.2 ± 0.7	852.5	364.0 ± 15.0	15.0 ± 0.6
707.5	897.8 ± 25.0	26.6 ± 0.7	857.5	339.6 ± 14.0	14.2 ± 0.6

$\sqrt{s'}$ [MeV]	$\sigma^{bare}_{\pi^+\pi^-(\gamma_{\mathrm{FSR}})}$ [nb]	$\lvert F_\pi\rvert^2$	$\sqrt{s'}$ [MeV]	$\sigma^{bare}_{\pi^+\pi^-(\gamma_{\mathrm{FSR}})}$ [nb]	$\lvert F_\pi\rvert^2$
712.5	978.6 ± 26.6	29.3 ± 0.8	862.5	310.0 ± 13.7	13.0 ± 0.6
717.5	1059.1 ± 27.9	32.0 ± 0.8	867.5	283.8 ± 13.0	12.1 ± 0.5
722.5	1086.0 ± 28.3	33.2 ± 0.9	872.5	256.5 ± 12.4	11.0 ± 0.5
727.5	1088.4 ± 27.7	33.6 ± 0.9	877.5	237.3 ± 11.4	10.3 ± 0.5
732.5	1158.8 ± 29.2	36.2 ± 0.9	882.5	229.7 ± 11.6	10.0 ± 0.5
737.5	1206.5 ± 29.6	38.2 ± 0.9	887.5	224.0 ± 11.6	9.9 ± 0.5
742.5	1229.9 ± 29.0	39.3 ± 0.9	892.5	196.1 ± 10.5	8.7 ± 0.4
747.5	1263.3 ± 30.3	40.9 ± 1.0	897.5	175.9 ± 9.7	7.9 ± 0.4

Table A.1: Results of the BESIII measurement of the cross section $\sigma^{bare}_{\pi^+\pi^-(\gamma_{\mathrm{FSR}})} \equiv \sigma^{bare}(e^+e^- \to \pi^+\pi^-(\gamma_{\mathrm{FSR}}))$ and the squared pion form factor $|F_\pi|^2$. The errors are statistical only. The value of $\sqrt{s'}$ represents the bin center.

Appendix B

Gounaris-Sakurai parametrization of the pion form factor

The Gounaris-Sakurai (GS) parametrization of the pion form factor $F_\pi(s)$ can be expressed as [64, 110]

$$F_\pi(s) = \frac{b(\rho)\frac{1+c_\omega BW_\omega^{KS}(s,m_\omega,\Gamma_\omega)}{1+c_\omega} + b(\rho') + b(\rho'') + b(\rho''')}{1 + c_{\rho'} + c_{\rho''} + c_{\rho'''}} \,, \tag{B.1}$$

$$b(\xi) = c_\xi BW_\xi^{GS}(s,m_\xi,\Gamma_\xi) \,. \tag{B.2}$$

It satisfies $F_\pi(0) = 1$. The complex amplitudes of the Breit-Wigner (BW) functions are given by

$$c_\xi = |c_\xi| e^{i\phi_\xi} \,, \tag{B.3}$$

whereas ϕ_ξ is the phase, and $|c_\xi|$ is the magnitude. The BW of the broad ρ, ρ', ρ'', and ρ'''' resonances are described as

$$BW^{GS}(s,m,\Gamma) = \frac{m^2(1 + a(m)\Gamma/m)}{m^2 - s + z(s,m,\Gamma) - im\Gamma(s,m,\Gamma)} \,, \tag{B.4}$$

and the BW of the ω resonance as

$$BW_\omega^{KS}(s,m,\Gamma) = \frac{m^2}{m^2 - s - im\Gamma} \,, \tag{B.5}$$

with

$$\Gamma(s,m,\Gamma) = \Gamma\frac{s}{m^2}\left(\frac{\beta_\pi(s)}{\beta_\pi(m^2)}\right)^2 , \tag{B.6}$$

where $\beta_\pi(s) = \sqrt{1-4m_\pi^2/s}$ is the pion velocity, and m_π the charged pion mass. This energy dependence is valid below 1 GeV. The further functions in the GS parametrization are:

$$a(m) = \frac{3m_\pi^2}{\pi k^2(m^2)}\ln\left(\frac{m+2k(m^2)}{2m_\pi}\right) + \frac{m}{2\pi g(m^2)} - \frac{m_\pi^2 m}{\pi g^3(m^2)} , \tag{B.7}$$

$$z(s,m,\Gamma) = \frac{\Gamma m^2}{g^3(m^2)}[g^2(s)(h(s)-h(m^2)) + (m^2-s)g^2(m^2)h'(m^2)] , \tag{B.8}$$

where

$$g(s) = \frac{1}{2}\sqrt{s}\beta_\pi(s) , \tag{B.9}$$

$$h(s) = \frac{2g(s)}{\pi\sqrt{s}}\ln\left(\frac{\sqrt{s}+2g(s)}{2m_\pi}\right) , \tag{B.10}$$

and $h'(s)$ is the derivative of $h(s)$.

Appendix C

Variables used as input for the artificial neural network

The variables considered for the training of the artificial neural network, as described in chapter 5, are presented below. Shown are the comparisons of the $\pi^+\pi^-\gamma$ and $\mu^+\mu^-\gamma$ MC samples, which are used for the training. They are scaled to the same arbitrary luminosity. The seven variables finally used as input for training the ANN are listed in Tab. 5.2.

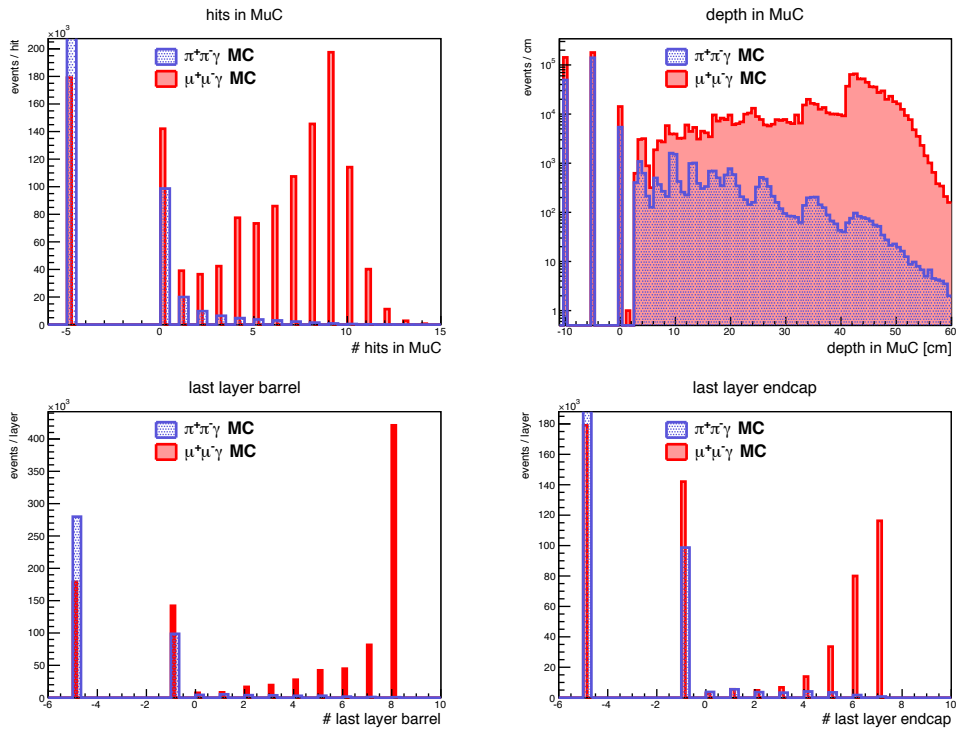

Figure C.1: MUC variables.

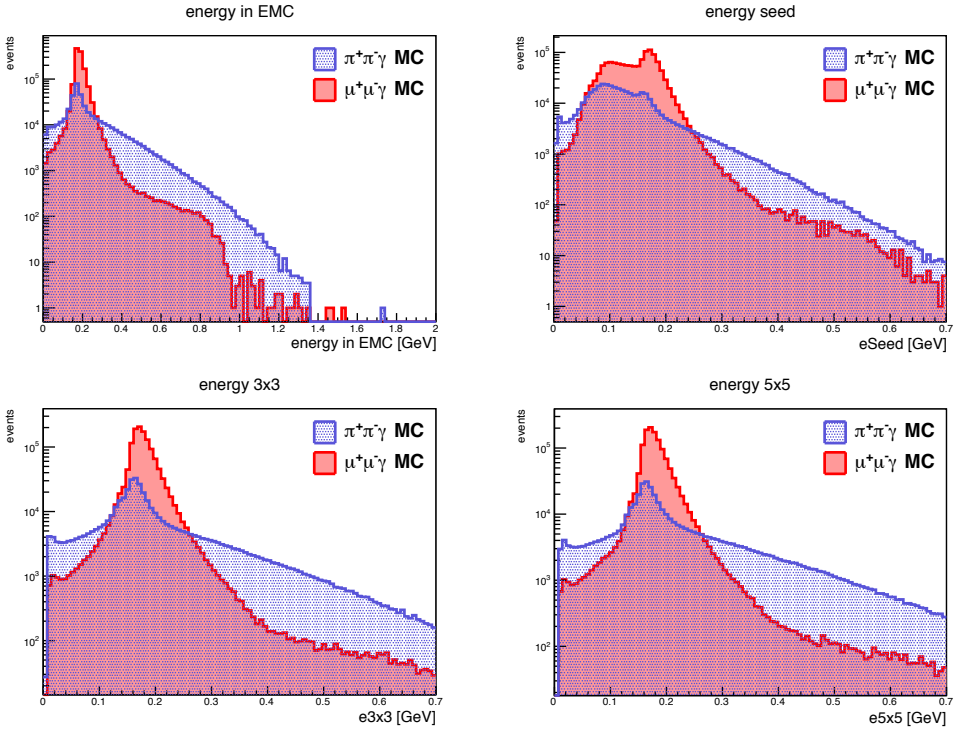

Figure C.2: Energy deposition in EMC.

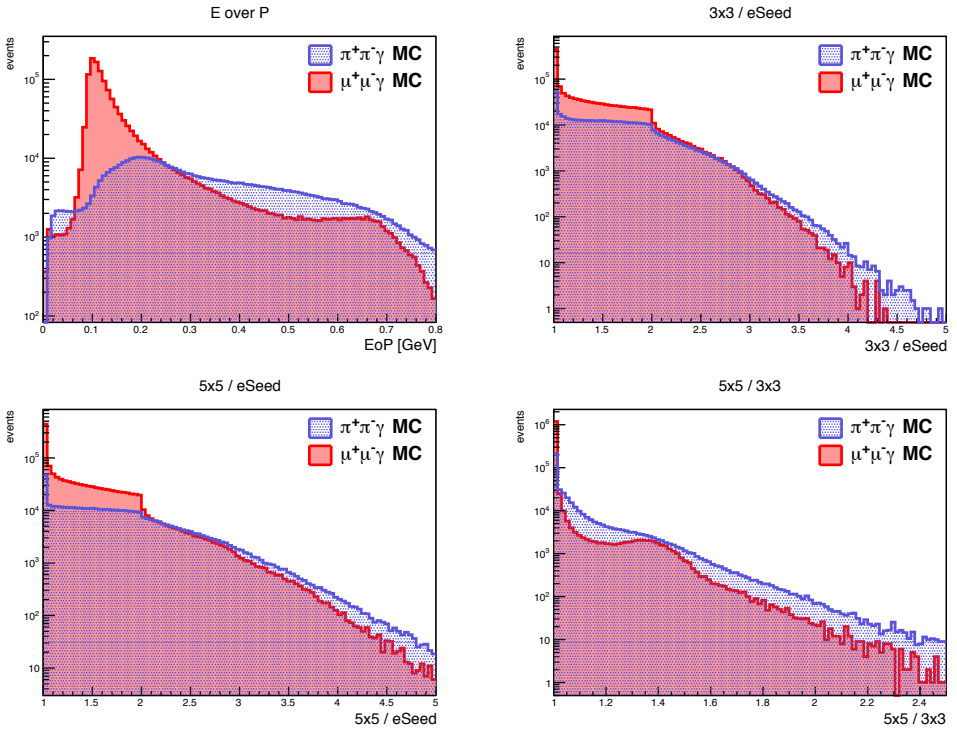

Figure C.3: E over P and energy ratios from EMC.

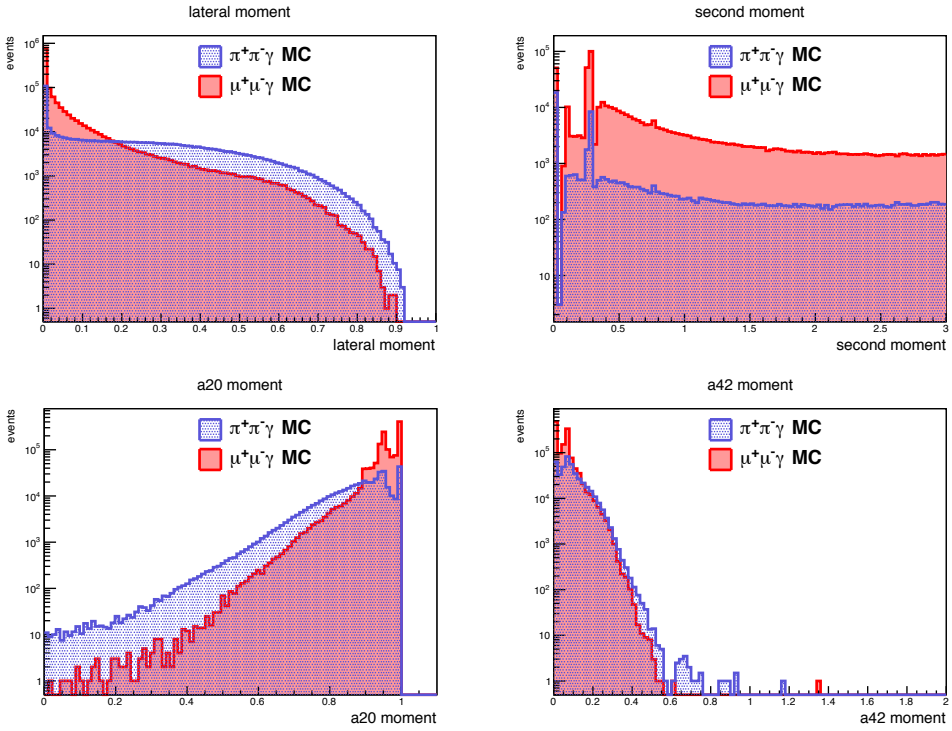

Figure C.4: Shower shape variables.

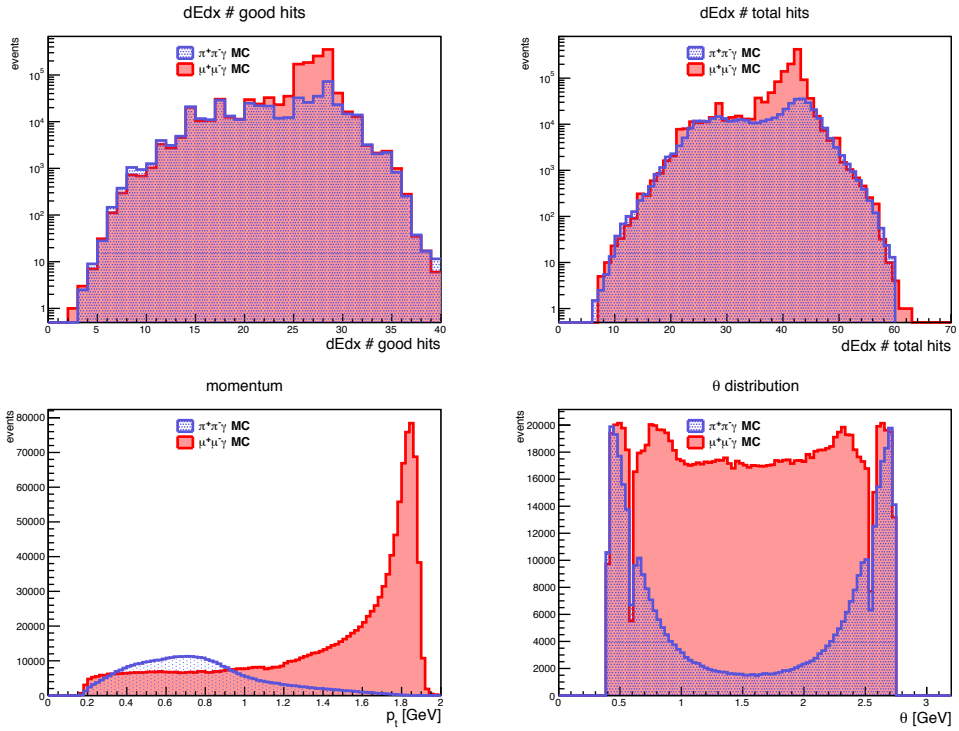

Figure C.5: MDC variables: dE/dx, transverse momentum and θ distribution.

Appendix D

Impact of the vacuum polarization correction

The ISR measurements of $\sigma^{\text{bare}}(e^+e^- \to \pi^+\pi^-(\gamma))$ from KLOE [60, 61, 62], *BABAR* [64], and BESIII have historically used different parametrizations of the vacuum polarization correction δ_{VP}. The earliest one, KLOE 08 and 10, have used a calculation by Fred Jegerlehner from 2003 (VP03). KLOE 12 used a calculation by Jegerlehner from 2009 (VP09) and *BABAR* the correction, which is implemented in the AfkQED event generator [121]. The latest version by Jegerlehner from 2012 (VP12) has been used in this work [107]. Since KLOE 08 and 10 used the normalization to the luminosity and radiator function, δ_{VP} has an impact on the extracted *bare* cross section. KLOE 12 and *BABAR* used the normalization to $\mu^+\mu^-\gamma$ events and, thus, δ_{VP} is needed to calculated the pion form factor, here. An issue has been found in VP03 and corrected in version VP09, affecting amongst others the energy region above the ρ-ω interference [105]. The different calculations can be seen in Fig. D.1.

For all comparisons presented in the main part of this thesis, the same VP correction [107] is used and hence the KLOE 08, 10, 12, and *BABAR* data sets have been modified accordingly. In Fig. D.2 the relative difference of the form factor squared from *BABAR*, KLOE, and the BESIII fit can be seen. Differently to Fig. 11.5 and 11.6 the original published data is shown here, not modifying the VP correction. The difference is hardly visible, since the VP correction used at the *BABAR* and KLOE 12 measurements are already very good. The impact of δ_{VP} on the KLOE 08 and 10 cross section measurements leads to different result of the dispersion integral, when using the originally published data. Differently to Tab. 11.2, the results, using the VP03

calculation as in the original publications, are calculated as:

$$\text{KLOE 08 (VP03)} : a_\mu^{\pi\pi,\text{LO}}(600-900\text{MeV}) = (368.9 \pm 0.4_{\text{stat}} \pm 2.3_{\text{sys,exp}} \pm 2.2_{\text{sys,theo}}) \cdot 10^{-10}$$
$$\text{KLOE 10 (VP03)} : a_\mu^{\pi\pi,\text{LO}}(600-900\text{MeV}) = (366.1 \pm 0.9_{\text{stat}} \pm 2.3_{\text{sys,exp}} \pm 2.2_{\text{sys,theo}}) \cdot 10^{-10}$$

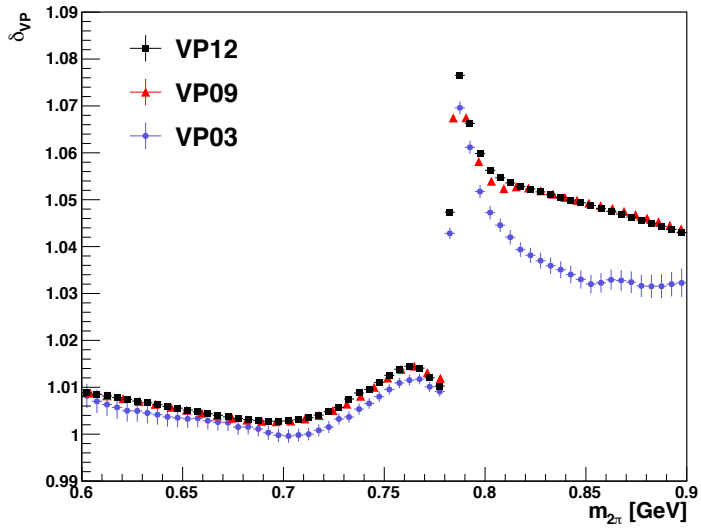

Figure D.1: The different vacuum polarization corrections calculated by Fred Jegerlehner in 2003 (VP03) as used by KLOE 08 and 10, 2009 (VP09) as used by KLOE 12, and 2012 (VP12) as used in this work [107].

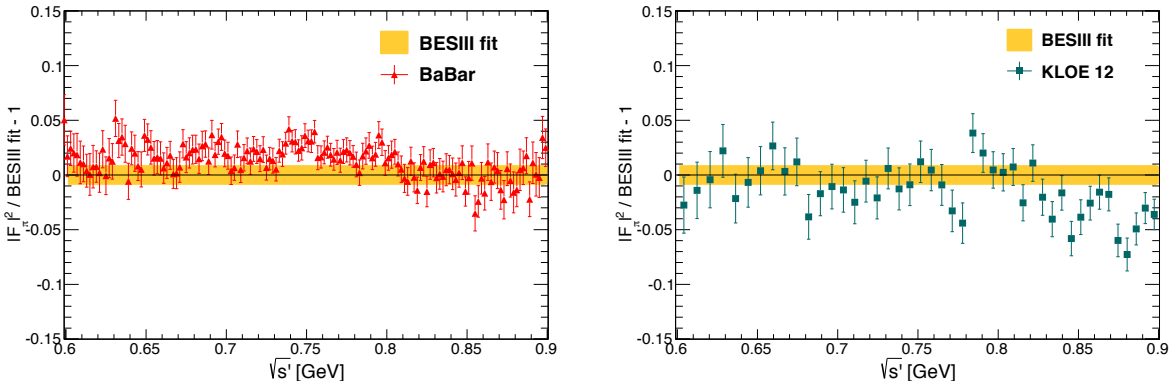

Figure D.2: Relative difference of the form factor squared from *BABAR* [64], KLOE [62], and BESIII fit. Statistic and systematic uncertainties are included in the data points. The width of the BESIII band shows the systematic uncertainty only. Here, the original published data is shown, not modifying the VP correction.

Appendix E

Calculation of $\Delta^{stat}_{a_\mu^{\pi\pi,\mathrm{LO}}}$ using the covariance matrix

The two pion contribution $a_\mu^{\pi\pi,\mathrm{LO}}$ is computed according to formula (11.2). After applying the unfolding procedure, the data points describing $\sigma^{\mathrm{bare}}(e^+e^- \to \pi^+\pi^-(\gamma_{\mathrm{FSR}}))$ are correlated, which has to be taken into account when calculating the statistical uncertainty of $a_\mu^{\pi\pi,\mathrm{LO}}$ [120], called $\Delta^{stat}_{a_\mu^{2\pi}}$ here.

This correlation can be described via a covariance matrix V, which is given by

$$V = \begin{pmatrix} \sigma_1^2 & \sigma_{12} & \dots & \sigma_{1n} \\ \sigma_{21} & \sigma_2^2 & \dots & \sigma_{2n} \\ \vdots & \vdots & \ddots & \vdots \\ \sigma_{n1} & \sigma_{n2} & \dots & \sigma_n^2 \end{pmatrix} . \tag{E.1}$$

It describes the correlations between the uncertainties σ_i and n data points, and is obtained as output of the SVD unfolding algorithm [104]. The diagonal elements σ_i^2 contain the squared statistical uncertainties of each data point. The off-diagonal elements σ_{ij} describe the correlation between σ_i and σ_j (i $\neq$ j), of each two data points:

$$\sigma_{ij} = \rho_{ij}\sigma_i\sigma_j \ , \tag{E.2}$$

$$-1 \leq \rho_{ij} \leq +1 \ , \tag{E.3}$$

where ρ_{ij} are the correlation coefficients. In case of uncorrelated events, the correlation coefficients are zero and, thus, V is diagonal.

In case of a binned data set with n data points and a discrete bin width Δs, one can calculate

the two pion contribution as

$$a_\mu^{\pi\pi,\mathrm{LO}}(600-900\,\mathrm{MeV}) = \frac{1}{4\pi^3}\int_{(0.6\mathrm{GeV})^2}^{(0.9\mathrm{GeV})^2} ds' K(s')\sigma^{bare}(e^+e^-\to\pi^+\pi^-(\gamma_{\mathrm{FSR}})) \tag{E.4}$$

$$\simeq \frac{1}{4\pi^3}\sum_{i=1}^{n}\sigma_i^{\pi\pi}K_i\Delta s\ , \tag{E.5}$$

where $\sigma_i^{\pi\pi}$ and K_i are the single, discrete, $\sigma^{\mathrm{bare}}(e^+e^-\to\pi^+\pi^-(\gamma_{\mathrm{FSR}}))$ and $K(s)$ values calculated at the bin center. Thus, the statistical uncertainty can then be computed as

$$(\Delta^{stat}_{a_\mu^{2\pi}})^2 = \sum_{i=1}^{n}\sum_{j=1}^{n}\delta_i\delta_j V_{ij} = \sum_{i=1}^{n}\delta_i^2\sigma_i^2 + \sum_{i=1}^{n}\sum_{\substack{j=1\\ j\neq i}}^{n}\delta_i\delta_j\sigma_{ij}\ , \tag{E.6}$$

with the partial derivatives

$$\delta_i \equiv \frac{\partial a_\mu^{\pi\pi,\mathrm{LO}}}{\partial\sigma_i^{\pi\pi}} = \frac{1}{4\pi^3}K_i\Delta s\ . \tag{E.7}$$

Appendix F

Dark photon search

Many theorical extensions of the Standard Model (SM) predict an additional $U(1)$ gauge boson, a so-called dark photon γ' [125]. Such additional bosons might be neutral under the SM gauge symmetries and, thus, invisible. However, their mass might be allowed in the range of SM masses [125]. A γ' might couple to the SM photon via a kinetic mixing [126] with a mixing parameter ϵ, and, hence, could be produced in e^+e^- annihilation and decay back to SM fermions. Furthermore, it was realized [127], that a dark photon on the MeV mass scale could explain also the presently seen deviation on the level of 3 to 4σ between the measurement and the SM prediction of $(g-2)_\mu$.

With the obtained tools and knowledge in the main part of this thesis, we search for the processes $e^+e^- \to \gamma'\gamma \to l^+l^-\gamma$ ($l = \mu$,e) with leptonic invariant masses m_{2l} between 1.5 and 3.4 GeV [113]. The ISR QED processes $e^+e^- \to \mu^+\mu^-\gamma$ and $e^+e^- \to e^+e^-\gamma$ are irreducible backgrounds. However, the dark photon width is expected to be smaller than the resolution of the experiment and, thus, a γ' signal would lead to a narrow structure on top of this continuous QED background.

The selection of $\mu^+\mu^-\gamma$ and $e^+e^-\gamma$ events is straight forward. To enhance statistics and to suppress non-ISR background, we investigate untagged ISR events, where the ISR photon is emitted at a small angle θ_γ with respect to the beam axis. It cannot be detected within the angular acceptance of the EMC and is predicted with a 1C kinematic fit. To select muons, the standard muon PID is used [73] for both charged tracks. To extract electrons, the ratio of measured energy in the EMC E, to the momentum p obtained from the MDC is used. Both charged tracks have to fulfill $E/p > 0.8$.

In this analysis, the dark photon mass range $m_{\gamma'}$ between 1.5 and 3.4 GeV is studied. Below 1.5 GeV the $\pi^+\pi^-\gamma$ cross section dominates and pollutes the spectra. Above 3.4 GeV one is

too close to the cms energy and, thus, the hadronic $q\bar{q}$ process can not be suppressed well. To get rid of any data-MC differences in the final result, a polynomial with four degrees of freedom is fitted to the data distribution, in order to describe the continuous QED processes. This fit is compared with the data points. The dark photon search is performed by scanning the difference between the data distribution and the fit performed. The largest observed significance is 2.9σ, combining the statistics of both investigated final states. The significance is defined as the difference between data and fit, divided by the corresponding statistical error, calculated for each invariant mass bin. The mass range around the narrow J/ψ resonance between 3.0 and 3.2 GeV is spared. As a conclusion, we observe no dark photon signal between 1.5 GeV $< m_{\gamma'} <$ 3.4 GeV, whereas $m_{\gamma'}$ is the dark photon mass, which is equal to the leptonic invariant mass m_{2l}. Hence, an exclusion limit can be set within this mass range. The exclusion limit is determined with the method by Rolke et al. [129]. A 90% confidence limit is obtained. The systematic uncertainties are included in the calculation of the exclusion limit.

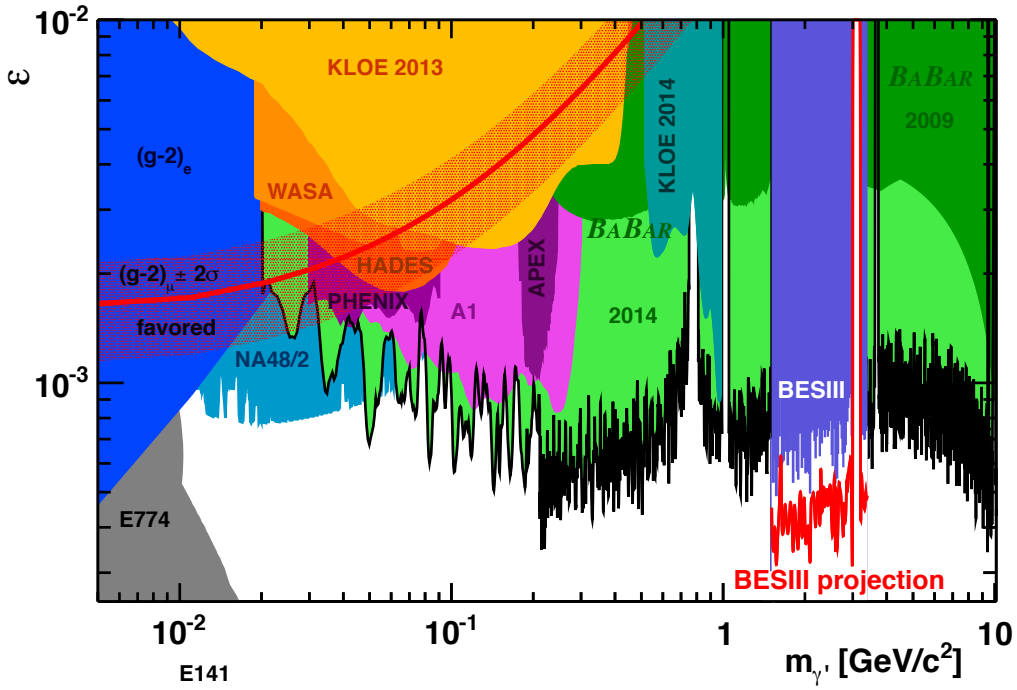

Figure F.1: Exclusion limit with 90% confidence limit on the mixing parameter ϵ as a function of the dark photon mass.

The final result, as a function of the mixing strength ϵ, is shown in Fig. F.1, after combining the statistics of both investigated final states and including the systematic uncertainties. This is the world's best limit in this dark photon mass range. It is worth to stress once more that the BESIII results, which are based on 2 years of data taking, are already competitive to the large *BABAR* data samples [134, 135], based on 9 years of running. This is possible due to the use of untagged ISR events for the dark photon search. The inclusion of already

existing and upcoming new data, will yield improved results in the future. The red histogram in Fig. F.1 displays a projection that shows what will be possible when including the already existing data sets at $\sqrt{s} = 4.23$ GeV, 4.26 GeV, 4.36 GeV, 4.42 GeV, and 4.60 GeV with a total integrated luminosity of about 3.7 fb^{-1} [133]. Also shown are the obtained exclusion limits from KLOE [136, 137], WASA-at-COSY [138], A1 at MAMI [139], HADES [140], NA48/2 [141], APEX [142], and the anomalous magnetic moment of the electron [143]. The ϵ values, which would explain the discrepancy between measurement and calculation of the anomalous magnetic moment of the muon [144] are displayed as red band. This analysis will be published in a separate paper in the near future.

Appendix G

Measurement of $\Gamma_{ee}(J/\psi)$

With the obtained tools and knowledge in the main part of this thesis, we study the process $e^+e^- \to \mu^+\mu^-\gamma$ with $\mu^+\mu^-$ invariant masses $m_{2\mu}$ between 2.8 and 3.4 GeV, which covers the charmonium resonance J/ψ. The cross section $\sigma_{J/\psi} \equiv \sigma(e^+e^- \to J/\psi\gamma \to \mu^+\mu^-\gamma)$ is proportional to $\Gamma_{ee}\cdot\mathcal{B}_{\mu\mu}$, where $\mathcal{B}_{\mu\mu} \equiv \mathcal{B}(J/\psi \to \mu^+\mu^-)$ is the branching fraction of the muonic decay of the J/ψ. With the precise measurement of $\mathcal{B}_{\mu\mu}$ from BESIII [152], one has the opportunity, to obtain $\Gamma_{ee}(J/\psi)$ with high precision. Untagged $e^+e^- \to \mu^+\mu^-\gamma$ events are used, applying a 1C kinematic fit and using the ANN requirement $y_{ANN} < 0.3$.

The differential cross section of $\sigma_{J/\psi\gamma}$ can be expressed in terms of the center of mass energy squared s as

$$\frac{d\sigma_{J/\psi}(s,m_{2\mu})}{dm_{2\mu}} = \frac{2m_{2\mu}}{s} H(s,m_{2\mu}) BW(m_{2\mu}), \tag{G.1}$$

where $H(s,m_{2\mu})$ is the radiator function, and $BW(m_{2\mu})$ the Breit-Wigner function. The Breit-Wigner function is

$$BW(m_{2\mu}) = \frac{12\pi\mathcal{B}_{\mu\mu}\Gamma_{ee}\Gamma_{tot}}{(m_{2\mu}^2 - M_{J/\psi}^2)^2 + M_{J/\psi}^2\Gamma_{tot}^2}, \tag{G.2}$$

in which Γ_{tot} and $M_{J/\psi}$ are the J/ψ full width and mass. Both values are taken from Ref [4]. The cross section $\sigma_{J/\psi\gamma}$ over a specified $m_{2\mu}$ range can be measured as:

$$\sigma_{J/\psi\gamma}(s) = \frac{N_{J/\psi}}{\epsilon\cdot\mathcal{L}} = \Gamma_{ee}\cdot\mathcal{B}_{\mu\mu}\cdot I(s), \tag{G.3}$$

where $N_{J/\psi}$ is the number of signal events within the mass range after background subtraction, ϵ is the selection efficiency obtained from MC simulation and applying the data-MC efficiency corrections studied in chapters 6, 7, and 8, $\mathcal{L}$ is the luminosity of the data set (see section

10.6.2), and $I(s)$ is the integral

$$I(s) \equiv \int_{m_{min}}^{m_{max}} \frac{2m_{2\mu}}{s} H(s,m_{2\mu}) b(m_{2\mu}) dm_{2\mu}, \tag{G.4}$$

in which $b(m_{2\mu}) \equiv BW(m_{2\mu})/\Gamma_{ee}\mathcal{B}_{\mu\mu}$. A mass range between $m_{min} = 2.8$ GeV and $m_{max} = 3.4$ GeV is chosen. $N_{J/\psi}$ is determined in this range. The above equations do not take into account interference effects of the resonant $\mu^+\mu^-$ production via J/ψ decays and the non resonant $e^+e^- \to \mu^+\mu^-\gamma$ QED production. At lowest order, this can be included by replacing $BW(m_{2\mu})$ with [153]

$$BW'(m_{2\mu}) = \frac{4\pi\alpha^2}{3m_{2\mu}^2}\left(\left|1-\zeta(m_{2\mu})\right|^2 - 1\right), \tag{G.5}$$

$$\zeta(m_{2\mu}) = \frac{3}{\alpha} \cdot \frac{\sqrt{\mathcal{B}_{\mu\mu}\Gamma_{ee}\Gamma_{tot}}M_{J/\psi}}{M_{J/\psi}^2 - m_{2\mu}^2 - iM_{J/\psi}\Gamma_{tot}}, \tag{G.6}$$

and $b(m_{2\mu})$ by its equivalent $b'(m_{2\mu}) \equiv BW'(m_{2\mu})/\Gamma_{ee}\mathcal{B}_{\mu\mu}$. The interference is anti-symmetrical around the peak, destructive below and constructive above. The radiator function weights lower photon energies, corresponding to higher muonic invariant masses, more than lower ones, which changes the $m_{2\mu}$ shape around the peak asymmetrically. The function $b'(m_{2\mu})$ depends on $\Gamma_{ee} \cdot \mathcal{B}_{\mu\mu}$. Hence, an iterative procedure is used for its extraction.

The number of J/ψ events $N_{J/\psi}$ is determined with a fit to data. The fit function $f(x)$ used is

$$f(x) = N_{J/\psi}\big[M(x) \otimes G(x)\big] + \big(N - N_{J/\psi}\big)p(x). \tag{G.7}$$

$M(x)$ describes the shape of the MC-simulated J/ψ peak. We extract it from a signal MC prediction of J/ψ production, including interference effects as simulated with the PHOKHARA event generator, using $\Gamma_{ee} \cdot \mathcal{B}_{\mu\mu}$ is an input. To describe the non-resonant QED production, a polynomial $p(x)$ of fourth order also has been added. N is the constant number of data events between 2.8 and 3.4 GeV. The fit to data is shown in Fig. G.1, using the PDG value for $\Gamma_{ee} \cdot \mathcal{B}_{\mu\mu}$ as input. Equation (G.3) is used to extract $\Gamma_{ee} \cdot \mathcal{B}_{\mu\mu}$ in an iterative process. In each iteration, we simulate the histogram $M(x)$ and calculate $I(s)$, using a $\Gamma_{ee} \cdot \mathcal{B}_{\mu\mu}$ input value, and extract the $\Gamma_{ee} \cdot \mathcal{B}_{\mu\mu}$ output with equation (G.3). This result is used as input for the next iteration. We choose the PDG value [4] as starting value. After three iterations the result converges stable within four decimal places, which corresponds to the experimental uncertainty. As final value we find

$$\Gamma_{ee} \cdot \mathcal{B}_{\mu\mu} = (333.4 \pm 2.5_{\text{stat}} \pm 4.4_{\text{sys}})\ \text{eV},$$

where the first error is the statistical uncertainty from the fitting procedure, and the second

error is the systematic uncertainty. With $\mathcal{B}_{\mu\mu} = (5.973 \pm 0.007_{stat} \pm 0.037_{sys})\%$ from the BESIII measurement [152], our measurement yields

$$\Gamma_{ee}(J/\psi) = (5.58 \pm 0.05_{\text{stat}} \pm 0.08_{\text{sys}})\,\text{keV}.$$

Our measurement of $\Gamma_{ee} \cdot \mathcal{B}_{\mu\mu}$ is consistent with the results from *BABAR* [149] and CLEO-c [150]. The measured value for $\Gamma_{ee}(J/\psi)$ is more precise, as summarized in Tab. G.1. This analysis will be published in a separate paper in the near future.

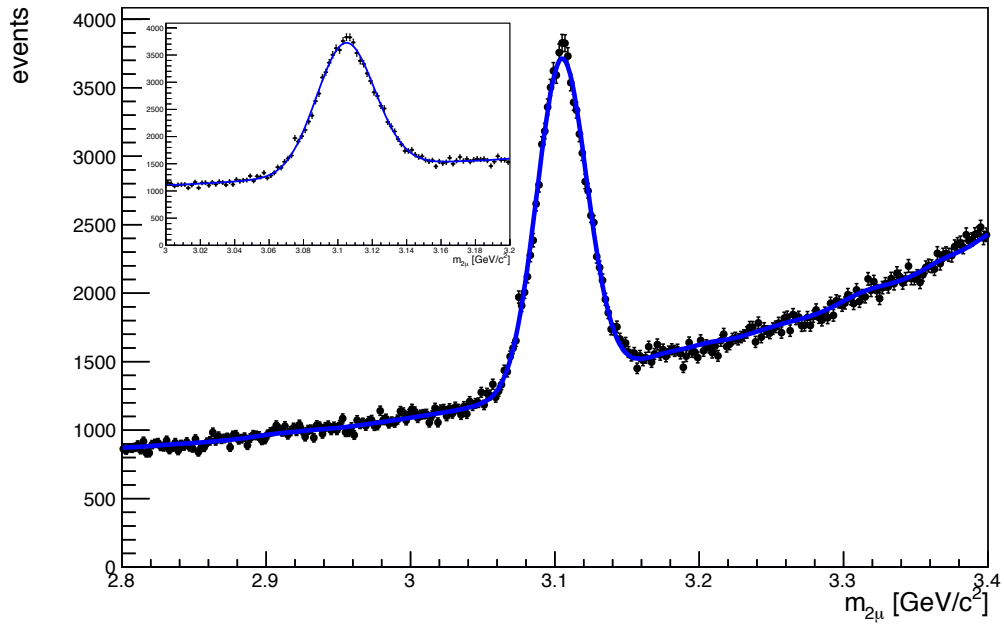

Figure G.1: Fit of the function from formula (G.7) to the data spectrum between 2.8 GeV $< m_{2\mu} <$ 3.4 GeV, using the PDG value of $\Gamma_{ee} \cdot \mathcal{B}_{\mu\mu}$ in the MC histogram for the fit. The inlay displays a zoom to the peak region.

measurement	$\Gamma_{ee}\mathcal{B}_{\mu\mu}$ [eV]	$\Gamma_{ee}(J/\psi)$ [keV]
BABAR	$330.1 \pm 7.7_{\text{stat}} \pm 7.3_{\text{sys}}$	5.61 ± 0.20
CLEO-c	$338.4 \pm 5.8_{\text{stat}} \pm 7.1_{\text{sys}}$	$5.68 \pm 0.11_{\text{stat}} \pm 0.13_{\text{sys}}$
this work	$333.4 \pm 2.5_{\text{stat}} \pm 4.4_{\text{sys}}$	$5.58 \pm 0.05_{\text{stat}} \pm 0.08_{\text{sys}}$

Table G.1: Results of the *BABAR* [149] and CLEO-c [150] measurement compared to this work.

Bibliography

[1] Atlas Collaboration, Physics Letters B**716**, 1-29 (2012).

[2] CMS Collaboration, Physics Letters B**716**, 30-61 (2012).

[3] M. Davier et al., Eur. Phys. J. C**71**, 1515 (2011).

[4] K.A. Olive et al. (Particle Data Group), Chinese Phys., Phys. Rev. D**38**, 090001 (2014).

[5] L. E. Kinster, W. V. Houston, Phys. Rev. **45**, 104 (1934).

[6] J. S. Schwinger, Phys. Rev. **73**, 416 (1948).

[7] G. W. Bennett et al., Phys. Rev. D**73**, 072003 (2006).

[8] J. Baley et al., Nucl. Phys. B**150** (1979).

[9] G. Charpak et al., Phys. Rev. Lett. **6**, 128 (1961); G. Charpak et al., Nuovo Cimento **22**, 1043 (1961).

[10] J. Bailey et al., Phys. Lett. B**28**, 287 (1968); Nuovo Cimento **A9**, 369 (1972).

[11] R. M. Carey et al., Phys Rev Lett. **82**, 1632 (1999).

[12] H. N. Brown et al., Phys. Rev. D**62**, 091101 (2000).

[13] H. N. Brown et al., Phys. Rev. Lett. **86**, 2227 (2001).

[14] G. W. Bennett et al., Phys. Rev. Lett. **89**, 101804 (2002).

[15] G. W. Bennett et al., Phys. Rev. Lett. **92**, 161802 (2004).

[16] F. Jegerlehner, Acta Phys.Polon. B**38**, 3021 (2007).

[17] R. Prigl et al., Nucl. Instr. and Methods Phys. Res. A**374**, 118 (1996).

[18] X. Fei, V. Hughes, R. Prigl, Nucl. Instr. and Methods Phys Res. A**394**, 349 (1997).

[19] W. Liu et al., Phys. Rev. Lett. **82**, 711 (1999).

[20] T. Kinoshita, M. Nio, Phys. Rev. D**53**, 4909 (1996).

[21] M. Nio, T. Kinoshita, Phys. Rev. D**55**, 7267 (1997).

[22] A. Czarnecki, S. I. Eidelman, S. G. Karshenboim, Phys. Rev. D**65**, 053004 (2002).

[23] B. Lee Roberts, Chin. Phys. C**34**, 741-744 (2010).

[24] Hiromi Iinuma (for J-PARC New g-2/EDM experiment collaboration) 2011 J. Phys.: Conf. Ser. **295**, 012032.

[25] M. Steinhauser, Int. J. Mod. Phys. Conf. Ser. **35**, 1460417 (2014).

[26] T. Aoyama et. al., Phys. Rev. Lett. **109**, 111808 (2012).

[27] T. Aoyama et. al., Phys. Rev. Lett. **109**, 111807 (2012).

[28] T. Aoyama et. al., Phys. Rev. Lett. **99**, 110406 (2007).

[29] T. Kinoshita and M. Nio, Phys. Rev. D**73**, 013003 (2006).

[30] T. Kinoshita and M. Nio, Phys. Rev. D**70**, 113001 (2004).

[31] T. Kinoshita and M. Nio, Phys. Rev. D**73**, 053007 (2006).

[32] T. Kinoshita, Nucl. Phys. B**144**, 206 (2005) (Proc. Supp.).

[33] M. Passera, J. Phys. G**31**, R75-R94 (2005).

[34] A. Czarnecki et. al., Phys. Rev. D**67**, 073006 (2003), Erratum *ibid.* Phys. Rev. D**73**, 119901 (2006).

[35] G. Degrassi and G.F. Giudice., Phys. Rev. D**58**, 053007 (1998).

[36] R. Jackiw and S. Weinberg, Phys. Rev. D**5**, 2396 (1972).

[37] G. Altarelli et. al.,Phys. Lett. B**40**, 415 (1972).

[38] I. Bars and M. Yoshimura,Phys. Rev. D**6**, 374 (1972).

[39] C. Gnendinger, D. Stöckinger, H. Stöckinger-Kim, Phys. Rev. D**88**, 053005 (2013).

[40] S. Heinemeyer, D. Stockinger and G. Weiglein, Nucl. Phys. B**699**, 103 (2004).

[41] T. Gribouk and A. Czarnecki, Phys. Rev. D**72**, 053016 (2005).

[42] A.Czarnecki, B. Krause and W.J. Marciano, Phys. Rev. Lett. **76**, 3267 (1996).

[43] A.Czarnecki, B. Krause and W.J. Marciano, Phys. Rev. D**52**, 2619 (1995).

[44] S. Peris, M. Perrottet and E. de Rafael, Phys. Lett. B**355**, 523 (1995).

[45] T. Kukhto et al., Nucl. Phys. B**371**, 567 (1992).

[46] K. Fujikawa, B.W. Lee and A.I. Sanda, Phys. Rev. D**6**, 2923 (1972).

[47] S. Eidelman and F. Jegerlehner, Z.Phys. C**67**, 585 (1995)

[48] F. Jegerlehner and Andreas Nyffeler, Nucl. Phys.Proc. Suppl. **181 − 182**, 135 (2008).

[49] R. Alemany et al., Eur. Phys. J. C**2**, 123 (1998).

[50] K. Hagiwara et al., JPHGB G**38**, 085003 (2011).

[51] B. Krause, Phys. Lett. B**390**, 392 (1997).

[52] Johan Bijnens, Elisabetta Pallante, and Joaqu'm Prades Phys. Rev. Lett. **75**, 3781 (1995).

[53] M- Knecht, A. Nyffeler, Phys. Rev. D**65**, 073034 (2002).

[54] J. Prades, E. de Rafael, and A. Vainshtein, Advanced series on directions in high energy physics 20, Editors B.L. Roberts and W. Marciano, arXiv:0901.0306 [hep-ph] (2009).

[55] R.R. Akhmetshinetal et al. (CMD2 Collaboration), Phys. Lett. B**578**, 285 (2004).

[56] R.R. Akhmetshinetal et al. (CMD2 Collaboration), Phys. Lett. B**648**, 28 (2007).

[57] M.N. Achasov et al. (SND Collaboration), ETP Lett. **103**, 380 (2006).

[58] Augustin et al, Phys. Rev. Lett. **20**, 126 (1968).

[59] A. Aloisio et al. (KLOE Collaboration), Phys.Lett. B**606**, 12-24 (2005).

[60] F. Ambrosino et al. (KLOE Collaboration), Phys. Lett. B**670**, 285-291 (2009).

[61] F. Ambrosino et al. (KLOE Collaboration), Phys. Lett. B**700**, 102-110 (2011).

[62] D. Babusci et al. (KLOE Collaboration), Phys. Lett. B**720**, 336-343 (2013).

[63] B. Aubert et al. (*BABAR* Collaboration), Phys. Rev. Lett. **103**, 231801 (2009).

[64] B. Aubert et al. (*BABAR* Collaboration), Phys. Rev. Lett. **103**, 231801 (2009).

[65] I.B. Vasserman et al. (TOF Collaboration), Sov. J. Nucl. Phys. **33**, 368 (1981).

[66] I.B. Vasserman et al. (OLYA Collaboration), Sov. J. Nucl. Phys. **30**, 519 (1979).

[67] L.M. Barkov et al. (OLYA, CMD Collaboration), Nucl. Phys. B**256**, 365 (1985).

[68] A. Quenzer et al. (DM1 Collaboration), Phys. Lett. B**76**, 512 (1978).

[69] D. Bisello et al. DM2 Collaboration, Phys. Lett. B**220**, 321 (1989).

[70] A. Höfer, J. Gluza and F. Jegerlehner, Eur. Phys. J. C**24**, 51 (2002).

[71] M. Davier et al., Eur. Phys. J. C**66**, 1 (2010).

[72] Shou-Xian Fang, Sen-Yu Chen, Particle Accelerators. Vol. 25 (1990)

[73] D. M. Asner, International Journal of Modern Physics A**24**, Issue 1 supp. (2009).

[74] M. Ablikim et al., Nuclear Instruments and Methods in Physics Research A**614**, 345-399 (2010).

[75] M. Ablikim et al., Phys. Rev. Lett. **110**, 252001 (2013).

[76] Yi-Fang Wang, Int.J.Mod.Phys. A**21**, 5371-5380 (2006).

[77] Yu-tie Liang et al., Nuclear Instruments and Methods in Physics Research A**603**, 325-327 (2009).

[78] Shu-Jun Wei et al., Nuclear Instruments and Methods in Physics Research A**598**, 323-327 (2009).

[79] N. Berger et al., Chinese Physics C**34**(12), 1779-1784 (2010).

[80] See http://linux.web.cern.ch/linux/scientific4/.

[81] Barrand, G. et al., Comput. Phys. Commun. **140**, 45 (2001).

[82] J. Allison et al., IEEE Transactions on Nuclear Science **53** No.1, 270-27 (2006).

[83] S. Agostinelli et al., Nuclear Instruments and Methods A**506**, 250-303 (2003).

[84] Yutie Liang et al., Nucl. Inst. & Meths. A, Vol. **603**, 325 (2009).

[85] Rene Brun and Fons Rademakers, Nucl. Inst. & Meth. in Phys. Res. A**389**, 81-86 (1997).

[86] BESIII Collaboration, Chinese Physics C Vol. **37**, No. 12, 123001 (2013).

[87] G. Rodrigo, H. Czyż, J. H. Kuhn, M. Szopa, Eur.Phys.J. C**24**, 71-82 (2002).

[88] H. Czyż, A. Grzelinska, A. Wapienik, Acta Phys. Polon. B**34**, 5219-5230 (2003).

[89] H. Czyż, A. Grzelinska, A. Wapienik, Acta Phys. Polon. B**38**, 3491 (2007).

[90] H. Czyz, J. H. Kühn and A. Wapienik, Phys. Rev. D**77**, 114005 (2008); H. Czyz and J. H. Kühn, Phys. Rev. D**80**, 034035 (2009); H. Czyz, A. Grzelinska and J. H. Kühn, Phys. Rev. D**81**, 094014 (2010); H. Czyz, M. Gunia and J. H. Kühn, JHEP **1308**, 110 (2013); F. Campanario, H. Czyz, J. Gluza, M. Gunia, T. Riemann, G. Rodrigo and V. Yundin, JHEP **1402**, 114 (2014).

[91] S. Jadach et al., Comput. Phys. Commun. **130**, 260 (2000).

[92] Babayaga.3.5: Information at http://www.lnf.infn.it/wg/sighad/.

[93] G. Balossini et al., Nucl. Phys. B**758**, 227-253 (2006).

[94] G. Balossini, C. Bignamini, C.M. Carloni Calame, G. Montagna, F. Piccinini and O. Nicrosini, Phys. Lett. B**663**, 209 (2008).

[95] V. Druzhinin, S. Eidelman, S. Serednyakov and E. Solodov, Rev. Mod. Phys. **83**, 1545 (2011).

[96] J. S. Schwinger, Vol. 3, Redwood City, USA Addison-Wesley:99 (1989).

[97] arXiv:1508.04008 [hep-ex]

[98] A. Hoecker et al., PoS ACAT, 040 (2007).

[99] D. N. Brown, J. Ilic and G. B. Mohanty, Nucl. Instr. Meth. A**592**, 254 (2008).

[100] F. Zemike, Physica **1**, 689 (1934).

[101] private communication with Yaqian Wang.

[102] arXiv:1504.07870 [hep-ex]

[103] B. Aubert et al., Phys. Rev. D**76**, 092005 (2007).

[104] A. Hoecker, V. Kartvelishvili, Nucl.Instrum.Meth. A**372**, 469-481 (1996).

[105] S. Actis et al. [Working Group on Radiative Corrections and Monte Carlo Generators for Low Energies Collaboration], Eur. Phys. J. C **66**, 585-686 (2010); Working Group on Radiative Corrections and MC Generators for Low Energies, http://www.lnf.infn.it/wg/sighad/;

[106] M. E. Peskin and D. V. Schroeder, *An Introduction to Quantum Field Theory*, Vol. 2, USA, Addison-Wesley, 135 (1995).

[107] F. Jegerlehner, Nucl. Phys. Proc. Suppl. **181 − 182**, 135 (2008); F. Jegerlehner, Z. Phys. C**32**, 195 (1986); www-com.physik.hu-berlin.de/∼fjeger/alphaQED.tar.gz (2015)

[108] K. Hagiwara, A.D. Martin, D. Nomura and T. Teubner, Phys. Lett. B**649**, 173 (2007).

[109] private communications with A. Hafner.

[110] G. J. Gounaris and J. J. Sakurai, Phys. Rev. Lett. **21**, 244 (1968).

[111] Private communications with Thomas Teubner; T. Teubner, contribution at the "High-precision QCD at low energy" workshop, Benasque, Spain (2015).

[112] arXiv:1507.08188 [hep-ex], submitted to PLB

[113] B. Kloss, contribution at the "Twelfth Conference on the Intersections of Particle and Nuclear Physics" (CIPANP), Vail, USA (2015).

[114] Private communications with Yaqian Wang; contribution at the "Tagung der deutschen physikalischen Gesellschaft", Dresden, Germany (2013).

[115] Private communications with Martin Ripka; contribution at the "Tagung der deutschen physikalischen Gesellschaft", Heidelberg, Germany (2015).

[116] B. Kloss, *Machbarkeitsstudien zur Messung von π^0 Übergangsformfaktoren bei BES-III*, Bachelor thesis, Institut für Kernphysik, Universität Mainz (2011).

[117] Private communications with Christoph Redmer and Yuping Guo; C. Redmer, contribution at the "International Workshop on e+e- collisions from Phi to Psi 2015" (PHIPSI) Conference, Hefei, China (2015); C. Redmer, EPJ Web of Conferences, Volume **72**: 00021 (2014); C. Redmer, MesonNet 2014 International Workshop Mini-proceedings, arXiv:1412.5451 [nucl-ex]

[118] A. Hahn, *Machbarkeitsstudien zur Messung von η und η' Übergangsformfaktoren bei BES-III*, Bachelor thesis, Institut für Kernphysik, Universität Mainz (2011).

[119] M. Diefenbach, *Analysis of space-like electromagnetic transition form factors of η and η' mesons at BESIII*, Master thesis, Institut für Kernphysik, Universität Mainz (2011).

[120] Private communication with Stefan Müller; S. E. Müller, contribution at the "13th Working Group on Rad. Corrections and MC Generators for Low Energies Meeting", Trento, Italy (2013).

[121] H. Czyz and J. Kühn, Eur. Phys. J. C. **18**, 497 (2001).

[122] K. Nakamura et al. (Particle Data Group), G**37**, 075021 (2010).

[123] J. Beringer et al. (Particle Data Group), Phys. Rev. D**86**, 010001 (2012).

[124] A. Hoecker and W. Marciano, J. Phys. G**37**, 075021 (2010), Updated August 2013.

[125] N. Arkani-Hamed, P. Finkbeiner, Tracy R. Slatyer, and Neal Weiner, Phys. Rev. D **79**, 015014 (2009).

[126] B. Holdom, Phys. Lett. B**166**, 196 (1986).

[127] M. Pospelov, Phys. Rev. D**80**, 095002 (2009).

[128] G. J. Feldman and R. D. Cousins, Phys. Rev., D**57**, 3873 (1998).

[129] W. Rolke, A. Lopez, J. Conrad and Fred James, Nucl. Instrum. Meth. A**551**, 493-503 (2005).

[130] J. D. Bjorken, R. Essig, P. Schuster, and N. Toro, Phys. Rev., D**80**, 075018 (2009).

[131] T. Beranek, H. Merkel and M. Vanderhaeghen, Phys. Rev. D**88**, 015032.

[132] J. D. Bjorken, R. Essig, P. Schuster, and N. Toro, Phys. Rev., D**80**, 075018 (2009).

[133] M. Ablikim et al. (BESIII Collaboration), Chinese Physics C**39**(12), 9 (2015).

[134] B. Aubert et al. (*BABAR* Collaboration), Phys. Rev. Lett. **103**, 081803 (2009).

[135] J.P. Lees et al. (*BABAR* Collaboration), Phys. Rev. Lett. **113**, 201801 (2014).

[136] F. Archilli et al. (KLOE-2 Collaboration), Phys. Lett. B**706**, 251 (2012).

[137] D. Babuski et al. (KLOE-2 Collaboration), Phys. Lett. B**720**, 111 (2013).

[138] P. Adlarson et al. (WASA-at-COSY Collaboration), Phys. Lett. B**726**, 187 (2013).

[139] H. Merkel et al. (A1 Collaboration), Phys. Rev. Lett. **112**, 221802 (2014).

[140] G. Agakishiev et al. (HADES Collaboration), Phys. Lett. B**731**, 265-271 (2014).

[141] J.R. Batley et al. (NA48/2 Collaboration), Phys. Lett. B**746**, 178-185 (2015).

[142] S. Abrahamyan et al. (APEX Collaboration), Phys. Rev. Lett. **107**, 191804 (2011).

[143] M. Endo, K. Hamaguchi and G. Mishima, Phys. Rev. D**86**, 095029 (2012).

[144] M. Pospelov, Phys. Rev. D**80**, 095002 (2009).

[145] Private communication with Henryk Czyz and Stefan Müller.

[146] A. Aloisio et al., Phys. Lett. B**606**, 12-24 (2005).

[147] A. Aloisio et al., Eur. Phys. J. C**33**, 656-658 (2004).

[148] S. Müller, ECONF **C0309101**, FRWP008 (2003).

[149] B. Aubert et al. (*BABAR* Collaboration), Phys. Rev. D**69**, 011103R (2003).

[150] G.S. Adams et al. (CLEO Collaboration), Phys. Rev. D**73**, 051103R (2006).

[151] Z. Li et al. (CLEO Collaboration), Phys. Rev. D**71**, 111103R (2005).

[152] BESIII Collaboration, Phys. Rev. D**88**, 032007 (2013).

[153] See, for example, F.A. Berends, G.J. Komen, Nucl. Phys. B**115**, 114 (1976).

[154] R. Barlow, *A Guide to the Use of Statistical Methods in the Physical Science*, Wiley (1989).

[155] V. Blobel, E. Lohmann, *Statistische und numerische Methoden der Datenanalyse*, Teubner (1998).

[156] W. Demtröder, *Experimentalphysik 4, Kern-, Teilchen- und Astrophysik*, Springer (2005).

[157] B. Povh, K. Rith, C. Scholz, F. Zetsche, *Teilchen und Kerne*, Springer (2008).

[158] C. Zimmermann, *Feasability Studies and First Measurements of Initial State Radiation Events at BES-III*, Diploma thesis, Institut für Kernphysik, Universität Mainz (2011).

[159] Andreas Hafner, *Measurement of the $e^+e^- \to \pi^+\pi^-\pi^+\pi^-$ Cross Section Using Initial State Radiation at BABAR*, PhD thesis, Institut für Kernphysik, Universität Mainz (2011).

Acknowledgements

Aus datenschutzrechtlichen Gründen entfernt

Curriculum vitae

Aus datenschutzrechtlichen Gründen entfernt

Measurement of the $e^+e^- \to \pi^+\pi^-$ Cross Section between 600 and 900 MeV Using Initial State Radiation

M. Ablikim[1], M. N. Achasov[9,f], X. C. Ai[1], O. Albayrak[5], M. Albrecht[4], D. J. Ambrose[44], A. Amoroso[49A,49C], F. F. An[1], Q. An[46,a], J. Z. Bai[1], R. Baldini Ferroli[20A], Y. Ban[31], D. W. Bennett[19], J. V. Bennett[5], M. Bertani[20A], D. Bettoni[21A], J. M. Bian[43], F. Bianchi[49A,49C], E. Boger[23,d], I. Boyko[23], R. A. Briere[5], H. Cai[51], X. Cai[1,a], O. Cakir[40A,b], A. Calcaterra[20A], G. F. Cao[1], S. A. Cetin[40B], J. F. Chang[1,a], G. Chelkov[23,d,e], G. Chen[1], H. S. Chen[1], H. Y. Chen[2], J. C. Chen[1], M. L. Chen[1,a], S. J. Chen[29], X. Chen[1,a], X. R. Chen[26], Y. B. Chen[1,a], H. P. Cheng[17], X. K. Chu[31], G. Cibinetto[21A], H. L. Dai[1,a], J. P. Dai[34], A. Dbeyssi[14], D. Dedovich[23], Z. Y. Deng[1], A. Denig[22], I. Denysenko[23], M. Destefanis[49A,49C], F. De Mori[49A,49C], Y. Ding[27], C. Dong[30], J. Dong[1,a], L. Y. Dong[1], M. Y. Dong[1,a], S. X. Du[53], P. F. Duan[1], E. E. Eren[40B], J. Z. Fan[39], J. Fang[1,a], S. S. Fang[1], X. Fang[46,a], Y. Fang[1], L. Fava[49B,49C], F. Feldbauer[22], G. Felici[20A], C. Q. Feng[46,a], E. Fioravanti[21A], M. Fritsch[14,22], C. D. Fu[1], Q. Gao[1], X. Y. Gao[2], Y. Gao[39], Z. Gao[46,a], I. Garzia[21A], K. Goetzen[10], W. X. Gong[1,a], W. Gradl[22], M. Greco[49A,49C], M. H. Gu[1,a], Y. T. Gu[12], Y. H. Guan[1], A. Q. Guo[1], L. B. Guo[28], Y. Guo[1], Y. P. Guo[22], Z. Haddadi[25], A. Hafner[22], S. Han[51], X. Q. Hao[15], F. A. Harris[42], K. L. He[1], X. Q. He[45], T. Held[4], Y. K. Heng[1,a], Z. L. Hou[1], C. Hu[28], H. M. Hu[1], J. F. Hu[49A,49C], T. Hu[1,a], Y. Hu[1], G. M. Huang[6], G. S. Huang[46,a], J. S. Huang[15], X. T. Huang[33], Y. Huang[29], T. Hussain[48], Q. Ji[1], Q. P. Ji[30], X. B. Ji[1], X. L. Ji[1,a], L. W. Jiang[51], X. S. Jiang[1,a], X. Y. Jiang[30], J. B. Jiao[33], Z. Jiao[17], D. P. Jin[1,a], S. Jin[1], T. Johansson[50], A. Julin[43], N. Kalantar-Nayestanaki[25], X. L. Kang[1], X. S. Kang[30], M. Kavatsyuk[25], B. C. Ke[5], P. Kiese[22], R. Kliemt[14], B. Kloss[22], O. B. Kolcu[40B,i], B. Kopf[4], M. Kornicer[42], W. Kühn[24], A. Kupsc[50], J. S. Lange[24], M. Lara[19], P. Larin[14], C. Leng[49C], C. Li[50], Cheng Li[46,a], D. M. Li[53], F. Li[1,a], F. Y. Li[31], G. Li[1], H. B. Li[1], J. C. Li[1], Jin Li[32], K. Li[33], K. Li[13], Lei Li[3], P. R. Li[41], T. Li[33], W. D. Li[1], W. G. Li[1], X. L. Li[33], X. M. Li[12], X. N. Li[1,a], X. Q. Li[30], Z. B. Li[38], H. Liang[46,a], Y. F. Liang[36], Y. T. Liang[24], G. R. Liao[11], D. X. Lin[14], B. J. Liu[1], C. X. Liu[1], F. H. Liu[35], Fang Liu[1], Feng Liu[6], H. B. Liu[12], H. H. Liu[16], H. H. Liu[1], H. M. Liu[1], J. Liu[1], J. B. Liu[46,a], J. P. Liu[51], J. Y. Liu[1], K. Liu[39], K. Y. Liu[27], L. D. Liu[31], P. L. Liu[1,a], Q. Liu[41], S. B. Liu[46,a], X. Liu[26], Y. B. Liu[30], Z. A. Liu[1,a], Zhiqing Liu[22], H. Loehner[25], X. C. Lou[1,a,h], H. J. Lu[17], J. G. Lu[1,a], Y. Lu[1], Y. P. Lu[1,a], C. L. Luo[28], M. X. Luo[52], T. Luo[42], X. L. Luo[1,a], X. R. Lyu[41], F. C. Ma[27], H. L. Ma[1], L. L. Ma[33], Q. M. Ma[1], T. Ma[1], X. N. Ma[30], X. Y. Ma[1,a], F. E. Maas[14], M. Maggiora[49A,49C], Y. J. Mao[31], Z. P. Mao[1], S. Marcello[49A,49C], J. G. Messchendorp[25], J. Min[1,a], R. E. Mitchell[19], X. H. Mo[1,a], Y. J. Mo[6], C. Morales Morales[14], K. Moriya[19], N. Yu. Muchnoi[9,f], H. Muramatsu[43], Y. Nefedov[23], F. Nerling[14], I. B. Nikolaev[9,f], Z. Ning[1,a], S. Nisar[8], S. L. Niu[1,a], X. Y. Niu[1], S. L. Olsen[32], Q. Ouyang[1,a], S. Pacetti[20B], P. Patteri[20A], M. Pelizaeus[4], H. P. Peng[46,a], K. Peters[10], J. Pettersson[50], J. L. Ping[28], R. G. Ping[1], R. Poling[43], V. Prasad[1], M. Qi[29], S. Qian[1,a], C. F. Qiao[41], L. Q. Qin[33], N. Qin[51], X. S. Qin[1], Z. H. Qin[1,a], J. F. Qiu[1], K. H. Rashid[48], C. F. Redmer[22], M. Ripka[22], G. Rong[1], Ch. Rosner[14], X. D. Ruan[12], V. Santoro[21A], A. Sarantsev[23,g], M. Savrié[21B], K. Schoenning[50], S. Schumann[22], W. Shan[31], M. Shao[46,a], C. P. Shen[2], P. X. Shen[30], X. Y. Shen[1], H. Y. Sheng[1], W. M. Song[1], M. R. Shepherd[19], X. Y. Song[1], S. Sosio[49A,49C], S. Spataro[49A,49C], G. X. Sun[1], J. F. Sun[15], S. S. Sun[1], Y. J. Sun[46,a], Y. Z. Sun[1], Z. J. Sun[1,a], Z. T. Sun[19], C. J. Tang[36], X. Tang[1], I. Tapan[40C], E. H. Thorndike[44], M. Tiemens[25], M. Ullrich[24], I. Uman[40B], G. S. Varner[42], B. Wang[30], D. Wang[31], D. Y. Wang[31], K. Wang[1,a], L. L. Wang[1], L. S. Wang[1], M. Wang[33], P. Wang[1], P. L. Wang[1], S. G. Wang[31], W. Wang[1,a], X. F. Wang[39], Y. D. Wang[14], Y. F. Wang[1,a], Y. Q. Wang[22], Z. Wang[1,a], Z. G. Wang[1,a], Z. H. Wang[46,a], Z. Y. Wang[1], T. Weber[22], D. H. Wei[11], J. B. Wei[31], P. Weidenkaff[22], S. P. Wen[1], U. Wiedner[4], M. Wolke[50], L. H. Wu[1], Z. Wu[1,a], L. G. Xia[39], Y. Xia[18], D. Xiao[1], H. Xiao[47], Z. J. Xiao[28], Y. G. Xie[1,a], Q. L. Xiu[1,a], G. F. Xu[1], L. Xu[1], Q. J. Xu[13], X. P. Xu[37], L. Yan[46,a], W. B. Yan[46,a], W. C. Yan[46,a], Y. H. Yan[18], H. J. Yang[34], H. X. Yang[1], L. Yang[51], Y. Yang[6], Y. X. Yang[11], M. Ye[1,a], M. H. Ye[7], J. H. Yin[1], B. X. Yu[1,a], C. X. Yu[30], J. S. Yu[26], C. Z. Yuan[1], W. L. Yuan[29], Y. Yuan[1], A. Yuncu[40B,c], A. A. Zafar[48], A. Zallo[20A], Y. Zeng[18], B. X. Zhang[1], B. Y. Zhang[1,a], C. Zhang[29], C. C. Zhang[1], D. H. Zhang[1], H. H. Zhang[38], H. Y. Zhang[1,a], J. J. Zhang[1], J. L. Zhang[1], J. Q. Zhang[1],

J. W. Zhang[1,a], J. Y. Zhang[1], J. Z. Zhang[1], K. Zhang[1], L. Zhang[1], X. Y. Zhang[33], Y. Zhang[1], Y. N. Zhang[41], Y. H. Zhang[1,a], Y. T. Zhang[46,a], Yu Zhang[41], Z. H. Zhang[6], Z. P. Zhang[46], Z. Y. Zhang[51], G. Zhao[1], J. W. Zhao[1,a], J. Y. Zhao[1], J. Z. Zhao[1,a], Lei Zhao[46,a], Ling Zhao[1], M. G. Zhao[30], Q. Zhao[1], Q. W. Zhao[1], S. J. Zhao[53], T. C. Zhao[1], Y. B. Zhao[1,a], Z. G. Zhao[46,a], A. Zhemchugov[23,d], B. Zheng[47], J. P. Zheng[1,a], W. J. Zheng[33], Y. H. Zheng[41], B. Zhong[28], L. Zhou[1,a], X. Zhou[51], X. K. Zhou[46,a], X. R. Zhou[46,a], X. Y. Zhou[1], K. Zhu[1], K. J. Zhu[1,a], S. Zhu[1], S. H. Zhu[45], X. L. Zhu[39], Y. C. Zhu[46,a], Y. S. Zhu[1], Z. A. Zhu[1], J. Zhuang[1,a], L. Zotti[49A,49C], B. S. Zou[1], J. H. Zou[1]

(BESIII Collaboration)

[1] *Institute of High Energy Physics, Beijing 100049, People's Republic of China*
[2] *Beihang University, Beijing 100191, People's Republic of China*
[3] *Beijing Institute of Petrochemical Technology, Beijing 102617, People's Republic of China*
[4] *Bochum Ruhr-University, D-44780 Bochum, Germany*
[5] *Carnegie Mellon University, Pittsburgh, Pennsylvania 15213, USA*
[6] *Central China Normal University, Wuhan 430079, People's Republic of China*
[7] *China Center of Advanced Science and Technology, Beijing 100190, People's Republic of China*
[8] *COMSATS Institute of Information Technology, Lahore, Defence Road, Off Raiwind Road, 54000 Lahore, Pakistan*
[9] *G.I. Budker Institute of Nuclear Physics SB RAS (BINP), Novosibirsk 630090, Russia*
[10] *GSI Helmholtzcentre for Heavy Ion Research GmbH, D-64291 Darmstadt, Germany*
[11] *Guangxi Normal University, Guilin 541004, People's Republic of China*
[12] *GuangXi University, Nanning 530004, People's Republic of China*
[13] *Hangzhou Normal University, Hangzhou 310036, People's Republic of China*
[14] *Helmholtz Institute Mainz, Johann-Joachim-Becher-Weg 45, D-55099 Mainz, Germany*
[15] *Henan Normal University, Xinxiang 453007, People's Republic of China*
[16] *Henan University of Science and Technology, Luoyang 471003, People's Republic of China*
[17] *Huangshan College, Huangshan 245000, People's Republic of China*
[18] *Hunan University, Changsha 410082, People's Republic of China*
[19] *Indiana University, Bloomington, Indiana 47405, USA*
[20] *(A)INFN Laboratori Nazionali di Frascati, I-00044, Frascati, Italy; (B)INFN and University of Perugia, I-06100, Perugia, Italy*
[21] *(A)INFN Sezione di Ferrara, I-44122, Ferrara, Italy; (B)University of Ferrara, I-44122, Ferrara, Italy*
[22] *Johannes Gutenberg University of Mainz, Johann-Joachim-Becher-Weg 45, D-55099 Mainz, Germany*
[23] *Joint Institute for Nuclear Research, 141980 Dubna, Moscow region, Russia*
[24] *Justus Liebig University Giessen, II. Physikalisches Institut, Heinrich-Buff-Ring 16, D-35392 Giessen, Germany*
[25] *KVI-CART, University of Groningen, NL-9747 AA Groningen, The Netherlands*
[26] *Lanzhou University, Lanzhou 730000, People's Republic of China*
[27] *Liaoning University, Shenyang 110036, People's Republic of China*
[28] *Nanjing Normal University, Nanjing 210023, People's Republic of China*
[29] *Nanjing University, Nanjing 210093, People's Republic of China*
[30] *Nankai University, Tianjin 300071, People's Republic of China*
[31] *Peking University, Beijing 100871, People's Republic of China*
[32] *Seoul National University, Seoul, 151-747 Korea*
[33] *Shandong University, Jinan 250100, People's Republic of China*
[34] *Shanghai Jiao Tong University, Shanghai 200240, People's Republic of China*
[35] *Shanxi University, Taiyuan 030006, People's Republic of China*
[36] *Sichuan University, Chengdu 610064, People's Republic of China*
[37] *Soochow University, Suzhou 215006, People's Republic of China*
[38] *Sun Yat-Sen University, Guangzhou 510275, People's Republic of China*
[39] *Tsinghua University, Beijing 100084, People's Republic of China*
[40] *(A)Istanbul Aydin University, 34295 Sefakoy, Istanbul, Turkey; (B)Dogus University, 34722 Istanbul,*

Turkey; (C)Uludag University, 16059 Bursa, Turkey
[41] *University of Chinese Academy of Sciences, Beijing 100049, People's Republic of China*
[42] *University of Hawaii, Honolulu, Hawaii 96822, USA*
[43] *University of Minnesota, Minneapolis, Minnesota 55455, USA*
[44] *University of Rochester, Rochester, New York 14627, USA*
[45] *University of Science and Technology Liaoning, Anshan 114051, People's Republic of China*
[46] *University of Science and Technology of China, Hefei 230026, People's Republic of China*
[47] *University of South China, Hengyang 421001, People's Republic of China*
[48] *University of the Punjab, Lahore-54590, Pakistan*
[49] *(A)University of Turin, I-10125, Turin, Italy; (B)University of Eastern Piedmont, I-15121, Alessandria, Italy; (C)INFN, I-10125, Turin, Italy*
[50] *Uppsala University, Box 516, SE-75120 Uppsala, Sweden*
[51] *Wuhan University, Wuhan 430072, People's Republic of China*
[52] *Zhejiang University, Hangzhou 310027, People's Republic of China*
[53] *Zhengzhou University, Zhengzhou 450001, People's Republic of China*

[a] *Also at State Key Laboratory of Particle Detection and Electronics, Beijing 100049, Hefei 230026, People's Republic of China*
[b] *Also at Ankara University,06100 Tandogan, Ankara, Turkey*
[c] *Also at Bogazici University, 34342 Istanbul, Turkey*
[d] *Also at the Moscow Institute of Physics and Technology, Moscow 141700, Russia*
[e] *Also at the Functional Electronics Laboratory, Tomsk State University, Tomsk, 634050, Russia*
[f] *Also at the Novosibirsk State University, Novosibirsk, 630090, Russia*
[g] *Also at the NRC "Kurchatov Institute", PNPI, 188300, Gatchina, Russia*
[h] *Also at University of Texas at Dallas, Richardson, Texas 75083, USA*
[i] *Also at Istanbul Arel University, 34295 Istanbul, Turkey*

Abstract

We extract the $e^+e^- \to \pi^+\pi^-$ cross section in the energy range between 600 and 900 MeV, exploiting the method of initial state radiation. A data set with an integrated luminosity of 2.93 fb^{-1} taken at a center-of-mass energy of 3.773 GeV with the BESIII detector at the BEPCII collider is used. The cross section is measured with a systematic uncertainty of 0.9%. We extract the pion form factor $|F_\pi|^2$ as well as the contribution of the measured cross section to the leading-order hadronic vacuum polarization contribution to $(g-2)_\mu$. We find this value to be $a_\mu^{\pi\pi,\mathrm{LO}}(600-900\ \mathrm{MeV}) = (368.2 \pm 2.5_{\mathrm{stat}} \pm 3.3_{\mathrm{sys}}) \cdot 10^{-10}$, which is between the corresponding values using the BaBar or KLOE data.

Keywords: Hadronic cross section, muon anomaly, initial state radiation, pion form factor, BESIII

1. Introduction

The cross section $\sigma_{\pi\pi} = \sigma(e^+e^- \to \pi^+\pi^-)$ has been measured in the past with ever increasing precision at accelerators in Novosibirsk [1, 2, 3], Orsay [4], Frascati [5, 6, 7, 8], and SLAC [9, 10]. More recently, the two most precise measurements have been performed by the KLOE collaboration in Frascati [8] and the BaBar collaboration at SLAC [9, 10]. Both experiments claim a precision of better than 1% in the energy range below 1 GeV, in which the $\rho(770)$ resonance with its decay into pions dominates the total hadronic cross section. A discrepancy of approximately 3% on the peak of the

$\rho(770)$ resonance is observed between the KLOE and BaBar spectra. The discrepancy is even increasing towards higher energies above the peak of the ρ resonance. Unfortunately, this discrepancy is limiting the current knowledge of the anomalous magnetic moment of the muon $a_\mu \equiv (g-2)_\mu/2$ [11], a precision observable of the Standard Model (SM). The accuracy of the SM prediction of $(g-2)_\mu$ is entirely limited by the knowledge of the hadronic vacuum polarization contribution, which is obtained in a dispersive framework by using experimental data on $\sigma(e^+e^- \to \text{hadrons})$ [11, 12, 13]. The cross section $\sigma(e^+e^- \to \pi^+\pi^-)$ contributes to more than 70% to this dispersion relation and, hence, is the most important exclusive hadronic channel of the total hadronic cross section. Currently, a discrepancy of 3.6 standard deviations [12] is found between the direct measurement of a_μ and its SM prediction. However, the discrepancy reduces to 2.4σ [14], when only BaBar data is used as input to the dispersion relation. In this letter we present a new measurement of the cross section $\sigma_{\pi\pi}$, obtained by the BESIII experiment at the BEPCII collider in Beijing.

The measurement exploits the method of initial state radiation (ISR), the same method as used by BaBar and KLOE. In the ISR method events are used in which one of the beam particles radiates a high-energy photon. In such a way, the available energy to produce a hadronic (or leptonic) final state is reduced, and the hadronic (or leptonic) mass range below the center-of-mass (cms) energy of the e^+e^- collider becomes available. In this paper, we restrict the studies to the mass range between 600 and 900 MeV/c^2, which corresponds to the ρ peak region.

The remainder of this letter is organized as follows: In section 2, the BESIII experiment is introduced. In section 3 we describe the data set used, the Monte Carlo (MC) simulation, the event selection of $e^+e^- \to \pi^+\pi^-\gamma$ events, and the data-MC efficiency corrections. The determination of the integrated luminosity of the data set is described in Section 4. A cross check of the used efficiency corrections using the well-known $e^+e^- \to \mu^+\mu^-\gamma$ QED process is performed in Section 5, before extracting the $\pi^+\pi^-$ cross section in Section 6.

2. The BESIII experiment

The BESIII detector is located at the double-ring Beijing electron-positron collider (BEPCII) [15].

The cylindrical BESIII detector covers 93% of the full solid angle. It consists of the following detector systems. (1) A Multilayer Drift Chamber (MDC), filled with helium gas, composed of 43 layers, which provides a spatial resolution of 135 μm, an ionization energy loss dE/dx resolution better than 6%, and a momentum resolution of 0.5% for charged tracks at 1 GeV/c. (2) A Time-of-Flight system (TOF), built with 176 plastic scintillator counters in the barrel part, and 96 counters in the endcaps. The time resolution is 80 ps in the barrel and 110 ps in the endcaps. For momenta up to 1 GeV/c, this provides a 2σ K/π separation. (3) A CsI(Tl) Electro-Magnetic Calorimeter (EMC), with an energy resolution of 2.5% in the barrel and 5% in the endcaps at an energy of 1 GeV. (4) A superconducting magnet producing a magnetic field of 1T. (5) A Muon Chamber (MUC) consisting of nine barrel and eight endcap resistive plate chamber layers with a 2 cm position resolution.

3. Data sample, event selection, and efficiency corrections

3.1. Data sample and MC simulations

We analyze 2.93 fb^{-1} (see Sect. 4) of data taken at a cms energy $\sqrt{s} = 3.773$ GeV, which were collected in two separate runs in 2010 and 2011. The Phokhara event generator [16, 17] is used to simulate the signal process $e^+e^- \to \pi^+\pi^-\gamma$ and the dominant background channel $\mu^+\mu^-\gamma$. The generator includes ISR and final state radiation (FSR) corrections up to next-to-leading order (NLO). Effects of ISR-FSR interference are included as well. The continuum $q\bar{q}$ ($q = u, d, s$) MC sample is produced with the KKMC event generator [18]. Bhabha scattering events are simulated with BABAYAGA 3.5 [19]. The Bhabha process is also used for the luminosity measurement. All MC generators have been interfaced with the GEANT4-based detector simulation [20, 21].

3.2. Event selection

Events of the type $e^+e^- \to \pi^+\pi^-\gamma$ are selected. Only a tagged ISR analysis is possible in the mass range $600 < m_{\pi\pi} < 900$ MeV/c^2, where $m_{\pi\pi}$ is the $\pi^+\pi^-$ invariant mass, *i.e.,* the radiated photon has to be explicitly detected in the detector. For untagged events, the photon escapes detection along the beam pipe; the hadronic system recoiling

against the ISR photon is therefore also strongly boosted towards small polar angles, resulting in no geometrical acceptance in the investigated $m_{\pi\pi}$ range.

We require the presence of two charged tracks in the MDC with net charge zero. The points of closest approach to the interaction point (IP) of both tracks have to be within a cylinder with 1 cm radius in the transverse direction and ± 10 cm of length along the beam axis. For three-track events, we choose the combination with net charge zero for which the tracks are closest to the IP. The polar angle θ of the tracks is required to be found in the fiducial volume of the MDC, $0.4\,\mathrm{rad} < \theta < \pi - 0.4\,\mathrm{rad}$, where θ is the polar angle of the track with respect to the beam axis. We require the transverse momentum p_t to be above 300 MeV/c for each track. In addition, we require the presence of at least one neutral cluster in the EMC without associated hits in the MDC. We require a deposited energy above 400 MeV. This cluster is then treated as the ISR photon candidate.

The radiative Bhabha process $e^+e^- \to e^+e^-\gamma(\gamma)$ has a cross section which is up to three orders of magnitude larger than the signal cross section. Electron tracks, therefore, need to be suppressed. An electron particle identification (PID) algorithm is used for this purpose, exploiting information from the MDC, TOF and EMC [22]. The probabilities for being a pion $P(\pi)$ and being an electron $P(e)$ are calculated, and $P(\pi) > P(e)$ is required for both charged tracks.

Using as input the momenta of the two selected track candidates, the energy of the photon candidate, as well as the four-momentum of the initial e^+e^- system, a four-constraint (4C) kinematic fit enforcing energy and momentum conservation is performed which tests the hypothesis $e^+e^- \to \pi^+\pi^-\gamma$. Events are considered to match the hypothesis if they fulfill the requirement $\chi^2_{\mathrm{4C}} < 60$. It turns out that the $\mu^+\mu^-\gamma$ final state can not be suppressed by means of kinematic fitting due to the limited momentum resolution of the MDC. An independent separation of pion and muon tracks is required.

We utilize a track-based muon-pion separation, which is based on the Artificial Neural Network (ANN) method, as provided by the TMVA package [23]. The following observables are exploited for the separation: the Zernicke moments of the EMC clusters [22], induced by pion or muon tracks, the ratio of the energy E of a track deposited in the EMC and its momentum p measured in the MDC, the ionization energy loss dE/dx in the MDC, and the depth of a track in the MUC. The ANN is trained using $\pi^+\pi^-\gamma$ and $\mu^+\mu^-\gamma$ MC samples. We choose the implementation of a Clermont-Ferrand Multilayer Perceptron (CFMlp) ANN as the method resulting in the best background rejection for a given signal efficiency. The output likelihood y_{ANN} is calculated after training the ANN for the signal pion tracks and background muon tracks. The response value y_{ANN} is required to be greater than 0.6 for each pion candidate in the event selection, yielding a background rejection of more than 90% and a signal loss of less than 30%.

3.3. Efficiency corrections

Given the accuracy of $\mathcal{O}(1\%)$ targeted for the cross section measurement, possible discrepancies between data and MC due to imperfections of the detector simulation need to be considered. We have investigated data and MC distributions concerning the tracking performance, the energy measurement, and the PID probabilities, both for the electron PID as well as the pion-muon separation. In order to produce test samples of muon and pion tracks over a wide range in momentum/energy and polar angle, we select samples of $\mu^+\mu^-\gamma$ and $\pi^+\pi^-\pi^+\pi^-\gamma$ events that have impurities at the per mille level. By comparing the efficiencies found in data with the corresponding results found in the MC samples, we determine possible discrepancies. Corresponding correction factors are computed in bins of the track momentum or energy and the track polar angle θ, and are applied to MC tracks to adjust the reconstructed number of events. While for the reconstruction of charged tracks and neutral clusters and for electron PID, the differences between data and MC are smaller than 1% on average, differences up to 10% occur in the ANN case. The corrections are applied separately for neutral clusters and for muon and pion tracks. Hence, we do not only obtain the corrections for the $\pi^+\pi^-\gamma$ signal events, but also for the dominating $\mu^+\mu^-\gamma$ background. The statistical errors of the correction factors are included in the statistical uncertainty of the measurement. Systematic uncertainties associated to the correction factors are presented in Sect. 6.5. The efficiency correction for the photon efficiency is obtained after the application of the kinematic fit procedure. The corresponding correction is therefore a combined correction of photon efficiency and differences between data and MC of

the $\chi^2_{\rm 4C}$ distribution. The systematic uncertainty for the contribution of the photon efficiency and $\chi^2_{\rm 4C}$ distribution is, hence, incorporated in the systematic effects associated with the efficiency corrections. The systematic uncertainty connected with the p_t requirement is also associated with the corresponding efficiency correction.

3.4. Background subtraction

The $\mu^+\mu^-\gamma$ background remaining after the application of the ANN is still of the order of a few percent, compared to 5×10^5 signal events. It is, however, known with high accuracy, as will be shown in the next section, and is subtracted based on MC simulation. Additional background beyond $\mu^+\mu^-\gamma$ remains below the one per mille level. Table 1 lists the remaining MC events after applying all requirements and scaling to the luminosity of the used data set.

Table 1: Total number of remaining non-muon background events between $600 < m_{\pi\pi} < 900$ MeV/c^2 obtained with MC samples.

Final state	Background events
$e^+e^-(n\gamma)$	12.0 ± 3.5
$\pi^+\pi^-\pi^0\gamma$	3.3 ± 1.8
$\pi^+\pi^-\pi^0\pi^0\gamma$	negl.
$K^+K^-\gamma$	2.0 ± 1.5
$K^0\overline{K^0}\gamma$	0.4 ± 0.6
$p\overline{p}\gamma$	negl.
continuum	3.9 ± 1.9
$\psi(3770) \to D^+D^-$	negl.
$\psi(3770) \to D^0\overline{D^0}$	negl.
$\psi(3770) \to$ non $\mathrm{D\overline{D}}$	3.1 ± 1.8
$\gamma\,\psi(2S)$	negl.
$\gamma\,J/\psi$	0.6 ± 0.8

4. Luminosity measurement using Bhabha events

The integrated luminosity of the data set used in this work was previously measured in Ref. [24] with a precision of 1.0% using Bhabha scattering events. In the course of this analysis, we re-measure the luminosity and decrease its systematic uncertainty by the following means: (1) Usage of the BABAYAGA@NLO [25] event generator with a theoretical uncertainty of 0.1%, instead of the previously used BABAYAGA 3.5 event generator with an uncertainty of 0.5% [19]. (2) Precise estimation of the signal selection efficiencies. In particular, the uncertainty estimate of the polar angle acceptance is evaluated by data-MC studies within the fiducial EMC detection volume, which is relevant for the luminosity study (0.13%). The very conservative estimate in [24] was based on acceptance comparisons with and without using the transition region between the EMC barrel and endcaps, leading to additional data-MC differences (0.75%). The other uncertainties of [24] remain unchanged and additional systematic uncertainties due to the uncertainty of $\sqrt{s}$ (0.2%) and the vacuum polarization correction ($< 0.01\%$) are taken into account. Finally, the total integrated luminosity amounts to $\mathcal{L} = (2931.8 \pm 0.2_{\rm stat} \pm 13.8_{\rm sys})\mathrm{pb}^{-1}$ with a relative uncertainty of 0.5%, which is consistent with the previous measurement [24].

5. QED test using $e^+e^- \to \mu^+\mu^-\gamma$ events

The yield of events of the channel $e^+e^- \to \mu^+\mu^-\gamma$ as a function of the two-muon invariant mass $m_{\mu\mu}$ can be compared to a precise prediction by QED, which is provided by the Phokhara generator. We select muon events according to the ANN method described previously and require $y_{\rm ANN} < 0.4$ for both tracks, resulting in a background rejection of more than 90% and a signal loss of less than 20%. All other requirements in the selection are exactly the same as for the $\pi^+\pi^-\gamma$ analysis. The remaining pion background after the $\mu^+\mu^-\gamma$ selection is much reduced, reaching 10% in the ρ peak region. A comparison between data and MC is shown in Fig. 1. The same data sample as used in the main analysis is also used here, but we present a larger mass range than for the $\pi^+\pi^-\gamma$ case. The efficiency corrections described in the previous section have been applied to MC on a track and photon candidate basis. The lower panel of Fig. 1 shows the relative discrepancy between data and MC. A good agreement over the full $m_{\mu\mu}$ mass range at the level of $(1.0 \pm 0.3 \pm 0.9)\%$ and $\chi^2/\mathrm{ndf} = 134/139$ is found, where the uncertainties are statistical and systematic, respectively. A difference in the mass resolution due to detector effects between data and MC is visible around the narrow J/ψ resonance. A fit in the mass range $600 < m_{\mu\mu} < 900$ MeV/c^2, which is the mass range studied in the main analysis, gives a relative discrepancy of $(2.0 \pm 1.7 \pm 0.9)\%$; this is illustrated in

the inset of the upper panel of Fig. 1. The theoretical uncertainty of the MC generator Phokhara is below 0.5% [16], while the systematic uncertainty of our measurement is 0.9%. The latter is dominated by the luminosity measurement, which is needed for the normalization of the data set. We consider the good agreement between the $\mu^+\mu^-\gamma$ QED prediction and data as a validation of the accuracy of our efficiency corrections. As a further cross check, we have applied the efficiency corrections also to a statistically independent $\mu^+\mu^-\gamma$ sample, resulting in a difference between data and MC of $(0.7 \pm 0.2)\%$ over the full mass range, where the error is statistical only.

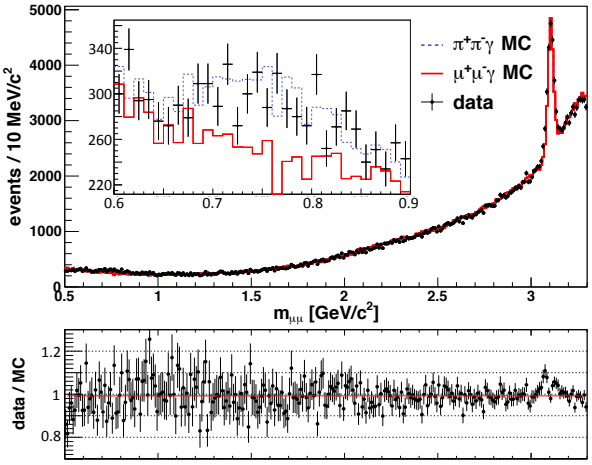

Figure 1: Invariant $\mu^+\mu^-$ mass spectrum of data and $\mu^+\mu^-\gamma$ MC after using the ANN as muon selector and applying the efficiency corrections. The upper panel presents the absolute comparison of the number of events found in data and MC. The inset shows the zoom for invariant masses between 0.6 and 0.9 GeV/c^2. The MC sample is scaled to the luminosity of the data set. The lower plot shows the ratio of these two histograms. A linear fit is performed to quantify the data-MC difference, which gives a difference of $(1.0 \pm 0.3 \pm 0.9)\%$. A difference in the mass resolution between data and MC is visible around the narrow J/ψ resonance.

6. Extraction of $\sigma(e^+e^- \to \pi^+\pi^-)$ and $|F_\pi^2|$

6.1. Methods

We finally extract $\sigma_{\pi\pi} = \sigma(e^+e^- \to \pi^+\pi^-)$ according to two independent normalization schemes.

In the first method, we obtain the bare cross section, *i.e.,* the cross section corrected for vacuum polarization effects, according to the following formula:

$$\sigma^{\rm bare}_{\pi\pi(\gamma_{\rm FSR})} = \frac{N_{\pi\pi\gamma} \cdot (1+\delta^{\pi\pi}_{\rm FSR})}{\mathcal{L} \cdot \epsilon^{\pi\pi\gamma}_{\rm global} \cdot H(s) \cdot \delta_{\rm vac}} \,, \qquad (1)$$

where $N_{\pi\pi\gamma}$ is the number of signal events found in data after applying all selection requirements described above and an unfolding procedure to correct for the mass resolution, $\mathcal{L}$ the luminosity of the data set, and H the radiator function. The global efficiency $\epsilon^{\pi\pi\gamma}_{\rm global}$ is determined based on the signal MC by dividing the measured number of events after all selection requirements $N^{\rm true}_{\rm measured}$ by that of all generated events $N^{\rm true}_{\rm generated}$. The true MC sample is used, with the full θ_γ range, applying the efficiency corrections mentioned in Section 3.3 but without taking into account the detector resolution in the invariant mass m:

$$\epsilon_{\rm global}(m) = \frac{N^{\rm true}_{\rm measured}(m)}{N^{\rm true}_{\rm generated}(m)} \,. \qquad (2)$$

The efficiency is found to depend slightly on $m_{\pi\pi}$ and ranges from 2.8% to 3.0% from lowest to highest $m_{\pi\pi}$. An unfolding procedure, which eliminates the effect of the detector resolution, is described in Sect. 6.2 and is applied before dividing by the global efficiency. The radiator function H is described in Sect. 6.4. As input for a_μ the bare cross section is needed. It can be obtained by dividing the cross section by the vacuum polarization correction $\delta_{\rm vac}$, which is also described in Sect. 6.4. As pointed out in Ref. [11], in order to consider radiative effects in the dispersion integral for a_μ, an FSR correction has to be performed. The determination of the correction factor $(1+\delta^{\pi\pi}_{\rm FSR})$ is described in Sect. 6.3.

In the second method, we use a different normalization than in the first method and normalize $N_{\pi\pi\gamma}$ to the measured number of $\mu^+\mu^-\gamma$ events, $N_{\mu\mu\gamma}$. Since $\mathcal{L}$, H, and $\delta_{\rm vac}$ cancel in this normalization, one finds the following formula:

$$\sigma^{\rm bare}_{\pi\pi(\gamma_{\rm FSR})} = \frac{N_{\pi\pi\gamma}}{N_{\mu\mu\gamma}} \cdot \frac{\epsilon^{\mu\mu\gamma}_{\rm global}}{\epsilon^{\pi\pi\gamma}_{\rm global}} \cdot \frac{1+\delta^{\mu\mu}_{\rm FSR}}{1+\delta^{\pi\pi}_{\rm FSR}} \cdot \sigma^{\rm bare}_{\mu\mu} \,, \qquad (3)$$

where $\epsilon^{\mu\mu\gamma}_{\rm global}$ is the global efficiency of the dimuon selection, already described in Sect. 5, $\delta^{\mu\mu}_{\rm FSR}$ is the FSR correction factor to the $\mu^+\mu^-$ final state, which can be obtained using the Phokhara event generator, $\sigma^{\rm bare}_{\mu\mu}$ is the exact QED prediction of the

dimuon cross section, given by [26, Eq. (5.13)]

$$\sigma_{\mu\mu}^{\rm bare} = \frac{4\pi\alpha^2}{3s'} \cdot \frac{\beta_\mu(3-\beta_\mu^2)}{2} \,, \qquad (4)$$

with the fine structure constant α, the cms energy $s' < s$ available for the creation of the final state, the muon velocity $\beta_\mu = \sqrt{1-4m_\mu^2/s'}$, and the muon mass m_μ. The contributions of radiator function, luminosity, and vacuum polarization to the systematic uncertainties of the bare cross section, cancel in the second method. The upper panel of Fig. 2 shows the comparison of the bare cross sections including FSR obtained with the first (black) and second method before unfolding (blue). The error bars are statistical only. They are much larger for the second method due to the limited $\mu^+\mu^-\gamma$ statistics in the mass range of interest. The lower panel shows the ratio of these cross sections. Again, a linear fit is performed to quantify the difference, which is found to be $(0.85 \pm 1.68)\%$ and $\chi^2/\mathrm{ndf} = 50/60$, where the error is statistical. Both methods agree within uncertainties. The first one is used in the analysis. Finally, the pion form factor as a function of s' can be calculated via

$$|F_\pi|^2(s') = \frac{3s'}{\pi\alpha^2\beta_\pi^3(s')}\sigma_{\pi\pi}^{\rm dressed}(s') \,, \qquad (5)$$

with the pion velocity $\beta_\pi(s') = \sqrt{1-4m_\pi^2/s'}$, the charged pion mass m_π, and the dressed cross section $\sigma_{\pi\pi}^{\rm dressed}(s') = \sigma(e^+e^- \to \pi^+\pi^-)(s')$ containing vacuum polarization, but corrected for FSR effects. The result is presented in Sect. 7.

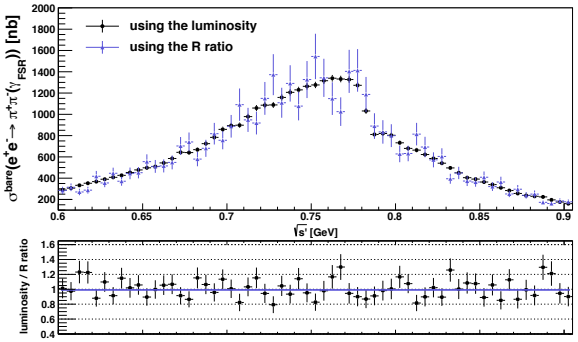

Figure 2: Comparison between the methods to extract $\sigma_{\pi\pi}$ explained in the text — using the luminosity (black) and normalizing by $\sigma_{\mu\mu}$ (blue). The lower panel shows the ratio of these results together with a linear fit (blue line) to quantify their difference.

6.2. Unfolding

In order to obtain the final result for $\sigma_{\pi\pi}$, one has to rectify the detector resolution effects, *i.e.,* the mass spectrum needs to be unfolded. To this end, the Singular Value Decomposition (SVD) method [27] is used. It requires two input variables — the response matrix and the regularization parameter τ. The SVD algorithm calculates an operator which cancels the detector smearing by inverting the response matrix. We obtain the response matrix in the full mass range between threshold and 3.0 GeV, using a signal MC sample. The matrix corresponds to the correlation of the reconstructed $m_{\pi\pi}$ spectrum, and the originally generated $m_{\pi\pi}$ values. With the choice of a bin width of 5 MeV/c^2, about 43% of events are found to be on the diagonal axis.

To find the value of the regularization parameter τ, we compare two independent methods, as suggested in Ref. [27]. On the one hand, we perform a MC simulation where τ is optimized such that unfolded and true distributions have the best agreement. On the other hand, we process an algorithm, described in [27], exploiting the singular values of the response matrix. Both methods favor a similar regularization parameter of $\tau \cong 72$.

To estimate the systematic uncertainties and to test the stability of the SVD method, we perform two cross checks. In both cases we use a $\pi^+\pi^-\gamma$ MC sample which is independent of the one used to determine the response matrix. We modify and then unfold the spectra in both checks. In the first cross check, the reconstructed spectrum is smeared with an additional Gaussian error, which results in an about 20% larger detector smearing than expected from MC simulation. The resulting unfolded spectrum reproduces the true one on the sub per mille level. In the second cross check, the mass of the ρ-resonance is varied systematically in the simulation in steps of 10 MeV/c^2 between 750 and 790 MeV/c^2. The response matrix is kept fixed and was determined with a ρ mass of 770 MeV/c^2. In all cases, the masses of the ρ peak after unfolding are found to be close to the initially simulated masses. From the comparisons of these checks, we take the maximum deviation of 0.2% as systematic uncertainty.

6.3. FSR correction

The correction factor $\delta_{\rm FSR}$ is determined with the Phokhara generator in bins of $m_{\pi\pi}$. Two dif-

ferent correction methods are used on the data to cross check whether it is applied correctly.

(1) The whole FSR contribution of the $\pi^+\pi^-\gamma$ events is calculated with Phokhara, by dividing a true MC spectrum including FSR in NLO by the spectrum without any FSR contribution. The resulting distribution is used to correct data. As pointed out in Ref. [11], for the dispersion integral for a_μ, the FSR correction for the process $e^+e^- \to \pi^+\pi^-$ needs then to be added again. We use the calculation by Schwinger assuming pointlike pions:

$$\sigma^{\rm dressed}_{\pi\pi(\gamma)} = \sigma^{\rm dressed}_{\pi\pi} \cdot \left[1 + \eta(s)\frac{\alpha}{\pi}\right], \qquad (6)$$

where $\eta(s)$ is the theoretical correction factor taken from [28]. In the ρ-peak region it is between 0.4% and 0.9%.

(2) A special version of the Phokhara generator is used [29], which, in contrast to the standard version of the generator, distinguishes whether a photon is emitted in the initial or the final state. In events in which photons have been radiated solely due to ISR, the momentum transfer of the virtual photon s_{γ^*} is equal to the invariant mass of the two pions $m^2_{\pi\pi}$. However, if an FSR photon is emitted, the invariant mass is lowered due to this effect and hence $m^2_{\pi\pi} < s_{\gamma^*}$. The effect can be removed by applying an unfolding procedure, using again the SVD algorithm. Here, the response matrix is $m^2_{\pi\pi}$ vs. s_{γ^*}, obtained from a MC sample that includes FSR in NLO. The regularization parameter τ is determined as described in Sect. 6.2. After applying the corrections for the radiative $\pi^+\pi^-\gamma$ process, which are of the order of 2%, one obtains the $\pi^+\pi^-(\gamma_{\rm FSR})$ cross section directly.

The difference between both methods is found to be (0.18 ± 0.13)%. Both methods are complementary and agree with each other within errors. The difference is taken as systematic uncertainty. Finally, the correction obtained with method (1) is used in the analysis.

6.4. Radiator function and vacuum polarisation correction

The radiator function is implemented within the Phokhara event generator with NLO precision. Hence, a very precise description is available with a claimed uncertainty of 0.5% [16].

To obtain the *bare* cross section, vacuum polarization effects $\delta_{\rm vac}$ must be taken into account. To this aim, the dressed cross section, including the vacuum polarization effects, is adjusted for the running of the coupling constant α [30]. Bare and dressed cross sections are related as follows:

$$\sigma^{\rm bare} = \frac{\sigma^{\rm dressed}}{\delta_{\rm vac}} = \sigma^{\rm dressed} \cdot \left(\frac{\alpha(0)}{\alpha(s)}\right)^2. \qquad (7)$$

The correction factors are taken from Ref. [31].

6.5. Summary of systematic uncertainties

Systematic uncertainties are studied within the investigated $m_{\pi\pi}$ range between 600 and 900 MeV/c^2. Sources are:

(1) Efficiency corrections: Each individual uncertainty is studied in bins of $m_{\pi\pi}$ with respect to three different sources. Firstly, the remaining background contaminations in the data samples are estimated with the corresponding MC simulation mentioned in Tab. 1. Their contribution is taken into account by multiplying the claimed uncertainties of the event generators and their fraction of the investigated signal events. Secondly, we vary the selection requirements (E/p, χ^2_{1C}, depth of a charged track in the MUC), which are used to select clean muon and pion samples for the efficiency studies, in a range of three times the resolution of the corresponding variable. The differences of the correction factors are calculated. Thirdly, the resolution of the correction factors, *i.e.,* the bin sizes of momentum and θ distributions, is varied by a factor two and the effects on the final correction factors are tested.

(2) Pion-muon separation: Additional uncertainties of using the ANN method for pion-muon separation are estimated by comparing the result from a different multivariate method, namely the Boosted Decision Tree (BDT) approach [23]. As a further cross check, the whole analysis is repeated without the use of a dedicated PID method.

(3) Residual background is subtracted using simulated events. The uncertainty is determined to be 0.1%.

(4) Angular acceptance: The knowledge of the angular acceptance of the tracks is studied by varying this requirement by more than three standard deviations of the angular resolution and studying the corresponding difference in the selected number of events. A difference of 0.1% in the result can be observed. The procedure is repeated for all other selection criteria. Their contribution to the total systematic uncertainty is found to be negligible.

(5) Unfolding: Uncertainties introduced by unfolding are smaller than 0.2%, as estimated by the two

cross checks mentioned in Sect. 6.2.
(6) FSR correction: The uncertainty due to the FSR correction is obtained by comparing two different approaches as described in Sect. 6.3. The uncertainty is found to be 0.2%.
(7) Vacuum Polarization: The uncertainty due to the vacuum polarization correction is conservatively estimated to be 0.2%.
(8) Radiator Function: The Radiator Function extracted from the Phokhara generator is implemented with a precision of 0.5%.
(9) Luminosity: The luminosity of the analyzed data set has been determined to a precision of 0.5%.
All systematic uncertainties are summarized in Tab. 2. They are added in quadrature, and a total systematic uncertainty for $\sigma^{\rm bare}(e^+e^- \to \pi^+\pi^-(\gamma_{\rm FSR}))$ of 0.9% is achieved, which is fully correlated amongst all data points.

Table 2: Summary of systematic uncertainties.

Source	Uncertainty (%)
Photon efficiency correction	0.2
Pion tracking efficiency correction	0.3
Pion ANN efficiency correction	0.2
Pion e-PID efficiency correction	0.2
ANN	negl.
Angular acceptance	0.1
Background subtraction	0.1
Unfolding	0.2
FSR correction $\delta_{\rm FSR}$	0.2
Vacuum polarization correction $\delta_{\rm vac}$	0.2
Radiator function	0.5
Luminosity $\mathcal{L}$	0.5
Sum	**0.9**

7. Results

The result for $\sigma^{\rm bare}(e^+e^- \to \pi^+\pi^-(\gamma_{\rm FSR}))$ as a function of $\sqrt{s} = m_{\pi\pi}$ is illustrated in Fig. 3 and given numerically in Tab. 4. The cross section is corrected for vacuum polarization effects and includes final state radiation. Besides the dominant $\rho(770)$ peak, the well-known structure of the ρ-ω interference is observed. The result for the pion form factor $|F_\pi|^2$ is shown in Fig. 4 and given numerically in Tab. 4. It includes vacuum polarization corrections, but, differently from the cross section shown in Fig. 3, final state radiation effects are excluded here. The red line in Fig. 4 illustrates a fit to data according to a parametrization proposed by Gounaris and Sakurai [32]. Here, exactly the same fit formula and fit procedure are applied as described in detail in Ref. [10]. Free parameters of

Table 3: Fit parameters and statistical errors of the Gounaris-Sakurai fit of the pion form factor. Also shown are the PDG 2014 values [33].

Parameter	BESIII value	PDG 2014
m_ρ [MeV/c^2]	776.0 ± 0.4	775.26 ± 0.25
Γ_ρ [MeV]	151.7 ± 0.7	147.8 ± 0.9
m_ω [MeV/c^2]	782.2 ± 0.6	782.65 ± 0.12
Γ_ω [MeV]	fixed to PDG	8.49 ± 0.08
$\lvert c_\omega \rvert$ [10^{-3}]	1.7 ± 0.2	-
$\lvert \phi_\omega \rvert$ [rad]	0.04 ± 0.13	-

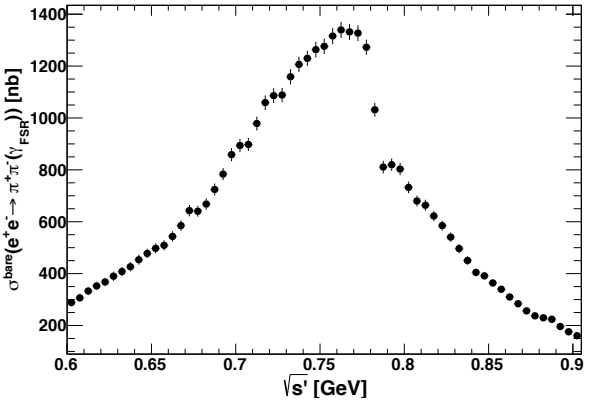

Figure 3: The measured bare $e^+e^- \to \pi^+\pi^-(\gamma_{\rm FSR})$ cross section. Only the statistical errors are shown.

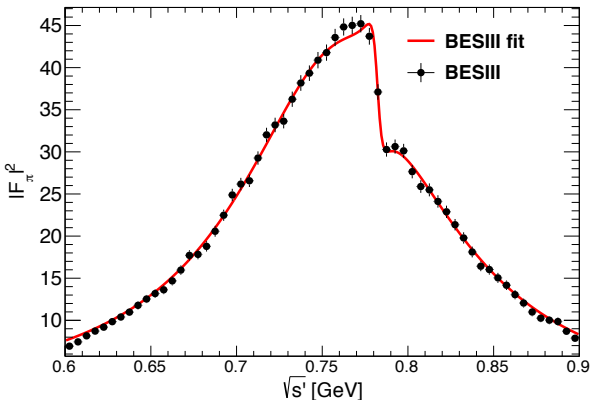

Figure 4: The measured squared pion form factor $|F_\pi|^2$. Only statistical errors are shown. The red line represents the fit using the Gounaris-Sakurai parametrization.

the fit are the mass and width Γ of the ρ meson, the mass of the ω meson, and the phase of the Breit-Wigner function $c_\omega = |c_\omega| e^{i\phi_\omega}$. The width of the ω meson is fixed to the PDG value [33]. The resulting values are shown in Tab. 3. As can be seen, the resonance parameters are in agreement with the PDG values [33] within uncertainties, except for Γ_ρ, which shows a 3.4σ deviation. Corresponding amplitudes for the higher ρ states, $\rho(1450)$, $\rho(1700)$, and $\rho(2150)$, as well as the masses and widths of those states were taken from Ref. [10], and the systematic uncertainty in Γ_ρ due to these assumptions has not been quantitatively evaluated.

The Gounaris-Sakurai fit provides an excellent description of the BESIII data in the full mass range from 600 to 900 MeV/c^2, resulting in $\chi^2/\text{ndf} = 49.1/56$. Figure 5 shows the difference between fit and data. Here the data points show the statistical uncertainties only, while the shaded error band of the fit shows the systematic uncertainty only.

In order to compare the result with previous measurements, the relative difference of the BESIII fit and data from BaBar [10], KLOE [6, 7, 8], CMD2 [1, 2], and SND [3] is investigated. Such a comparison is complicated by the fact, that previous measurements used different vacuum polarization corrections. Therefore, we consistently used the vacuum polarization correction from Ref. [31] for all the comparisons discussed in this section. The KLOE 08, 10, 12, and BaBar spectra have, hence, been modified accordingly. The individual comparisons are illustrated in Figs. 5 and 6. Here, the shaded error band of the fit includes the systematic error only, while the uncertainties of the data points include the sum of the statistical and systematic errors. We observe a very good agreement with the KLOE 08 and KLOE 12 data sets up to the mass range of the ρ-ω interference. In the same mass range the BaBar and KLOE 10 data sets show a systematic shift, however, the deviation is, not exceeding 1 to 2 standard deviations. At higher masses, the statistical error bars in the case of BESIII are relatively large, such that a comparison is not conclusive. There seem to be a good agreement with the BaBar data, while a large deviation with all three KLOE data sets is visible. There are indications that the BESIII data and BESIII fit show some disagreement in the low mass and very high mass tails as well. We have also compared our results in the ρ peak region with data from Novosibirsk. At lower and higher masses, the statistical uncertainties of the Novosibirsk results are too large to draw definite conclusions. The spectra from SND and from the 2006 publication of CMD-2 are found to be in very good agreement with BESIII in the ρ peak region, while the 2004 result of CMD-2 shows a systematic deviation of a few percent.

We also compute the contribution of our BESIII cross section measurement $\sigma^{\text{bare}}(e^+e^- \to \pi^+\pi^-(\gamma_{\text{FSR}}))$ to the hadronic contribution of $(g-2)_\mu$,

$$a_\mu^{\pi\pi,\text{LO}}(0.6 - 0.9\,\text{GeV}) = \frac{1}{4\pi^3} \int\limits_{(0.6\text{GeV})^2}^{(0.9\text{GeV})^2} \text{ds}' \text{K}(\text{s}') \sigma^{\text{bare}}_{\pi\pi(\gamma)} \,, \tag{8}$$

where $K(s')$ is the kernel function [11, Eq. (5)]. As summarized in Fig. 7, the BESIII result, $a_\mu^{\pi\pi,\text{LO}}(600-900\text{ MeV}) = (368.2 \pm 2.5_{\text{stat}} \pm 3.3_{\text{sys}}) \cdot 10^{-10}$, is found to be in good agreement with all three KLOE values. A difference of about 1.7σ with respect to the BaBar result is observed.

8. Conclusion

A new measurement of the cross section $\sigma^{\text{bare}}(e^+e^- \to \pi^+\pi^-(\gamma_{\text{FSR}}))$ has been performed with an accuracy of 0.9% in the dominant $\rho(770)$ mass region between 600 and 900 MeV/c^2, using the ISR method at BESIII. The energy dependence of the cross section appears compatible with corresponding measurements from KLOE and BaBar within approximately one standard deviation. The two-pion contribution to the hadronic vacuum polarization contribution to $(g-2)_\mu$ has been determined from the BESIII data to be $a_\mu^{\pi\pi,\text{LO}}(600 - 900\text{ MeV}) = (368.2 \pm 2.5_{\text{stat}} \pm 3.3_{\text{sys}}) \cdot 10^{-10}$. By averaging the KLOE, BaBar, and BESIII values of $a_\mu^{\pi\pi,\text{LO}}$ and assuming that the five data sets are independent, a deviation of more than 3σ between the SM prediction of $(g-2)_\mu$ and its direct measurement is confirmed. For the low mass region < 600 MeV/c^2 and the high mass region > 900 MeV/c^2, the BaBar data was used in this calculation.

9. Acknowledgements

The BESIII collaboration thanks the staff of BEPCII and the IHEP computing center for their strong support. We thank Thomas Teubner for the recalculation of $a_\mu^{\pi\pi,\text{LO}}(600 - 900\text{ MeV})$ and Fedor Ignatov for the useful discussions. This work is supported in part by National Key Basic Research Program of China under Contract

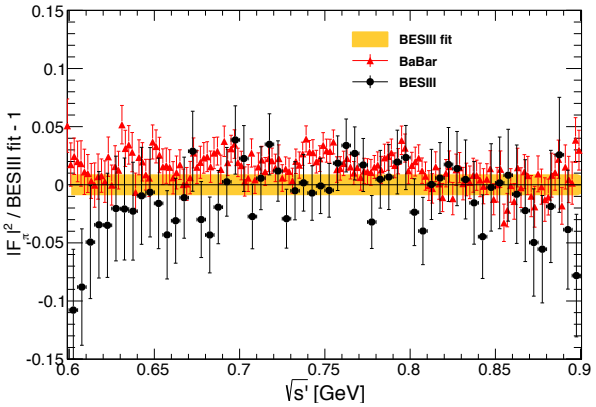

Figure 5: Relative difference of the form factor squared from BaBar [10] and the BESIII fit. Statistical and systematic uncertainties are included in the data points. The width of the BESIII band shows the systematic uncertainty only.

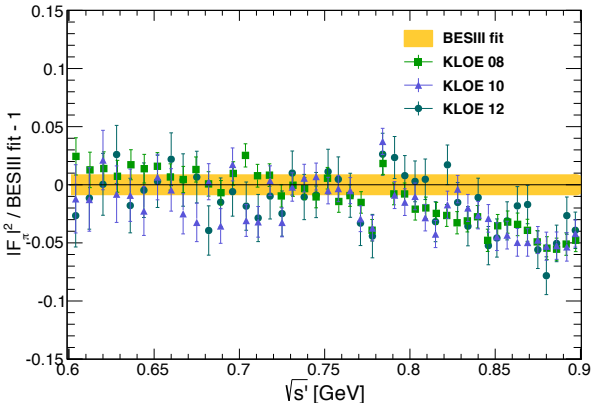

Figure 6: Relative difference of the form factor squared from KLOE [6, 7, 8] and the BESIII fit. Statistical and systematic uncertainties are included in the data points. The width of the BESIII band shows the systematic uncertainty only.

No. 2015CB856700; National Natural Science Foundation of China (NSFC) under Contracts Nos. 11125525, 11235011, 11322544, 11335008, 11425524; the Chinese Academy of Sciences (CAS) Large-Scale Scientific Facility Program; the CAS Center for Excellence in Particle Physics (CCEPP); the Collaborative Innovation Center for Particles and Interactions (CICPI); Joint Large-Scale Scientific Facility Funds of the NSFC and CAS under Contracts Nos. 11179007, U1232201, U1332201; CAS under Contracts Nos. KJCX2-YW-N29, KJCX2-YW-N45; 100 Talents Program of CAS; National 1000 Talents Program of China; INPAC and Shanghai Key Laboratory for Particle Physics and Cosmology; German Research Foundation DFG under Contract No. Collaborative Research Center CRC-1044; Istituto Nazionale di Fisica Nucleare, Italy; Ministry of Development of Turkey under Contract No. DPT2006K-120470; Russian Foundation for Basic Research under Contract No. 14-07-91152; The Swedish Resarch Council; U. S. Department of Energy under Contracts Nos. DE-FG02-04ER41291, DE-FG02-05ER41374, DE-FG02-94ER40823, DESC0010118; U.S. National Science Foundation; University of Groningen (RuG) and the Helmholtzzentrum fuer Schwerionenforschung GmbH (GSI), Darmstadt; WCU Program of National Research Foundation of Korea under Contract No. R32-2008-000-10155-0.

References

References

[1] R.R. Akhmetshin et al. [CMD2 Collaboration], Phys. Lett. B **578**, 285 (2004).
[2] R.R. Akhmetshin et al. [CMD2 Collaboration], Phys. Lett. B **648**, 28 (2007).
[3] M.N. Achasov et al. [SND Collaboration], JETP **101**, 1053 (2005).
[4] J.E. Augustin et al., Phys. Rev. Lett. **20**, 126 (1968).
[5] A. Aloisio et al. [KLOE Collaboration], Phys. Lett. B **606**, 12 (2005).
[6] F. Ambrosio et al. [KLOE Collaboration], Phys. Lett. B **670**, 285 (2009).
[7] F. Ambrosino et al. [KLOE Collaboration], Phys. Lett. B **700**, 102 (2011).
[8] D. Babusci et al. [KLOE Collaboration], Phys. Lett. B **720**, 336 (2013).
[9] B. Aubert et al. [BABAR Collaboration], Phys. Rev. Lett. **103**, 231801 (2009).
[10] J. P. Lees et al. [BABAR Collaboration], Phys. Rev. D **86**, 032013 (2012).
[11] S. Eidelman, F. Jegerlehner, Z.Phys. C **67**, 585 (1995).
[12] M. Davier, A. Hoecker, B. Malescu and Z. Zhang, Eur. Phys. J. C **71**, 1515 (2011).
[13] K. Hagiwara, R. Liao, A.D. Martin, Daisuke Nomura, T. Teubner, J. Phys. G **38**, 085003 (2011).
[14] M. Davier, A. Hoecker, B. Malescu, C. Z. Yuan and Z. Zhang, Eur. Phys. J. C **66**, 1 (2010).
[15] M. Ablikim et al. [BESIII Collaboration], Nucl. Instrum. Meth. A **614**, 345 (2010).
[16] G. Rodrigo, H. Czyż, J. H. Kuhn, M. Szopa, Eur. Phys. J. C **24**, 71 (2002).
[17] H. Czyż, J. H. Kuhn and A. Wapienik, Phys. Rev. D **77**, 114005 (2008).

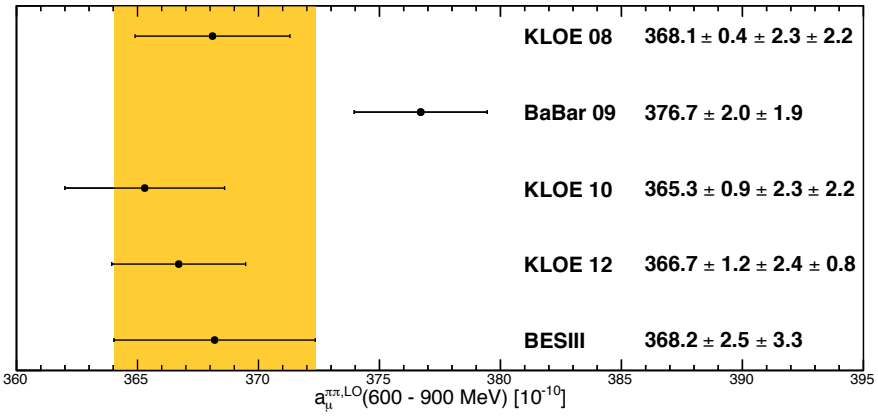

Figure 7: Our calculation of the leading-order (LO) hadronic vacuum polarization 2π contributions to $(g-2)_\mu$ in the energy range 600 - 900 MeV from BESIII and based on the data from KLOE 08 [6], 10 [7], 12 [8], and BaBar [10], with the statistical and systematic errors. The statistical and systematic errors are added quadratically. The band shows the 1σ range of the BESIII result.

[18] S. Jadach, B. F. L. Ward and Z. Was, Comput. Phys. Commun. **130**, 260 (2000).

[19] G. Balossini, C. M. C. Calame, G. Montagna, O. Nicrosini and F. Piccinini, Nucl. Phys. B **758**, 227 (2006).

[20] J. Allison et al. [GEANT4 Collaboration], IEEE Transactions on Nuclear Science **53**, 270 (2006).

[21] S. Agostinelli et al. [GEANT4 Collaboration], Nucl. Instrum. Meth. A **506**, 250 (2003).

[22] D. M. Asner et al., Int. J. Mod. Phys. A **24**, 1 (2009).

[23] A. Hoecker. P. Speckmayer, J. Stelzer, J. Therhaag, E. Von Toerne and H. Voss, PoS ACAT **040** (2007).

[24] M. Ablikim et al. [BESIII Collaboration], Chin. Phys. C **37**, 123001 (2013).

[25] G. Balossini, C. Bignamini, C.M. Carloni Calame, G. Montagna, F. Piccinini and O. Nicrosini, Phys. Lett. B **663**, 209 (2008).

[26] M. E. Peskin and D. V. Schroeder, *An Introduction to Quantum Field Theory*, Vol. 2, USA, Addison-Wesley, 135 (1995).

[27] A. Hoecker, V. Kartvelishvili, Nucl. Instrum. Meth. A **372**, 469 (1996).

[28] J. S. Schwinger, *Particles, Sources and Fields*, Vol. 3, Redwood City, USA Addison-Wesley, 99 (1989).

[29] Private communication with H. Czyz.

[30] A. Höfer, J. Gluza and F. Jegerlehner, Eur. Phys. J. C **24**, 51 (2002).

[31] F. Jegerlehner, Nucl. Phys. Proc. Suppl. **181 – 182**, 135 (2008); F. Jegerlehner, Z. Phys. C **32**, 195 (1986); www-com.physik.hu-berlin.de/∼fjeger/alphaQED.tar.gz (2015)

[32] G. J. Gounaris and J. J. Sakurai, Phys. Rev. Lett. **21**, 244 (1968).

[33] K.A. Olive et al. [Particle Data Group], Chin. Phys. C **38**, 090001 (2014).

Table 4: Results of the BESIII measurement of the cross section $\sigma^{\rm bare}_{\pi^+\pi^-(\gamma_{\rm FSR})} \equiv \sigma^{\rm bare}(e^+e^- \to \pi^+\pi^-(\gamma_{\rm FSR}))$ and the squared pion form factor $|F_\pi|^2$. The errors are statistical only. The value of $\sqrt{s'}$ represents the bin center. The 0.9% systematic uncertainty is fully correlated between any two bins.

$\sqrt{s'}$ [MeV]	$\sigma^{\rm bare}_{\pi^+\pi^-(\gamma_{\rm FSR})}$ [nb]	$\lvert F_\pi\rvert^2$	$\sqrt{s'}$ [MeV]	$\sigma^{\rm bare}_{\pi^+\pi^-(\gamma_{\rm FSR})}$ [nb]	$\lvert F_\pi\rvert^2$
602.5	288.3 ± 15.2	6.9 ± 0.4	752.5	1276.1 ± 29.8	41.8 ± 1.0
607.5	306.6 ± 15.5	7.4 ± 0.4	757.5	1315.9 ± 31.3	43.6 ± 1.0
612.5	332.8 ± 16.3	8.2 ± 0.4	762.5	1339.3 ± 30.9	44.8 ± 1.0
617.5	352.5 ± 16.3	8.7 ± 0.4	767.5	1331.9 ± 30.8	45.0 ± 1.0
622.5	367.7 ± 16.6	9.2 ± 0.4	772.5	1327.0 ± 30.6	45.2 ± 1.0
627.5	390.1 ± 17.7	9.8 ± 0.4	777.5	1272.7 ± 29.2	43.7 ± 1.0
632.5	408.0 ± 18.0	10.4 ± 0.5	782.5	1031.5 ± 26.7	37.1 ± 0.9
637.5	426.6 ± 18.1	11.0 ± 0.5	787.5	810.7 ± 24.2	30.3 ± 0.8
642.5	453.5 ± 19.0	11.8 ± 0.5	792.5	819.7 ± 23.8	30.6 ± 0.8
647.5	477.7 ± 18.5	12.5 ± 0.5	797.5	803.1 ± 23.3	30.1 ± 0.8
652.5	497.4 ± 19.5	13.2 ± 0.5	802.5	732.4 ± 22.1	27.7 ± 0.8
657.5	509.2 ± 19.4	13.6 ± 0.5	807.5	679.9 ± 20.6	25.9 ± 0.7
662.5	543.4 ± 19.9	14.7 ± 0.5	812.5	663.6 ± 21.0	25.5 ± 0.8
667.5	585.0 ± 20.5	16.0 ± 0.6	817.5	622.2 ± 19.9	24.1 ± 0.7
672.5	642.7 ± 22.2	17.7 ± 0.6	822.5	585.0 ± 19.5	22.9 ± 0.7
677.5	640.5 ± 21.0	17.8 ± 0.6	827.5	540.8 ± 18.1	21.4 ± 0.7
682.5	668.0 ± 21.9	18.8 ± 0.6	832.5	496.4 ± 17.7	19.8 ± 0.7
687.5	724.4 ± 22.9	20.6 ± 0.6	837.5	450.4 ± 16.8	18.1 ± 0.6
692.5	783.5 ± 23.2	22.5 ± 0.7	842.5	404.7 ± 15.2	16.4 ± 0.6
697.5	858.6 ± 25.3	24.9 ± 0.7	847.5	391.3 ± 15.4	16.0 ± 0.6
702.5	893.8 ± 25.4	26.2 ± 0.7	852.5	364.0 ± 15.0	15.0 ± 0.6
707.5	897.8 ± 25.0	26.6 ± 0.7	857.5	339.6 ± 14.0	14.2 ± 0.6
712.5	978.6 ± 26.6	29.3 ± 0.8	862.5	310.0 ± 13.7	13.0 ± 0.6
717.5	1059.1 ± 27.9	32.0 ± 0.8	867.5	283.8 ± 13.0	12.1 ± 0.5
722.5	1086.0 ± 28.3	33.2 ± 0.9	872.5	256.5 ± 12.4	11.0 ± 0.5
727.5	1088.4 ± 27.7	33.6 ± 0.9	877.5	237.3 ± 11.4	10.3 ± 0.5
732.5	1158.8 ± 29.2	36.2 ± 0.9	882.5	229.7 ± 11.6	10.0 ± 0.5
737.5	1206.5 ± 29.6	38.2 ± 0.9	887.5	224.0 ± 11.6	9.9 ± 0.5
742.5	1229.9 ± 29.0	39.3 ± 0.9	892.5	196.1 ± 10.5	8.7 ± 0.4
747.5	1263.3 ± 30.3	40.9 ± 1.0	897.5	175.9 ± 9.7	7.9 ± 0.4